Thermal Modelling of a Natural-Convection-Cooled, Oil-Immersed Distribution Transformer

by

Robert Michael Marko

A thesis
presented to the University of Manitoba
in fulfilment of the
thesis requirement for the degree of
Master of Science
in
Mechanical Engineering

Winnipeg, Manitoba, Canada 1997

THE UNIVERSITY OF MANITOBA

FACULTY OF GRADUATE STUDIES

*****

COPYRIGHT PERMISSION PAGE

THERMAL MODELLING OF A NATURAL-CONVECTION-COOLED, OIL-IMMERSED DISTRIBUTION TRANSFORMER

BY

ROBERT MICHAEL MARKO

A Thesis/Practicum submitted to the Faculty of Graduate Studies of The University of Manitoba in partial fulfillment of the requirements of the degree

MASTER of SCIENCE

Abstract

A computer code was developed to implement a numerical model that predicts the temperature field in and around the core and windings of a natural-convection-cooled distribution transformer. The computer code also predicts the two-dimensional flow of transformer oil around the core and windings of a transformer. A key feature of the presented model is its detailed treatment of the geometry in two dimensions. The model requires detailed information about the transformer geometry and materials so that it can predict the effect they have on the temperature field within the transformer. A solver was developed based on the additive correction multigrid solver algorithm so that it could solve this conjugate heat transfer problem.

The mathematical model consisted of a set of differential equations expressing conservation of mass, momentum, and energy, over a Cartesian domain. The fluid was assumed to have Newtonian and laminar flow characteristics. The energy equation was modified to allow for conjugate heat transfer between a solid and the surrounding fluid. A method for modelling the windings as a homogeneous material was also introduced. The transport equations were discretized using a finite volume approach, and the pressure-velocity coupling was handled using the SIMPLEC algorithm.

A series of tests were performed to validate the computer code. Then the code was compared against another transformer model to show that it could model the general transient temperature trends. A parametric study was conducted to show the effect of two ambient conditions, and the effect of having the oil viscosity modelled as a function of temperature, on the solutions. The effect of modelling the core and windings as a homogeneous region was also explored.

The code was then tested against the ANSI loading guides for overloads. The results showed that although the maximum hotspot temperatures by the code were relatively close to those predicted by the loading guides, the maximum oil temper-

ature predicted was much lower than ANSI. The difference between the maximum temperatures was decreased when variable viscosity was employed.

Acknowledgements

I would like to thank my supervisors, Dr. S. Ormiston and Dr. Raghuveer, for their help and advice throughout the course of this study. Thanks to my students colleagues, Brent Timmerman, Peregrin Maksimovich, and Lloyd Penner, who helped with some of the ideas and concepts within the thesis. I would also like to thank Carte International Inc, Winnipeg, Manitoba, for their assistance, including a tour of their facilities.

This work was funded by Manitoba Hydro and the Natural Sciences and Engineering Research Council of Canada. Their support is gratefully acknowledged. I would especially like to thank Erni Wiebe and Glenn Paskaruk of Manitoba Hydro.

I would also like thank my girlfried, Leanne, for her patience and support during the years I spent finishing my Master of Science degree.

Contents

Abstract i

Acknowledgements iii

List of Tables x

List of Figures xiii

Nomenclature xxi

1 Introduction 1

1.1 Overview 1

1.2 Literature Review 4

1.2.1 Overview of Previous Work 5

1.2.2 Experimental Investigations 6

1.2.3 Correlation Models 9

1.2.4 Lumped Models 11

1.2.5 Equivalent Circuit Models 12

1.2.6 Finite Element and Finite Difference Models 14
1.2.7 Detailed Theoretical Analysis of Transformer Components 15
1.3 Scope and Objectives 17
1.4 Outline 22

2 The Mathematical Model **24**
2.1 Introduction 24
2.2 Governing Equations 25
2.3 General Boundary Conditions 26
2.4 Transformer Model Boundary Conditions 27
2.5 Internal Boundary Conditions 28
2.5.1 Energy Equation 28
2.5.2 Momentum Equations 29

3 Grid Generation **30**
3.1 Introduction 30
3.2 The Grid Layout 30
3.3 Grid Regions 33
3.3.1 Uniform Grid 33
3.3.2 Grid Expansion from the First Control Volume 34
3.3.3 Grid Expansion from the Last Control Volume of the Previous Grid 36

3.3.4 Grid Expansion Based on the Last Control Volume for the Current Region 37

3.4 Boundary Control Volumes 37

3.5 Grid Information Generated for the Solution Domain 38

4 The Numerical Solution Procedure **44**

4.1 Introduction 44

4.2 Discretization Equation for General Transport Equation in 2-D 44

4.2.1 Conservation of Mass 46

4.2.2 General Transport Equation 48

4.3 Distorted Transient Formulation 53

4.4 Exponential Upwind Grid Weighting 54

4.5 Energy Equation Discrete Boundary Conditions 59

4.6 Nodal Velocity Storage Location 63

4.7 Momentum Equations Boundary Conditions 64

4.8 SIMPLEC Algorithm 67

4.9 Pressure Correction 68

4.9.1 The Pressure Correction Equation 69

4.9.2 Boundary Conditions for the Pressure Correction Equation 69

4.9.3 Pressure Reference Specification 72

4.10 Solid Regions 72

4.11 The PVT-Loop 73

4.12 The Overall Steady State Convergence 75

5 Algebraic Equation Solvers **77**

5.1 Introduction 77

5.2 Line-Gauss Seidel with Relaxation in Two-Dimensions (LGS2d) 78

5.3 LU Decomposition (LUD2d) 78

5.4 Additive Correction Multigrid (ACM2d) 79

5.4.1 ACM2d Overview 79

5.4.2 ACM2d Equations 81

5.4.3 ACM2d Solution Procedure 86

5.5 Conjugate Additive Correction Multigrid (CACM2d) 90

6 Computer Code Validation Tests **94**

6.1 One-Dimensional Conduction Test Problems 95

6.1.1 Homogeneous Material 95

6.1.2 Composite Material 97

6.2 Two-Dimensional Conduction Test Problem 98

6.3 Lid-Driven Cavity Test Problems 102

6.3.1 Isothermal 102

6.3.2 Non-Isothermal 108

6.4 Natural Convection Benchmark Test 110
6.5 Conjugate Heat Transfer Test Problem 113
6.6 Conjugate Tests with an Oil-Filled Cavity 119
6.6.1 Oil-Filled Cavity with Two Thick Walls 120
6.6.2 Narrow Fluid Cavity With One thick Wall 122
6.6.3 PVT-Loop Tests 129

7 Transformer Simulations **130**
7.1 Introduction 130
7.2 Comparison of Results with Alegi and Black 131
7.2.1 Model Development 131
7.2.2 Two-Dimensional Flow Model: 49 kVA Load 144
7.2.3 Two-Dimensional Flow Model: 71 kVA Load 164
7.3 Parametric Study 174
7.3.1 Properties 176
7.3.2 Results of Parametric Study 179
7.4 Comparison with ANSI 195
7.4.1 Model Setup 195
7.4.2 Results 197

8 Closure **203**
8.1 Summary 203
8.2 Conclusions 204
8.3 Recommendations 207

A Transformer Model Selection **216**

A.1 Three-Dimensional Models 216

A.2 Two-Dimensional Models 217

A.2.1 Cylindrical Model: Single Winding and Core 218

A.2.2 Front Profile Model 219

A.2.3 Side Profile Model 220

B Details of the Computation Grids **221**

B.1 54 × 51 Grid 221

B.2 73 × 73 Grid 225

B.3 100 × 102 Grid 227

B.4 100 × 152 Grid 229

C Time and Grid Independence Test Results **231**

C.1 Time Independence 232

C.2 Grid Independence 243

D Effective Winding Thermal Conductivity **247**

D.1 Background 247

D.2 Theory for Equivalent Thermal Conductivity 248

D.3 Square Windings 252

List of Tables

4.1 Terms of the general transport equation 45

6.1 Conduction solver comparison of temperature solution. 100

6.2 Conduction field comparison of two-dimensional conduction solutions. 102

6.3 Comparison of solver effectiveness for the velocity field in the lid-driven cavity test problem. 106

6.4 Lid driven cavity field comparison of velocity solutions. 107

6.5 Comparison of solver effectiveness for the temperature field in the lid-driven cavity test problem. 109

6.6 Lid driven cavity field comparison of temperature solutions. 110

6.7 Nusselt numbers for natural convection in a cavity. 112

6.8 Natural convection solver comparison (V-cycle). 113

6.9 Natural convection solver comparison (flexible-cycle). 114

6.10 Nusselt numbers for natural convection in a cavity. 117

6.11 Properties for the narrow fluid cavity model. 124

6.12 Results for the $k_s/k_f = 10^{10}$ conjugate model with narrow fluid cavity. 124

6.13 Results for the $k_s/k_f = 1/0.45$ conjugate model with narrow fluid cavity. 125

6.14 Results for the $k_s/k_f = 1/0.45$ narrow fluid cavity with left side heat flux. 127

6.15 Results for the $k_s/k_f = 1/0.45$ narrow fluid cavity with heat generation in the solid. 127

7.1 Alegi and Black transformer data. 132

7.2 Alegi and Black thermophysical property expressions and definitions of symbols. 134

7.3 The Alegi and Black approximate model dimensions used in the present study. 140

7.4 Tank convection coefficients for the two-dimensional transformer flow model loaded at 49 kVA for comparison with Alegi and Black. 141

7.5 Tank convection coefficients for the two-dimensional transformer flow model loaded at 71 kVA for comparison with Alegi and Black. 143

7.6 Rayleigh number calculated based on Equation (7.26) for the 49 kVA load Alegi and Black simulation case. 158

7.7 Calculated effective convection coefficients at steady state for the two-dimensional transformer flow model: 49 kVA load. 159

7.8 Time constants evaluated from the two-dimensional transformer flow model: 49 kVA load Alegi and Black simulation case. 162

7.9 Rayleigh numbers calculated based on several different methods from literature for the 71 kVA load run. 173

7.10 Calculated effective convection coefficients at steady state for the two-dimensional transformer flow model: 71 kVA load Alegi and Black simulation case. 174

7.11 Parametric study run matrix. 175

7.12 Assumed transformer characteristics at rated load from ANSI. 176

7.13 Properties for the nonhomogeneous model. 177

7.14 Dimensions assumed for the square conductor windings. 178

7.15 Properties for the homogeneous solid regions. 179

7.16 Parametric study temperature rise results. 192

7.17 Parametric study steady state heat flow distribution. 193

7.18 Parametric study Rayleigh number results. 194

7.19 Breakdown of runs used for the ANSI load guides comparison. 196

7.20 Properties for the ANSI loading guide comparison model. 197

7.21 Average temperature rise over ambient temperature; results for the ANSI comparison runs. 198

B.1 Grid region specified parameters for the 54×51 grid. 222

B.2 Grid region parameters for the 73×73 grid. 226

B.3 Grid region parameters for the 100×102 grid. 228

B.4 Grid region parameters for the 100×152 grid. 230

C.1 Time and grid independence run matrix. 231

List of Figures

1.1 Simplified cross-section of a natural convection oil-cooled distribution transformer. 2

1.2 Relative location of the high and low voltage windings. 3

1.3 Dimension nomenclature for the naturally oil-cooled pole-mounted distribution transformer cross-section. 19

1.4 Several views of an oil-immersed distribution transformer. 20

1.5 Magnified view of the transformer windings cross-section. 21

2.1 External boundary conditions for the transformer model. 28

2.2 Internal boundary conditions for flow along solid regions. 29

3.1 Dividing the domain into grid regions made up of control volumes. . . 31

3.2 Grid regions for a complicated domain. 32

3.3 A typical uniform grid region. 33

3.4 A typical expanding grid region. 34

3.5 Specifying the starting control volume size based on the last control volume of the previous grid. 36

3.6 The boundary control volumes surrounding the solution domain. . . . 38

3.7 The grid indices for the solution domain. 39

3.8 The indexing and notation for the reference control volume and its neighbouring control volumes. 40

3.9 The quadrant nomenclature for a control volume. 41

3.10 The coordinate nomenclature for a control volume. 41

3.11 The nomenclature for the control volume length segments. 42

3.12 The nomenclature for the control volume area segments. 42

3.13 The volume nomenclature for the control volume segments. 43

4.1 General control volume nomenclature. 46

4.2 Conservation of mass control volume. 47

4.3 Harmonic mean nomenclature. 53

4.4 A typical control volume cluster for the one-dimensional problem. . . 55

4.5 Nomenclature for the exponential upwinding scheme. 56

4.6 Comparison of the relative difference between uniform vs. non-uniform grid α-equations on the face temperatures. 59

4.7 Fictitious control volume nomenclature for Dirichlet boundary conditions. 60

4.8 Fictitious control volume nomenclature for a Neumann boundary conditions. 61

4.9 Fictitious control volume nomenclature for Newton boundary conditions. 62

4.10 Staggered grid for U-velocity. 64

4.11 Staggered grid for V-velocity. 65

4.12 Right U-velocity boundary control volume. 66

4.13 Pressure correction boundary conditions. 70

4.14 PVT-loop flowchart for a single time step. 74

5.1 Additive correction multigrid reducing low frequency errors and introducing high frequency errors. 81

5.2 An example of the levels involved when solving an ACM model. . . . 82

5.3 Schematic showing the assembly of one-dimensional control volumes on the fine grid to create blocks for the coarser grid. 83

5.4 Schematic showing the assembly of two-dimensional control volumes on the fine grid to create blocks for the coarser grid. 86

5.5 Flowchart showing an example of the V-cycle algorithm with only five levels. 87

5.6 The flexible cycle of B.R. Hutchinson and G. D. Raithby. 88

5.7 CACM2d assembling the control volumes into coarser blocks while keeping the solid region separate from the fluid. 92

5.8 Illustration showing the CACM algorithm assembling the level 1 control volumes for the level 2 blocks in a composite two-dimensional region. 93

6.1 One-dimensional conduction benchmark. 96

6.2 One-dimensional conduction benchmark with two materials. 98

6.3 Boundary conditions for conduction benchmark. 99

6.4 Lid-driven cavity test problem. 103

6.5 Velocity centerline profiles for the square cavity ($Re_{Lid} = 400$). 104

6.6 The velocity centerline profiles for the square cavity ($Re_{Lid} = 5000$). . 105

6.7 Lid driven cavity nomenclature for the temperature benchmark. . . . 108

6.8 Boundary conditions for natural convection in a cavity. 111

6.9 Conjugate benchmark; natural convection with finite walls. 115

6.10 Nomenclature for the conjugate Nusselt number calculation for natural convection within a square cavity with finite walls. 116

6.11 Temperature contours in the thick walled cavity for $Ra^* = 10^6$. 118

6.12 Streamlines for the thick walled cavity for $Ra^* = 10^6$. 119

6.13 Illustration showing the setup and nomenclature for the square oil cavity with two conjugate walls test. 121

6.14 Schematic illustration of a narrow cavity, conjugate heat transfer model with dirichlet boundary conditions. 123

6.15 Schematic illustration of a narrow cavity, conjugate heat transfer test with a constant heat flux. 126

6.16 Schematic illustration of a narrow cavity, conjugate heat transfer test with energy generation within the solid. 128

7.1 Alegi and Black lumped model energy flow diagram. 132

7.2 Dimension nomenclature for the Alegi and Black comparison model. . 138

7.3 Model layout showing the nomenclature of θ, the temperature rise above ambient. 145

7.4 Comparison of the 49 kVA load results showing the temperature rise above the ambient temperature of 20°C. 146

7.5 Elapsed time temperature results at steady state; starting from a datum of $t_0 = 138,225$ seconds for the 49 kVA Alegi and Black simulation case. 149

7.6 Elapsed time streamline results at steady state; starting from a datum of $t_0 = 138,225$ seconds for the 49 kVA Alegi and Black simulation case. 150

7.7 Elapsed time streamline results at steady state; starting from a datum of $t_0 = 138,255$ seconds for the 49 kVA Alegi and Black simulation case. 151

7.8 Elapsed time streamline results at steady state; starting from a datum of $t_0 = 138,285$ seconds for the 49 kVA Alegi and Black simulation case. 152

7.9 Elapsed time streamline results at steady state; starting from a datum of $t_0 = 138,315$ seconds for the 49 kVA Alegi and Black simulation case. 153

7.10 Normalized tank surface heat flow for the two-dimensional transformer flow model: 49 kVA load. 154

7.11 Steady state heat flow check for the two-dimensional transformer flow model: 49 kVA load. 155

7.12 Rayleigh numbers evaluated from the two-dimensional transformer flow model: 49 kVA load. 156

7.13 Normalized transient temperature to determine the time constants of the core and windings for the two-dimensional transformer flow model: 49 kVA load for the Alegi and Black simulated case. 161

7.14 Normalized transient temperature to determine the time constants of the side and top oil regions for the two-dimensional transformer flow model: 49 kVA load for the Alegi and Black simulated case. 163

7.15 Comparison of the 71 kVA load results showing the temperature rise above the ambient temperature of 20°C. 165

7.16 Elapsed time temperature results at steady state; starting from a datum of $t_0 = 235,675$ seconds for the 71 kVA Alegi and Black simulation case. 167

7.17 Elapsed time streamline results at steady state; starting from a datum of $t_0 = 235,675$ seconds for the 71 kVA Alegi and Black simulation case. 168

7.18 Elapsed time streamline results at steady state; starting from a datum of $t_0 = 235,705$ seconds for the 71 kVA Alegi and Black simulation case. 169

7.19 Normalized tank surface heat flow for the two-dimensional transformer flow model: 71 kVA load. 170

7.20 Steady state heat flow check for the two-dimensional transformer flow model: 71 kVA load. 171

7.21 Rayleigh numbers evaluated from the two-dimensional transformer flow model: 49 kVA. 172

7.22 Parametric study case A1. 180

7.23 Parametric study case A2. 181

7.24 Parametric study case A3. 182

7.25 Parametric study case A4. 183

7.26 Parametric study case B1. 184

7.27 Parametric study case B2. 185

7.28 Parametric study case B3. 186

7.29 Parametric study case B4. 187

7.30 Parametric study case C2. 188

7.31 Parametric study case C4. 189

7.32 Parametric study case D2. 190

7.33 Parametric study case D4. 191

7.34 Step loading the transformer. 196

7.35 Transient temperature monitoring for run ANSI1. 199

7.36 Transient temperature monitoring for run ANSI2. 200

7.37 Transient temperature monitoring for run ANSI3. 201

7.38 Transient temperature monitoring for run ANSI4. 202

A.1 Various views of a two winding transformer. 217

A.2 Cylindrical model of a single winding and the core. 218

A.3 Front profile model of a tranformer. 219

A.4 2-D side profile model of a transformer. 220

B.1 Grid regions for the grid independence transformer grid. 223

B.2 54×51 Grid for the grid independence check. 224

B.3 73×73 Grid for the grid independence check. 225

B.4 100×102 Grid for the grid independence check. 227

B.5 100×152 Grid for the grid independence check. 229

C.1 Region layout for transformer model. 232

C.2 Alegi and Black time independence run for 54x41 grid: core and windings. 234

C.3 Alegi and Black time independence run for 54x41 grid: right oil cavity. 235

C.4 Alegi and Black time independence run for 54x41 grid: top oil cavity. 236

C.5 Alegi and Black time independence run for 100x102 grid: core and windings. 237

C.6 Alegi and Black time independence run for 100x102 grid: right oil cavity. 238

C.7 Alegi and Black time independence run for 100x102 grid: top oil cavity. 239

C.8 Alegi and Black time independence run for 73x73 grid: core and windings. 240

C.9 Alegi and Black time independence run for 73x73 grid: right oil cavity. 241

C.10 Alegi and Black time independence run for 73x73 grid: top oil cavity. 242

C.11 Alegi and Black grid independence run: core and windings. 244

C.12 Alegi and Black grid independence run: right oil cavity. 245

C.13 Alegi and Black grid independence run: top oil cavity. 246

D.1 A typical windings section that must have effective thermal conductivities calculated for both the x and y directions. 249

D.2 Equivalent circuit illustration for constant heat flow. 250

D.3 Equivalent circuit illustration for parallel isotherms. 251

D.4 Cross-section of the square winding. 253

D.5 Equivalent circuit illustration for constant heat flow in the x direction of the square winding. 253

D.6 Equivalent circuit illustration for parallel isotherms in the x direction of the square winding. 254

Nomenclature

A	area [m^2]
a	coefficient in algebraic equation
$\bar{a}$	coefficient in algebraic equation for multigrid
a_P^*	sum of neighbouring coefficients ($\sum a_{np} = a_E + a_W + a_N + a_S$)
Bi	Biot number
b	source term in algebraic equation
$\bar{b}$	source term in algebraic equation for multigrid
C_t	lumped thermal capacitance of the solid [hrs]
c_p	specific heat [J/kg K]
D	diffusion coefficient [m^2/s]
d	length segment of control volume [m]
d	SIMPLEC weighting term for velocity correction
E	distorted transient time factor (E-factor)
e	PVT-loop relaxation term
f	function
f	interpolation coefficient
G	equal to $\frac{\xi_P M_P^o}{\Delta t}$
Gr	Grashof number
g	gravitational acceleration [m/s^2]

H	height [m]
h	convection coefficient [W/m^2 K]
$\overline{h}$	average convection coefficient [W/m^2 K]
h_a	height of the air gap [m]
h_c	height of the core [m]
h_g	height of the column of oil above the core and windings [m]
h_o	height of the windings above the bottom of the core [m]
h_t	height of the tank [m]
h_w	height of the windings [m]
ib	index for the first control volume in the x direction
ie	index for the last control volume in the x direction
J	total heat flux [W/m^2]
jb	index for the first control volume in the y direction
je	index for the last control volume in the y direction
k	thermal conductivity [W/m K]
L	length of domain region [m]
l	inner length of the conjugate benchmark test problem [m]
M	mass [kg]
m	mass [kg]
$\dot{m}$	mass flow rate [kg/s]
N	number of control volumes
N	multigrid level number
Nu	Nusselt number
$\overline{Nu}$	average Nusselt number
P	pressure [N/m^2]
P'	pressure correction [N/m^2]
Pe	Peclet number

Pr	Prandtl number
Q	rate of energy generated [W]
Q	lagged part of linearlized source term [W]
$\overline{Q}$	average heat flow
$\dot{Q}'''$	volumetric rate of energy generated [W/m^3]
q	heat flow [W]
R	active nodal part of linearized source term [W]
R	thermal resistance [K/W]
$\widetilde{R}$	residual of control volume
R_t	resistance to convection heat transfer [K/m^{2}W]
Ra	Rayleigh number
Ra^*	Rayleigh number for conjugate benchmark test problem
Ra^*	Rayleigh number for protruding heat sources
Re	Reynolds number
r	grid aspect ratio
S	linearized source term
T	temperature [K]
$\overline{T}$	average temperature [K]
T^*	normalized temperature [K]
T_w	wall interface temperature for a control volume [K]
t	time [s]
U	x direction velocity component [m/s]
V	y direction velocity component [m/s]
$\forall$	volume [m^3]
W	width [m]
w	inner width of the conjugate model [m]
x	distance in the x direction [m]

x_c	half the width of the core (or the width of the core in the symmetrical transformer cross-section view) [m]
x_d	width of a duct [m]
x_t	radius of the tank in the Alegi and Black test problem [m]
x_w	total thickness of the windings around the core [m]
y	distance in the y direction [m]

Greek Letters

α	convective weighting coefficient for upwind differencing
α	thermal diffusivity [m^2/s]
α	absorptivity
β	diffusive weighting coefficient for upwind differencing
β	thermal coefficient of volume expansion [1/K]
Γ	general diffusion coefficient [m^2/s]
Δ	measure of field change per step, compared to convergence criterion
δ	correction
δz	depth of tank [m]
ϵ	relative error
ϵ	convergence criterion
ϵ	emissivity
ϵ_L	multigrid residual reduction convergence criterion at a level
ϵ_s	multigrid residual reduction stall criterion
η	grid expansion coefficient
θ	temperature rise above ambient ($T - T_\infty$) [K]
κ	loop count for PVT-loop

λ	solver iteration count
ξ	specific heat for energy equation, otherwise equal to 1.0
μ	absolute viscosity [kg/m s]
ν	kinematic viscosity [m^2/s]
ρ	density [kg/m^3]
σ	Stefan-Boltzmann constant (5.67×10^{-8} W/m^2K^4)
τ	time constant [hrs]
Φ	boundary condition value
ϕ	general variable (referring to U or V Velocity, T or P')
$\tilde{\phi}$	best estimate of general variable (ϕ)
ω	iteration count for a visit at a level in the multigrid algorithm

Subscripts

$A+B$	Alegi and Black
avg	average
B	bottom
b	boundary
C	cold
c	conduction
c	core
$c+w$	core, and coil assembly (windings)
$calavg$	calculated average
$crit$	critical
cu	copper
E, W, N, S	referring to the nodal quantities to the east, west, north, and south

	of the present control volume
e, w, n, s	referring to the face quantities to the east, west, north, and south of the present control volume
eds	exponential differencing scheme
eff	effective
eq	equivalent
f	fictitious
f	fluid
f	film (used for fluid properties)
$free$	free convection only
gen	generation
H	hot
HV	high voltage
$HV1$	HV winding section number one
$HV2$	HV winding section number two
i	control volume indexing in x direction
i	incident radiation
j	control volume indexing in y direction
k	multigrid block index for x direction
L	left
L	level
LV	low voltage
l	multigrid block index for y direction
NE, NW, SE, SW	referring to the nodal quantities to the northeast, northwest, southeast, and southwest of the present control volume
nb	neighbour points
o	fluid oil

P	referring to the present control volume
p	reference to the last control volume of the previous grid region
pvt	PVT-loop
R	right
r	radiation, radiated
rad	radiation, radiated
s	solid
sur	surface
$spec$	specified
ss	steady state
T	top
t	tank
u	uniform grid
w	coil assembly (windings)
x	x direction
y	y direction
∞	surrounding or ambient

Superscripts

c	mass conservation
n	iteration number
o	old
p	pressure correction
T	temperature
u	U velocity

v	V velocity
$''$	surface flux
$'''$	volumetric
$+$	right, or top, region/control volume
$-$	left, or bottom, region/control volume
$\cdot$	rate
$\bar{}$	averaged
$*$	guessed or old values

Acronyms

ACM2d	Additive correction multigrid solver in two-dimensions
CACM2d	Conjugate additive correction multigrid solver in two-dimensions
LGS2d	Line-Gauss Seidel solver in two-dimensions
LUD2d	LU Decomposition solver in two-dimensions
NX	number of control volumes in the x direction
NY	number of control volumes in the y direction
SIMPLEC	SIMPLE-Consistent

Chapter 1

Introduction

1.1 Overview

Electric utilities use power station generators to produce electrical power. The voltage level varies in the process of conveying the electrical power from the generating station to the consumer. A transformer at the power station is used to increase, or 'step up', the voltage and then transmission lines convey the electrical energy to a substation. The transformer, or transformers, at the substation reduce, or 'step down', the voltage. Once the voltage is down to distribution levels, the electrical energy is distributed to customers via a distribution grid [7].

Transformers are stationary devices capable of converting alternating current (AC) energy from one voltage level to another. While power transformers aid in the transmission and sub-transmission of high voltages, distribution transformers reduce the voltage, typically between 4 kV and 35 kV, to a level used by the customer (480 V or less).

Figure 1.1 shows the main components of a natural convection oil-cooled, distribution transformer. The transformer consists of a closed magnetic circuit (the core)

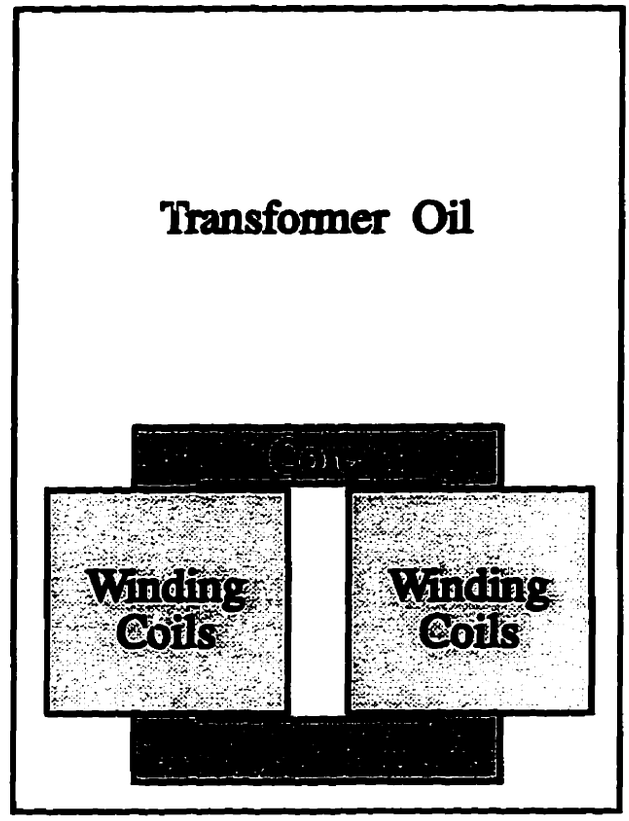

Figure 1.1: Simplified cross-section of a natural convection oil-cooled distribution transformer.

with two coils, or windings, of insulated conductors wound around the core. The current in the input, or primary, coil creates a magnetic field. This field induces a voltage across the output, or secondary coil. The secondary coil of a distribution transformer is designed to deliver energy at a lower level of voltage relative to the input voltage. For a distribution transformer, the high voltage winding is the primary coil and the low voltage winding is the secondary coil. The low and high voltage windings are shown in Figure 1.2.

As the current passes through the copper or aluminum windings, energy is lost

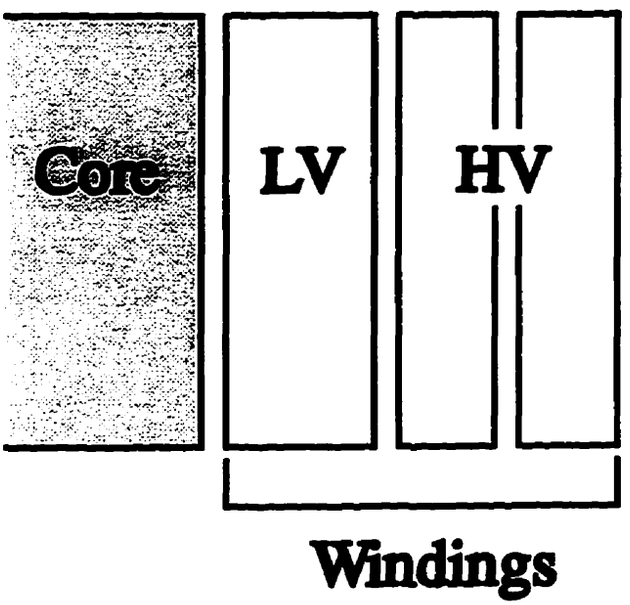

Figure 1.2: Relative location of the high (primary) and low (secondary) voltage windings.

because of electrical resistance power losses (Power = Current^2 $\times$ Resistance). The energy losses raise the temperature of the windings. Various methods of dissipating energy to the surroundings are employed to cool the windings. The temperature rise is controlled by transferring energy generated from the transformer to a cooling fluid, such as oil or air.

Excess heating accelerates the aging of the transformer insulation. When the oil-paper insulation is subjected to thermal stress, the oil and paper components of the insulation may be irreversibly damaged. The thermal stress reduces the mechanical and dielectric performance of the insulation [22].

There is a need to optimize the design and application of transformers. Manufacturers and utilities try to reduce the capital and operational costs of transformers. Since modern transformers are believed to be underrated and therefore possess some

inherent reserve capacity beyond the nameplate rating, many utilities wish to establish higher loading capability limits for either operation during normal system conditions, during emergencies, or both. Although the thermal phenomena within a transformer are not fully understood, transformers are used well above their nameplate ratings. The risk is felt to be acceptable and justified in order to maximize the economic capacity of a transformer [40].

While attempting to maintain the transformer's electrical performance, the designers must try to decrease the weight of the transformer and to increase the heat transfer from the windings and core. The size and position of the core and windings, the volume of oil, and the size of the tank all affect the rate at which heat is removed from the windings. Ducts are usually placed within the windings to increase the heat transfer by allowing the oil to flow over more winding surface area. The conducting and insulating materials may vary in composition and proportion between transformers. The design of the transformer must also account for changes in the ambient conditions, including parameters such as incident solar radiation, and ambient temperature and air flow. The load on the transformer may be either constant, or cycle over a period of time.

1.2 Literature Review

In order to provide some background to the present work, a review of previous research is given in this section. The section begins by giving an overview of existing literature. A literature review is then given for each type of investigation: experimental, correlation models, lumped models, equivalent circuit models, and finite element and finite difference based models. This is followed by a review of the detailed theoretical work done on the transformer components.

1.2.1 Overview of Previous Work

There have been several models derived to predict the hotspot temperature of the transformer windings. These models range from simple correlations to complicated three-dimensional finite element models. Since it is difficult to obtain direct measurements of the hotspot temperature, no models have been thoroughly validated.

Previous research may be grouped into five categories. They are experimental work, transformer correlations, lumped models, equivalent circuit models, and finite element and finite difference models. An example of a transformer correlation is the ANSI loading guide [3]. Correlation models tend to simplify the problem to the point where changes in the geometry have little effect on the overall solution. Lumped models improve upon transformer correlations, but they still do not account for the exact physical dimensions of the transformer. Coupled flow and thermal circuits take the principles of lumped models a step further by including more transformer components in the model. In those models, attempts are made to include the effects of the coolant flow around the core and windings and through the ducts. Detailed numerical models in the literature further divide the model but they still do not calculate the detailed oil flow field around the transformer.

It is difficult to determine experimentally the temperature field within the transformer tank. When sensors are inserted into the transformer they disturb the normal winding construction and therefore alter the thermal properties of the windings. Computer models can help in the prediction of the temperature field. Although most models give overall values such as hotspot temperature and top oil temperature, a detailed numerical solution may help to improve the design. Past computer models have divided the transformer into small sections and produced an approximate solution using a finite element method, but these computer models only use correlations to model the convective heat loss from the core and windings to the oil, from the oil

to the tank walls, and from the tank walls to the environment.

The following subsections present brief descriptions of the existing solution methods used to study the temperature, velocity, and pressure fields within transformers.

1.2.2 Experimental Investigations

The multiflow method presented by Carruthers and Norris [10] in 1969 determined the hottest-spot temperature based on measurements made during a single temperature-rise test on a transformer. Their work showed that the multiflow method would allow for higher average winding-temperature rises without any increase in either the hottest-spot temperature or the hottest-oil temperature. Rele and Palmer [57] developed an improved method of measuring and calculating temperature rise test data by statistical curve fitting the data. The method developed gave better agreement between measurement and calculated results than previous methods.

Aubin et al. [4] developed new methods for measuring the hottest spot temperature in a power transformer. Several methods were considered, but only two measuring approaches were selected for testing. The first method used a heat degradable compound which was added to the transformer oil. A disadvantage of this method is the tendency for the compound to deposit on the windings since it could not be dissolved by the oil. The second method involved taking an oil sample from the cooling ducts. A Teflon tube piped the oil away to a location where the temperature could be measured with a thermocouple. This method required that the hottest spot location must be known in advance.

In 1981, Beavers [6] showed that hot-resistance measurements can be used to determine the effective oil temperature and time constant of each individual winding, as well as the winding temperature at the instant of shutdown. The method Beavers described assumed that the windings cool exponentially from the highest average

temperature, at the instant of shutdown, to the average oil temperature. The results of his model agreed closely with the American Standards Association Test Code.

Buchan [8] reported that the presence of hot spots can be detected by the continuous measurement of dissolved carbon dioxide gas in the transformer oil. The production of carbon dioxide from the oil/paper insulation speeds up dramatically at a threshold temperature of 140°C.

McNutt et al. [40] embedded fiber optic temperature sensors directly within the windings of a large auto-transformer to measure hot spot temperatures under a variety of loading conditions. The experiment demonstrated that accurate conductor temperature data can be obtained, but that probe insertion methods are critical. The data calculated can be used with industry loading guide equations (ANSI/IEEE C57.92-1981) to improve the prediction under any loading conditions.

Pierce [47] conducted a comprehensive thermal test program on a 2000 kVA cast-resin dry type transformer. Three hundred embedded thermocouples were used to determine the hottest spot temperature and to obtain data to develop mathematical models. The test data indicated that the hottest spot temperature allowance used in the IEC standard is too low, and the IEEE standard appears conservative up to a 115°C average winding temperature rise. The data indicated that the ratio of hottest spot temperature rise to average temperature rise at different loads only varied slightly. Pierce recommended that the ratio be different between self-cooled and forced-air transformers. The time constants were also found to be different for the high voltage winding and the low voltage winding.

Dooher and Elliott [16] measured the transient and steady-state responses of a three-phase 30-MVA (megavoltampere) natural convection type, non-directed flow power transformer. The temperature responses were measured under two oil cooling conditions - natural air (OA) and forced air convection (FA) - and under a third

condition with a forced oil auxiliary cooling system (FOA). The results show that the industry loading guide equations developed by IEEE (ANSI C57.92-1981) do not provide accurate winding temperature predictions under these conditions. The data also showed that the top oil temperature is not an effective indicator of transformer operating conditions. The temperature in the windings was found to vary nonlinearly from bottom to top. The auxiliary cooler significantly reduced winding temperatures, but the oil flow must be optimized to maximize heat transfer. Dooher and Elliott finally conclude that an auxiliary cooling device can safely extend the rating of a large core-type transformer beyond its nameplate rating.

Nauert [44] mentions that by 1994, Union Electric Co. (U.E.) stopped using only a single specification of nameplate rating for a transformer. Instead they now specifiy load profile, ambient temperature, acceptance criteria, and the means of evaluation. Lahoti and Flowers [36] developed an evaluation of transformer loading capabilities, including the combined effect of thermal aging of insulation, short circuit stresses, and transient overvoltages, as well as limitations on the transformer components other than the windings.

Several researchers have investigated the effect of sub-zero temperatures on transformers. Barrios and Council [5] presented a method for establishing winter loading guidelines based on data collected from several overloaded transformer runs at different ambient temperatures. Eastgate [18] examined the effect of sub-zero transformer operation by running detailed heating cycles for a typical range of distribution transformers. They concluded that oil-immersed transformers may be freely used down to temperatures of $-20°C$. Operation in cooler temperatures may be cause for concern. Au Yeung and Walker [66] validated the extrapolation of the ANSI guidelines on the loss of insulation life of distribution transformers during cold load pickup at low ambient temperatures. After testing the transformers at ambient temperatures between $0°C$ and $-40°C$ the researchers concluded that the ANSI guidelines are con-

servative when predicting transformer life expectancy at low ambient temperatures. Lampe [37] explored the use of power transformers and shunt reactors at temperatures below −50°C, and concluded that cold starts should be avoided and that only approved naphtenic oils with low viscosity should be used. For distribution transformers, Miller et al. [41] attempted to predict the cold load peak duration produced from electrically heated homes after a power outage. A "lumped heat" capacity method is used to predict the magnitude of the cold load peak for a given home. A hypothetical subdivision of ten homes of various sizes was modelled, and the effect of the cold load on a 100 kW distribution transformer was determined.

The experimental results found in literature tend not to contain enough information to be used in a numerical model. For the present work, the important information that can be gleaned from these sources is that top oil is not a good indicator of hot spot temperature, and that each winding has a different time constant.

1.2.3 Correlation Models

A simple transformer model is made up of a set of correlations. The correlations may model transient and steady-state conditions using the results of previously tested models. The most well known set of transformer correlations is the ANSI Standards [3]. These loading guides are used to estimate the top-oil rise, the hottest-spot temperature, and the percent loss of life of the transformer based on the transformer nameplate rating, ratio of losses between the windings and the core, time constant of the transformer unit, the hottest-spot conductor temperature rise over oil, and the load profile expected to act on the unit.

Although the ANSI Standards are widely used, the loading guide approximations cause transformers to be over designed [48]. The temperatures predicted by the ANSI guide are well above the actual values. In an attempt to increase the accuracy of the

standards, many modifications have been published. Pierce wrote several papers describing his improvements to the ANSI loading guides. These modified loading guides accounted for oil viscosity and electrical resistance changing with temperature, cooling duct oil rise, and the hot spot location [48]. An experiment was conducted on a full size winding assembly imbedded with thermocouples. The results of the experiment were used to improve the existing winding loading guides.

Another modified prediction model was designed by Pierce [52, 49, 53] based on analysis and testing to account for the type of liquid coolant, cooling mode, winding duct oil temperature rise, resistance and viscosity changes, and ambient temperature and load changes during a load cycle. The equations make use of both the top and bottom oil temperature rises. They were developed based on fluid flow and heat transfer principles. The improved loading equations give a more accurate method of predicting liquid and winding hottest spot temperatures in liquid-filled transformers during transient loading conditions. The improved loading equations predict more loading capacity for non-directed FOA units, and less loading capability for FA rated units during high, short duration overloads. The equations were verified using test data. With this model, Pierce attempted to account for the time lag between the top oil temperature rise and the oil temperature rise in the winding cooling ducts by using a transient forward marching finite difference calculation procedure.

Pierce [50] also reported that six full size test windings were manufactured with imbedded thermocouples. On these windings, 133 test runs were performed to obtain temperature rise data. Pierce suggests that a constant ratio of hottest-spot winding temperature rise to average winding temperature rise should be used in product standards for the insulation temperature classes. A ratio of 1.5 is suggested for ventilated dry type transformers above 500 kVA. Different hottest spot temperature allowances should be used for ventilated dry type transformers 500 kVA and below.

In 1984, Buchan and Green [9] suggested that the constants used by the ANSI loading guides needed to be modified. They developed new constants based on their theoretical work to make a more versatile and accurate model. A theoretical analysis of heat input and heat flow by conduction, convection, and radiation, provided a guide for adjusting the ANSI model. Heat run tests were performed on four different transformers - three with a 10 kVA ratings and one with a 25 kVA rating. Their experimental work showed that they improved the ANSI loading guides from an accuracy of ±10°C to within ±2°C of measured results. They also describe the development of a more versatile and accurate model.

In 1983, Wilde [63] analyzed the characteristics of residential customer loads and determined the effect of these loads at low ambient temperatures. A first order thermal model is used. Two outages during the winter of 1982 on the Ottawa Hydro system were used to validate the model.

1.2.4 Lumped Models

Several researchers have tried to improve upon the predictions of the ANSI loading guides by designing lumped models. The model consists of several components, and energy conservation is applied to each part. The model is called "lumped" because the entire system is the sum of a few homogeneous, isotropic components. The isotropic components may represent many smaller nonhomogeneous objects that are lumped together to simplify the problem. For instance, the windings that are made up of the conducting material, oil, and insulating paper, are lumped together for purpose of simplifying the model. The set of energy balance equations is used to model the transient heat transfer once the appropriate boundary conditions have been prescribed.

Allen and Childs [2] designed a disc type windings transformer model made up

of thermal and fluid flow circuits. The thermal model presented contained several finite difference and lumped models that are connected by a thermal circuit. The electrical analogue network calculates the oil flow rate in the duct circuits. The two circuits are solved by iteration. Allen and Childs found very good agreement when they compared their model with their experimental results.

In 1990, Alegi and Black [1] developed a thermal model for predicting the real-time temperatures of an oil-immersed, forced-air cooled transformer. The thermal model consisted of a set of three differential equations that were used to solve for the time-varying temperatures of the core and coil assembly, the oil, and the tank. Expressions for the convection heat transfer coefficients are used between the components even though these correlations are only for steady-state problems. Heat transfer by incident solar radiation, thermal radiation exchange with the environment, and ambient convection cooling the tank and the cooling tubes, are all included in the model. Only the experimental results for a 75 kVA transformer were used to validate the theory. The model was tested with two step loads, each applied after the transformer achieved a steady-state condition. The run was performed indoors without a cooling assembly, and without incident solar radiation on the transformer. The predicted results for the run were conservative by approximately 5°C at steady state when compared with the temperature measurements. The model was then used to analyze a 5,000 kVA transformer run for a 24 hour load cycle. This transformer had a cooling assembly and was exposed to incident solar radiation.

1.2.5 Equivalent Circuit Models

An improvement on the lumped sum model is the equivalent circuit model. The transformer components are divided up into smaller pieces so that the temperature can be predicted in more detail. Each piece is coupled by the heat transfer and

convective flow between the pieces.

Imre et al. [29] modelled the coupled problem by designing both a mass flow and a heat flow network to determine the steady state temperature field in a naturally oil-cooled disc-type transformer. While the mass network was for non-isothermal flow conditions, the heat flow network model of the coil was prepared so that the heat capacitance of the cooling media flow corresponded to the branch fluxes in the mass flow network. The networks were solved together by iteration.

Yamaguchi et al. [65] presented another method of calculating the flow rates of circulating oil in self-cooled transformers. The flow rate is calculated by equating the pressure loss with the thermal driving force in a circulating loop. The pressure loss and the velocity distribution in the horizontal ducts were calculated using an oil flow circuit in the winding. The calculated and measured results agreed within 15% when compared with a testing apparatus.

In 1984 Lindsay [39] modelled an oil-filled transformer as a fifth order system. The transformer was considered to consist of five parts: the high voltage windings, the low voltage windings, the core, the oil, and the tank. A systematic procedure was developed to determine the eight thermal conductances of its analogous circuit. The thermal conductances varied as a function of the mean temperature rise of the oil. The model was set up to predict the response of a transformer to a typical daily load cycle. The model was tested on the steady-state simulations of two identical pole-mounted transformers rated at 10 kVA, 230/115 V. The predicted rise in temperatures agreed well with the actual values, even when the load was changing rapidly. The weakness of this model is that the thermal conductances must be obtained as a function of the mean oil temperature rise through previous experimental results on a specific transformer.

1.2.6 Finite Element and Finite Difference Models

Finite element or finite difference models represent a further refinement of the equivalent circuits models. The transformer, tank, and oil, are broken down further into smaller elements or volumes. Although differing in mathematical approach, each method defines a smaller region (smaller than the lumped model) called a finite element or a control volume. A governing differential equation is solved discretely over all the smaller regions to get a higher resolution of the local temperature field. This method is also used to calculate the details of the fluid flow.

Szpiro et al. [61] only modelled the flow of the transformer coolant through disc winding sections of five and eight ducts. The model uses two-dimensional Cartesian momentum and the mass conservation equations. The flow is calculated using the stream function-vorticity method. A central difference finite difference approximation is used for the two-dimensional flow calculations in the ducts.

Hwang et al. [28] compared winding temperature predictions from a finite element based method with the measured values of a 10 kVA oil-immersed wire-wound single phase distribution transformer. The results of several 60 Hz tests validated the prediction algorithm and illustrated that the position of the hot-spot remains basically unchanged when harmonics are introduced in the numerical model.

Douglas and Jessee [45] presented their own model for analyzing high-frequency transformers in 1992. Their model is based on the simultaneous solution of coupled, nonlinear thermal and electromagnetic equations. The transformer is modelled as two-dimensional and axisymmetric. Natural convection in the air gaps between the windings and the core is neglected. A quasi-steady formulation of the heat-conduction equation eliminated the time dependency of the thermal problem.

In 1994, Carstea [11] developed a finite element method for calculating the temperature field in natural and forced flow, oil-immersed transformers. Cylindrical

coordinates were used to model the steady-state temperature rise of the transformer windings. The heat transfer within the ducts was assumed to be by conduction only. Convection heat transfer from the core and the windings to the oil was modelled by a correlation that employs an average Nusselt number. Radiation heat transfer was neglected, but the model accounted for oil property changes with temperature.

Pierce [51] presented a three-dimensional finite difference model for the thermal conduction within a transformer core and windings. Three different thermal conductivities were used to represent the nonhomogeneous nature of the windings. The code accounted for radiation and convection using correlations for heat transfer from the windings and the core to the oil. Test data from six layer type test windings and a three phase 2500 kVA prototype was used to refine the model. The purpose of the windings test was to obtain a correlation for the local heat transfer coefficient in the cooling ducts.

1.2.7 Detailed Theoretical Analysis of Transformer Components

There has been extensive research conducted for each transformer component. Information about components, such as duct heat transfer and oil properties, is important to the understanding of the transformer heat transfer physics. This section gives a brief overview of the work in this field.

Stenkvist [59] decribed the oil flow in large oil-immersed transformers. Both forced oil cooling and natural oil cooling were described in detail, based on experimental results. An attempt was made to explain the behavior of the oil flow.

Langhame et al. [38] compared the test results of a reference naphthenic oil and an experimental paraffinic oil at low temperatures. The test results show that the viscous properties of the parraffinic oil are unacceptable for use below $-20°C$.

Kunes [34] conducted several tests to obtain data on the characteristics of thermosiphon oil flow in transformers. The paper reports that there is a correlation between the relative elevation of the heat source and the heat sink, and the top-to-bottom oil temperature difference. Good oil circulation occurs when the transformer core-and-coil assembly is positioned low in the tank. The tests confirm that when the transformer is positioned high in the tank, poor oil circulation results in high top-to-bottom oil temperature differences and a high hot-spot temperature rise. Kunes also states that only the oil adjacent to the hot and cold surfaces is active in heating and cooling the oil. The bulk of the oil does not take an active role in the heat transfer process. A recommendation to reduce the central oil column is given.

Taylor et al. [62] studied the heat-transfer properties of cooling ducts in natural convection transformer coils. Two types of windings were investigated: vertical-layer winding and disc winding. Taylor et al. stated that their data may be used to predict the hot-spot temperature of a transformer in service.

Moore [43] discussed in detail the radiation exchange between the environment and a corrugated body such as a transformer tank. Moore concerned himself with finding the total radiation per unit length from a rectangular slot that is infinitely long, 2 inches wide, and 8 inches deep.

Montsinger and Wetherill [42] validated some test results on transformers subjected to service conditions using radiation theory. The test results show no advantage for light colors on lowering the transformer temperatures in a hot climate. The radiation calculations accounted for the ratio of the area of the surface exposed to the sun to the total surface dissipating energy, the difference in thermal capacities, and the case where the test piece is also dissipating energy. Montsinger and Wetherill concluded that the color of the tank paint may only affect the transformer temperature by one or two degrees centigrade when the tranformer operates in direct sunlight.

Gupta et al. [22] summarized the state of insulation aging about insulation life and remaining life of operating power transformers. Aging mechanisms such as thermal, electrical, mechanical, and environmental are summarized, as well as general information about the prediction of insulation life.

Rele [56] reviewed the basic principles of transformer thermal design. The focus was to reduce the cost of cooling the transformer without exceeding temperature limits. Rele presented calculations assuming that the top oil temperature in every winding is the same as the top oil temperature in the tank. Experiments were performed on a 49 MVA single-phase prototype transformer.

1.3 Scope and Objectives

There are many models attempting to predict the phenomena inside the transformer. Some are based on correlations, simplifying the geometry of the problem and reducing the parameters to one time constant. Lumped-sum models improve upon these approximations but still oversimplify the transformer model by not accounting for the position of the transformer relative to the bulk of the oil coolant and the tank, and by considering only one temperature to be representative of a whole region. Equivalent circuit models couple the heat fluxes between components, and some even attempt to account for the fluid flow, but they do not contain enough detail of the transformer to properly capture the thermal behavior of the system. Previous work with finite element and finite difference models has attempted to model the transformer with more precision by accounting for the physical dimensions of the core and windings. However, none of these models has accurately resolved the flow of oil around the core and windings simultaneously with a temperature field calculation. The flow of oil is the principle medium of energy dissipation. A more accurate prediction of oil flow and heat transfer in the oil should significantly improve the transformer thermal

model.

Although there are many models to predict either the average or hotspot temperatures of transformers, they all neglect the effect of many geometric details and thermal properties. But even with their considerable assumptions some models still produce reasonable hotspot temperature predictions. Nevertheless, a detailed model is needed to improve the accuracy of hotspot temperature and location predictions so that manufacturers and utility companies can economically maximize the use of a transformer, and designers can assess the effect of geometric and material changes.

The objective of the thesis is to develop a transformer model that improves the prediction of hot spot temperatures within the distribution transformer. The oil flow field must be calculated in conjunction with the temperature field of the entire transformer in order to simulate the conjugated heat transfer problem. The modelling method must be able to calculate the transient response of the transformer to various load and ambient conditions. The model must also be able to predict the effect of winding geometry, tank size, and different insulating materials, including the oil type, on the hotspot temperature.

There are many parameters that must be considered in the thermal design of a transformer. These parameters include the geometry of the tank and the transformer, the thermal and physical properties of the cooling fluid, the core, and the windings and their insulating material, and the ambient conditions. Designing a transformer model that can simulate the thermal effect of every dimension of the transformer would take a prohibitive amount of computer time. Therefore, the scope of the thesis was narrowed to simplify the modelling and analysis of a transformer run. Figure 1.3 defines the key dimensions of the naturally oil-cooled distribution transformer studied in this work. The cross-section shown does not represent the cross-section throughout the transformer, but instead it corresponds to the cross-sectional slice shown in Figure 1.4.

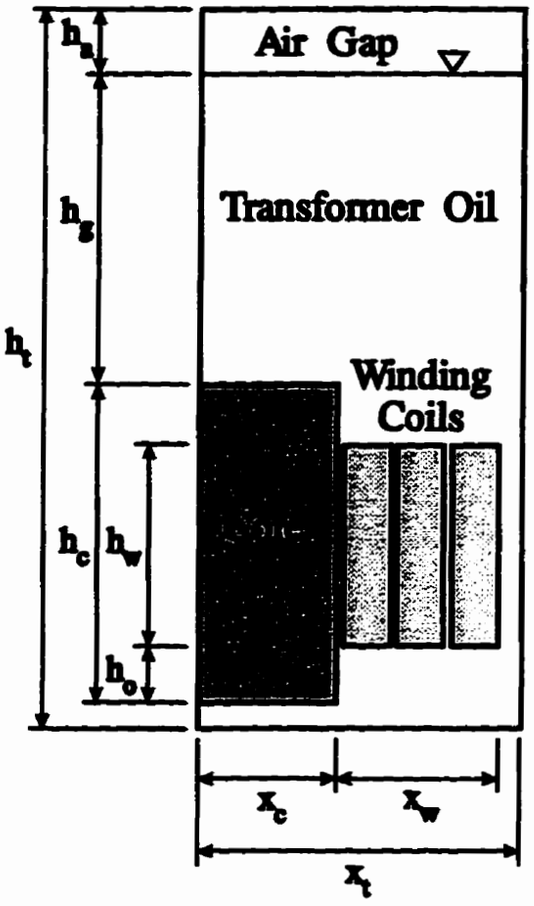

Figure 1.3: Dimension nomenclature for the naturally oil-cooled pole-mounted distribution transformer cross-section.

This slice may be used to model an entire transformer because it demonstrates all the heat transfer modes found within the entire naturally-cooled transformer assembly. It is assumed that this simplified model of the transformer will be a reasonable starting point for the development of a detailed model.

Figure 1.5 shows a magnified view of a transformer windings cross-section to illustrate the individual dimensions of each winding and the ducts. The geometries and properties of the windings play an important role in determining the temperature

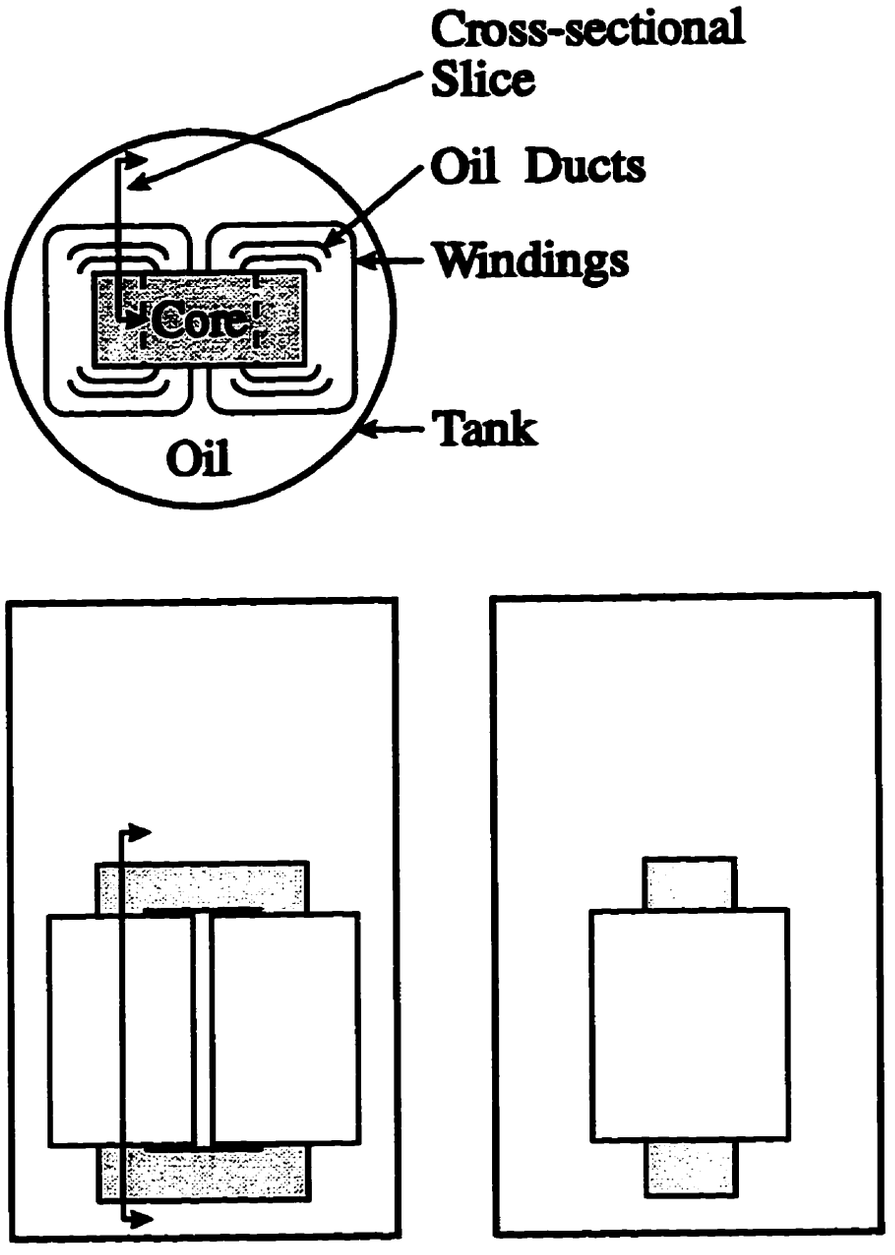

Figure 1.4: Several views of an oil-immersed distribution transformer.

field. The model must be sensitive to these parameters since they may affect the hotspot temperature and location.

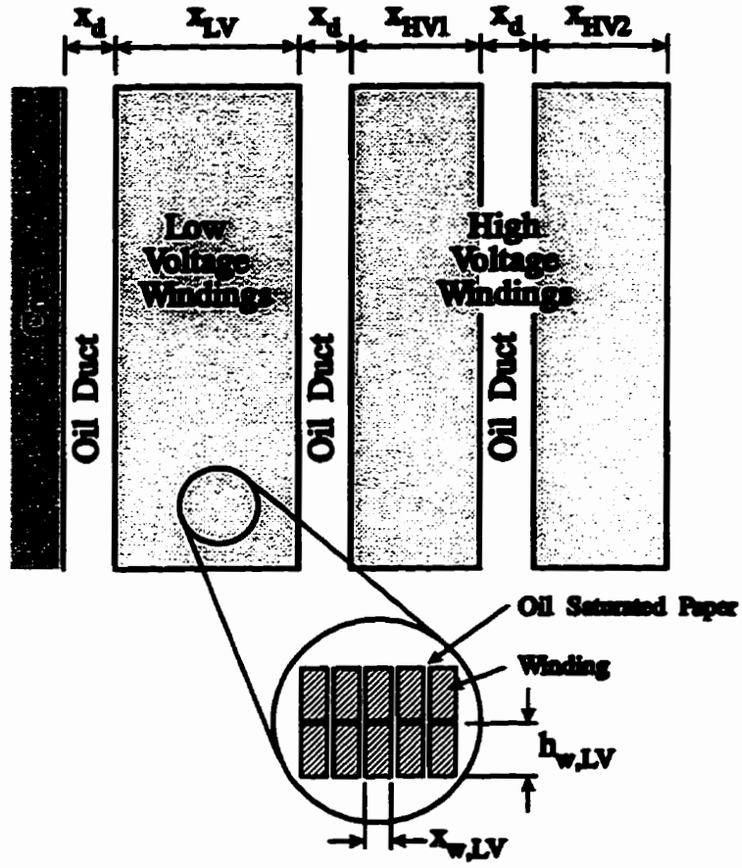

Figure 1.5: Magnified view of the transformer windings cross-section.

1.4 Outline

The remainder of this thesis is arranged as follows: Chapter 2 presents the mathematical model based on the Navier-Stokes and energy conservation equations in two dimensions. The theory behind the solid regions and the buoyancy force acting on the fluid is introduced.

Chapter 3 presents the method used to generate the computational grids used in this work. The basic nomenclature of the grid system, and a general method of specifying the control volumes within grid regions, is described.

Chapter 4 describes the numerical model. The integration of the governing equations and the derivation of the algebraic equation set are presented. There is a detailed discussion given for each of the equation terms. A method of coupling the temperature and velocity fields is described in detail. Special regions within the grid that represent the solids are also discussed.

Chapter 5 presents an explanation of the numerical solution method. The solvers that were used are discussed, including modifications done to the additive correction multigrid solver.

Chapter 6 presents test problems used to validate the computer code. Problems with known results or published solutions are solved. Each test is chosen to validate particular aspects of the code and the methods used. This chapter also details the steps that were taken to make sure that the code could solve the specified transformer model.

Chapter 7 presents and discusses the results of the transformer application. The chapter shows the model simplifications and assumptions used for the thesis and presents and discusses the results of the simulations performed.

Chapter 8 provides a summary of the main results in this work and draws relevant

conclusions.

Chapter 2

The Mathematical Model

2.1 Introduction

The fluid flow and heat transfer in a transformer is modelled in this work using the Navier-Stokes equations for incompressible flow, and the conservation of energy equation. The mathematical model used in the thesis consists of four equations: energy conservation, U and V-momentum conservation, and mass conservation. The solution of the energy equation produces the temperature field, and the momentum equations determine the velocities in the fluid. The mass conservation equation ensures that fluid entering a control volume also leaves the control volume and is used as the constraint on pressure.

The equations are restricted to two-dimensional, incompressible, laminar flow of a Newtonian fluid. The properties are held constant except in selected cases where the oil viscosity is prescribed as a function of temperature.

2.2 Governing Equations

The energy conservation equation is given by Equation (2.1). The first term on the left-hand side of the energy conservation equation represents the energy storage. The second and third terms represent the advection of energy by the moving fluid. On the right hand side of the equation, the first two terms are the energy diffusion terms, and the last term represents the energy generation per unit volume.

$$c_p\frac{\partial}{\partial t}(\rho T) + c_p\frac{\partial}{\partial x}(\rho UT) + c_p\frac{\partial}{\partial y}(\rho VT) = \frac{\partial}{\partial x}(k_x\frac{\partial T}{\partial x}) + \frac{\partial}{\partial y}(k_y\frac{\partial T}{\partial y}) + \dot{Q}''' \tag{2.1}$$

The momentum conservation equations in two-dimensions, Equations (2.2) and (2.3), are used to calculate the velocity fields. The first term in each equation represents the change in momentum over time. The second and third terms on the left-hand side of the equations represent the advection of momentum. The first two terms on the right-hand side of the equations account for the net viscous forces, and the third term represents the pressure forces. The last term of the y direction momentum equation represents the bouyancy force used when solving a natural convection problem.

$$\frac{\partial}{\partial t}(\rho U) + \frac{\partial}{\partial x}(\rho UU) + \frac{\partial}{\partial y}(\rho VU) = \frac{\partial}{\partial x}\left(\mu\frac{\partial U}{\partial x}\right) + \frac{\partial}{\partial y}\left(\mu\frac{\partial U}{\partial y}\right) - \frac{\partial P}{\partial x} \tag{2.2}$$

$$\begin{aligned}\frac{\partial}{\partial t}(\rho V) + \frac{\partial}{\partial x}(\rho UV) + \frac{\partial}{\partial y}(\rho VV) &= \frac{\partial}{\partial x}(\mu\frac{\partial V}{\partial x}) + \frac{\partial}{\partial y}(\mu\frac{\partial V}{\partial y}) \\ &- \frac{\partial P}{\partial y} + \rho_\infty\beta g\,(T - T_\infty)\end{aligned} \tag{2.3}$$

Natural convection is the body force driving fluid flow within a naturally oil-cooled transformer. A bouyancy force is the net effect of body forces acting on a fluid in which there are density gradients. For this model, the density gradient is induced by a temperature gradient in the fluid, and the body force is due to the

gravitational field, g, acting in the negative y direction. The bouyancy force in the y direction momentum equation is modelled by using the Boussinesq approximation. In that term, ρ_∞ is the average fluid density, β is the thermal coefficient of volume expansion, and T_∞ is the average fluid temperature.

Equation (2.4) is the continuity equation. In that equatino, the first term accounts for the mass storage, and the other two terms describe the change of mass flow in both the x and y directions, respectively.

$$\frac{\partial}{\partial t}(\rho) + \frac{\partial}{\partial x}(\rho U) + \frac{\partial}{\partial y}(\rho V) = 0 \tag{2.4}$$

2.3 General Boundary Conditions

Boundary conditions are necessary to solve the four differential equations. Four boundary conditions are needed to define the two-dimensional domain for each equation because the U, V, and T equations have elliptic forms. Elliptic phenomena are such that the conditions at a given location are influenced by changes in conditions on either side of that location.

There are three types of boundary conditions that are common to most heat transfer models: Dirichlet, Neumann, and Newton boundary conditions. Dirichlet boundary conditions exist when the boundary value or function is specified. For the energy equation, it is expressed as

$$T_b = T_{spec} \tag{2.5}$$

Similiarly, for velocity it is expressed as

$$U_b = U_{spec} \tag{2.6a}$$

$$V_b = V_{spec} \tag{2.6b}$$

for each of the U-velocity and V-velocity momentum equations respectively.

The Neumann boundary condition specifies the field gradient on the boundary. In the energy equation the heat flux, q''_{spec}, at the boundary is expressed as

$$q''_b = -k\frac{dT}{dx}\Big| = q''_{spec} \tag{2.7}$$

For velocity, the Neumann boundary condition is expressed as the spacial change of velocity at the boundary.

$$\frac{dU}{dx} = \frac{dU}{dx}\Big|_{spec} \quad \text{and} \quad \frac{dV}{dy} = \frac{dV}{dy}\Big|_{spec} \tag{2.8}$$

These conditions are often used to specify symmetry and fully developed flow by setting the velocity gradient to zero.

Finally the Newton, or mixed, boundary condition describes the relationship between the gradient and the specified value. Only the energy equation uses this boundary condition type because it can be used to specify energy convection at the outside surface of the domain. Convective heat transfer at a boundary is specified by the equation,

$$q''_b = -k\frac{dT}{dx}\Big| = h_\infty (T_b - T_\infty) \tag{2.9}$$

2.4 Transformer Model Boundary Conditions

Figure 2.1 shows the boundary conditions of the transformer model. The bottom, top, and reight side are modelled using a Newton boundary condition. Although the top, bottom, and right side all share the same ambient temperature, each has its own convection coefficient. The left side is modelled as insulated since symmetry is implemented to simplify the model. Therefore, the left side is a Neuman boundary condition with the prescribed heat flux equal to zero.

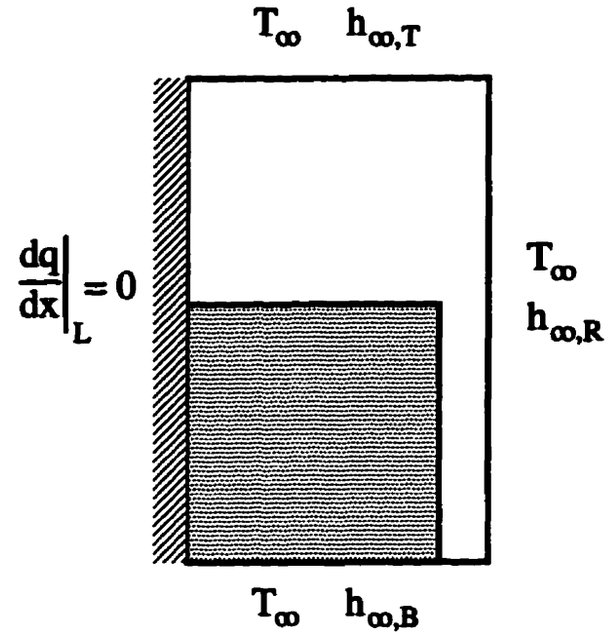

Figure 2.1: External boundary conditions for the transformer model.

2.5 Internal Boundary Conditions

A conjugate heat transfer problem is defined as one consisting of both fluid and solid regions. The energy distribution within the solid is dependent on the energy distribution in the fluid, and vice versa. A solid region is defined as a region through which thermal energy is exchanged only by conduction. The transformer model consists of solid regions that represent the core and the windings. The rest of the domain is made up of the transformer oil.

2.5.1 Energy Equation

The energy equation does not need to differentiate between a solid and a fluid as long as the correct thermal properties are used. Energy is conserved across the solid-

fluid interface and the temperature is continuous at the interface. Thermal contact resistance is neglected.

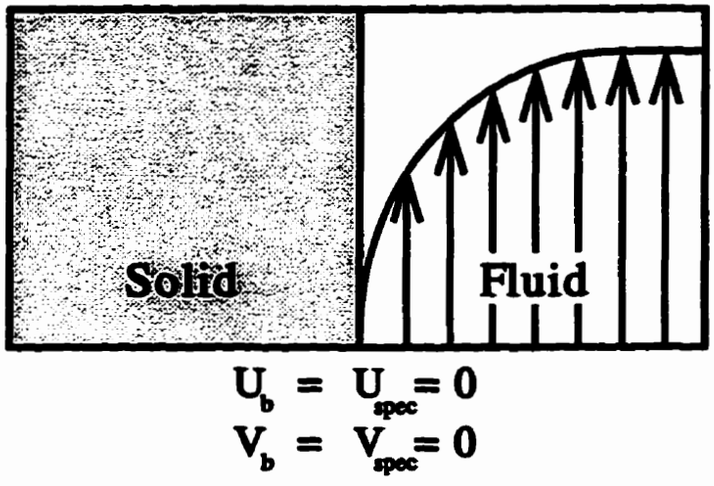

Figure 2.2: Internal boundary conditions for flow along solid regions.

2.5.2 Momentum Equations

The momentum and continuity equations are only solved in the fluid regions because there is no motion in the solid region. The internal boundary conditions are imposed on the surface of the solid-fluid interface. Figure 2.2 illustrates that the boundary conditions are modelled by setting Dirchlet boundary conditions, U_{spec} and V_{spec}, equal to zero on the surface of the solid.

Chapter 3

Grid Generation

3.1 Introduction

In order to derive algebraic equations from the governing partial differential equations, the solution domain must be divided up into control volumes. This chapter describes how the domain is divided into control volumes. The collection of control volumes in the solution domain is also called the computational grid, or simply the grid. The geometric quantities defined for the grid are used in Chapter 4, which describes the discretization of the mathematic model for a typical control volume.

3.2 The Grid Layout

The simplest grid to generate would be one that has uniform control volume spacing. However, that type of grid is limited by how well you can resolve the grid in areas of strong gradients. If a portion of the domain needs refinement then the entire grid is refined. This is computationally expensive since very large numbers of control

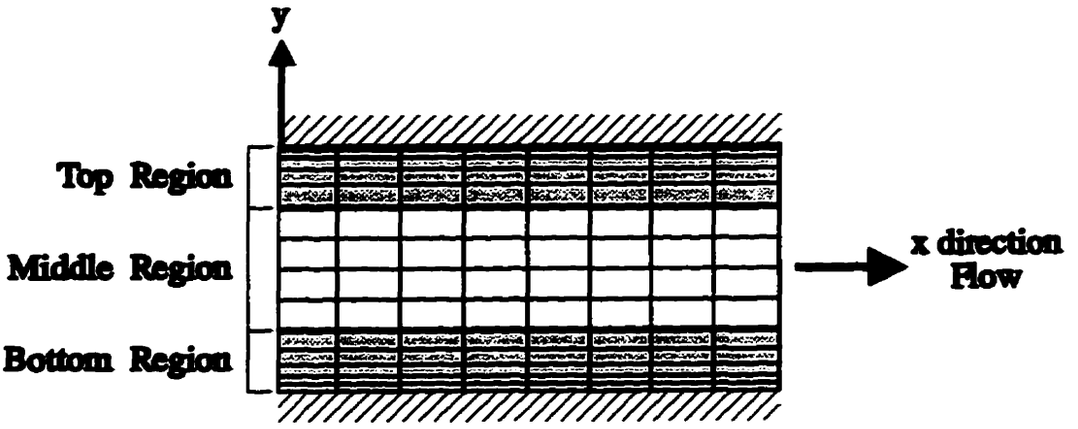

Figure 3.1: Dividing the domain into grid regions (dark lines) made up of control volumes (finer lines).

volumes are required to solve the problem. Computational effort increases with the number of control volumes.

In order to reduce the number of control volumes needed, a grid generator was developed that can produce non-uniformly spaced grids. This grid generator allows more control volumes to be placed where needed without having to increase the grid resolution of the entire domain.

To isolate the areas where more control volumes are needed, grid regions were developed. A grid region is a subdivision of the domain where the grid may be specified. Figure 3.1 shows an example of a duct model being broken up in the y direction into three grid regions: the top, middle, and bottom regions. Each of these regions represents a grid with the same rate of grid expansion between control volumes (ie. the top region uses one grid expansion value to determine the size of control volumes in the y direction). The top and bottom regions are used to more accurately model the higher velocity gradients found near the walls. The top region starts with a very fine control volume grid near the wall, and then expands to a coarser

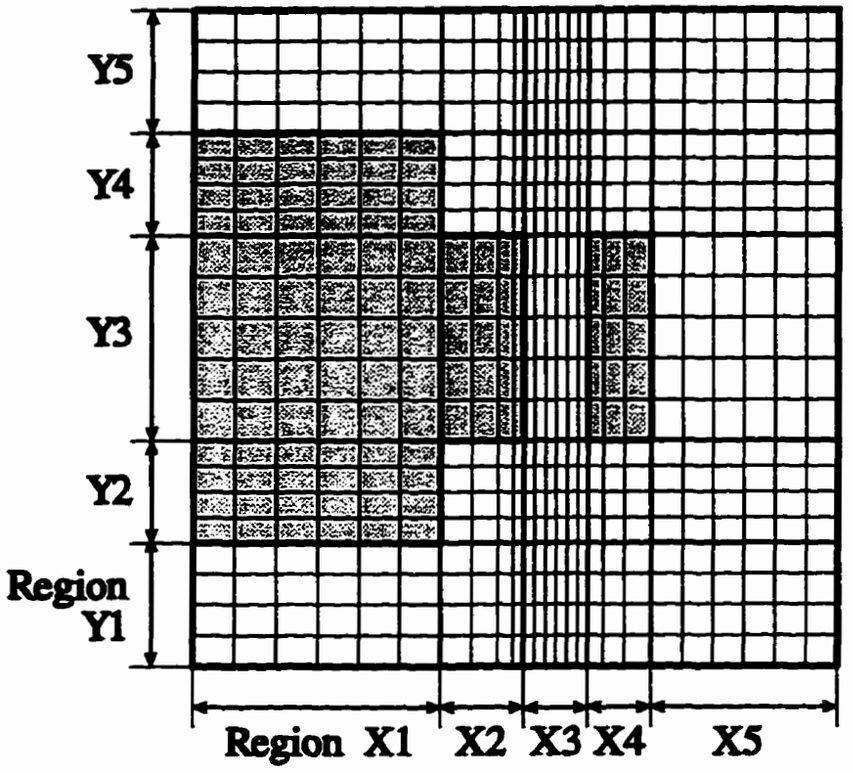

Figure 3.2: Grid regions for a complicated domain.

grid. The middle grid is modelled with uniform control volumes. The bottom grid region is the mirror image of the first grid region. For more complicated structures, as shown in Figure 3.2, the grid in both the x and y directions is broken up into many grid regions before being further divided into control volumes. It is hoped that by using a non-uniformly spaced grid, and placing control volumes where they are expected to be needed, that the number of control volumes needed for the problem will be reduced.

It is desirable to limit the expansion factor between neighbouring control volumes to a value less than two or greater than one half for reasons discussed in Section 4.4.

3.3 Grid Regions

Inside a grid region, control volumes are either expanded or contracted along the length of the region. Each grid region can only perform one type of expansion or contraction. For simplicity, the term *grid expansion* is used for both expansions and contractions. There are four types of grid region expansion: uniform grid, grid expansion from the first control volume, grid expansion from the last control volume of the previous grid, and grid expansion based on the last control volume for the current region. The following subsections describe all four region types.

3.3.1 Uniform Grid

The uniform grid region is the most common type. Once the length of the region, L_x, and the number of control volumes, N_x, for the x-axis are known the size of the control volumes is calculated from the equation,

$$\Delta x = \frac{L_x}{(N_x)} \tag{3.1}$$

Figure 3.3 shows a typical uniform grid region in the x direction. The size of the control volumes in the y direction are calculated in a similar manner.

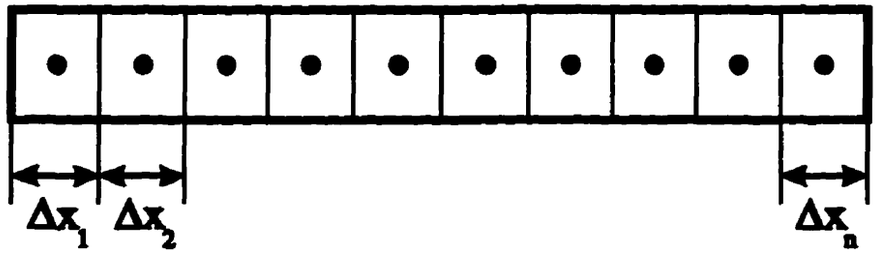

Figure 3.3: A typical uniform grid region in which all values of Δx are equal.

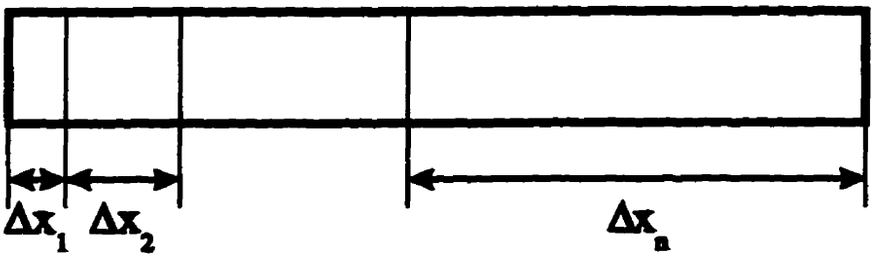

Figure 3.4: A typical expanding grid region where Δx_2 is a factor larger than Δx_1.

3.3.2 Grid Expansion from the First Control Volume

Unlike a uniform grid, a non-uniform grid allows for finer grid resolution where it is required. The expansion, or contraction, of the grid in a grid region is shown in Figure 3.4. The second control volume, Δx_2, is a factor η_x larger than Δx_1. This can be written as

$$\Delta x_i = \eta_x \Delta x_{i-1} \tag{3.2}$$

where η_x represents the grid multiplier for the x direction and i indicates the current control volume. The grid multiplier can either expand the grid with a value greater than 1.0, or contract the grid with a value below 1.0.

Grid expansion can have one control volume specified as a reference to calculate η. This could be any control volume in the grid region. The total length of a region is defined as the sum of control volume lengths. When the expansion is referenced to the first control volume, then the total length of the region equals

$$L_x = \sum_{i=1}^{N_x} \Delta x_i \tag{3.3}$$

If the control volume length, Δx_i, is defined as

$$\Delta x_i = \Delta x_1 (\eta_x)^{i-1} \tag{3.4}$$

Then

$$L_x = \sum_{i=1}^{N_x} \Delta x_1 (\eta_x)^{i-1} \tag{3.5}$$

The region type, ***grid expansion from first control volume***, has several specified parameters. These are the region length, L_x, number of control volumes, N_x, and starting control volume length, Δx_1. Based on this information, the value of η_x is calculated for the x region. The Newton-Raphson Method is used to solve Equation (3.3) for η_x. Equation (3.6) shows the equation used in the iterative solution for η_x.

$$\eta_{x,m} = \eta_{x,m-1} - \frac{\left\{ \sum_{i=1}^{N_x} \Delta x_1 (\eta_{x,m-1})^{i-1} \right\} - L_x}{\sum_{i=1}^{N_x} \Delta x_1 (i-1)(\eta_{x,m-1})^{i-2}} \tag{3.6}$$

The term, $\eta_{x,m-1}$, refers to the solution of the previous iteration, or the initial guess when $m = 1$. The value of $\eta_{x,m}$ is determined after iterating Equation (3.6) anywhere between five and thirty times to obtain a relative error, ϵ, of 1.0×10^{-5}. The relative error is calculated by the equation,

$$\epsilon = \frac{|\eta_{x,m} - \eta_{x,m-1}|}{\eta_{x,m}} \tag{3.7}$$

Using the calculated value of η_x, the rest of the x region control volume lengths are calculated by starting with the first control volume and then multiplying each consecutive control volume by η_x (for example, $\Delta x_2 = \eta_x \Delta x_1$, $\Delta x_3 = \eta_x \Delta x_2$, etc.). The control volumes for the y regions are calculated in a similar manner.

3.3.3 Grid Expansion from the Last Control Volume of the Previous Grid

This method is similiar to that discussed in Section 3.3.2 except that the starting control volume length is defined based on the previous grid region, as shown in Figure 3.5. The variable, η_p, represents the multiplier between grids. For example if η_p is equal to 1.5 for the new region, the starting control volume would be 1.5 times larger than the last control volume of the previous grid region. This procedure allows the grid to adjust itself to a previous grid region and maintain a specified grid aspect ratio. The ratio of neighbouring control volume sizes is not allowed to exceed 2.0 (or drop below 0.5).

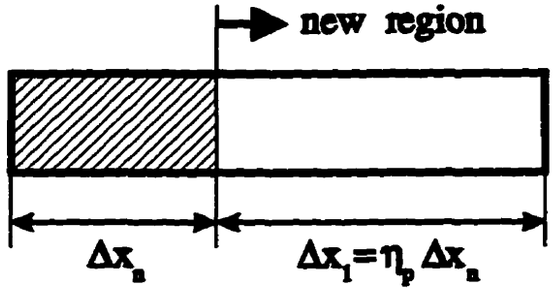

Figure 3.5: Specifying the starting control volume size based on the last control volume of the previous grid.

3.3.4 Grid Expansion Based on the Last Control Volume for the Current Region

The final type of grid region is the grid expansion from the last control volume. The value of η_x is calculated after the grid region length, L_x, the number of control volumes, N_x, and the last control volume size, Δx_n, are specified. The derivation of the η_x solution begins by rearranging Equation (3.4) in terms of Δx_1 for Δx_n,

$$\Delta x_1 = \frac{\Delta x_n}{(\eta_x)^{N_x-1}} \tag{3.8}$$

Equation (3.8) is substituted into Equation (3.3) to get

$$\begin{aligned} L_x &= \sum_{i=1}^{N_x} \frac{\Delta x_n}{(\eta_x)^{N_x-1}} (\eta_x)^{i-1} \\ &= \sum_{i=1}^{N_x} \Delta x_n (\eta_x)^{i-N_x} \end{aligned} \tag{3.9}$$

Using the Newton-Raphson Method, Equation (3.9) is solved in terms of η_x.

$$\eta_{x,m} = \eta_{x,m-1} - \frac{\left\{ \sum_{i=1}^{N_x} \Delta x_n (\eta_{x,m-1})^{i-N_x} \right\} - L_x}{\sum_{i=1}^{N_x} \Delta x_n (i - N_x)(\eta_{x,m-1})^{i-N_x-1}} \tag{3.10}$$

The same convergence criterion as Equation (3.7) is used for Equation (3.10). Once the value of η_x is determined, Equation (3.8) is used to calculate Δx_1. From Δx_1 each consecutive control volume length is calculated by multiplying the previous control volume length by η_x. The y region control volumes are calculated in a similiar manner.

3.4 Boundary Control Volumes

Boundary conditions are applied around the perimeter of the grid, as shown in Figure 3.6. All of the solution domain boundary control volumes are zero-width volumes,

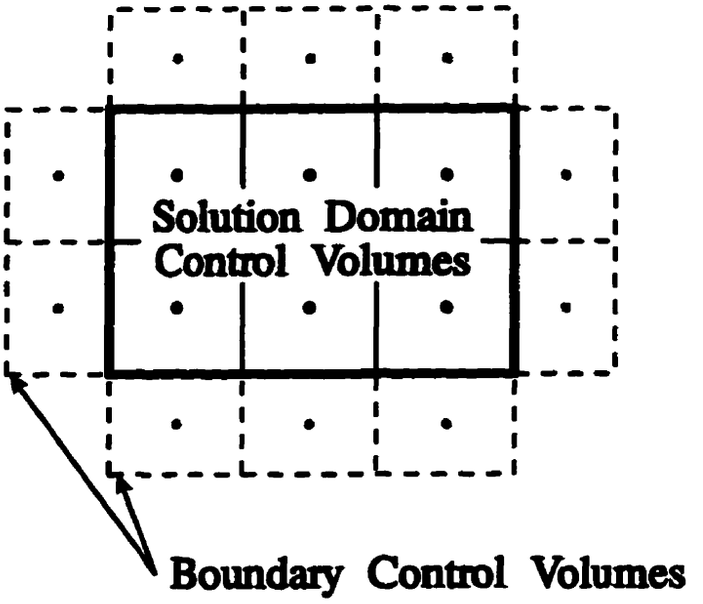

Figure 3.6: The boundary control volumes (dashed lines) surrounding the solution domain.

which means that the boundary nodes are located directly on the boundary. Figure 3.6 shows non-zero width boundary control volumes only for illustration purposes. These control volumes are used to set the boundary conditions for the model.

3.5 Grid Information Generated for the Solution Domain

Each control volume is indentified by i and j indices. Figure 3.7 shows the index convention used in the computer code. The grid indices for the x direction start at 2 and end at $N_x + 1$. The grid indices for the y direction start at 2 and end at $N_y + 1$. Although not shown in the figure, the boundary control volumes are indexed at either

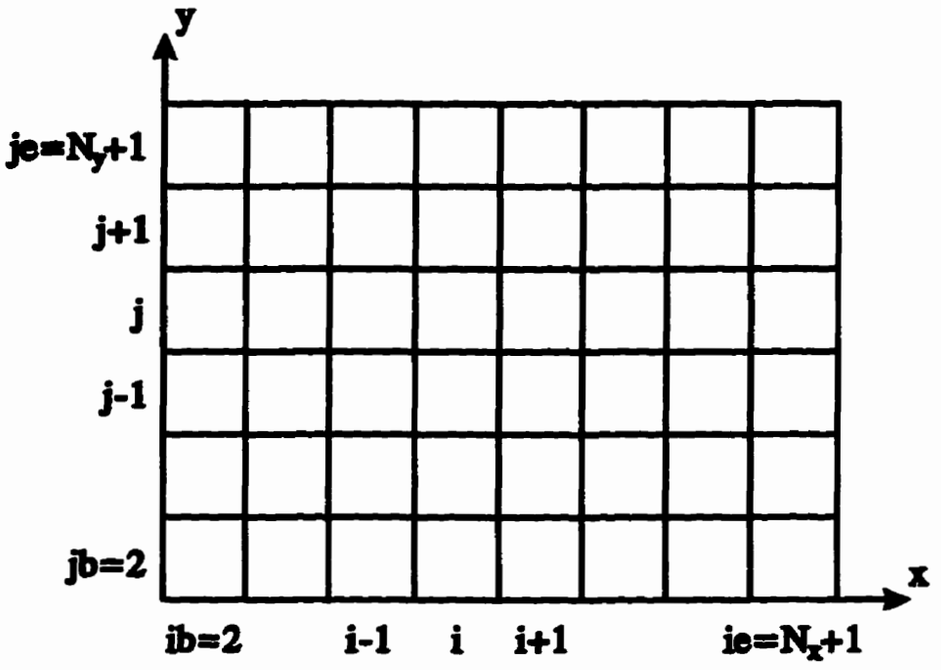

Figure 3.7: The grid indices for the solution domain.

1, or at $N_x + 2$ and $N_y + 2$.

Figure 3.8 shows the indexing and notation for neighbouring control volumes. The capital letters, E, W, N, and S, represent the nodes neighbouring the P node, or the current reference node. The nomenclature for the neighbouring control volumes represents the four compass points: east, west, north, and south. The lower case letters, e, w, n, and s, represent the face values of the P control volume.

There are several geometric features that are stored for each control volume of the grid, including the boundary control volumes even though they are *zero-width*. Figure 3.9 shows the nomenclature for each quadrant within a control volume. The names, NW, NE, SW, and SE are the compass directions: northwest, northeast, southwest, and southeast. Figure 3.10 shows the coordinate and the nomenclature used to locate the corners and center of every control volume. The coordinates are

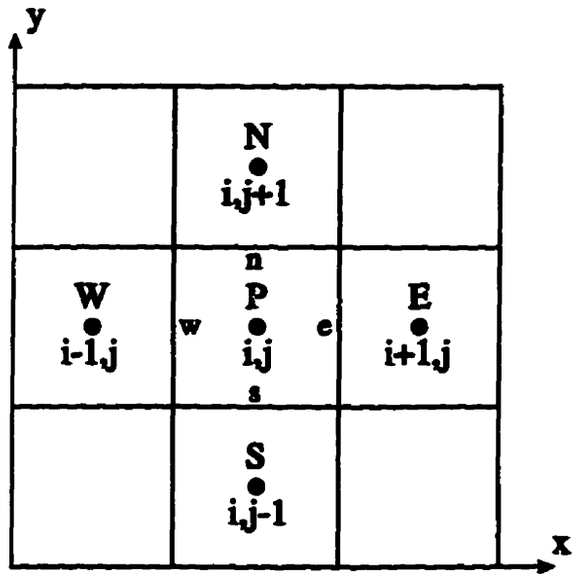

Figure 3.8: The indexing and notation for the reference control volume and its neighbouring control volumes.

based on the domain origin in the lower left corner. Figure 3.11 shows the nomenclature used for the control volume length segments. The d_i lengths represent the control volume length segments in the x direction, and the d_j lengths represent the control volume length segments in the y direction. Figure 3.12 illustrates the nomenclature for the control volume area segments for a control volume. The domain has a uniform depth Δz. Figure 3.13 demonstrates the four quadrant volume segments of the control volume.

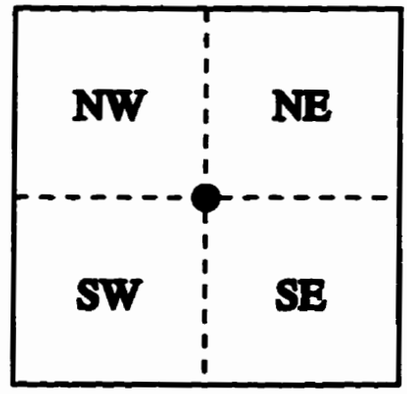

Figure 3.9: The quadrant nomenclature for a control volume.

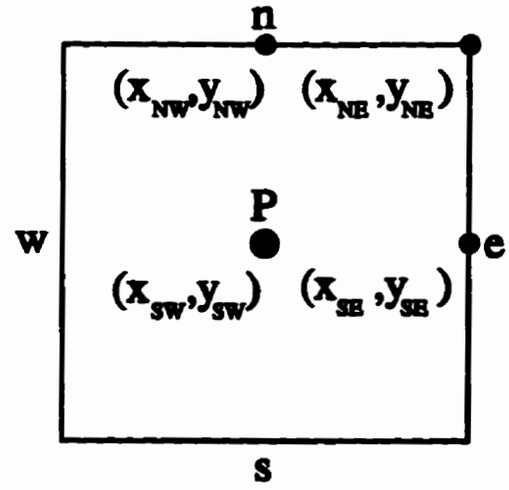

Figure 3.10: The coordinate nomenclature for a control volume.

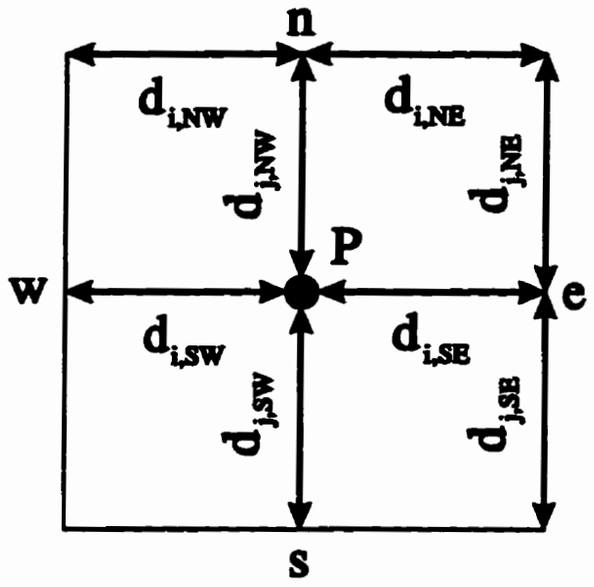

Figure 3.11: The nomenclature for the control volume length segments.

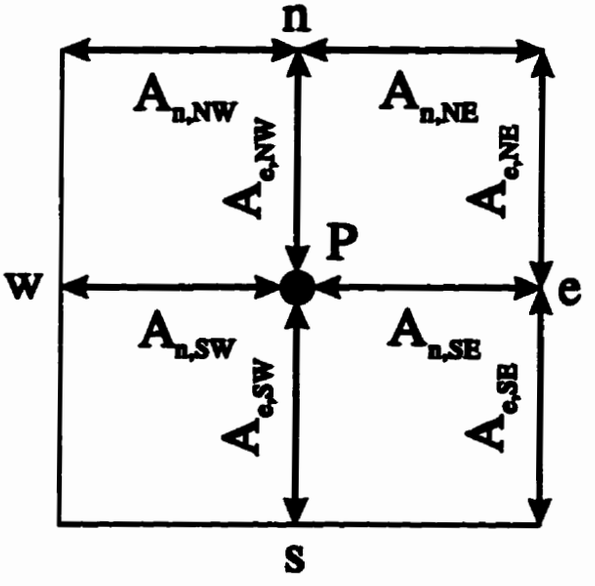

Figure 3.12: The nomenclature for the control volume area segments.

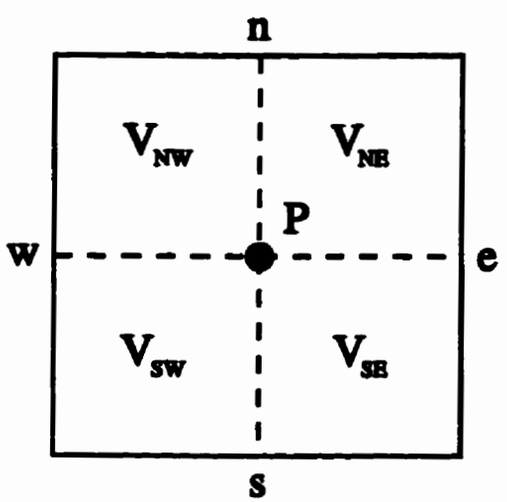

Figure 3.13: The volume nomenclature for the control volume segments.

Chapter 4

The Numerical Solution Procedure

4.1 Introduction

This chapter describes how the mathematical model given in Chapter 2 is used to derive a set of algebraic equations using a process called discretization. The governing equations of the mathematical model are integrated over the control volumes described in Chapter 3. This chapter begins by showing the derivation of a generally-applicable discretization equation. The following sections then describe the details of the discretized equation set, including modifications that are particular to the solution of a conjugate heat transfer problem.

4.2 Discretization Equation for General Transport Equation in 2-D

The mathematical model is discretized in a manner similiar to that presented by Patankar [46]. Since the form of the energy, mementum, and mass conservation

equations are similiar, a general transport equation for a property, ϕ, is introduced:

$$\xi\frac{\partial}{\partial t}(\rho\phi) + \xi\frac{\partial}{\partial x}(\rho U\phi) + \xi\frac{\partial}{\partial y}(\rho V\phi) = \frac{\partial}{\partial x}(\Gamma_x\frac{\partial\phi}{\partial x}) + \frac{\partial}{\partial y}(\Gamma_y\frac{\partial\phi}{\partial y}) + \dot{S}''' \quad (4.1)$$

This equation can be used for energy, momentum, and mass conservation by setting the appropriate ϕ, ξ, Γ, and $\dot{S}'''$ terms as given in Table 4.1. The thermal conductivities, k_x and k_y, may be different from each other for anisotropic materials such as transformer windings. Because the specific heat is not constant throughout the domain, the variable, ξ, is introduced. For all equations except the energy conservation equation ξ is set to a value of 1.0.

Figure 4.1 shows the control volume nomenclature used when discretizing Equation (4.1) . The ϕ terms represent the field value at the nodes. The δ_x and δ_y terms are distances between the nodes. The geometric quantities are derived as presented in Chapter 3.

Equation	ϕ	ξ	Γ_x	Γ_y	$\dot{S}'''$
Mass Conservation	1	1	0	0	0
X-Direction Momentum Conservation	U	1	μ	μ	$-\frac{\partial P}{\partial x} + f_x'''$
Y-Direction Momentum Conservation	V	1	μ	μ	$-\frac{\partial P}{\partial y} + f_y'''$
Energy Conservation	T	c_p	k_x	k_y	$\dot{Q}'''$

Table 4.1: Terms of the general transport equation

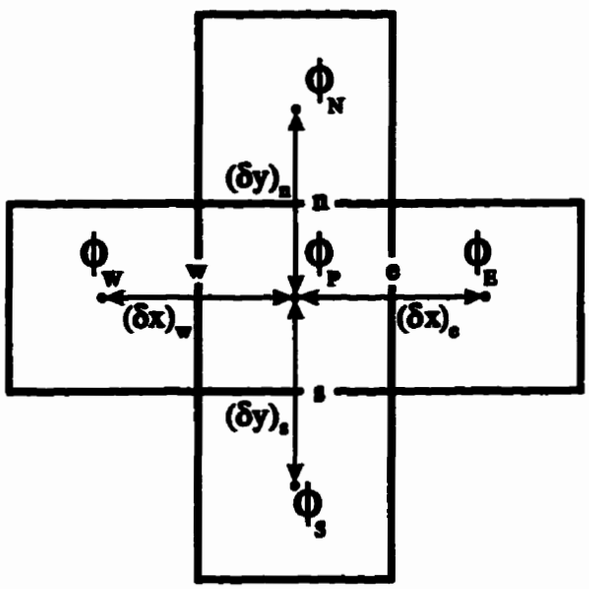

Figure 4.1: General control volume nomenclature.

4.2.1 Conservation of Mass

The conservation of mass equation is the first equation discretized. Using the values in Table 4.1 for mass conservation, Equation (4.1) takes the form of Equation (2.4).

The conservation of mass equation is integrated over the control volume shown in Figure 4.2 to get Equation (4.2).

$$\underbrace{\int_t^{t+\Delta t}\int_{\forall}\frac{\partial}{\partial t}(\rho)\,d\forall\,dt}_{M-I} + \underbrace{\int_t^{t+\Delta t}\int_{\forall}\frac{\partial}{\partial x}(\rho U)\,d\forall\,dt}_{M-II} + \underbrace{\int_t^{t+\Delta t}\int_{\forall}\frac{\partial}{\partial y}(\rho V)\,d\forall\,dt}_{M-III} = 0 \qquad (4.2)$$

The conservation of mass equation is broken up into three terms: $M-I$, $M-II$, and $M-III$. Each term is integrated separately before being combined to form the final discretization equation. The $M-I$ term of Equation (4.2) is integrated as

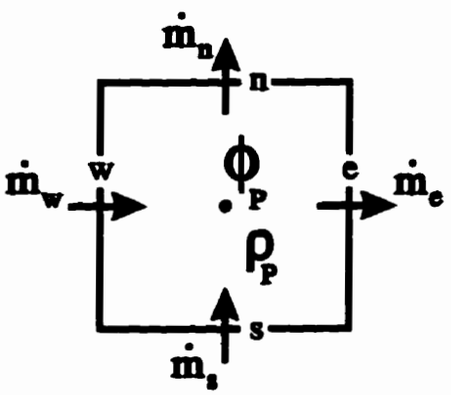

Figure 4.2: Conservation of mass control volume.

follows

$$M\!-\!I \;=\; \int_{\forall}\int_{t}^{t+\Delta t} \frac{\partial}{\partial t}(\rho)\,\mathrm{d}t\,\mathrm{d}\forall \;\approx\; (\rho_P - \rho_P^o)\,\forall_P \;=\; (M_P \;-\; M_P^o) \tag{4.3}$$

The superscript, "o" represents an old time step value. It is implied that a variable is a new time step value when it has no superscript. $M\!-\!II$ is integrated by expanding $d\forall = dx dA$.

$$\begin{aligned} M\!-\!II \;&=\; \int_{t}^{t+\Delta t}\int_{A}\int_{w}^{e} \frac{\partial}{\partial x}(\rho U)\,\mathrm{d}x\,\mathrm{d}A\,\mathrm{d}t \\ &\approx\; \int_{t}^{t+\Delta t} \{\rho_e A_e U_e \;-\; \rho_w A_w U_w\}\,\mathrm{d}t \\ &=\; (\dot{m}_e \;-\; \dot{m}_w)\,\Delta t \end{aligned} \tag{4.4}$$

Similiarly, $M-III$ is integrated to get Equation (4.5):

$$M\!-\!III \;=\; (\dot{m}_n \;-\; \dot{m}_s)\,\Delta t \tag{4.5}$$

When terms $M\!-\!I$, $M\!-\!II$, and $M\!-\!III$, are substituted back into Equation (4.2) and the equation is divided by Δt, the discretized conservation of mass equation becomes

$$\frac{(M_P - M_P^o)}{\Delta t} \;=\; (-\,\dot{m}_e + \dot{m}_w - \dot{m}_n + \dot{m}_s) \tag{4.6}$$

4.2.2 General Transport Equation

Equation (4.1) is integrated over the typical control volume shown in Figure 4.1.

$$\underbrace{\int_t^{t+\Delta t}\int_{\forall} \xi\frac{\partial}{\partial t}(\rho\,\phi)\,\mathrm{d}\forall\mathrm{d}t}_{T-I} + \underbrace{\int_t^{t+\Delta t}\int_{\forall} \xi\frac{\partial}{\partial x}(\rho\,U\,\phi)\,\mathrm{d}\forall\mathrm{d}t}_{T-II}$$
$$+\underbrace{\int_t^{t+\Delta t}\int_{\forall} \xi\frac{\partial}{\partial y}(\rho\,V\,\phi)\,\mathrm{d}\forall\mathrm{d}t}_{T-III} = \underbrace{\int_t^{t+\Delta t}\int_{\forall} \frac{\partial}{\partial x}(\Gamma\frac{\partial\phi}{\partial x})\,\mathrm{d}\forall\mathrm{d}t}_{T-IV}$$
$$+\underbrace{\int_t^{t+\Delta t}\int_{\forall} \frac{\partial}{\partial y}(\Gamma\frac{\partial\phi}{\partial y})\,\mathrm{d}\forall\mathrm{d}t}_{T-V} + \underbrace{\int_t^{t+\Delta t}\int_{\forall} S'''\,\mathrm{d}\forall\mathrm{d}t}_{T-VI} \tag{4.7}$$

The integration of the general transport equation is broken into six parts and each part is integrated separately over the control volume. First, the $T-I$ term of Equation (4.7) is integrated as follows

$$\begin{aligned} T\text{-}I &= \int_t^{t+\Delta t}\int_{\forall} \xi\frac{\partial}{\partial t}(\rho\,\phi)\,\mathrm{d}\forall\mathrm{d}t \\ &\approx \xi_P\,(\rho_P\,\phi_P - \rho_P^o\,\phi_P^o)\,\forall_P \\ &= \xi_P\,(M_P\,\phi_P - M_P^o\,\phi_P^o) \end{aligned} \tag{4.8}$$

The integration of the $T-II$ term produces

$$\begin{aligned} T\text{-}II &= \int_t^{t+\Delta t}\int_{\forall} \xi\frac{\partial}{\partial x}(\rho\,U\,\phi)\,\mathrm{d}\forall\mathrm{d}t \\ &\approx \xi_P\int_t^{t+\Delta t}\{\rho_e\,U_e\,A_e\,\phi_e - \rho_w\,U_w\,A_w\,\phi_w\}\,\mathrm{d}t \\ &= \xi_P\int_t^{t+\Delta t}\{\dot{m}_e\,\phi_e - \dot{m}_w\,\phi_w\}\,\mathrm{d}t \end{aligned} \tag{4.9}$$

Introducing the following interpolations for east and west face values of ϕ,

$$\phi_e = \left(\tfrac{1}{2}+\alpha_e\right)\phi_P + \left(\tfrac{1}{2}-\alpha_e\right)\phi_E \tag{4.10a}$$

$$\phi_w = \left(\tfrac{1}{2}+\alpha_w\right)\phi_W + \left(\tfrac{1}{2}-\alpha_w\right)\phi_P \tag{4.10b}$$

where α_e and α_w are the convection weight factors discussed later in Section 4.4. Using the fully implicit scheme, the $T-II$ term is

$$\begin{aligned} T\text{-}II &= \xi_P \Big\{ \dot{m}_e \left(\tfrac{1}{2} - \alpha_e\right) \phi_E - \dot{m}_w \left(\tfrac{1}{2} + \alpha_w\right) \phi_W \\ &+ \left[\dot{m}_e \left(\tfrac{1}{2} + \alpha_e\right) - \dot{m}_w \left(\tfrac{1}{2} - \alpha_w\right) \right] \phi_P \Big\} \Delta t \end{aligned} \tag{4.11}$$

Similiarly, term $T-III$ is approximated using the convection weight factors,

$$\begin{aligned} T\text{-}III &= \xi_P \Big\{ \dot{m}_n \left(\tfrac{1}{2} - \alpha_n\right) \phi_E - \dot{m}_s \left(\tfrac{1}{2} + \alpha_s\right) \phi_W \\ &+ \left[\dot{m}_n \left(\tfrac{1}{2} + \alpha_n\right) - \dot{m}_s \left(\tfrac{1}{2} - \alpha_s\right) \right] \phi_P \Big\} \Delta t \end{aligned} \tag{4.12}$$

Term $T-IV$ is also integrated to give

$$\begin{aligned} T\text{-}IV &= \int_t^{t+\Delta t} \int_V \frac{\partial}{\partial x} \left(\Gamma \frac{\partial \phi}{\partial x} \right) \mathrm{d}V \mathrm{d}t \\ &\approx \int_t^{t+\Delta t} \left\{ \Gamma_e A_e \left. \frac{\partial \phi}{\partial x} \right|_e - \Gamma_w A_w \left. \frac{\partial \phi}{\partial x} \right|_w \right\} \mathrm{d}t \end{aligned} \tag{4.13}$$

The derivatives, $\left.\frac{\partial \phi}{\partial x}\right|_e$ and $\left.\frac{\partial \phi}{\partial x}\right|_w$, are approximated by

$$\left. \frac{\partial \phi}{\partial x} \right|_e \approx \beta e \frac{(\phi_E - \phi_P)}{(\delta x)_e} \tag{4.14a}$$

$$\left. \frac{\partial \phi}{\partial x} \right|_w \approx \beta_w \frac{(\phi_P - \phi_W)}{(\delta x)_w} \tag{4.14b}$$

where β_e and β_w are the diffusion weight factors discussed in Section 4.4. When Equations (4.14a) and (4.14b) are substituted into Equation (4.13), term $T-IV$ becomes

$$T\text{-}IV = \int_t^{t+\Delta t} \left\{ \Gamma_e A_e \beta_e \frac{(\phi_E - \phi_P)}{(\delta x)_e} - \Gamma_w A_w \beta_w \frac{(\phi_P - \phi_W)}{(\delta x)_w} \right\} \mathrm{d}t \tag{4.15}$$

For a fully implicit formulation, Equation (4.15) can be written as

$$\begin{aligned} T\text{-}IV &= \left\{ \frac{\Gamma_e A_e \beta_e}{(\delta x)_e}(\phi_E - \phi_P) - \frac{\Gamma_w A_w \beta_w}{(\delta x)_w}(\phi_P - \phi_W) \right\} \Delta t \\ &= \left\{ \frac{\Gamma_e A_e \beta_e}{(\delta x)_e}\phi_E + \frac{\Gamma_w A_w \beta_w}{(\delta x)_w}\phi_W \right. \\ &\qquad \left. - \left(\frac{\Gamma_e A_e \beta_e}{(\delta x)_e} + \frac{\Gamma_w A_w \beta_w}{(\delta x)_w} \right) \phi_P \right\} \Delta t \end{aligned} \tag{4.16}$$

Similiarly, term $T - V$ with the following approximations,

$$\left.\frac{\partial \phi}{\partial y}\right|_n \approx \beta_n \frac{(\phi_N - \phi_P)}{(\delta y)_n} \tag{4.17a}$$

$$\left.\frac{\partial \phi}{\partial y}\right|_w \approx \beta_s \frac{(\phi_P - \phi_S)}{(\delta y)_s} \tag{4.17b}$$

becomes

$$\begin{aligned} T\text{-}V &= \left\{ \frac{\Gamma_n A_n \beta_n}{(\delta x)_n}\phi_N + \frac{\Gamma_s A_s \beta_s}{(\delta x)_s}\phi_S \right. \\ &\qquad \left. - \left(\frac{\Gamma_n A_n \beta_n}{(\delta y)_n} + \frac{\Gamma_s A_s \beta_s}{(\delta y)_s} \right) \phi_P \right\} \Delta t \end{aligned} \tag{4.18}$$

Finally, a step-wise profile assumption is used for term $T - VI$ to give

$$T\text{-}VI = \int_t^{t+\Delta t} \int_{\mathcal{V}} \dot{S}''' \, \mathrm{d}\mathcal{V} \, \mathrm{d}t \approx \bar{S}''' \mathcal{V}_P \, \Delta t = S_P \, \Delta t \tag{4.19}$$

After all the terms are assembled into the original Equation (4.7) and divided by Δt, the following equation is obtained:

$$\begin{aligned} &\frac{\xi_P (M_P \phi_P - M_P^o \phi_P^o)}{\Delta t} \\ &+ \xi_P \left\{ \dot{m}_e \left(\tfrac{1}{2} - \alpha_e\right)\phi_E - \dot{m}_w \left(\tfrac{1}{2} + \alpha_w\right)\phi_W + \left[\dot{m}_e \left(\tfrac{1}{2} + \alpha_e\right) - \dot{m}_w \left(\tfrac{1}{2} - \alpha_w\right) \right] \phi_P \right\} \\ &+ \xi_P \left\{ \dot{m}_n \left(\tfrac{1}{2} - \alpha_n\right)\phi_N - \dot{m}_s \left(\tfrac{1}{2} + \alpha_s\right)\phi_S + \left[\dot{m}_n \left(\tfrac{1}{2} + \alpha_n\right) - \dot{m}_s \left(\tfrac{1}{2} - \alpha_s\right) \right] \phi_P \right\} \\ &= \frac{\Gamma_e A_e \beta_e}{(\delta x)_e}\phi_E + \frac{\Gamma_w A_w \beta_w}{(\delta x)_w}\phi_W - \left(\frac{\Gamma_e A_e \beta_e}{(\delta x)_e} + \frac{\Gamma_w A_w \beta_w}{(\delta x)_w} \right) \phi_P \\ &+ \frac{\Gamma_n A_n \beta_n}{(\delta y)_n}\phi_N + \frac{\Gamma_s A_s \beta_s}{(\delta y)_s}\phi_S - \left(\frac{\Gamma_n A_n \beta_n}{(\delta y)_n} + \frac{\Gamma_s A_s \beta_s}{(\delta y)_s} \right) \phi_P + S_P \end{aligned} \tag{4.20}$$

The source term is linearized so that $S_P = Q_P + R_P\phi_P$. The terms are gathered and Equation (4.20) is written in the form,

$$a_P\phi_P = a_E\phi_E + a_W\phi_W + a_N\phi_N + a_S\phi_S + b_P \tag{4.21}$$

where,

$$\begin{aligned}
a_E &= \beta_e D_e - \tfrac{1}{2}\dot{m}_e\xi_P + |\dot{m}_e||\alpha_e|\xi_P \\
a_W &= \beta_w D_w + \tfrac{1}{2}\dot{m}_w\xi_P + |\dot{m}_w||\alpha_w|\xi_P \\
a_N &= \beta_n D_n - \tfrac{1}{2}\dot{m}_n\xi_P + |\dot{m}_n||\alpha_n|\xi_P \\
a_S &= \beta_s D_s + \tfrac{1}{2}\dot{m}_s\xi_P + |\dot{m}_s||\alpha_s|\xi_P \qquad (4.22a) \\
a_P &= \frac{\xi_P M_P}{\Delta t} + \dot{m}_e(\tfrac{1}{2} + \alpha_e)\xi_P + \dot{m}_w(\tfrac{1}{2} - \alpha_w)\xi_P \\
&\quad + \dot{m}_n(\tfrac{1}{2} + \alpha_n)\xi_P + \dot{m}_s(\tfrac{1}{2} - \alpha_s)\xi_P - R_P \qquad (4.22b) \\
b_P &= \frac{\xi_P M_P^o}{\Delta t}\phi_P^o + Q_P \qquad (4.22c)
\end{aligned}$$

To obtain an expression for a_P that relates it to the sum of neighbour coefficients, a_P^*, Equation (4.22b) is written as

$$a_P = \underbrace{\frac{\xi_P M_P}{\Delta t} + \xi_P(\dot{m}_e - \dot{m}_w + \dot{m}_n - \dot{m}_s)}_{G} + a_P^* - R_P \tag{4.23}$$

where,

$$a_P^* = \sum a_{np} = a_E + a_W + a_N + a_S \tag{4.24}$$

The G term in Equation (4.23) is equal to $\frac{\xi_P M_P^o}{\Delta t}$ as shown below. Using Equation (4.6), the mass conservation equation can be written as

$$\frac{M_P}{\Delta t} + \dot{m}_e - \dot{m}_w + \dot{m}_n - \dot{m}_s = \frac{M_P^o}{\Delta t} \tag{4.25}$$

So from Equation (4.23),

$$G = \xi_P\frac{M_P^o}{\Delta t} \tag{4.26}$$

Therefore, Equation (4.23) becomes

$$a_P = \frac{\xi_P M_P^o}{\Delta t} + a_P^* - R_P \tag{4.27}$$

The diffusion terms are defined as,

$$D_e = \frac{\Gamma_e A_e}{(\delta x)_e} \tag{4.28a}$$

$$D_w = \frac{\Gamma_w A_w}{(\delta x)_w} \tag{4.28b}$$

$$D_n = \frac{\Gamma_n A_n}{(\delta y)_n} \tag{4.28c}$$

$$D_s = \frac{\Gamma_s A_s}{(\delta y)_s} \tag{4.28d}$$

The value of Γ at a face uses the harmonic mean of the neighboring control volume. The nomenclature for Equation (4.29) is shown in Figure 4.3.

$$\Gamma_e = \frac{\Gamma_P \Gamma_E}{\left(f_e \Gamma_P + (1 - f_e)\Gamma_E\right)} \tag{4.29}$$

where,

$$f_e = \frac{(\delta x)_{e^+}}{(\delta x)_e} \tag{4.30}$$

Γ_w, Γ_n, and Γ_s are evaluated in an analogous way. Also the mass flow rate at a face is calculated using the equations,

$$\dot{m}_e = \rho_e A_e U_e \tag{4.31a}$$

$$\dot{m}_w = \rho_w A_w U_w \tag{4.31b}$$

$$\dot{m}_n = \rho_n A_n V_n \tag{4.31c}$$

$$\dot{m}_s = \rho_s A_s V_s \tag{4.31d}$$

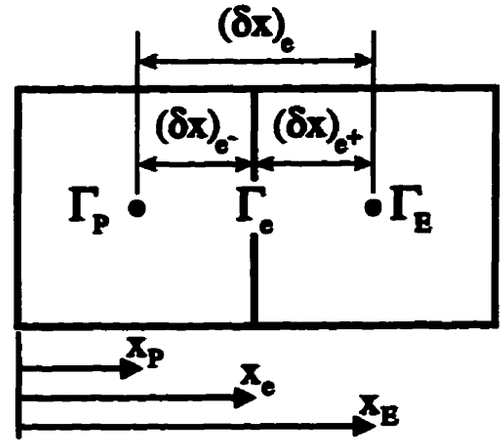

Figure 4.3: Harmonic mean nomenclature.

4.3 Distorted Transient Formulation

The steady-state solution of the domain can be obtained by either solving the equation sets at discrete time steps until the fields no longer change, or by using the so-called "distorted transient" formulation developed by Raithby and Schneider [55]. This section details how the discretized general transport equation is modified so that both true transient and distorted transient models are made available in the same equation set.

First the time step, Δt, is defined as

$$\Delta t = E^{\phi}\left\{\frac{\xi_P M_P^o}{(a_P^* - R_P)}\right\} \tag{4.32}$$

where the term in braces is a time step-like quantity. The above equation is rearranged in terms of $\frac{\xi_P M_P^o}{\Delta t}$ so that it can be substituted into the a_P and b_P coefficients.

$$\frac{\xi_P M_P^o}{\Delta t} = \frac{(a_P^* - R_P)}{E^{\phi}} \tag{4.33}$$

Equation (4.33) is then substituted into Equations (4.27) and (4.22c).

$$a_P = (a_P^* - R_P)\left(1 + \frac{1}{E^\phi}\right) \tag{4.34}$$

$$b_P = \frac{(a_P^* - R_P)}{E^\phi}\phi_P^o + Q_P \tag{4.35}$$

By comparing Equations (4.27) and (4.22c) with Equations (4.34) and (4.35), new coefficients are written to combine both true transient and distorted transient.

$$a_P = (a_P^* - R_P)\left(1 + \frac{1}{E^\phi}\right) + \frac{\xi_P M_P^o}{\Delta t} \tag{4.36}$$

$$b_P = \left\{\frac{(a_P^* - R_P)}{E^\phi} + \frac{\xi_P M_P^o}{\Delta t}\right\}\phi_P^o + Q_P \tag{4.37}$$

In order to specify true transient, E^ϕ is specified as a very large number (such as 1.0×10^{30}), and Δt is set to the desired value. For distorted transient Δt is set as a very large number (such as 1.0×10^{30}) and E^ϕ is set to the desired value.

4.4 Exponential Upwind Grid Weighting

In a solid, the face values of ϕ are calculated by a linear interpolation. The general transport equation uses an exponential scheme to approximate the face value of ϕ. The general scheme recovers the linear interpolation in the case where the velocity is zero (in a solid).

Patankar [46] described the exponential scheme in detail for uniform grids. Since some of the models in this work required non-uniform grids, the standard formulation was extended. The following one-dimensional formulation removes the uniform grid assumptions. Similiar equations are derived for the two-dimensional grid.

The convection weight factors for the east and west interfaces are defined in Equations (4.10a) and (4.10b),and Equations (4.14a) and (4.14b). Figure 4.4 illustrates the nomenclature for these equations.

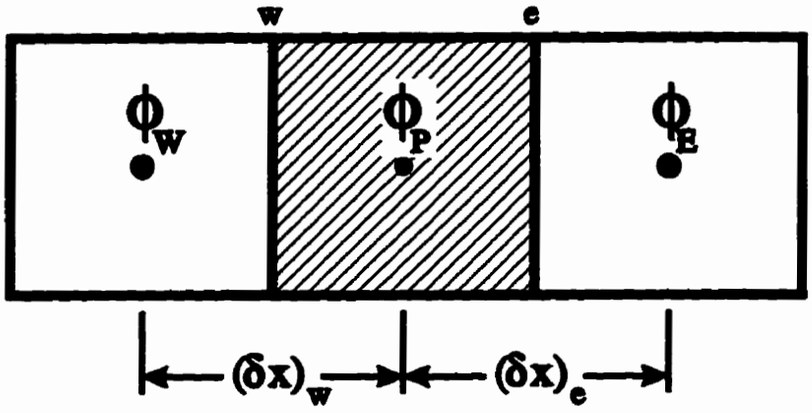

Figure 4.4: A typical control volume cluster for the one-dimensional problem.

A total flux, J, is defined so that it is made up of the convection flux $\rho U\phi$ and the diffusion flux $-\frac{\Gamma}{\xi}\frac{d\phi}{dx}$.

$$J = \rho U\phi - \frac{\Gamma}{\xi}\frac{d\phi}{dx} \tag{4.38}$$

Since the governing equation in one dimension (assuming constant ξ) is

$$\frac{d}{dx}(\rho U\phi) = \frac{d}{dx}\left(\frac{\Gamma}{\xi}\frac{d\phi}{dx}\right) \tag{4.39}$$

the total flux equation becomes,

$$\frac{dJ}{dx} = 0 \tag{4.40}$$

When the domain $0 \leq x \leq L$ is used, with the boundary conditions

$$\text{At} \quad x = 0, \quad \phi = \phi_0, \tag{4.41a}$$

$$\text{At} \quad x = L, \quad \phi = \phi_L \tag{4.41b}$$

the solution of Equation (4.39) is

$$\frac{\phi - \phi_0}{\phi_L - \phi_0} = \frac{\exp\left[(Pe)x/L\right] - 1}{\exp\left[Pe\right] - 1} \tag{4.42}$$

where Pe is a Peclet number defined by

$$Pe \equiv \frac{\rho \xi u L}{\Gamma} \tag{4.43}$$

When Equation (4.40) is integrated over the typical control volume to give

$$J_e A_e - J_w A_w = 0 \tag{4.44}$$

Then Equation (4.38) is modified to give

$$J_e A_e = \rho_e U_e A_e \phi_e - \frac{\Gamma_e}{\xi} A_e \left.\frac{d\phi}{dx}\right|_e \tag{4.45}$$

The equations for ϕ_e and $\left.\frac{d\phi}{dx}\right|_e$ are derived from the exact solution, Equation (4.42), and applied between x_P and x_E. Figure 4.5 illustrates the nomenclature of the following equations. The Pe_e term is calculated using the value of U_e.

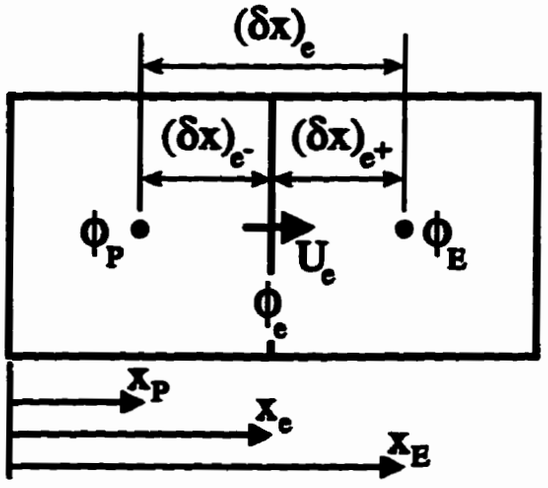

Figure 4.5: Nomenclature for the exponential upwinding scheme.

$$\phi_e = \phi_P + (\phi_E - \phi_P)\frac{\exp\left[(Pe)_e\frac{(x_e-x_P)}{x_E-x_P}\right]-1}{\exp\left[(Pe)_e\right]-1} \tag{4.46}$$

$$\left.\frac{d\phi}{dx}\right|_e = (\phi_E - \phi_P)\frac{\exp\left[(Pe)_e\frac{(x_e-x_P)}{x_E-x_P}\right]}{\exp\left[(Pe)_e\right]-1}\frac{(Pe)_e}{x_E-x_P} \tag{4.47}$$

To determine the exact values of α_e and β_e, Equations (4.10a) and (4.14a) are compared to Equations (4.46) and (4.47) to give

$$\alpha_e = \tfrac{1}{2} - \frac{\exp\left[(Pe)_e f_e\right]-1}{\exp\left[(Pe)_e\right]-1} \tag{4.48a}$$

$$\beta_e = (Pe_e)\frac{\exp\left[(Pe)_e f_e\right]}{\exp\left[(Pe)_e\right]-1} \tag{4.48b}$$

where

$$f_e = \frac{\delta x_{e^+}}{\delta x_e} = \frac{(x_e - x_P)}{(x_E - x_P)} \tag{4.49}$$

Similiarly,

$$\alpha_w = \tfrac{1}{2} - \frac{\exp\left[(Pe)_w f_w\right]-1}{\exp\left[(Pe)_w\right]-1} \tag{4.50a}$$

$$\beta_w = (Pe_w)\frac{\exp\left[(Pe)_w f_w\right]}{\exp\left[(Pe)_w\right]-1} \tag{4.50b}$$

where

$$f_w = \frac{\delta x_{w^-}}{\delta x_w} = \frac{(x_P - x_w)}{(x_P - x_W)} \tag{4.51}$$

For the uniform grid, the α and β coefficients are obtained by setting f_e in Equation (4.48) equal to one half.

$$\alpha_e = \tfrac{1}{2} - \frac{\exp\left[(Pe)_e/2\right]-1}{\exp\left[(Pe)_e\right]-1} \tag{4.52a}$$

$$\beta_e = (Pe_e)\frac{\exp\left[(Pe)_e/2\right]}{\exp\left[(Pe)_e\right]-1} \tag{4.52b}$$

Figure 4.6 shows the relative difference between the uniform and non-uniform grid α-equations as a function of the grid Peclet number. The error is defined as the difference of the non-uniform grid and the uniform grid face temperatures, $T_{e,new}$ and $T_{e,eds}$, divided by the uniform grid face temperature, $T_{e,eds}$. As the grid aspect ratio increases, the amount of error also increases. Also, the error increases with a larger temperature ratio, T_E/T_P. The plot illustrates that significant error is only introduced when the temperature ratio is relatively large and the Peclet number is low. This situation may occur only with coarse grids because in fine grids the temperature ratio is usually small. Also, the Peclet number is usually much greater than a value of five and therefore any error will be very small. In the transformer, adjacent node temperature ratios in the oil are not expected to exceed 1.1 since the grid is refined in the regions of high oil temperature gradients. Therefore the uniform grid approximation is valid as long as the grid aspect ratio is kept under 2.0.

Calculating the weighting terms, α and β, is computationally expensive because Equations (4.52a) and (4.52b) require the use of the exponential function. To reduce the calculation time Raithby and Schneider [55] used an approximation for the uniform-grid α and β weightings, shown in Equations (4.53). Since the uniform-grid was proved valid in Figure 4.6, then the approximations used by Raithby and Schneider are also expected to be valid.

$$|\alpha| = \frac{\frac{1}{2}(Pe)^2}{5 + Pe^2} \tag{4.53a}$$

$$\beta = \frac{1 + 0.005Pe^2}{1 + 0.05Pe^2} \tag{4.53b}$$

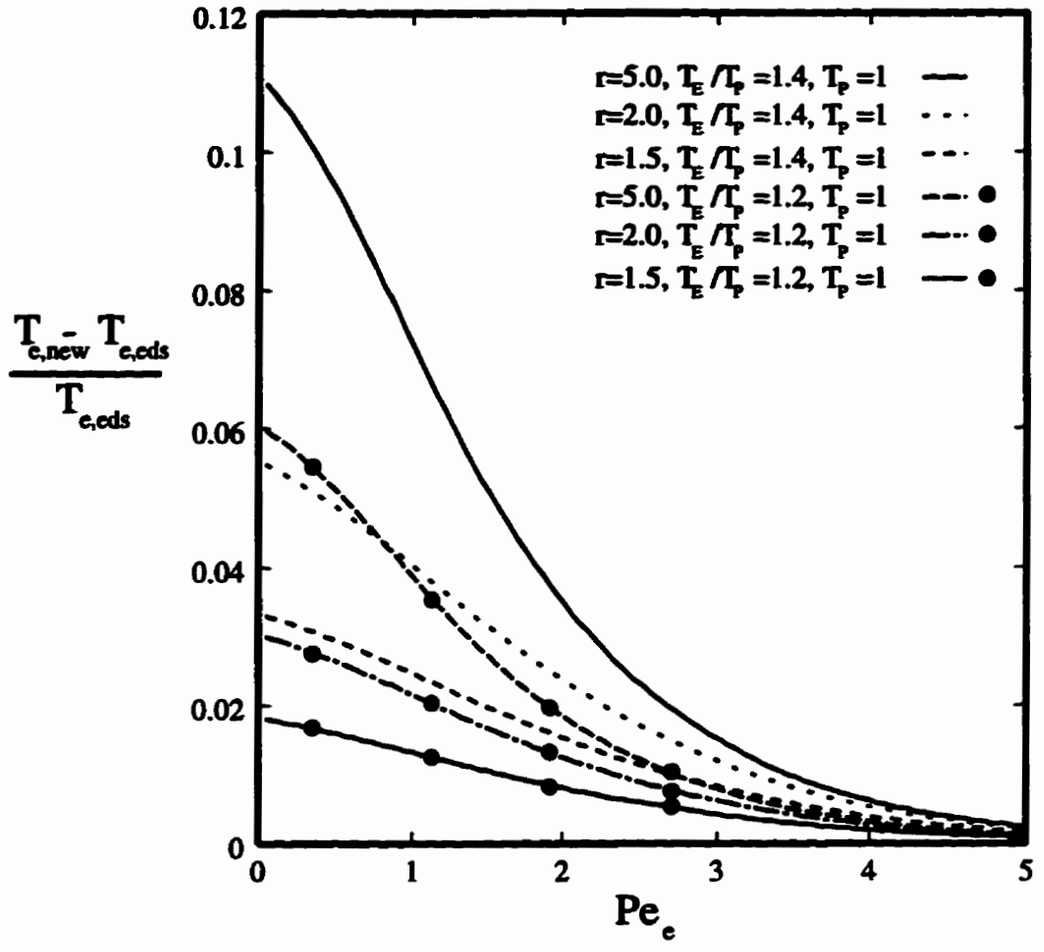

Figure 4.6: Comparison of the relative difference between uniform vs. non-uniform grid α-equations on the face temperatures.

4.5 Energy Equation Discrete Boundary Conditions

As described in Section 2.3 there are three types of boundary conditions applicable to the energy equation. The boundary conditions of the energy equation are handled in a similiar manner to Patankar [46]. Figure 4.7 illustrates the nomenclature for a

full width fictitious control volume on the left boundary. For the energy equation, all fictitious control volumes have zero width. This means that the $T_{P,f}$ node is placed on the boundary so that $T_{P,f} = T_b$.

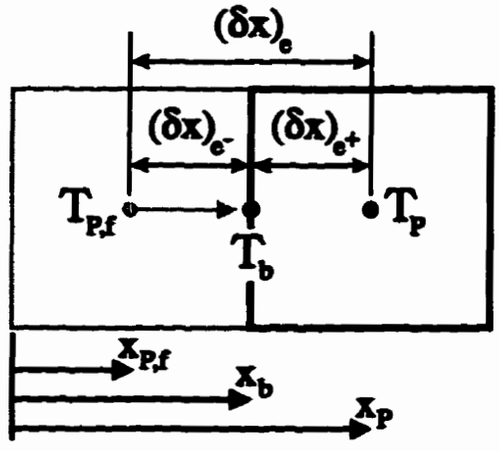

Figure 4.7: Fictitious control volume nomenclature for Dirichlet boundary conditions.

For Dirichlet boundary conditions, the fictitious control volume coefficients are

$$a_{P,f} = 1.0 \tag{4.54a}$$

$$a_{E,f} = -\frac{(1-f_L)}{f_L} \tag{4.54b}$$

$$b_f = \frac{T_{spec}}{f_L} \tag{4.54c}$$

where,

$$f_L = \frac{(\delta x)_{e^+,f}}{(\delta x)_{e,f}} \tag{4.55}$$

Since the boundary control volume is zero-width, the term, f_L becomes equal to unity. The remaining coefficients are set to zero so that the energy equation take the form

$$a_{P,f}T_{P,f} = a_{E,f}T_P + b_f \tag{4.56}$$

Neumann boundary conditions have the flux specified for the boundary, as illustrated in Figure 4.8. The coefficients for the fictitious control volume are

$$a_{P,f} = 1.0 \tag{4.57a}$$

$$a_{E,f} = 1.0 \tag{4.57b}$$

$$b_f = \frac{q''_{spec}(\delta x)_{e,f}}{k_L} \tag{4.57c}$$

with the remaining coefficients set to zero. The value of k_L refers to the thermal conductivity of the control volume next to the fictitious control volume. It is assumed that the fictitious control volume has the same properties as its neighbour. Although it is not relevant for the energy equation, this assumption becomes important for the full-width momentum boundary control volumes.

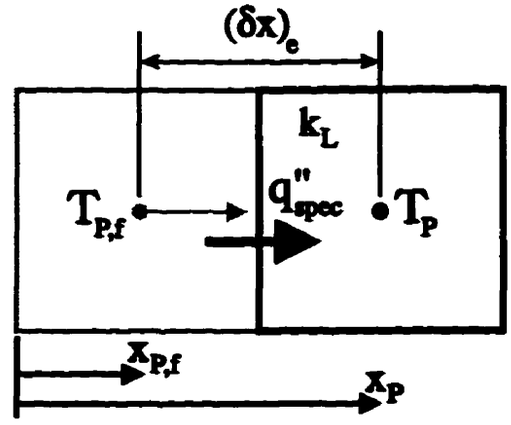

Figure 4.8: Fictitious control volume nomenclature for a Neumann boundary conditions.

The last boundary condition used for the energy equation is the Newton, or mixed, boundary condition. Figure 4.9 shows the nomenclature for the Newton boundary

condition. The coefficients are derived to be

$$a_{P,f} = 1.0 \tag{4.58a}$$

$$a_{E,f} = \frac{[1.0 - (1 - f_L)(Bi)_L]}{1.0 + f_L (Bi)_L} \tag{4.58b}$$

$$b_f = \frac{(Bi)_L T_{\infty,L}}{[1.0 + f_L (Bi)_L]} \tag{4.58c}$$

where,

$$(Bi)_L = \frac{h_{\infty,L} (\delta x)_e}{k_L} \tag{4.59a}$$

$$fe_L = \frac{(\delta x)_{e^+,f}}{(\delta x)_{e,f}} \tag{4.59b}$$

The remaining coefficients are set to zero. The variable, T_∞, represents the ambient temperature, and h_∞ represents the convection heat transfer coefficient at the boundary surface.

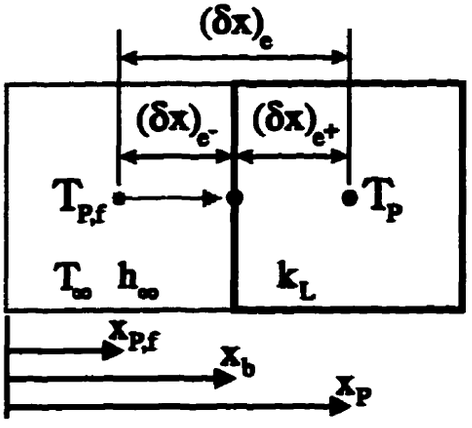

Figure 4.9: Fictitious control volume nomenclature for Newton boundary conditions.

Before solving the set of equations, the coefficients of the fictitious control volumes are absorbed into their neighbouring control volumes. This is done by modifying the

coefficients of the neighbouring control volumes. The coefficient changes are derived by rearranging Equation (4.56) in terms of $T_{P,f}$ and substituting it in for T_W in Equation (4.21) as it is applied to the energy equation. The subscript, ib, refers to the first interior control volume in the domain.

$$a_{P,ib} = a_{P,ib} - a_{W,ib}\frac{a_{E,f}}{a_{P,f}} \tag{4.60a}$$

$$b_{ib} = b_{ib} + a_{W,ib}\frac{b_f}{a_{P,f}} \tag{4.60b}$$

$$a_{W,ib} = 0 \tag{4.60c}$$

The $a_{E,ib}$, $a_{N,ib}$, and $a_{s,ib}$ terms are left unchanged. The derivations for the coefficient changes of the other boundaries are done in a similiar manner. Once the matrix of equations are solved for interior nodal values, the values of the fictitious control volumes are specified to be consistent with the boundary control volume equations.

4.6 Nodal Velocity Storage Location

The numerical model uses a "staggered" grid for the velocity components, as discussed by Patankar [46]. In the staggered grid, the velocity components are calculated for the points that lie on the faces of the control volumes. Thus, the x direction velocity, U, is calculated at the faces that are normal to the x direction. The grid is generated based on the main grid, which is used by the energy equation. Each control volume in each of the staggered grids is created by dividing two control volumes of the main grid exactly in half, as shown in Figure 4.10 and Figure 4.11. The dashed lines represent the staggered grid on top of the main grid (solid lines).

The boundary control volumes of the staggered grids are modelled so that the velocity nodes are directly on the main grid boundary. For example, for the U-velocity staggered grid, the top and bottom control volumes are zero-width, and the

left and right control volumes are half-width.

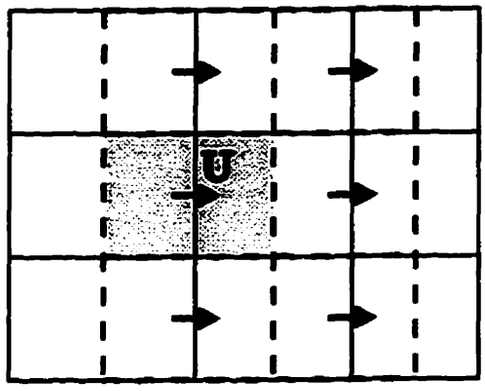

Figure 4.10: Staggered grid for U-velocity.

4.7 Momentum Equations Boundary Conditions

There are only two types of boundary conditions for the momentum equations: Dirichlet (velocity specified) and Neumann (velocity gradient specified). Although the velocity grids are staggered from the main grid, the boundary conditions are handled in a similiar manner to that described in Section 4.5.

Figure 4.12 shows the boundary control volume for the right U-velocity boundary. The $U_{P,f}$ node represents the velocity at the boundary, and the subscript, *ie*, represents the last interior control volume in the x direction. There is one less column than the main grid for the staggered U-momentum equation set, and one less row for the staggered V-momentum equation set. Unlike the zero-width fictitious control volumes of the main grid boundaries, the right boundary of the U-velocity staggered grid is a half control volume since the staggered grid is shifted by half a control vol-

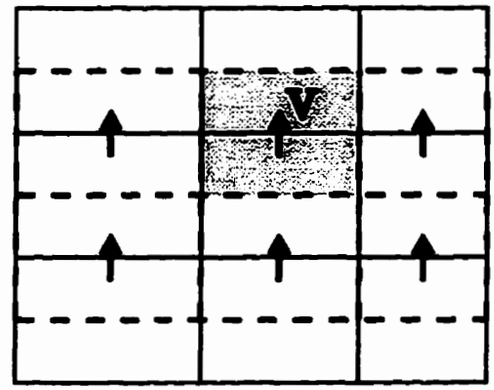

Figure 4.11: Staggered grid for V-velocity.

ume. Dirichlet boundary conditions are used to specifiy boundary velocities. For example, the velocity of the transformer tank walls are specified as zero. The velocity is specified by modifying the fictitious velocity control volume coefficients as follows:

$$a_{P,f} = 1.0 \tag{4.61a}$$

$$a_{W,f} = -\frac{(1-f_R)}{f_R} \tag{4.61b}$$

$$b_{P,f} = \frac{U_{spec}}{f_R} \tag{4.61c}$$

where

$$f_R = \frac{(\delta x)_{w^-,f}}{(\delta x)_{w,f}} \tag{4.62}$$

The remaining coefficients of the right fictitious control volume are set equal to zero. Thus the equation for the fictitious control volume takes the form

$$a_{P,f}U_{P,f} = a_{W,f}U_{W,f} + b_f \tag{4.63}$$

The rest of the boundaries are set up in a similiar manner. Equation (4.62) distinguishes between zero-width and full-width fictitous control volumes by using the grid parameters described in Section 3.5.

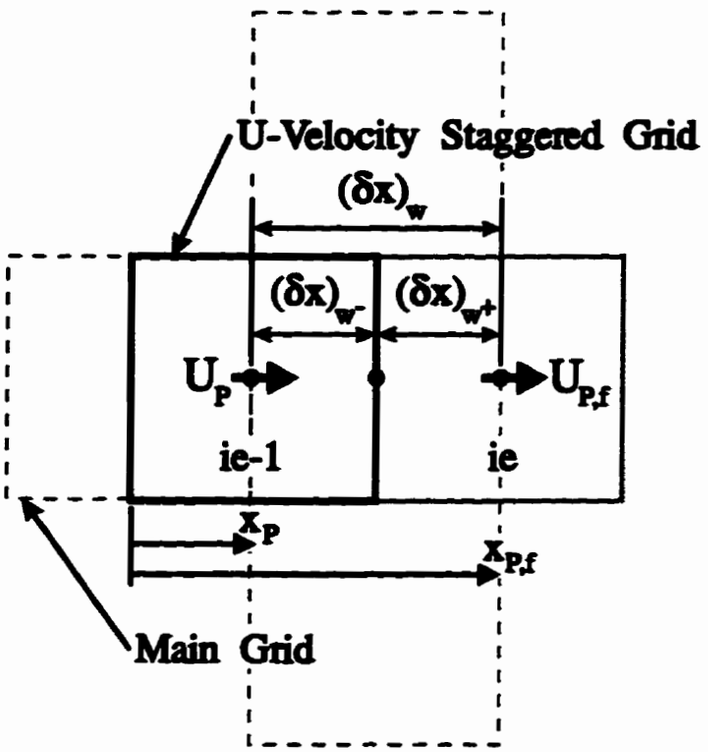

Figure 4.12: Right U-velocity boundary control volume.

The Neumann boundary conditions specify a velocity gradient. The fictitious staggered control volume coefficients are derived by first letting

$$\left(\frac{dU}{dx}\right)_{spec} = \frac{U_{P,f} - U_P}{(\delta x)_{w,f}} \tag{4.64}$$

Equation (4.64) is rearranged in terms of the fictitious velocity.

$$U_{P,f} = U_P + (\delta x)_{w,f}\left(\frac{dU}{dx}\right)_{spec} \tag{4.65}$$

By inspection, the coefficients at the fictitious control volume are set to reflect the

Neumann boundary conditions:

$$a_{P,f} = 1.0 \tag{4.66a}$$

$$a_{W,f} = +(\delta x)_{w,f}\left(\frac{dU}{dx}\right)_{spec} \tag{4.66b}$$

$$b_{P,f} = 1.0 \tag{4.66c}$$

The remaining coefficients of the right fictitious control volume are set equal to zero.

The other momentum equation boundary conditions are derived in a similiar manner for both the U- and V-velocity staggered grids. The top and bottom of the U-velocity grid, and the left and right sides of the V-velocity grid, have zero-width control volumes. The rest are full-width control volumes.

Once the fictitious control volume coefficients are derived, they are absorbed into the neighbouring control volumes in the same way as the coefficients of the energy equations were in the previous section. Again, once the equations are solved then the velocities of the fictitious control volumes are solved using the ficticious control volume coefficients.

4.8 SIMPLEC Algorithm

When the momentum equations are solved, the velocity fields conserve momentum but they do not neccessarily conserve mass. The pressure correction algorthim corrects the velocity fields so that they conserve mass. The numerical solution method adopted in this work uses the SIMPLEC algorithm described by Van Doormaal and Raithby [17] to determine the pressure correction values. The algorthim steps are listed below.

1. Guess the pressure field, P^*.

2. Using velocities from initial conditions (or a previous iteration) the coefficients are calculated for the momentum equations, U^* and V^*.

3. The pressure correction equation coefficients are calculated.

4. Solve for U^* using the momentum equation,

$$a_P^u U_P^* = \sum a_{NP}^u U_{NP}^* + b_P^u + C_P^u(P_P^* - P_E^*) \tag{4.67}$$

5. Solve for V^* using the momentum equation,

$$a_P^v V_P^* = \sum a_{NP}^v V_{NP}^* + b_P^v + C_P^v(P_P^* - P_E^*) \tag{4.68}$$

6. Calculate the P' equation source term, b_P^p, using the values of U^* and V^*, and then solve for the pressure correction, P', using the equation,

$$a_P^p P_P' = \sum a_{NP}^p P_{NP}' + b_P^p \tag{4.69}$$

7. Correct for the final U, V, and P fields using the equations,

$$P_P = P_P^* + P_P' \tag{4.70a}$$

$$U_P = U_P^* + d_e^u(P_P' - P_E') \tag{4.70b}$$

$$V_P = V_P^* + d_n^v(P_P' - P_N') \tag{4.70c}$$

where,

$$d_e^u = \frac{C^u}{a_P^u - \sum a_{NP}^u} \tag{4.71a}$$

$$d_n^v = \frac{C^v}{a_P^v - \sum a_{NP}^v} \tag{4.71b}$$

8. Repeat steps 4-7 until adequate convergence has been achieved in the linear equation sets (mass and momentum).

4.9 Pressure Correction

The SIMPLEC algorithm requires that the velocity fields be corrected to conserve mass. This correction is also used on the pressure field. The following subsections show the derivation for the pressure correction equation.

4.9.1 The Pressure Correction Equation

The pressure correction, P', equation is derived from the continuity equation, Equation (2.4), when ξ is set equal to 1.0. Following the derivation by Patankar [46] the pressure correction equation has the form,

$$a_P^p P_P^p = \sum a_{NP}^p P_{NP}^p + b_P^p \tag{4.72}$$

where,

$$a_E^p = \rho_e A_e d_e^u \tag{4.73a}$$

$$a_W^p = \rho_w A_w d_w^u \tag{4.73b}$$

$$a_N^p = \rho_n A_n d_n^v \tag{4.73c}$$

$$a_S^p = \rho_s A_s d_s^v \tag{4.73d}$$

$$a_P^p = a_E^p + a_W^p + a_N^p + a_S^p = \sum a_{NP}^p \tag{4.73e}$$

$$b_P = -(\dot{m}_e)^* + (\dot{m}_w)^* - (\dot{m}_n)^* + (\dot{m}_s)^* = -\Delta M^* \tag{4.73f}$$

The asterisk superscript, also called "starred" values, are used to designate values calculated directly from the momentum equations using the guessed pressure field P^*.

4.9.2 Boundary Conditions for the Pressure Correction Equation

A general method is needed to assert the pressure correction boundary conditions. The pressure correction boundary conditions, shown in Figure 4.13, are based on the mass conservation equation (Equation (4.6)). The right boundary condition is used as an example of the derivation. Since M_P equals M_P^o when using incompressible flow

assumptions, the equation reduces to

$$a_W^c U_W + a_E^c U_E + a_N^c V_N + a_S^c V_S = 0 \tag{4.74}$$

where,

$$\begin{aligned} a_W^c &= \rho_w A_w & a_E^c &= \rho_e A_e \\ a_S^c &= \rho_s A_s & a_N^c &= \rho_n A_n \end{aligned} \tag{4.75}$$

The fictitious velocity boundary condition is described by Equation (4.63).

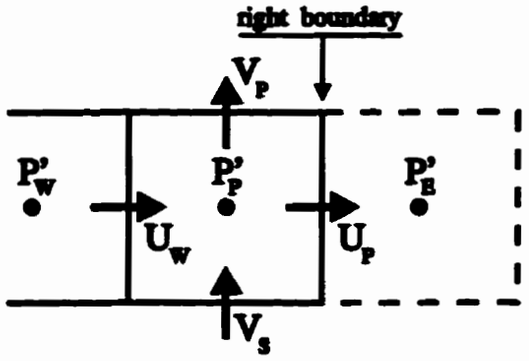

Figure 4.13: Pressure correction boundary conditions.

$$a_{P,f} U_P = a_{W,f} U_W + b_{P,f}^u \tag{4.76}$$

Equation (4.76) is substituted into Equation (4.74), and then the equation is rearranged in terms of velocities to get

$$\left[a_W^c + a_E^c \frac{a_{W,f}^u}{a_{P,f}^u} \right] U_W + a_N^c V_P + a_S^c V_S + \frac{a_E^c b_{P,f}^u}{a_{P,f}^u} = 0 \tag{4.77}$$

The velocities are then replaced with their U^* and V^* pressure corrections, given by Equations (4.70b) and (4.70c), respectively. The resulting equation is rearranged in

terms of P' to get

$$a_P^p P_P' = a_E^p P_E' + a_W^p P_W' + a_N^p P_N' + a_S^p P_S' + b_P^p \tag{4.78}$$

where,

$$a_E^p = 0 \tag{4.79a}$$

$$a_W^p = \left(a_W^c + a_E^c \frac{a_{W,f}^u}{a_{P,f}^u}\right) d_W^u = a_W^c d_w^u + \underbrace{a_E^c \frac{a_{W,f}^u}{a_{P,f}^u} d_w^u} \tag{4.79b}$$

$$a_N^p = -a_N^c d_n^v \tag{4.79c}$$

$$a_S^p = a_S^c d_s^v \tag{4.79d}$$

$$a_P^p = \sum a_{NP}^p \tag{4.79e}$$

$$b_P^p = a_W^c U_W^* + a_E^c U_P^* + a_N^c V_P^* + a_S^c V_S^* = -\Delta M^* \tag{4.79f}$$

The term with the underbrace in the a_W^p equation is simply added onto the original coefficient. For the boundary conditions in a corner, the two boundary terms are added onto the original coefficients. For example, the pressure correction coefficients for the upper right corner would be:

$$a_E^p = 0 \tag{4.80a}$$

$$a_W^p = a_W^c d_w^u + \frac{a_{W,F}^u}{a_{P,F}^u} d_w^u \tag{4.80b}$$

$$a_N^p = 0 \tag{4.80c}$$

$$a_S^p = a_S^c d_s^v + \frac{a_{S,F}^v}{a_{P,F}^v} d_s^v \tag{4.80d}$$

$$a_P^p = \sum a_{NP}^p \tag{4.80e}$$

$$b_P^p = \Delta M^* \tag{4.80f}$$

4.9.3 Pressure Reference Specification

Sometimes it is necessary to specify the value of P' since certain boundary conditions created a redundant equation, as discussed by Van Doormaal and Raithby [17]. The continuity equation is replaced by setting one of the P' control volume values equal to zero. The pressure field is also modified to maintain a reference pressure in one of the control volumes. The rest of the pressure field is shifted to maintain the reference pressure.

4.10 Solid Regions

In a solid region the velocity is zero throughout the entire region. Each control volume in the region is modelled as a homogenous material. As described in Section 2.5, the energy equation does not require special boundary conditions for solid regions. The only calculation needed is the face value of the thermal conductivity which is determined using the harmonic mean.

The solid face velocity boundary conditions are treated in the same way as the boundary conditions of the outer model domain. Dirichlet boundary conditions are used to ensure a zero velocity profile along the edges of a solid. The interior control volume coefficients for the U and V equations are all set to zero except for a_P, which is set equal to unity. Thus the velocity field within the solid is calculated as zero.

The pressure correction coefficients are modified so that the entire region within a block would specify a zero pressure field. All the P' equation coefficients for control volumes in a solid region are set to zero except for a_P which is set equal to one. For the fluid control volumes beside the solid, the coefficients of all the terms that connect the pressure correction equation to the solid are set to zero. This removes any effect

the solid may have on the pressure correction. For example, all fluid control volumes to the right of a solid have the a_W^p terms set to zero.

4.11 The PVT-Loop

Natural convection is a phenomenon where the temperature and the velocity of a fluid are interdependent. When modelling this phenomenon, a strong interaction of the temperature and velocity fields is observed. Because they represent the physics, the algebraic equation sets are coupled. This may lead to instabilities when attempting to solve the conjugate transformer model with a segregated solution method, especially when using large time steps. In an attempt to reduce the instabilities, a PVT-loop was introduced. Rather than use a new algorithm that performs a simultaneous coupled equation solution, a modified version of the standard algorithm was examined. Figure 4.14 shows the PVT-loop algorithm used. This loop was repeated until convergence is reached for a given time step. The PV-loop is discussed in Section 4.8, and is nested within the PVT-loop. The velocity and pressure correction coefficients are calculated before the PVT-loop as a means of adding relaxation to the solution of the complete equation set. Since the mass flows from the previous time steps are used for the momentum equations, this kept the U-velocity and V-velocity equations uncoupled from each other. Only the source terms of the velocity equations are changed inside the PVT-loop to account for the updated pressure and temperature fields. Before the energy equation coefficients are calculated, new mass flows are solved so that the temperature field can accurately reflect the change in enthalpy. Once all the fields have been calculated, then the PVT-loop is checked for suitable convergence. The convergence for iteration $\kappa + 1$ is checked with the equation,

$$\epsilon_{pvt} = \frac{|(\phi^{\kappa+1} - \phi^{\kappa})_{max}|}{\phi_{max}^{\kappa+1} - \phi_{min}^{\kappa+1}} \tag{4.81}$$

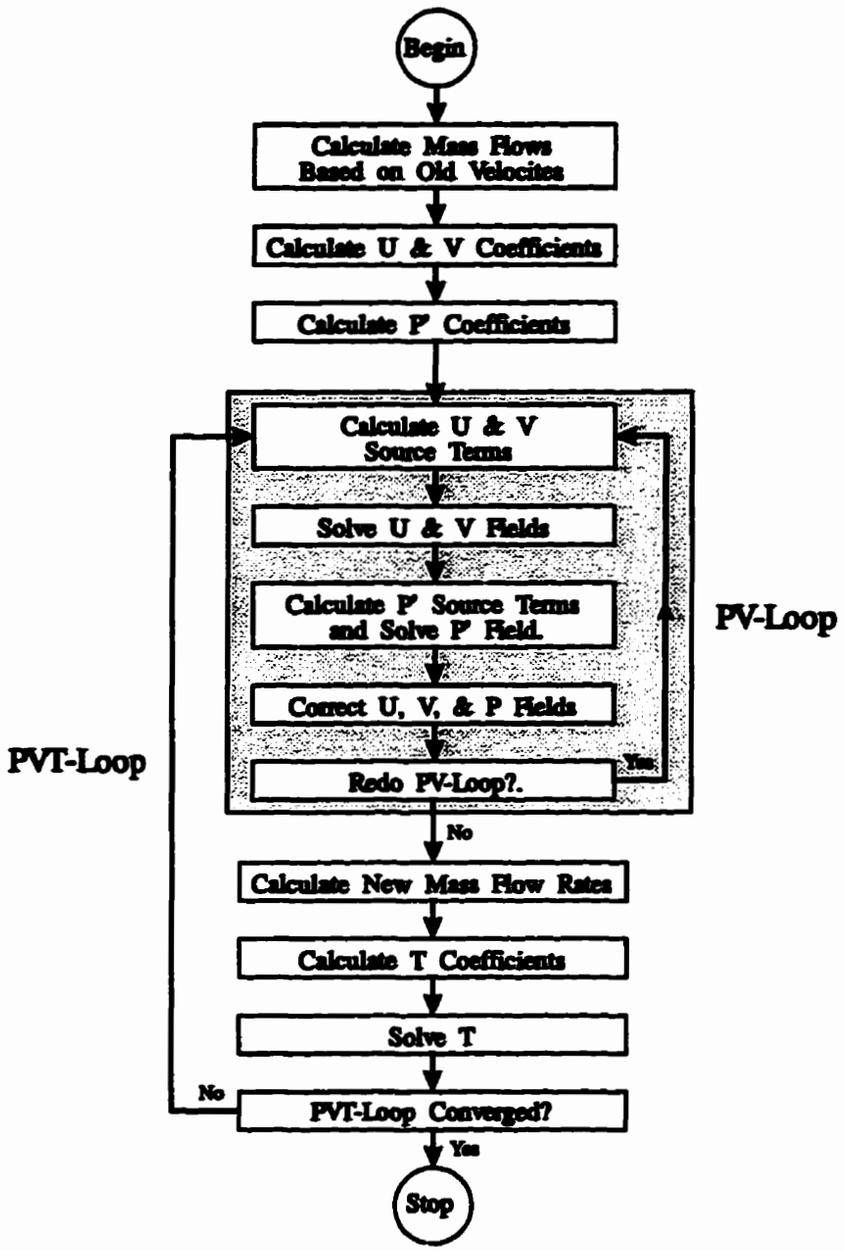

Figure 4.14: PVT-loop flowchart for a single time step.

Once the PVT-Loop is converged, then the time step is finished and the solution progresses to the next time step.

Relaxation is also applied to the energy and momentum equations within the loop. The relaxation employed is similiar to that used by P. F. Galpin et al. [19]. With the relaxation term, e^T, the energy equation becomes

$$a_P T_P^{\kappa+1}\left(1+\frac{1}{e^T}\right) = a_E T_E^{\kappa+1} + a_W T_W^{\kappa+1} + a_N T_N^{\kappa+1} + a_S T_S^{\kappa+1} + \left(b_P + \frac{a_P}{e^T} T_P^{\kappa}\right) \tag{4.82}$$

The relaxation term is set up so that as the solution of the temperature field approaches the final solution, then the term is cancelled out of the equation ($a_p T_p^{\kappa+1}/e^T \approx a_p T_p^{\kappa}/e^T$ since $T_p^{\kappa+1} \approx T_p^{\kappa}$).

Similiarly, the momentum equations become

$$\begin{aligned} a_P U_P^{\kappa+1}\left(1+\frac{1}{e^U}\right) &= a_E U_E^{\kappa+1} + a_W U_W^{\kappa+1} + a_N U_N^{\kappa+1} + a_S U_S^{\kappa+1} \\ &+ \left(b_P + \frac{a_P}{e^U} U_P^{\kappa}\right) \end{aligned} \tag{4.83}$$

$$\begin{aligned} a_P V_P^{\kappa+1}\left(1+\frac{1}{e^V}\right) &= a_E V_E^{\kappa+1} + a_W V_W^{\kappa+1} + a_N V_N^{\kappa+1} + a_S V_S^{\kappa+1} \\ &+ \left(b_P + \frac{a_P}{e^V} V_P^{\kappa}\right) \end{aligned} \tag{4.84}$$

The relaxation term increases the diagonal dominance of the equations. When the equation set is converged within the PVT-loop, then the relaxation terms in Equations (4.82) to (4.84) cancel.

4.12 The Overall Steady State Convergence

When there is negligible difference in the four solution fields between time steps, the model has obtained overall steady state convergence. The steady state convergence

check that was applied to the temperature, velocity, and pressure fields is

$$\frac{|(\phi - \phi^o)_{max}|}{\phi_{max} - \phi_{min}} \leq \epsilon_{ss} \tag{4.85}$$

The difference between the new and old fields is divided by the new field range so that the difference is normalized by a non-zero value. A typical value of ϵ_{ss} is 1.0×10^{-5}.

Chapter 5

Algebraic Equation Solvers

5.1 Introduction

This chapter presents the four algorithms used to solve the discretization equations derived in Chapter 4. The four solvers are Line-Gauss Seidel with relaxation (LGS2d), LU Decomposition (LUD2d), Additive Correction Multigrid (ACM2d), and Conjugate Additive Correction Multigrid (CACM2d). For a given solution, whether steady state or transient, only one solver is used on each equation set.

As part of this work the effectiveness of the four different solvers was investigated briefly. The LGS2d solver, a standard line solver, and the LUD2d solver, a standard direct solver, are both commonly used to solve computational fluid dynamic problems. The ACM2d has been developed relatively recently; it makes use of several levels of grid resolution to solve for the desired field. The CACM2d is a new solver based on the ACM2d that was specially adopted to improve its use on conjugate heat transfer problems.

5.2 Line-Gauss Seidel with Relaxation in Two-Dimensions (LGS2d)

The LGS2d solver, also known as Line Successive Over Relaxation (LSOR), sweeps with a TDMA (Tri-Diagonal Matrix Algorithm) line solver to solve each row and column of the two-dimensional model [46]. The direction of the line solver is alternated by first solving columns from left to right, then solving rows from bottom to top, to complete one iteration. The solver converges when the residual is reduced below the criterion, $\epsilon_{overall}$. The residual reduction of $\epsilon_{overall}$ is defined for iteration λ by Equation (5.1).

$$\epsilon_{overall} = \frac{R^{\lambda}}{R^{0}} \tag{5.1}$$

The residual, R, is defined in Equation (5.2). The sum of the magnitude of the residuals in all control volumes is normalized by the total number of control volumes. The initial residual, R^0, is calculated before the solver algorithm is applied to the equation set.

$$R = \frac{\sum_{j=1}^{n}\sum_{i=1}^{m}\left|\left(a_E\phi_E + a_W\phi_W + a_N\phi_N + a_S\phi_S + b_P - a_P\phi_P\right)\right|}{N_x \times N_y} \tag{5.2}$$

5.3 LU Decomposition (LUD2d)

The LUD2d algorithm used was a banded storage direct solver. Because of the computational cost for large number of nodes it is not practical to use the LUD2d solver for the transformer model. It was therefore used just to produce a benchmark solution against which the other solver solutions could be compared.

5.4 Additive Correction Multigrid (ACM2d)

The ACM2d solver is based on the additive correction multigrid algorithm by Hutchinson and Raithby [27, 26, 54]. ACM2d is a method of accelerating the convergence of an algebraic equation set for a two-dimensional domain. The algorithm uses the original (fine grid) equation set, plus other coarser grids that are built by gathering the control volumes of the finer grid into larger blocks. For example, a 40×40 grid represents the finest, or starting grid. The algorithm them builds coarser grids, 20×20, 10×10, etc. to help with the convergence of the original equation set. The coarser grids are used to help move the solution field information around to the other control volumes faster than if only the fine grid was used. The ACM2d solver uses the LGS2d solver on the equation sets at each multi-grid level. The so-called flexible cycle algorithm is implemented since it had a faster convergence rate than the V and W-cycles. A cycle is the method by which the algorithm moves between grid levels. In this thesis, the multigrid algorithm only solves the temperature and pressure correction equations since LGS2d alone is considered adequate for the solution of the momentum equations.

5.4.1 ACM2d Overview

Additive correction multigrid (ACM) is a multigrid method where the equation set is solved on several grid densities to accelerate the convergence of an equation set. Each of these grids are increasingly coarser than the last. The ACM procedure forms the coarse-grid equations by asserting integral conservation over blocks of control volumes. The corrections calculated on the coarser grids are added to the finer grids in order to preserve the integral balances. In this work the grids are made coarser by a factor of two control volumes into one, although other combinations could be used.

When solving the finest grid, the solver quickly reduces the high frequency error, or relative error. The high frequency error is the relative error of a control volume based on the values of its neighbours. The information about the neighbouring control volumes is quickly assessed and calculated in the solution of the equations. On the other hand, iterative solvers need many more iterations to reduce low frequency errors, or the absolute error. The low frequency error is the error of the control volume's currently calculated value relative to the final answer. Information about the control volumes on one end of the model takes several iterations to arrive at the control volumes on the other end of the domain.

As shown for the one-dimensional grid in Figure 5.1, ACM reduces the low frequency error introduced by the boundary conditions, Φ_1 and Φ_2, by solving a coarser grid. The correction calculated on the coarser grid is added to the finer grid. The new high frequency errors are quickly solved on the finer grid [54].

Figure 5.2 illustrates the ACM grid levels. The "flexible cycle" ACM solver begins with the finest grid (Level 1). When the solution convergence rate on this grid begins to slow down (or stall) the "flexible cycle" solver moves to a coarser grid. The coarser grid is used to calculate the correction to be applied to the finer grid. When the solution convergence rate for the correction field slows down, the ACM solver moves on to the next coarser grid. This third level is the correction for the correction field of level 2. This continues until either level *N* quickly reduces its residual, or until the correction equations on a very coarse level are solved simultaneously with a direct solver. When level *N* is solved adequately, then the correction field is added onto level *N-1*. Now level *N-1* is solved again until it either quickly converges or stalls. If the solution of the level stalls then the solver will return back to level *N* to reduce the low frequency error again. If level *N-1* quickly converges, then the correction solved by level *N-1* is added to level *N-2*. This continues until level 2 adds the correction to level 1, and level 1 quickly converges to the answer.

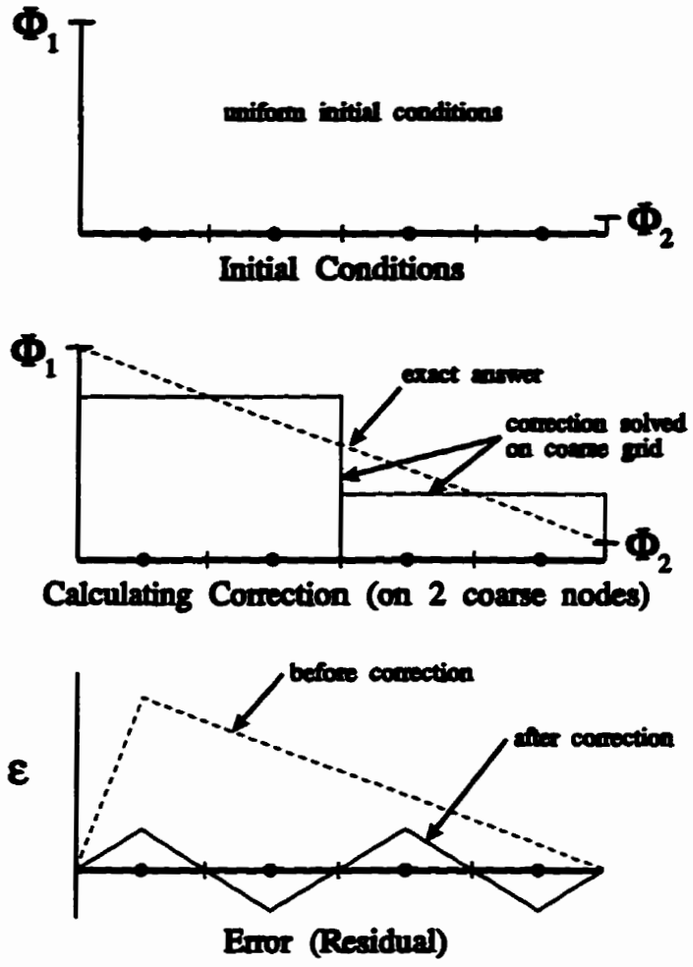

Figure 5.1: Additive correction multigrid reducing low frequency errors and introducing high frequency errors [54]. The two boundary conditions in this illustration are represented by Φ_1 and Φ_2.

5.4.2 ACM2d Equations

This subsection describes the general multigrid equations. It shows how the equations may be assembled based on the control volume equations from the finer grid. The derivation and assembly procedure described here follows the work of Raithby [54].

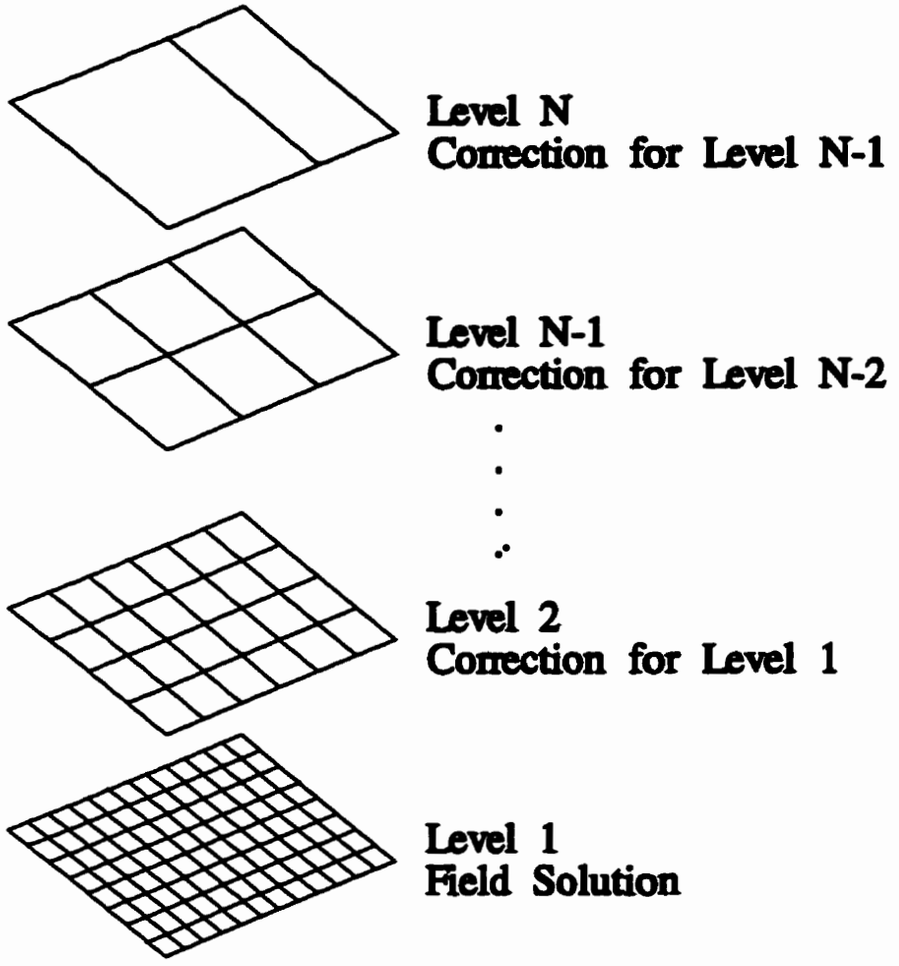

Figure 5.2: An example of the levels involved when solving an ACM model.

In the description below, the equations are first derived for a one-dimensional grid, and then extended to two dimensions.

Each two-dimensional control volume from the base grid, or level 1, is represented by Equation (4.21). For a one-dimensional grid, this equation takes the form

$$a_P\phi_P = a_E\phi_E + a_W\phi_W + b_P \tag{5.3}$$

To form each additive correction (AC) equation for the level 2 block, Equa-

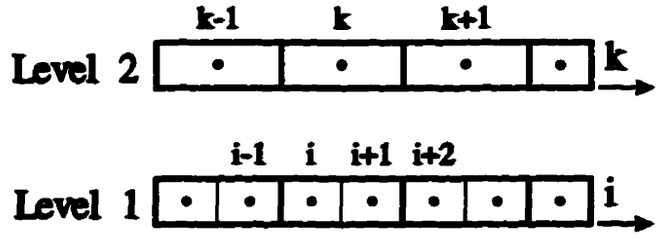

Figure 5.3: Schematic showing the assembly of one-dimensional control volumes on the fine grid to create blocks (denoted by thick lines) for the coarser grid.

tion (5.3) is summed for each control volume being assembled. For instance, the k blocks shown in Figure 5.3 may have one and two control volumes added together to form the basis of the new equations.

First, let $\phi_i = \tilde{\phi}_i + \delta_k$ where $\tilde{\phi}_i$ is the best estimate of ϕ_i and δ_k is the correction added to $\tilde{\phi}_i$ to obtain an improved value of ϕ_i. The value of δ_k is uniformly applied to all control volumes in a block.

Inserting the new ϕ_i into Equation (5.3) produces the following equation for the i control volume:

$$a_{P,i}(\phi_i + \delta_k) = a_{E,i}(\phi_{i+1} + \delta_k) + a_{W,i}(\phi_{i-1} + \delta_{k-1}) + b_{P,i} \qquad (5.4)$$

Note that the ϕ_{i-1} term has the correction, δ_{k-1}, applied to it since that control volume is assembled into block *k-1*.

A similiar equation is written for the neighboring *i+1* control volume.

$$a_{P,i+1}(\phi_{i+1} + \delta_k) = a_{E,i+1}(\phi_{i+2} + \delta_{k+1}) + a_{W,i+1}(\phi_i + \delta_k) + b_{P,i+1} \qquad (5.5)$$

These two equations are summed together and then rearranged in terms of δ_k to get

$$\begin{aligned}(a_{P,i} + a_{P,i+1} - a_{E,i} - a_{W,i+1})\,\delta_k \;&=\; a_{W,i}\delta_{k-1} + a_{E,i+1}\delta_{k+1} \\ &+ \underbrace{(a_{E,i}\tilde{\phi}_{i+1} + a_{W,i}\tilde{\phi}_{i-1} + b_{P,i} - a_{P,i}\tilde{\phi}_i)}_{\tilde{R}_i} \\ &+ \underbrace{(a_{E,i+1}\tilde{\phi}_{i+2} + a_{W,i+1}\tilde{\phi}_i + b_{P,i+1} - a_{P,i+1}\tilde{\phi}_{i+1})}_{\tilde{R}_{i+1}} \qquad (5.6)\end{aligned}$$

where the last two terms, $\tilde{R}_i$ and $\tilde{R}_{i+1}$, are the equation residuals of the two assembled control volumes. Equation 5.6 is simplified to get

$$\bar{a}_{P,k}\delta_k \;=\; \bar{a}_{E,k}\delta_{k+1} + \bar{a}_{W,k}\delta_{k-1} + \bar{b}_{P,k} \qquad (5.7)$$

where

$$\bar{a}_{P,k} \;=\; a_{P,i} + a_{P,i+1} - a_{E,i} - a_{W,i+1} \qquad (5.8a)$$

$$\bar{a}_{E,k} \;=\; a_{E,i+1} \qquad (5.8b)$$

$$\bar{a}_{W,k} \;=\; a_{W,i} \qquad (5.8c)$$

$$\bar{b}_{P,k} \;=\; \tilde{R}_i + \tilde{R}_{i+1} \qquad (5.8d)$$

An analogous equation is assembled for each coarse-grid block. Once these coarser grid equations are solved, the resulting correction are applied to the finer grid. After all the corrections are applied, then the finer grid is re-solved. Note that the coarser grid equation set solved by iteration may also stall after the high frequency errors are reduced. This process could then be applied to assemble an even coarser grid so that a correction could be solved for the correction grid.

Using the procedure shown for the one-dimensional grid, the two-dimensional grid equation is:

$$\bar{a}_{P,kl}\delta_{kl} \;=\; \bar{a}_{E,kl}\delta_{k+1l} + \bar{a}_{W,kl}\delta_{k-1l} + \bar{a}_{N,kl}\delta_{kl+1} + \bar{a}_{S,kl}\delta_{kl-1} + \bar{b}_{P,kl} \qquad (5.9)$$

where,

$$\bar{a}_{P,kl} = a_{P,ij} + a_{P,i+1j} + a_{P,ij+1} + a_{P,i+1j+1} - a_{E,ij} - a_{N,ij} - a_{W,i+1j} - a_{N,i+1j} - a_{E,ij+1} - a_{S,ij+1} - a_{W,i+1j+1} - a_{S,i+1j+1} \quad (5.10a)$$

$$\bar{a}_{E,kl} = a_{E,i+1j} + a_{E,i+1j+1} \quad (5.10b)$$

$$\bar{a}_{W,kl} = a_{W,ij} + a_{W,ij+1} \quad (5.10c)$$

$$\bar{a}_{N,kl} = a_{N,ij+1} + a_{N,i+1j+1} \quad (5.10d)$$

$$\bar{a}_{S,kl} = a_{S,ij} + a_{S,i+1j} \quad (5.10e)$$

$$\bar{b}_{P,kl} = \widetilde{R}_{ij} + \widetilde{R}_{i+1j} + \widetilde{R}_{ij+1} + \widetilde{R}_{i+1j+1}. \quad (5.10f)$$

The values of $\widetilde{R}$ are the residual of each control volume on the finer grid.

$$\widetilde{R}_{ij} = a_{E,ij}\tilde{\phi}_{i+1j} + a_{W,ij}\tilde{\phi}_{i-1j} + a_{N,ij}\tilde{\phi}_{ij+1} + a_{S,ij}\tilde{\phi}_{ij-1} + b_{P,ij} - a_{P,ij}\tilde{\phi}_{ij} \quad (5.11a)$$

$$\widetilde{R}_{i+1j} = a_{E,i+1j}\tilde{\phi}_{i+2j} + a_{W,i+1j}\tilde{\phi}_{ij} + a_{N,i+1j}\tilde{\phi}_{i+1j+1} + a_{S,i+1j}\tilde{\phi}_{i+1j-1} + b_{P,i+1j} - a_{P,i+1j}\tilde{\phi}_{i+1j} \quad (5.11b)$$

$$\widetilde{R}_{ij+1} = a_{E,ij+1}\tilde{\phi}_{i+1j+1} + a_{W,ij+1}\tilde{\phi}_{i-1j+1} + a_{N,ij+1}\tilde{\phi}_{ij+2} + a_{S,ij+1}\tilde{\phi}_{ij} + b_{P,ij+1} - a_{P,ij+1}\tilde{\phi}_{ij+1} \quad (5.11c)$$

$$\widetilde{R}_{i+1j+1} = a_{E,i+1j+1}\tilde{\phi}_{i+2j+1} + a_{W,i+1j+1}\tilde{\phi}_{ij+1} + a_{N,i+1j+1}\tilde{\phi}_{i+1j+2} + a_{S,i+1j+1}\tilde{\phi}_{i+1j} + b_{P,i+1j+1} - a_{P,i+1j+1}\tilde{\phi}_{i+1j+1} \quad (5.11d)$$

Figure 5.4 shows how the level 1 grid control volumes (the finest mesh) are combined to form the level 2 grid in two dimensions. The darker lines represent the level 2 mesh. The blocks are formed by trying to assemble two blocks in each direction. Sometimes rectangular blocks are formed out of the remaining control volumes. New correction equations are derived for these coarse blocks using the method described above.

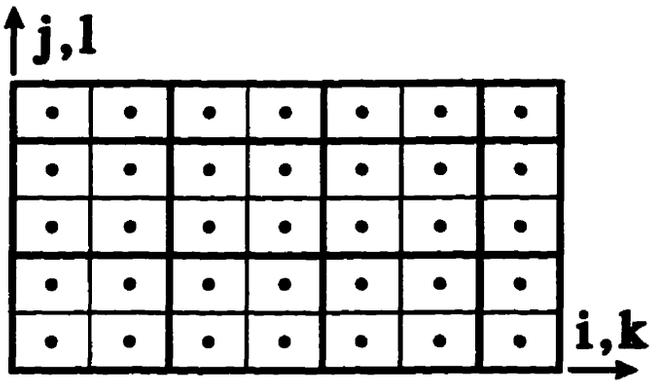

Figure 5.4: Schematic showing the assembly of two-dimensional control volumes on the fine grid to create blocks (denoted by thick lines) for the coarser grid.

5.4.3 ACM2d Solution Procedure

The previous subsection, ACM2d Equations, described the derivation of the AC equations. This subsection outlines the strategies involved in solving the correction equations.

There are several common strategies for moving between grid levels. In this work, the V-cycle and the flexible cycle methods were investigated. Figure 5.5 shows an example of the V-cycle. The algorithm starts at level 1 (the finest grid), and performs one iteration at each level until it reaches the N level. At the N level the solver will attempt to solve the correction equations to a tight convergence criterion. The equation set is solved either by a direct solver (Gauss elimination in this case) or by solving the equations using LGS2d until convergence ($\epsilon_N = \epsilon_{overall}$, the convergence criterion of the solver). The correction from level N is added to level N-1, and LGS2d solves the equation until it reaches the required level residual reduction, ϵ_L. The level residual reduction is the requirement of the solver to reduce the residual for a given level. In this work a value of ϵ_L equal to 0.25 was used. Once this criterion is met, the

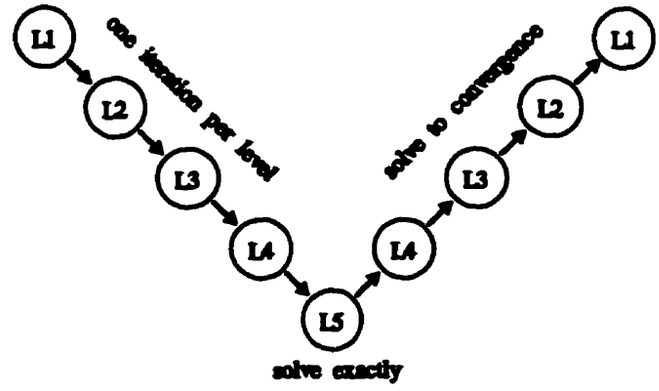

Figure 5.5: Flowchart showing an example of the V-cycle algorithm with only five levels.

correction is added onto the next level, and the solution proceeds to the next finest level. Eventually the correction is added onto level 1. LGS2d then solves the original set of equations until the solution stalls. A solution is considered stalled when the residuals are not changing a significant amount relative to each other. The residual reduction stall criterion, ϵ_s, defined by Hutchinson and Raithby [27], is satisfied when

$$\epsilon_s R^{\omega-1} \geq R^{\omega} \tag{5.12}$$

where $R^{\omega-1}$ is the residual for iteration $\omega-1$. In this work ϵ_s was set to 0.6. Once the solution of level 1 stalled, the V-cycle was restarted by collecting the residual from level 1 and reassembling the source term of level 2. This procedure continues until the solver criterion, $\epsilon_{overall}$, is achieved on level 1 as defined by Equation (5.1). The value of R^0 is calculated before any V-cycles equation solutions are performed.

The main disadvantage of the V-cycle algorithm is that it often solves level corrections that are not needed. Since the V-cycle is very rigid in its design, it cannot optimize the convergence of the field by either staying at the coarser levels to reduce

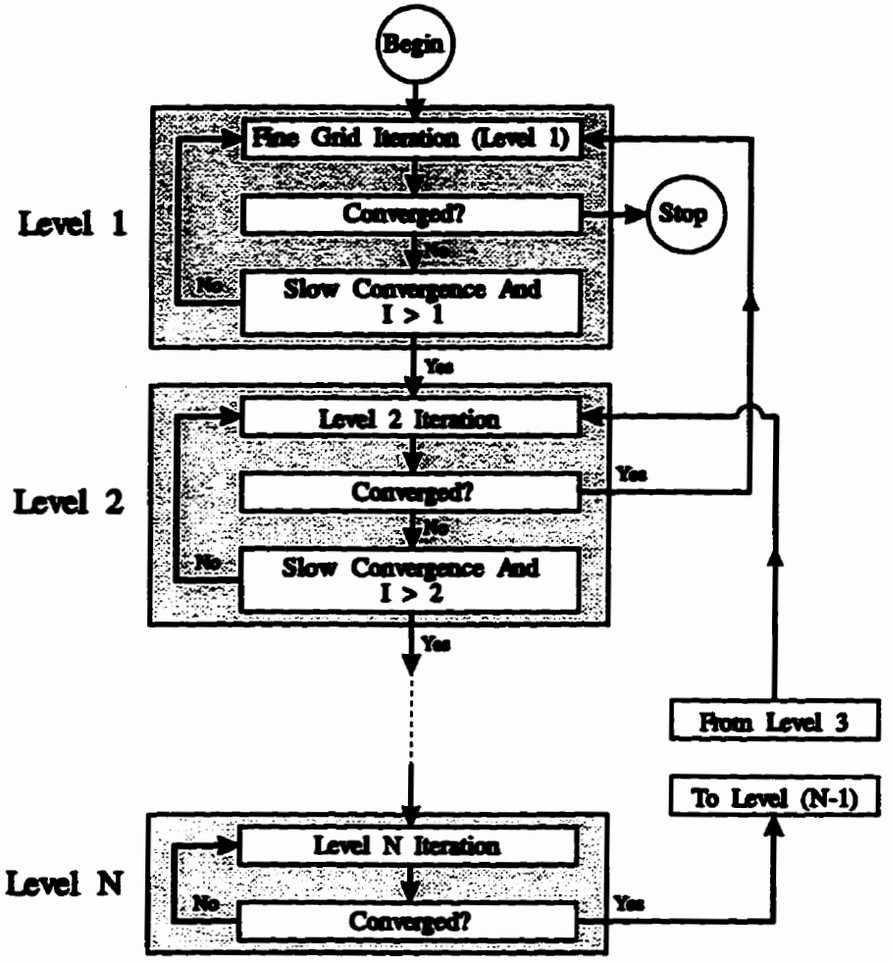

Figure 5.6: The flexible cycle of B. R. Hutchinson and G. D. Raithby [27] is used to determine when coarse-grid correction equations are to be employed.

the low frequency errors, or by spending time at level one when the field equations are solving with a fast convergence rate. Therefore another strategy is needed to improve convergence.

The flexible cycle, as described by Hutchinson and Raithby [27], improves upon the V-cycle algorithm. A flowchart of the flexible cycle is shown in Figure 5.6. The solver starts with one iteration of LGS2d on the first level equation set. If the solution

is converged to the solver criterion, $\epsilon_{overall}$, then the solver stops. Otherwise the solver will continue iterating on level 1 until the LGS2d solver begins to stall. This stall criterion, ϵ_s, is the same as used for the V-cycle. Once the solver stalls on level 1, the residuals of the level 1 control volumes are assembled to create the source terms of level 2. After the solver iterates on level 2, the correction equations are checked for convergence. The correction equation set is converged when the correction residual reduction criterion, ϵ_L, has satisfied the equation,

$$\epsilon_L R_L^0 \geq R_L^\omega \tag{5.13}$$

If the level 2 correction equation set has not converged on a solution, the LGS2d solver continues solving this equation set until it meets the convergence criterion or until it stalls. The convergence is considered stalled if the ratio of residuals between iterations is greater than ϵ_s. If the solution stalls, then the residuals of the correction equations are assembled together to create the source terms of level 3. These new equations are a correction for the correction equations of level 2. The algorithm continues until level N is reached. If LGS2d stalls on level *N-1*, the solver creates the new source terms of level N. The solver iterates with LGS2d until the level has met the ϵ_L convergence criterion. Alternatively, a direct solver can be used at level N if there are only a few blocks on this final grid. In this work Gauss elimination was used at level N if it was a 2×2 grid, otherwise LGS2d was used.

Once level N has been solved, the correction is applied to level *N-1* and the solver continues by trying to solve the finer grid equations. Eventually, the solver will work its way back to level 1 where the corrections from level 2 are added to the field of level 1. Iteration using LGS2d continues until it stalls on level 1 again, or until the solver converges. Convergence on level 1 is obtained when Equation (5.1) is satisfied. The value of R^0 is the residual calculated before any iterations have been performed by the solver.

Sometimes the flexible cycle will oscillate among the coarser levels because at times a correction applied to a finer grid solution field can induce a divergence from the final solution rather than improve the convergence. This may cause the finer grid to stall prematurely, and so the solver tries to use another coarser grid correction equation set to improve the convergence. If the new correction increases the divergence this can continue indefinitely. To prevent the solver from wasting time on the coarser levels, a maximum number of work units is set for the solver. A work unit (WU) represents the time required to solve one LGS2d iteration on the finest level. As an approximation, each two-dimensional level was assumed to take one-quarter the time of the previous level. Therefore level 1 takes one WU, level 2 takes 0.25 WU's, level 3 takes 0.0625 WU's, and so on. Monitoring CPU time usage in a few test cases indicated that this approximation is very close to the actual time it takes to solve large grids.

5.5 Conjugate Additive Correction Multigrid (CACM2d)

The CACM2d solver is the same as the ACM2d solver except that the CACM2d distinguishes between solid and fluid regions in the solution domain. Figure 5.8 shows a conjugate model with the coarser multigrid control volumes straddling the fluid and two different solids. Sun and Emery [60] discussed how they used multigrid to solve their conjugate domain. They explained that the correction calculated for a coarser block straddling a solid and a fluid region would not improve the solution. If this correction is applied to the finer grid solution field then the solution of the equations near the discontinuity will diverge [60]. For example, the additive correction for the pressure correction field is calculated for a coarser grid straddling a fluid-solid

interface. The solid has a residual of zero, and the fluid some nominal value. When the residuals are added together, the residual you wish to reduce is now halved. When this correction is added to the finer grid, it will drive the solution in both the solid and the fluid regions further away from the final solution because it had not been calculated properly for each region. In the CACM2d method, these higher level, or coarser, control volumes are not allowed to straddle across two different solid region control volumes, or across a solid-fluid interface. This approach maintains the clustering of uniform property control volumes. Sun and Emery adjusted their solver so that no correction is applied near the discontinuity [60].

To ensure that the higher level control volumes did not straddle two different materials, control volumes are categorized according to the type of material. The material type is either a fluid or a solid.

Figure 5.7 illustrates the algorithm in one-dimension. For the second level, the CACM2d algorithm first combines every pair of control volumes until the second control volume in a set is a different material. The solver then kept the two control volumes separate and continues 'joining' control volumes together, starting with the

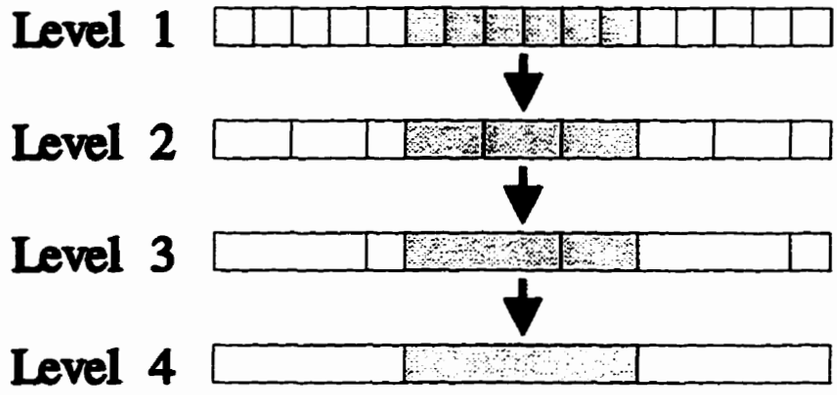

Figure 5.7: CACM2d assembling the control volumes into coarser blocks while keeping the solid region (shaded area) separate from the fluid.

new material control volume. This continues until the second level is complete. The third and fourth levels are also assembled in a similiar manner, each relying on the information stored in the previous level to determine which control volumes are to be joined together. In the example, the final level has only one control volume for each material type. Figure 5.8 shows how CACM2d creates control volume blocks in two dimensions by avoiding blocks that straddled different materials.

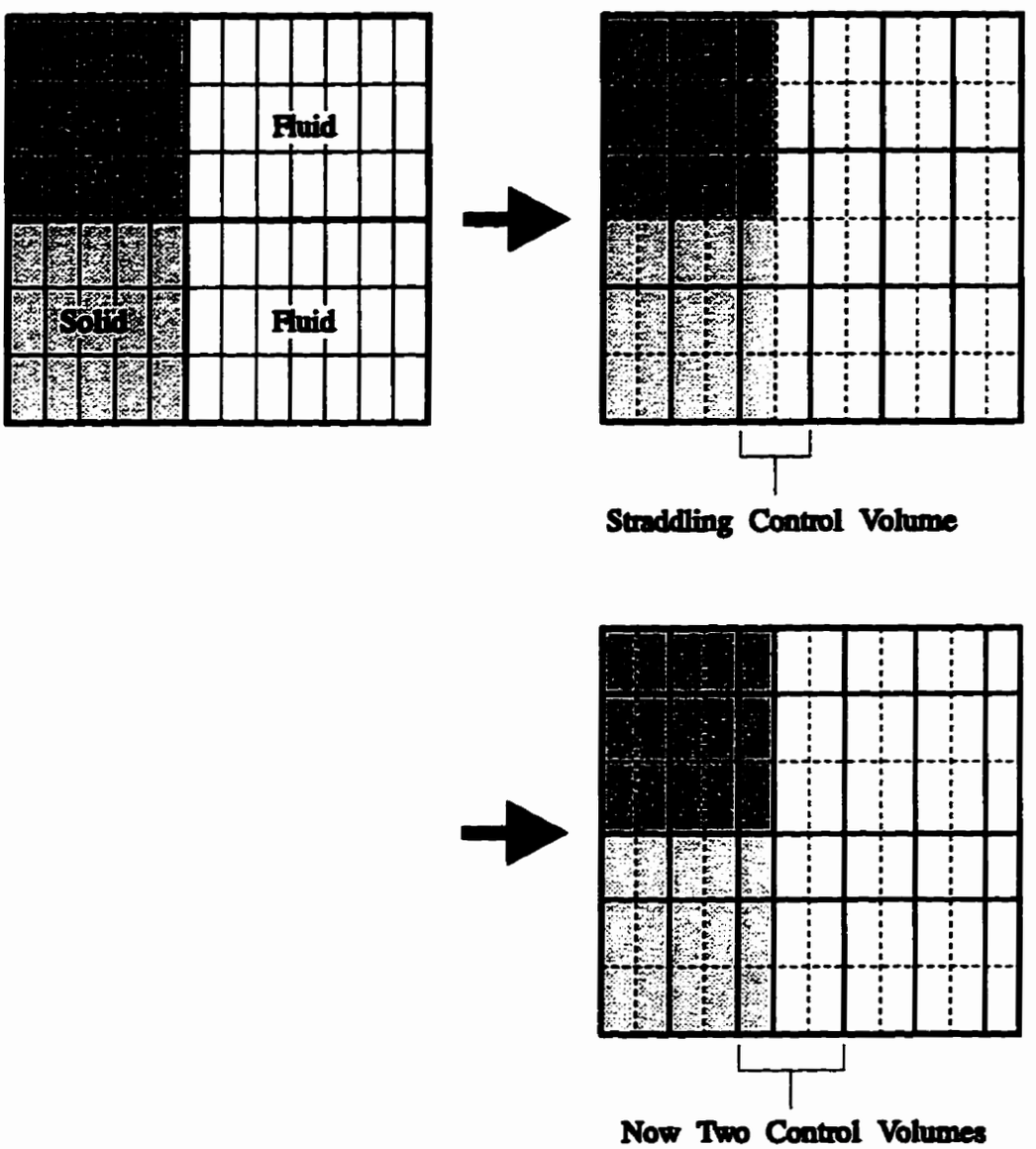

Figure 5.8: Illustration showing the CACM algorithm assembling the level 1 control volumes for the level 2 blocks (darker lines) in a composite two-dimensional region. The algorithm prevents blocked regions from straddling different materials.

Chapter 6

Computer Code Validation Tests

This chapter describes the validation tests performed on the computer code developed in this work. Two types of tests were performed: tests on the equation solvers and tests on the flow and heat transfer equation set results. The results are presented for the different solvers for each flow or heat transfer problem. There were five solution algorithms tested: LUD2d, LGS2d, V-cycle ACM, flexible-cycle ACM, and CACM. These solver were described in Chapter 5. Both ACM solvers and the CACM solver use LGS2d to solve the equation sets for each multigrid level.

The tests started with the energy equation sets by modelling pure conduction. Next, the momentum equations sets were tested with isothermal flow tests. Finally the coupling of all the equations sets were examined with natural convection flow tests. In some cases, the efficiency of the solvers were compared. The solver efficiency was measured by either looking at the total computational time spent, or by counting the number of work units used. A work unit, or WU, was defined in Chapter 5. The work units of the LUD2d solver were not calculated.

After the equation sets were validated on conduction, flow and natural convection cases, the tests presented at the end of this chapter were used to learn what may

be required to simulate transformer models. This knowledge was used to help in modelling the transformer problems presented in Chapter 7.

6.1 One-Dimensional Conduction Test Problems

The first step in validating the numerical model was to test the energy equation. This was done by testing both one-dimensional and two-dimensional conduction models. The convergence to steady state of the conduction test problem was determined with the equation,

$$\frac{|T^{n+1} - T^n|}{T^{n+1}_{max} - T^{n+1}_{min}} \leq 1 \times 10^{-5} \tag{6.1}$$

When Equation (6.1) is satisfied at all temperature nodes, the code reports that steady state convergence has been met, and then performs postprocessing on the results. The convergence of the steady state solution is also checked by calculating the overall energy balance on the solution domain, and then normalizing the result with the sum of the out flowing energy and the stored energy. The energy balance calculation used is

$$\frac{Q_{in} - Q_{out} - Q_{stored}}{Q_{out} + Q_{stored}} \times 100\% \tag{6.2}$$

The balance shown in Equation (6.2) is checked to be sure that it is less than 1%.

6.1.1 Homogeneous Material

The energy equation was first tested by solving the one-dimensional conduction test problem, shown in Figure 6.1. The temperature on the left boundary, T_1, was set to 0 K and the right boundary, T_2, was set to 100 K. The domain was solved to steady state by setting the values of the time step, Δt, and the energy equation E-factor,

E^T, to a very large number (1×10^{30}). The thermal conductivity of air at 300 K was used. The grid is a 50×1 control volume matrix (one control volume is used in the y direction since the test problem is set up to be one-dimensional).

The LGS2d solver obtained convergence with four coefficient updates, and reduced the energy balance to an error of 0.0211%. The LUD2d direct solver required two coefficient updates for a heat balance of 0.00246%. The ACM solver took four coefficient updates to obtain the heat balance of 0.0111%. In all three cases, the temperature field is linearly increasing in the x direction. The only errors present, relative to an exact solution of the equations, were due to numerical round-off.

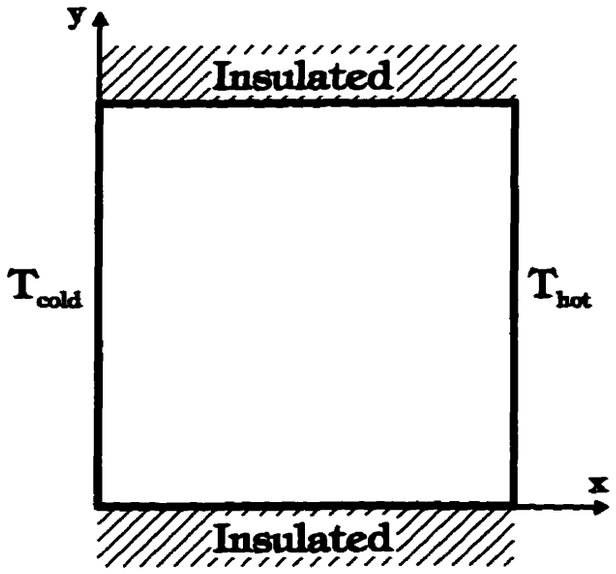

Figure 6.1: One-dimensional conduction benchmark.

The model was then rotated 90-degrees counter-clockwise to test the y direction coefficients. The LGS2d solver required four coefficient updates to achieve a heat

balance of 0.0348%. The LUD2d solver required only two coefficient updates to get a heat balance of 0.00247%. The ACM solver performed three coefficient updates to get 0.0220%.

The transient calculations of the code were also tested by replacing the left boundary condition with a insulated wall ($q''_L = 0$). The remaining properties were set for air at 300 K. When the results were compared with an analytical solution, they were found to agree with each other very well.

6.1.2 Composite Material

To test the energy equation for a nonhomogeneous domain, the one-dimension conduction benchmark model was extended to consist of two materials. As shown in Figure 6.2, the solids are arranged in series. The thermal conductivities are equal to $k_1 = 1$ W/m^{2}K and $k_2 = 100$ W/m^{2}K. The left temperature, T_{cold}, is 0.0 K and the right temperature, T_{hot}, is 1.0 K. The cavity measures one metre by one metre, and consists of exactly half of each material. The model was broken up into a 40×40 control volume grid. The rest of the model is identical to the one-dimensional single material model presented in Section 6.1.1.

The ACM solver took 3 coefficient updates to reduce the heat balance to 0.00602%. The LUD2d solver took 2 coefficient updates to reduce the heat balance to 0.0188%. The interface between the two materials was calculated to have a temperature of 0.990099 K using the following equation:

$$T_{interface} = \frac{k_1 T_C + k_2 T_H}{k_1 + k_2} \tag{6.3}$$

The LUD2d solver calculated the temperature as 0.990102 K (which is an error of 0.00035%). Another test point was taken inside the left material at 0.3625 m (15^{th} control volume) from the left side. The temperature determined by the code matched the analytical answer equally well.

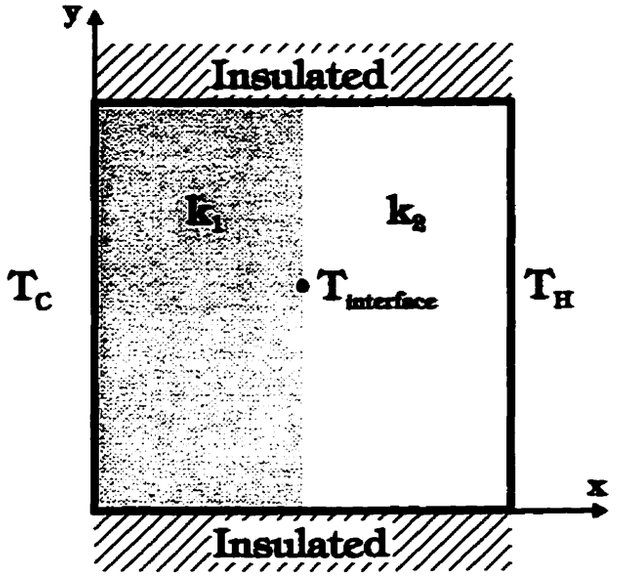

Figure 6.2: One-dimensional conduction benchmark with two materials.

Various permutations of the model were tried with similiar results.

6.2 Two-Dimensional Conduction Test Problem

The code was tested against the two-dimensional benchmark test problem shown schematically in Figure 6.3. The hot temperature located at the top of the model, T_{hot}, is equal to 100 K and the cold temperature sides, T_{cold}, is equal to 0 K. The solution domain is one meter square, and the grid was modelled as 41 × 41 control volumes. The thermal conductivity of the domain is equal to 0.0263 W/m K. A steady state convergence criterion of 10^{-5} was used and the values of Δt and E^T were set to 1×10^{30}. For comparison, the analytical solution was calculated using the

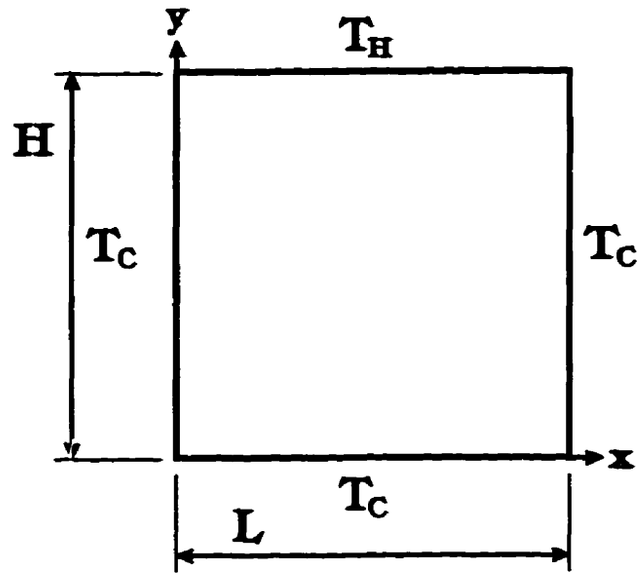

Figure 6.3: Boundary conditions for conduction benchmark.

equation presented by Incropera and De Witt [30], as shown in Equation (6.4).

$$\frac{T(x,y) - T_{cold}}{T_{hot} - T_{cold}} = \frac{2}{\pi} \sum_{n=1}^{\infty} \frac{(-1)^{n+1} + 1}{n} sin\left(\frac{n\pi x}{L}\right) \frac{sinh(n\pi y/L)}{sinh(n\pi W/L)} \tag{6.4}$$

When the analytical solution was compared with the numerical solution, there was a maximum error of 0.000667%.

The same model was then used to test the efficiency of the ACM solver. In this case, the grid resolution was increased from 41×41 to 64×64 to better demonstrate the abilities of the multigrid algorithm. Also, an E-factor of 30 was used for the energy equation to slow down the solution and help demonstrate the efficiency of the solvers. The conduction test results are shown in Table 6.1. In the table there are eight columns. The first column, Solver Type, lists the solver used in the test run. The ACM solvers list in parenthesis the maximum multigrid level set for the run. The second column, # Coarsest Level CV's, shows the grid size for the coarsest level. The Computational Time is the time the computer spend solving the problem. The fifth

Solver Type	# Coarsest Level CV's	Computational Time	Work Units WU(T)	%Heat Balance	Coefficient Updates
LGS2d	64 × 64	1272 s	1185	2.1684%	504
LUD2d	64 × 64	23060 s	N/A	2.1596%	422
LUD2d††	64 × 64	109.4 s	N/A	0.0046%	2
V-cycle (1)	64 × 64	1334 s	1185	2.1684%	504
V-cycle (2)	32 × 32	1211 s	924	2.0754%	441
V-cycle (3)	16 × 16	1221 s	1004	2.0423%	429
V-cycle (4)	8 × 8	1233 s	1037	2.0407%	429
V-cycle (5)	4 × 4	1236 s	1046	2.0407%	429
V-cycle (6)	2 × 2	1237 s	1048	2.0407%	429
V-cycle (7)	1 × 1	1237 s	1048	2.0407%	429
F-cycle (1)	64 × 64	1304 s	1185	2.1684%	504
F-cycle (2)†	32 × 32	1346 s	1185	2.1684%	504
F-cycle (3)†	16 × 16	1357 s	1185	2.1684%	504
F-cycle (4)†	8 × 8	1360 s	1185	2.1684%	504
F-cycle (5)†	4 × 4	1360 s	1185	2.1684%	504
F-cycle (6)†	2 × 2	1361 s	1185	2.1684%	504
F-cycle (7)†	1 × 1	1360 s	1185	2.1684%	504

Table 6.1: Conduction solver comparison of temperature solution.

†The flexible-multigrid solver would not advance beyond the first level.
††LUD2d solution with E^T-factor set to 1.0×10^{30}.

column, Work Units, shows the number of work units used to solve the temperature field for the model. There are no WU entries for the LUD2d solver since it would be difficult to accurately measure the time to solve one iteration on the finest grid using LGS2d without running an iteration and thereby affecting the results. The second last column, % Heat Balance, shows how closely energy was conserved. The final column, Coefficient Updates, shows the number of iterations required for the model to reach steady state in the temperature field using the distorted transient solution method.

The results demonstrate that for pure conduction the multigrid algorithm may not be very efficient. The second level V-cycle showed the best time results but the gain relative to LGS2d was still not significant. The flexible-cycle ACM solver spent most of the calculation time on the finest grid level since the set of equations converged very quickly. Therefore excess time was consumed in the solver setting up the multigrid coefficients for the equation sets. Note that the LUD2d test with the E^T-factor set to 1.0×10^{30} obtained a better heat balance than the other runs. This suggests that the other runs were not as tightly converged as the LUD2d test run. The distorted transient runs may have "stalled" as they approached steady state, and therefore the solution algorthm considered them as tightly converged solution.

The results were compared against the LUD2d results by taking the difference of the fields and dividing by the range of the LUD2d field, using Equation (6.5). The results are shown in Table 6.2. As the table illustrates, the normalized temperature difference remains constant for all solvers except the seven-level V-cycle ACM. The flexible-cycle solver did not continue past level 1 into the higher levels and therefore the results were equivalent to the LGS2d solver. The seven-layer V-cycle ACM solution had the highest normalized temperature difference. This was attributed to the high frequency errors introduced by multigrid that were not eliminated by the time the convergence criterion was satisfied.

$$\Delta T^* = \frac{| T_{LUD2d} - T_{solver} |}{T_{LUD2d,max} - T_{LUD2d,min}} \tag{6.5}$$

Max Field Difference	LGS2d	V-Cycle (1 Level)	V-Cycle (7 Levels)	Flexible-Cycle (1 Level)	Flexible-Cycle (7 Levels)
ΔT^{*}_{max}	0.00018	0.00018	0.00114	0.00018	0.00018
⊙ position (x,y)	(25,7)	(25,7)	(65,1)	(25,7)	(25,7)

Table 6.2: Conduction field comparison of two-dimensional conduction solutions.

6.3 Lid-Driven Cavity Test Problems

After the conduction terms of the energy equation were validated, the next step was to test the momentum equations and the advection terms of the energy equation. First an isothermal lid-driven cavity model was solved. Once the velocity fields for the domain were calculated, the temperature field was determined from the energy equation.

6.3.1 Isothermal

The solution of this test problem helps to examine the accuracy of the velocity and the pressure correction solution algorithm. Figure 6.4 schematically shows the test problem. The domain is square, with all sides equal to one meter in length. The properties of the fluid, except density, are equal to those of air at atmospheric pressure and 300 K. The lid velocity is equal to one meter per second in the positive x direction. The Reynolds number is defined as:

$$Re_{Lid} = \frac{\rho L U_{Lid}}{\mu} \tag{6.6}$$

where the parameters are the density, ρ, length of the cavity wall, L, lid velocity, U_{Lid}, and absolute viscosity of the fluid, μ. The density value was adjusted to obtain

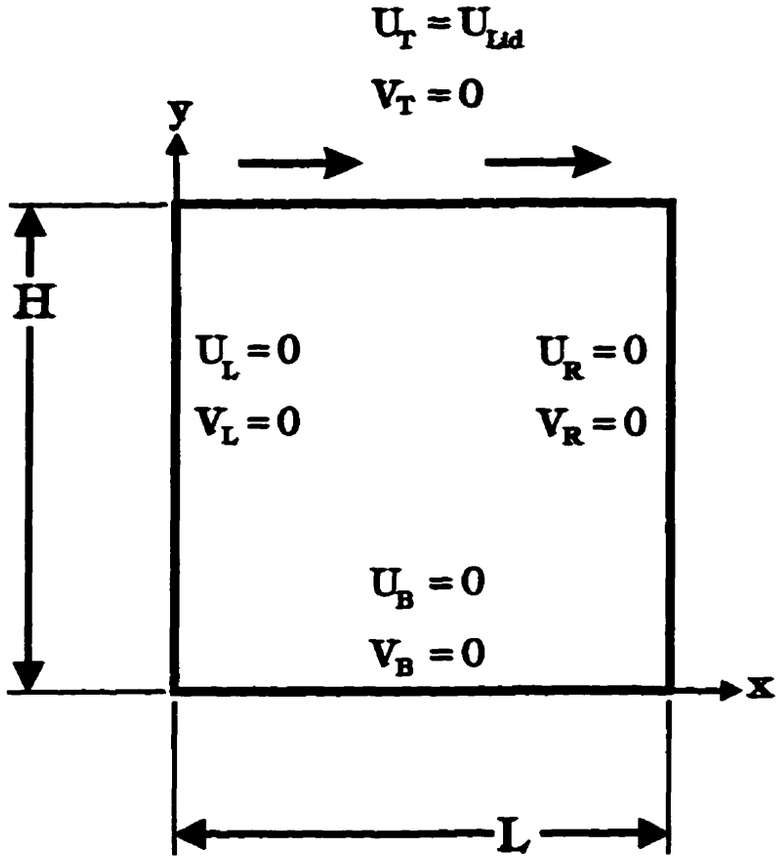

Figure 6.4: Lid-driven cavity test problem.

the desired Reynolds number for comparison with literature. The solution was run to a steady state criterion of 1×10^{-6} using an E-factor of 5.0 for the velocity solutions.

Figures 6.5 and 6.6 show the horizontal and vertical centerline velocity profiles compared with Ghia et al. [20]. The staggered grid used for the velocity calculations created some difficulties when comparing results with Ghia et al. In order to avoid interpolating the velocity between control volumes for comparison with the Ghia et al. published results, the grids were modified by adding either a column or a row. A 130×129 grid was used for the U-velocity profile comparison, and a 129×130 grid

was used for the V-velocity profile comparison.

The addition of a column or row of control volumes should not have affected the results significantly. The cavity with the Reynolds number of 400 showed very good agreement with Ghia et al., except for a point on the V-direction centerline profile. The error on this centerline profile was attributed to a data error in the paper since the other points showed very good agreement. However, the results of the present work for a Reynolds number of 5,000 did not compare well with Ghia et al. This deviation was attributed to the exponential upwinding scheme used in the present work compared to the first-order accurate upwind differential scheme (with a second-order accurate term as a deferred correction) use by Ghia et al. The significant influence of the upwind scheme was demonstrated by Jessee and Fiveland [31].

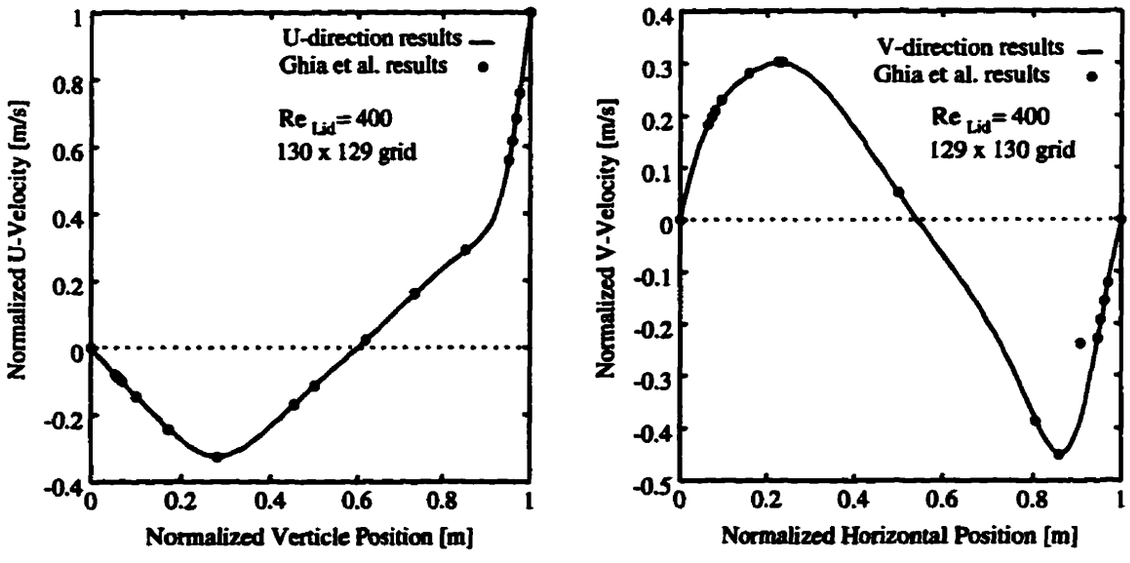

(a) U-velocity.

(b) V-velocity.

Figure 6.5: Velocity centerline profiles for the square cavity ($Re_{Lid} = 400$).

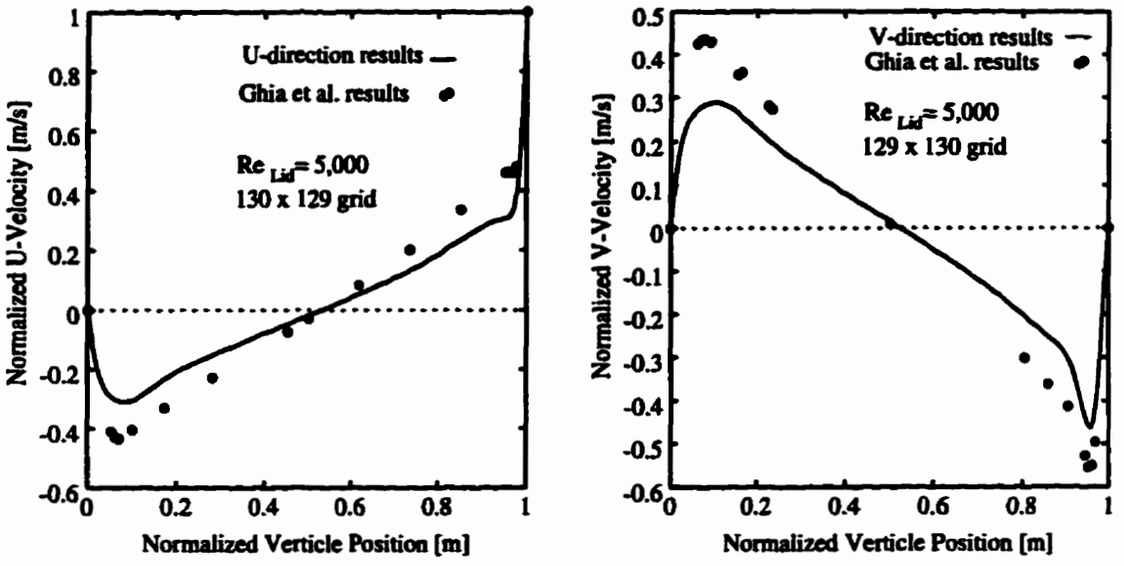

(a) U-velocity.

(b) V-velocity.

Figure 6.6: The velocity centerline profiles for the square cavity ($Re_{Lid} = 5000$).

The efficiency of the multigrid algorithm for this problem was examined. Since the velocity is not a function of temperature, the velocity field was solved first. The model was standardized for each test by maintaining all input parameters between models, and the results were compared between the solvers. The lid velocity for these tests cases was set equal to 0.1 m/s. The Reynolds number, calculated using Equation (6.6), is 20.8. Table 6.3 is a summary of the test run results. Only the type of the pressure correction solver was varied since this equation set required the most iterations. The solvers iterated until the convergence criterion of 1×10^{-5} was achieved.

The research indicated that the LUD2d solver was more efficient solving the pressure correction equation set than the LGS2d solver. As expected, the V-cycle ACM solver required less CPU time than the LGS2d solver. The V-cycle ACM solver needed

Solver Type	# Coarsest Level CV's	Computational Time	Work Units WU(P')	Coefficient Updates
LGS2d	64 x 64	15,460 s	68,700	229
LUD2d	64 x 64	13,090 s	N/A	230
V-cycle (1)	64 x 64	19,520 s	68,700	229
V-cycle (2)	32 x 32	14,500 s	43,380	229
V-cycle (3)	16 x 16	9,563 s	28,360	230
V-cycle (4)	8 x 8	7,137 s	20,570	230
V-cycle (5)	4 x 4	5,912 s	16,630	230
V-cycle (6)	2 x 2	5,200 s	14,580	230
V-cycle (7)	1 x 1	3,909 s	10,280	230
F-cycle (1)	64 x 64	16,160 s	68,700	229
F-cycle (2)	32 x 32	17,210 s	73,440	229
F-cycle (3)	16 x 16	18,830 s	74,320	230
F-cycle (4)	8 x 8	9,308 s	34,710	230
F-cycle (5)	4 x 4	4,614 s	12,370	230
F-cycle (6)	2 x 2	3,449 s	8,716	230
F-cycle (7)	1 x 1	3,212 s	7,893	230

Table 6.3: Comparison of solver effectiveness for the velocity field in the lid-driven cavity test problem. The resolution of the fine grid was 64×64 control volumes.

one-sixth the work units and one quarter of the CPU time of the LGS2d solver for a 64x64 control volume grid. The flexible-cycle solver required less than one-eighth the work units of the LGS2d solver and one fifth of the CPU time. These results indicated that the flexible-cycle ACM was the fastest solver when solving the velocity field for a lid-driven cavity model.

In addition to computational effort comparisons, specific field values were also compared in the results for the different solvers. Field differences were calculated relative to the value at the same node in the LUD2d solution. The maximum differences in velocity, pressure, and stream function are reported in Table 6.4. The field results were exactly the same for the LGS2d, V-cycle with one level, and the flexible-cycle with one level. This was expected since the ACM algorithm using an LGS2d solver only on the first level is essentially the same as an ordinary LGS2d solver. When the number of levels was increased, the accuracy of the results also increased since the higher levels removed the low-frequency error modes.

Field	LGS2d	V-Cycle (1 Level)	V-Cycle (7 Levels)	Flexible-Cycle (1 Level)	Flexible-Cycle (7 Levels)
Normalized U-velocity	4.1172×10^{-6}	4.1172×10^{-6}	1.2319×10^{-7}	4.1172×10^{-6}	1.5398×10^{-7}
@ position (i,j)	(33,50)	(33,50)	(36,65)	(33,50)	(2,65)
Normalized V-velocity	6.4453×10^{-6}	6.4453×10^{-6}	1.2207×10^{-7}	6.4453×10^{-6}	2.1973×10^{-7}
@ position (i,j)	(16,33)	(16,33)	(2,62)	(16,33)	(2,64)
Normalized Pressure	1.1333×10^{-6}	1.1333×10^{-6}	8.0950×10^{-8}	1.1333×10^{-6}	2.1587×10^{-7}
@ position (i,j)	(1,65)	(1,65)	(5,65)	(1,65)	(1,65)
Normalized Stream Function	1.5563×10^{-5}	1.5563×10^{-5}	3.6364×10^{-7}	1.5563×10^{-5}	2.8382×10^{-7}
@ position (i,j)	(32,33)	(32,33)	(65,60)	(32,33)	(44,49)

Table 6.4: Lid driven cavity field comparison of velocity solutions.

6.3.2 Non-Isothermal

The LUD2d-solved velocity field was next used to test the temperature solution field. Using the solution of the velocity field, the temperature field was calculated using the different solvers. The temperature boundary conditions prescribed for this model are illustrated in Figure 6.7. For the results described next, the values of T_H were 300 K and 100 K, respectively.

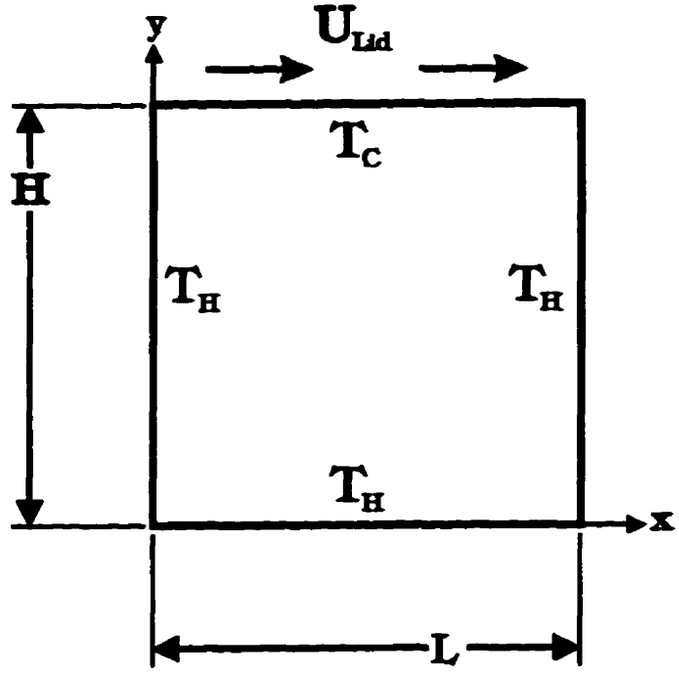

Figure 6.7: Lid driven cavity nomenclature for the temperature benchmark.

Table 6.5 displays the results for the tests of solver efficiency for the non-isothermal lid driven cavity test problem. The LUD2d solver took over eighteen times more CPU time to solve the temperature field than LGS2d. The V-cycle ACM did not

Solver Type	# Coarsest Level CV's	Computational Time	Work Units WU(T)	% Heat Balance	Coefficient Updates
LGS2d	64 x 64	287.4 s	254.0	1.48906%	350
LUD2d	64 x 64	5413.0 s	N/A	1.43908%	329
V-cycle (1)	64 x 64	302.0 s	254.0	1.48906%	350
V-cycle (2)	32 x 32	277.5 s	214.8	1.38141%	334
V-cycle (3)	16 x 16	240.3 s	240.3	1.35665%	331
V-cycle (4)	8 x 8	284.1 s	248.1	1.35544%	331
V-cycle (5)	4 x 4	284.9 s	250.0	1.35547%	331
V-cycle (6)	2 x 2	285.5 s	250.5	1.35535%	331
V-cycle (7)	1 x 1	285.1 s	250.6	1.35535%	331
F-cycle (1)	64 x 64	295.2 s	254.0	1.48906%	350
F-cycle †(2)	32 x 32	306.2 s	254.0	1.48906%	350
F-cycle †(3)	16 x 16	309.0 s	254.0	1.48906%	350
F-cycle †(4)	8 x 8	309.0 s	254.0	1.48906%	350
F-cycle †(5)	4 x 4	309.3 s	254.0	1.48906%	350
F-cycle †(6)	2 x 2	309.2 s	254.0	1.48906%	350
F-cycle †(7)	1 x 1	309.3 s	254.0	1.48906%	350

Table 6.5: Comparison of solver effectiveness for the temperature field in the lid-driven cavity test problem. The resolution of the fine grid was 64 x 64 control volumes.

†This run converged only using the first (finest) level.

significantly improve the solution of the field over the LGS2d solver. The flexible ACM solved only the finest grid equation set without having to use any additive corrections to speed up the convergence.

The LUD2d solver again was used as the basis of comparison for the temperature field value. Table 6.6 shows that the LGS2d, V-cycle with one level, and both flexible-cycle test runs, have the same maximum temperature field difference. Since the flexible-cycle converged rapidly on the fine grid, it did not need to use the coarser grid levels; most of the ACM solvers behaved as ordinary LGS2d solvers. Only the multi-layered V-cycle test case showed a slightly smaller deviation from the LUD2d

field values since it was forced to use the coarser grids.

Maximum Field Difference	LGS2d	V-Cycle (1 Level)	V-Cycle (7 Levels)	Flexible-Cycle (1 Level)	Flexible-Cycle (7 Levels)
Normalized Temperature	7.7393×10^{-4}	7.7393×10^{-4}	5.7037×10^{-4}	7.7393×10^{-4}	7.7393×10^{-4}
⊙ position (i,j)	(18,24)	(18,24)	(31,35)	(18,24)	(18,24)

Table 6.6: Lid driven cavity field comparison of temperature solutions.

6.4 Natural Convection Benchmark Test

The next step is to test the ability of the computer code to calculate the field of a natural convection problem. The first natural convection test was done on the test problem shown schematically in Figure 6.8. The fluid properties are for air at atmospheric pressure and 300 K. The square cavity had a side length, L, of one meter. A computational grid with 80 × 80 uniformly spaced control volumes was used. The E^T factor was set to 5, the E^U and E^V factors were both set to 3, and the steady-state convergence criterion was specified as 10^{-5}. The hot temperature, T_H, was set to 5 K, and the low temperature, T_C, was set to -5 K. The fluid density was varied to get Rayleigh numbers between 10^3 and 10^6. The value of the Rayleigh number, Ra, was calculated from the equation,

$$Ra = \frac{\rho^2 g \beta \Delta T L^3 c_p}{\mu k}. \tag{6.7}$$

Table 6.7 reports the Nusselt Number comparison between the present work and two benchmark results from the literature [25, 15].

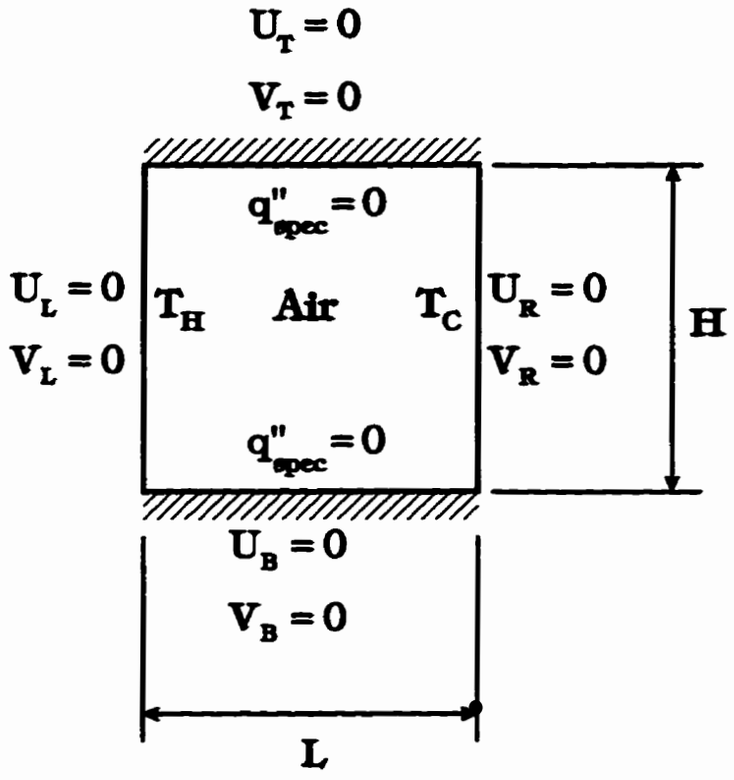

Figure 6.8: Boundary conditions for natural convection in a cavity.

The Nusselt number, as given by M. Hortmann et al. [25], is defined by the equation,

$$\overline{Nu} = \frac{\overline{Q}}{Q_c} \tag{6.8}$$

where $\overline{Q}$ is the actual heat flow across the cavity and Q_c is the heat flow from pure conduction. Q_c is defined as

$$Q_c = \frac{\mu}{Pr} \frac{T_H - T_C}{L} H \tag{6.9}$$

where H is the height of the cavity, which in this case is equal to the side length, L. The heat flow, $\overline{Q}$, is the average of the sum of the convection and diffusion fluxes

through the CV faces along any verticle grid line (i = constant).

$$Q_i = \sum_{j=jb}^{je} \left(\dot{m}_e c_p T_e - k_e A_e \left. \frac{dT}{dx} \right|_e \right)_{ij} \tag{6.10}$$

The average value is given by:

$$\overline{Q} = \frac{1}{N_x + 1} \sum_{i=ib-1}^{ie} Q_i \tag{6.11}$$

The values of Q_i are summed starting from $ib - 1$ so that the heat flow through every control volume face is considered in the calculation of $\overline{Q}$. The results shown in Table 6.7 indicate that the the code produced results very similiar to other natural convection benchmarks.

Rayleigh Number	Present Work 80×80	Hortmann [25]	Davis [15]
10^3	1.11733	-	1.118
10^4	2.24981	2.24475	2.243
10^5	4.54192	4.52164	4.519
10^6	8.96487	8.82513	8.800

Table 6.7: Nusselt numbers for natural convection in a cavity.

To further test the efficiency of the ACM solver, comparisons were made between the different solvers. The results of these comparisons are summarized in Tables 6.8 and 6.9. The full ACM flexible-cycle solver solved the benchmark in one-fifth the time of the LGS2d solver, and in one-ninth the time of the LUD2d solver. Note that

Solver Type		Computational	Work Units		% Heat	Coefficient	Nusselt
For T	For P'	Time	WU(T)	WU(P')	Balance	Updates	Number
LGS2d	LGS2d	11,560 s	167	49200	0.1647%	165	4.51878
LUD2d	LUD2d	21,170 s	N/A	N/A	0.3330%	195	4.54996
V (1)	V (1)	14,020 s	167	49,200	0.1647%	165	4.51878
V (1)	V (2)	9,714 s	166	29,880	0.0410%	159	4.51273
V (1)	V (4)	4,592 s	166	13,510	0.0107%	154	4.51025
V (1)	V (7)	2,833 s	165	7,325	0.0774%	163	4.51495
V (2)	V (1)	13,160 s	144.8	45,900	0.3034%	154	4.51850
V (2)	V (2)	8,566 s	144.8	26,270	0.1526%	140	4.51314
V (2)	V (4)	4,431 s	145.8	12,910	0.1184%	146	4.51573
V (2)	V (7)	2,747 s	144.8	7,160	0.1797%	160	4.52291
V (4)	V (1)	13,070 s	159.4	45,560	0.4327%	153	4.52071
V (4)	V (2)	8,894 s	159.4	27,350	0.2771%	146	4.51696
V (4)	V (4)	5,060 s	156.7	14,880	0.2293%	166	4.53010
V (4)	V (7)	3,089 s	156.7	8,080	0.2953%	179	4.54100
V (7)	V (1)	13,110 s	161.0	45,560	0.4294%	153	4.52097
V (7)	V (2)	9,011 s	161.0	27,350	0.2778%	146	4.51704
V (7)	V (4)	5,398 s	158.3	15,930	0.2353%	177	4.54062
V (7)	V (7)	3,093 s	158.3	8,081	0.2934%	179	4.54077

Table 6.8: Natural convection solver comparison (V-cycle).

the flexible-cycle solver did not use any multigrid levels to solve the energy equation even though it was allowed to solve up to seven levels. The energy equation converged rapidly on the finest grid level.

6.5 Conjugate Heat Transfer Test Problem

As a final test to validate the code, a conjugate benchmark was modelled. This model is similiar to the natural convection benchmark described in Section 6.4. In this case the cavity was surrounded by walls of finite thickness. Figure 6.9 shows the layout of

Solver Type		Computational	Work Units		% Heat	Coefficient	Nusselt
For T	For P'	Time	WU(T)	WU(P')	Balance	Updates	Number
LGS2d	LGS2d	11,560 s	167	49,200	0.1647%	165	4.51878
LUD2d	LUD2d	21,170 s	N/A	N/A	0.3330%	195	4.54996
F (1)	F (1)	12,110 s	167	49,200	0.1647%	165	4.51878
F (1)	F (2)	12,920 s	166	50,780	0.0386%	160	4.51295
F (1)	F (4)	5,188 s	165	16,210	0.0685%	158	4.51237
F (1)	F (7)	2,264 s	162	5,590	0.0759%	162	4.51413
F (2) †	F (1)	12,120 s	167.0	49,200	0.1647%	165	4.51878
F (2) †	F (2)	12,910 s	166.0	50,780	0.0386%	160	4.51295
F (2) †	F (4)	5,204 s	165.0	16,210	0.0685%	158	4.51237
F (2) †	F (7)	2,278 s	165.0	5,590	0.0759%	162	4.51413
F (4) †	F (1)	12,130 s	167.0	49,200	0.1647%	165	4.51878
F (4) †	F (2)	12,910 s	166.0	50,780	0.0386%	160	4.51295
F (4) †	F (4)	5,207 s	165.0	16,210	0.0685%	158	4.51237
F (4) †	F (7)	2,284 s	156.0	5,590	0.0759%	162	4.51413
F (7) †	F (1)	12,170 s	167.0	49,200	0.1647%	165	4.51878
F (7) †	F (2)	12,920 s	166.0	50,780	0.0386%	160	4.51295
F (7) †	F (4)	5,210 s	165.0	16,210	0.0685%	158	4.51237
F (7) †	F (7)	2,281 s	165.0	5,590	0.0759%	162	4.51413
F (7) †	LUD2d	9342 s	165.0	N/A	0.0870%	163	4.51487
LUD2d	F (7)	12670 s	N/A	6714	0.3234%	195	4.54980

Table 6.9: Natural convection solver comparison (flexible-cycle).

†This run converged using only the first (finest) level.

the model. The fluid properties are the same as for the previous natural convection benchmark. The grid used was 80 × 80 (40 × 40 in the cavity). The size of the cavity is 0.6 meters along each wall, and the outside wall length measures 1.0 m. The thermal conductivity of the solid was set to be ten times greater than the fluid (air). For comparison with the results presented by Kim and Viskanta [32], the density of the solid can be said to be 2000 times greater than the fluid, and the specific heat is uniform throughout the domain. A steady state criterion of 10^{-5} was used.

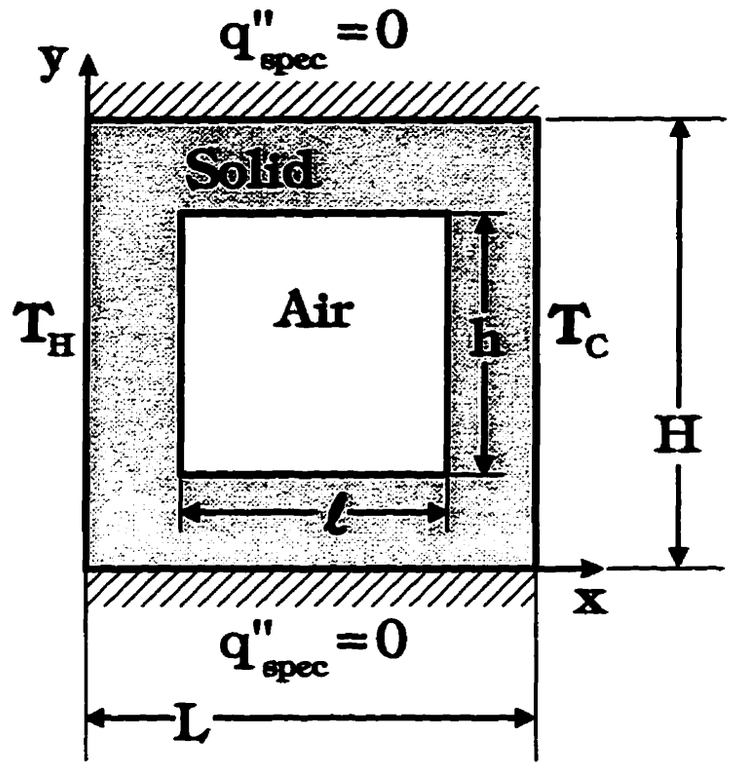

Figure 6.9: Conjugate benchmark; natural convection with finite walls.

Several tests were run with different Rayleigh numbers by changing the density of the fluid (and the solid density, accordingly). The Rayleigh number was calculated using the following equation:

$$Ra^* = \frac{g\beta l^4(T_H - T_C)}{\nu\alpha L} \tag{6.12}$$

The Nusselt numbers were then calculated locally and averaged at each interior surface of the cavity walls. The formulation of the Nusselt number is based on the equation given by Kim and Viskanta [32], although it was modified to ensure an energy balance. The step-by-step details of the modification are given below.

Figure 6.10 illustrates the nomenclature used to calculate the Nusselt number. First, the heat flow across the fluid-block control volume interface is defined for the

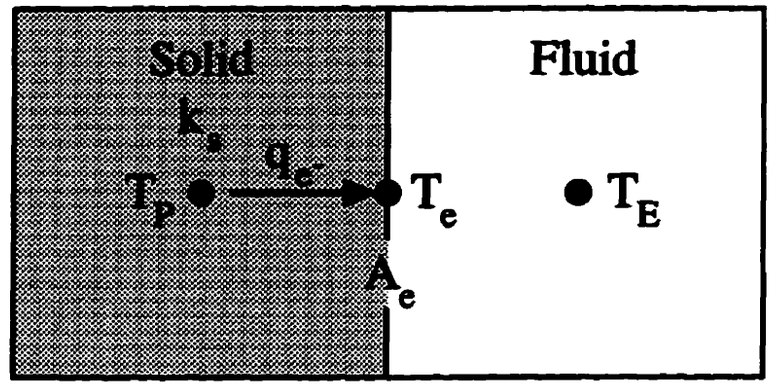

Figure 6.10: Nomenclature for the conjugate Nusselt number calculation for natural convection within a square cavity with finite walls.

left vertical wall:

$$q_{e^-} = -k_s A_e \left.\frac{\partial T}{\partial x}\right|_{e^-} \tag{6.13}$$

Then, the heat flow is defined in terms of the convection coefficient, h_x, for the control volume face.

$$q_{e^+} = A_e h_x \left(T_e - (T_H + T_C)/2\right) \tag{6.14}$$

$$= A_e h_x \left(T_e - \overline{T}\right) \tag{6.15}$$

Next, Equation (6.15) is rearranged in terms of the local convection coefficient to get

$$h_x = \frac{q_{e^+}}{A_e \left(T_e - \overline{T}\right)} \tag{6.16}$$

and since $q_{e^-} = q_{e^+}$, Equation (6.13) can be substituted in for q_{e^+}.

$$h_x = \frac{-k_s A_e \left.\frac{\partial T}{\partial x}\right|_{e^-}}{A_e \left(T_e - \overline{T}\right)} \tag{6.17}$$

Thus the local Nusselt number is defined as

$$Nu_x = \frac{l}{k_f} h_x = \frac{l}{k_f} \frac{-k_s A_e \left.\frac{\partial T}{\partial x}\right|_{e^-}}{A_e \left(T_e - \overline{T}\right)} \tag{6.18}$$

The average Nusselt number is calculated by averaging the local nusselt number over the area of the cavity wall.

$$\overline{Nu} = \frac{1}{A_{tot}} \sum_{j=jb}^{je} \frac{k_s}{k_f} \frac{-A_e \frac{\partial T}{\partial x}\Big|_{e^-}}{(T_e - \overline{T})} \tag{6.19}$$

The equations required to calculate the Nusselt numbers for the other walls can be derived in a similiar manner.

The results calculated by the code developed in this thesis are compared against the benchmarked results given by Kim and Viskanta [33]. The results are summarized in Table 6.10, and the temperature contours and the streamlines are shown in Figures 6.11 and 6.12.

Result Type	$\overline{Nu}_H$	$\overline{Nu}_C$	$\overline{Nu}_T$	$\overline{Nu}_B$
Kim & Viskanta [33]	3.801	3.781	1.017	1.057
Nu based on $T_{wall} - \overline{T}$	14.19	17.00	6.606	60.85
Nu based on $T_H - T_C$	7.425	7.571	2.522	2.666

Table 6.10: Nusselt numbers for natural convection in a cavity.

The Nusselt numbers based on the $T_{wall} - \overline{T}$ are much higher than those of Kim and Viskanta for all sides of the cavity. The $\overline{Nu}_B$ results are the highest because the wall temperature approaches the average fluid temperature at two control volumes. When the difference of the two temperatures, $T_{wall} - \overline{T}$, becomes very small, the value of the Nusselt number becomes very large. There is a large discrepancy between the Kim and Viskanta results and those from Equation (6.19) because there appears to

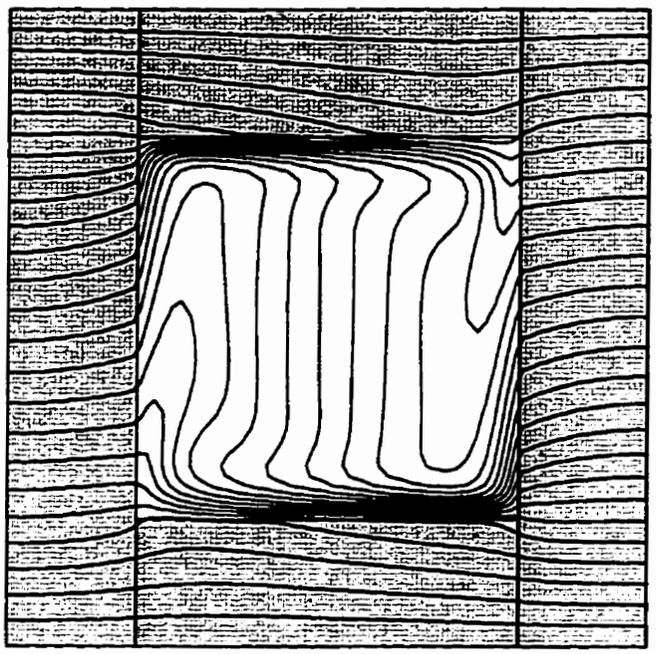

Figure 6.11: Temperature contours in the thick walled cavity for $Ra^* = 10^6$.

be an error in the derivation of the Nusselt number in Kim and Viskanta [32]. The "$T_H - T_C$" Nusselt number is calculated using Equation (6.8). In this case the cavity is treated like the convection cavity without finite walls. The average temperatures of the interior left and right walls are used for T_H and T_C, respectively.

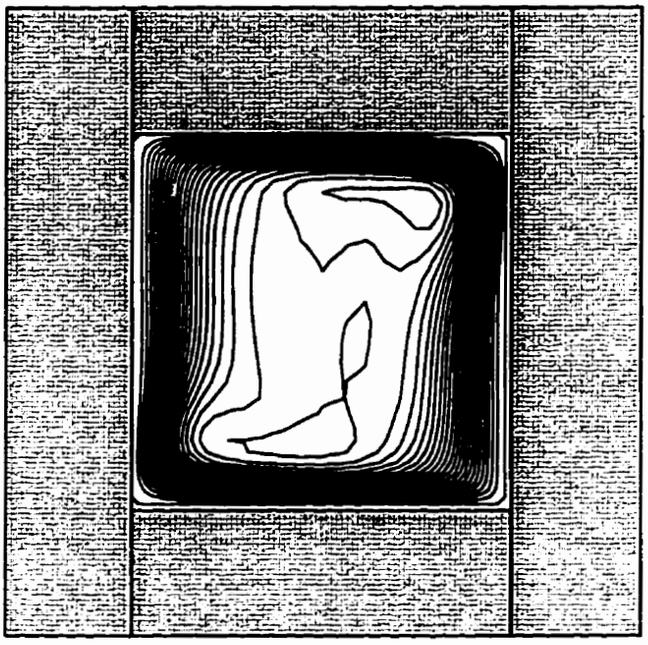

Figure 6.12: Streamlines for the thick walled cavity for $Ra^* = 10^6$.

6.6 Conjugate Tests with an Oil-Filled Cavity

These series of tests set the basis for the transformer runs described in Chapter 7. These problems examine the sensitivity of the conjugate domain solution to changes in fluid-solid thermal conductivity ratio, the width-height ratio of the cavity, and the boundary conditions.

The test problems began by modelling a simple geometry in order to build an understanding of solving conjugate problems. When the trends of the simple model

were understood, more complexity was added to the transformer model.

Based on the test described in Chapter 6, the CACM2d solver was selected for the solution of the transformer model. This solver was used to calculate the temperature and the pressure correction fields. LGS2d was used to calculate the velocity fields since they tended to converge quickly without a multigrid solver.

6.6.1 Oil-Filled Cavity with Two Thick Walls

The first test is similiar to the standard natural convection cavity described in Section 6.4. In this test problem, the fluid in the cavity is transformer oil (properties at 300 K). The density of the oil was specified to obtain a Rayleigh number of 10^4. The Rayleigh number, using Equation (6.7), was calculated for the cavity by calculating the average temperatures on the left and right solid-oil interfaces. As shown in Figure 6.13, solid walls were placed beside the cold and hot sides with properties all equal to that of transformer oil except for the thermal conductivity. The thermal conductivity of the solid regions was changed throughout the series of tests. If the thermal conductivity is high enough, the temperature throughout the left block would be nearly equal to T_{hot} and the temperature throughout the right block would be nearly equal to T_{cold}. The value of ΔT for the interior cavity would equal the difference of T_{hot} and T_{cold}. In this case, the behaviour of the fluid flow should be nearly the same as the fluid cavity with isothermal walls, which is the standard benchmark test problem discussed in Section 6.4. The top and bottom of the domain is insulated. A uniform 41×41 grid was used for the cavity, and each of the solid walls on either side had an additional five control volumes across their width.

Several tests were run by varying the ratio of the solid to oil thermal conductivities, k_s/k_o. Ratios of 10^5, 10^3, 10^2, 10, 5, 3, and 1, were analyzed. The runs showed that as the k_s/k_o ratio is reduced, the Rayleigh number decreases from 0.972×10^4 for

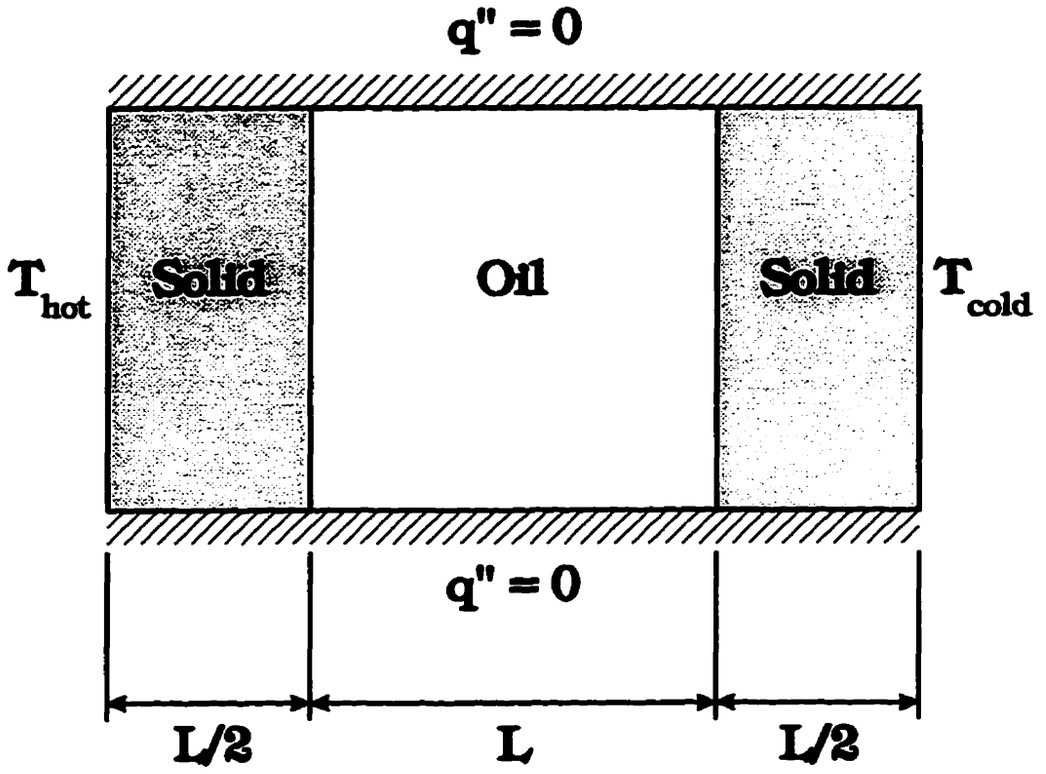

Figure 6.13: Illustration showing the setup and nomenclature for the square oil cavity with two conjugate walls test.

$k_s/k_o = 10^5$ to 0.163×10^4 for $k_s/k_o = 1$. This is attributed to the increasing thermal resistance in the solid walls causing a larger temperature drop across the finite wall. As the ratio of $k_s/k_o = 10^5$ decreased to $k_s/k_o = 1$, the amount of work units required for a solution almost doubled. Over 60% of the work for the $k_s/k_o = 10^5$ test case was spent computing the pressure correction field, while approximately 64% of the time was spent on the same task in the $k_s/k_o = 1$ test case.

This test case illustrates that as the temperature gradients inside solid increase, the number of work units required to solve the problem also increases. Therefore, it is expected that the closer the core and winding thermal conductivity is to the oil

thermal conductivity, the greater will be the CPU time that is required to solve the transformer simulation.

6.6.2 Narrow Fluid Cavity With One thick Wall

The next series of test problems consisted of a solid beside a narrow cavity filled with transformer oil, as shown in Figure 6.14. The purpose of this test is to determine the effect of having a tall and narrow cavity on the solution time and stability. This geometry is specified so that it is nearly that of a transformer cross-section. These tests, therefore, provided some experience in computing transformer-like problems. Also, the solid region properties were specified to be a homogeneous representation of the core and winding region in a transformer.

The first test case uses Dirichlet boundary conditions to specify a temperature on the boundary of the domain. All the walls were specified with the same temperature, except one which was given a higher temperature. The next test case took the average heat flux induced by the Dirichlet boundary conditions and used that value to replace the boundary condition of the higher temperature wall with a heat flux specification. The final test case used the total energy added to the previous tests cases divided by the volume of the solid as the energy generation within the solid. The heat flux on the left wall was removed, and instead the wall was treated as insulated.

Wall Boundaries with Specified Temperatures

The solid was approximated by a homogenous core-and-winding-like material (the approximations are based on a actual dimensions of an aluminum-wound winding). All the properties are listed in Table 6.11. The width of the solid is 0.1 meters, the fluid cavity is 0.015 meters, and the height of the cavity is 0.8 meters. These dimensions were chosen to reflect the dimensions of a typical, small-sized, distribution

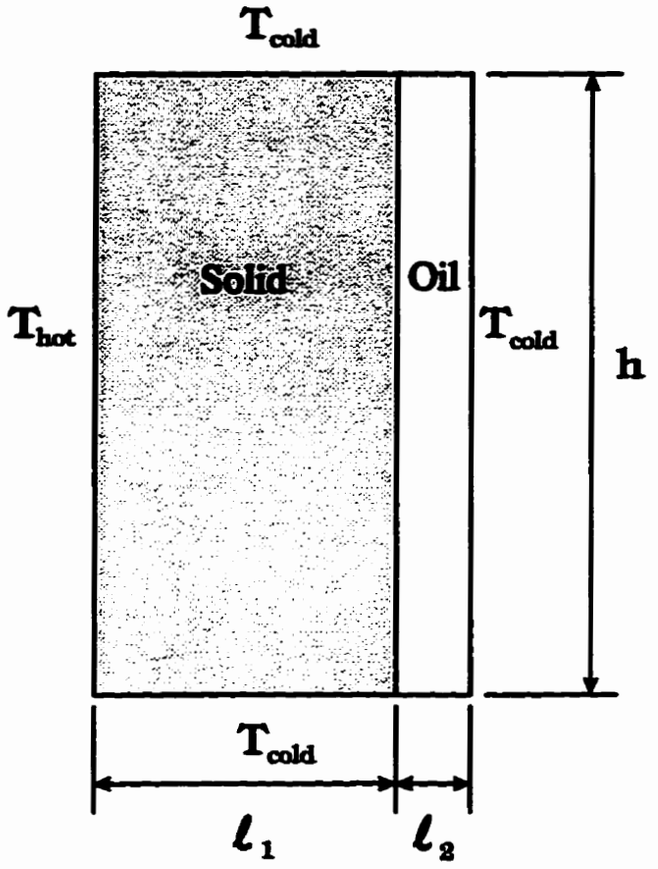

Figure 6.14: Schematic illustration of a narrow cavity, conjugate heat transfer model with dirichlet boundary conditions.

transformer. The Dirichlet boundary conditions were specified with a T_H of 5°C on the left hand side (on the *windings* side) and T_C of 0°C on the remaining sides. The higher temperature is used to simulate a power generation within windings.

Two sets of runs were conducted. The first set of runs were for $k_s/k_f = 10^{10}$, and a time step of 1, 2, and 3 seconds. The fluid properties remained constant throughout all the runs, only the thermal conductivity of the solid was changed. The results are summarized in Table 6.12. The solution proved to be unstable with larger time steps;

Property	Oil at 72°C	Core and Windings
Density	834.96 kg/m^3	2180 kg/m^3
Thermal Conductivity	0.45 W/m·K	by ratio
Specific Heat	1875.69 J/kg·K	1032 J/kg·K

Table 6.11: Properties for the narrow fluid cavity model.

Time Step	Total Steps	Total Time [hrs]	Work Units				Ra	Nu	Interface T
			T	U	V	P'			
1	534	0:08:54.00	1,228	1,105	1,142	119,400	7.870×10^4	2.4222	3.8548 K
2	917	0:30:34.00	1,380	2,459	1,555	114,600	7.874×10^4	2.4235	3.8566 K
3	10,000 †	8:20:00.00	10,520	29,890	17,920	817,200	7.873×10^4	2.4232	3.8563 K

Table 6.12: Results for the $k_s/k_f = 10^{10}$ conjugate model with narrow fluid cavity.

†This run did not reach steady state because of oscillations.

the time step of three seconds did not converge to a steady state value. The Rayleigh and the Nusselt numbers are determined based on the calculated average temperatures of the left and right walls, using Equations (6.7) through (6.11). The Nusselt number varied little between the different time steps, even if the time step of three seconds is considered. The number of work units is also recorded so that a prediction could be made about how long a transformer problem may take to solve. These values indicate how the solution time will increase as the test problem is modified to become more transformer-like.

The next set of runs were for a ratio of $k_s/k_f = 1/0.45$. This ratio is close to the actual ratio found between the windings in a transformer and the oil. The results are

Time Step	Total Steps	Total Time [hrs]	Work Units				Ra	Nu	Interface T
			T	U	V	P'			
2	6,463	3:35:26.00	6,463	12,900	13,560	1,478,000	1.623×10^4	0.3053	0.7949 K
3	4,705	3:55:15.00	5,652	9,396	10,200	983,000	1.634×10^4	0.3084	0.8005 K

Table 6.13: Results for the $k_s/k_f = 1/0.45$ conjugate model with narrow fluid cavity.

summarized in Table 6.13. The results for the one second time step are not shown because the test case would have taken over 10,000 time steps to converge. It is important to note that the solution of the $k_s/k_f = 1/0.45$ ratio problem is able to be solved with a larger time step.

Wall Boundary with a Specified Heat Flux

The model from Section 6.6.2 used Dirichlet boundary condition to simulate the heat generation within the windings. For this test case, the T_H boundary condition was replaced with the equivalent heat flux. The heat flux was based on the average heat flow (50 W) found on the left face of the $k_s/k_f = 1/0.45$ test case in the Dirichlet test problems. The heat flux applied to the left face is 62.5 W/m^2. Figure 6.15 shows the new boundary conditions. Only the $k_s/k_f = 1/0.45$ case was analyzed.

The purpose of the test was to see if changing the boundary condition would have a significant effect on the solution time and stability. A summary of the results is shown in Table 6.14. Although the results show that solution stability is not a problem, the new boundary condition increases the simulated time required to obtain steady state. In the previous subsection, three to four hours was required to reach steady state convergence. With the heat flux applied to the left side, the simulated time increased to at least eleven hours. The three second time step run was stopped because it was taking a long time to reach steady state. The longer simulation time makes sense

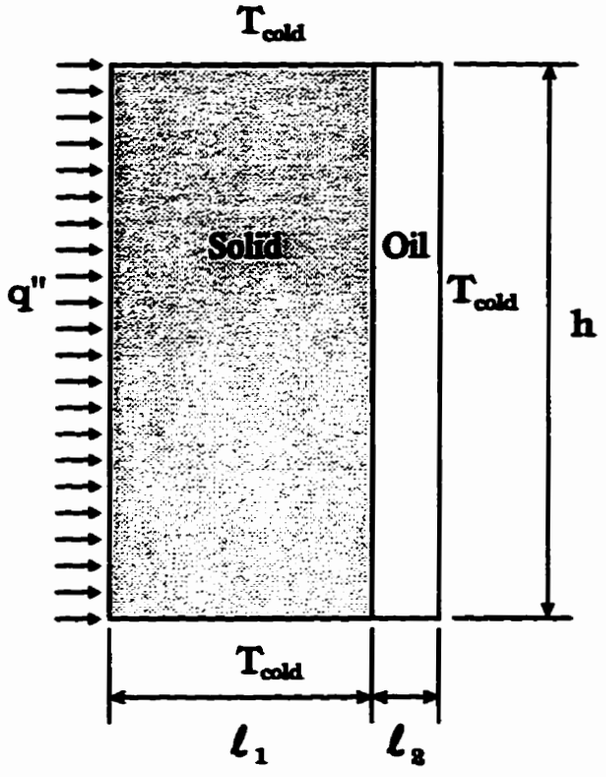

Figure 6.15: Schematic illustration of a narrow cavity, conjugate heat transfer test with a constant heat flux.

because the left temperature is no longer held constant. The wall boundary increases in temperature with the rest of the model. The left wall temperature increased from an average of 0.8 K in the Dirichlet test cases, to 1.0 K. The Rayleigh number increased from 1.6×10^4 to 2.0×10^4, and the Nusselt number increased from approximately 0.30 to 0.34.

These results show that the computer time required to solve the transformer model could be substantial since none of the transformer walls are held at a constant temperature.

Time Step	Total Steps	Total Time [hrs]	Work Units				Ra	Nu	Interface T [K]
			T	U	V	P'			
4	9972	11:04:48.00	12,080	20,030	19,310	1,958,000	2.018×10^4	0.33411	0.98859
8	5936	13:11:28.00	10,660	14,150	13,060	913,700	2.046×10^4	0.33688	1.00195
10	5050	14:01:40.00	8,911	12,200	11,780	697,900	2.052×10^4	0.33754	1.00513
20	3201	17:47:00.00	5,974	8,581	8,311	387,900	2.067×10^4	0.33902	1.01232

Table 6.14: Results for the $k_s/k_f = 1/0.45$ narrow fluid cavity with left side heat flux.

Heat Generation within the Solid

The 50 W heat flow used on the left side of the previous test problem was used to calculate an equivalent volumetric energy generation rate for the next variation of this model. Dividing this value by the volume area of the solid gives a heat generation rate of 625 W/m^3, and the left side was insulated to match a symmetry condition of a transformer model. Appendix A describes the justification for using this transformer cross-section as the model.

The test problem layout conditions are shown in Figure 6.16, and the results are summarized in Table 6.15. Only runs with a time step of 15 and 20 seconds were

Time Step	Total Steps	Total Time [hrs]	Work Units				Ra	Nu	Interface T [hrs]
			T	U	V	P'			
15	3866	16:06:30.00	7,364	10,590	9,799	476,400	2.158×10^4	0.63951	1.05702
20	4604	25:34:40.00	82,500	13,050	13,050	541,300	2.165×10^4	0.63937	1.06045

Table 6.15: Results for the $k_s/k_f = 1/0.45$ narrow fluid cavity with heat generation in the solid.

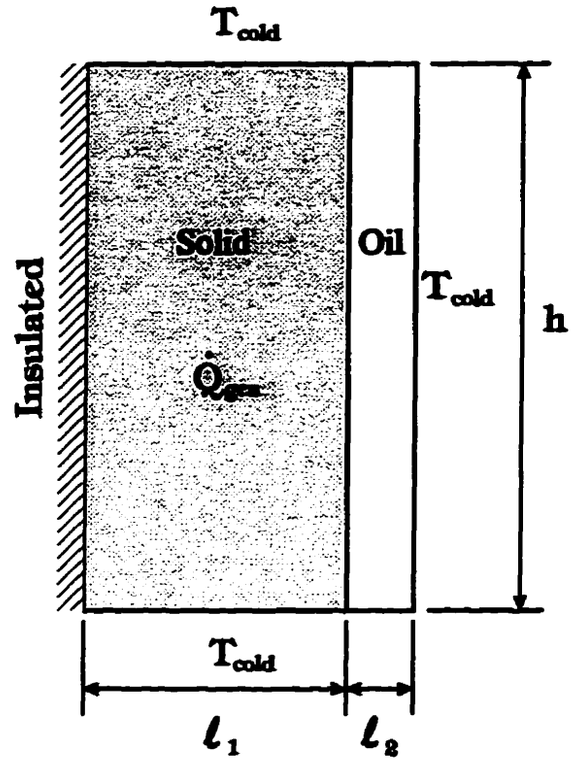

Figure 6.16: Schematic illustration of a narrow cavity, conjugate heat transfer test with energy generation within the solid.

conducted because the purpose of these tests were just to see if the switch from a heat flux on the left side to heat generation inside the solid would affect the results significantly.

The results showed that the simulated time increased from between fourteen and seventeen hours in the previous test cases, to between sixteen and twenty-five hours. The number of work units required increased by 50%, and the fluid-solid interface temperature increased from 1.01 K to 1.06 K. Both the Rayleigh and the Nusselt numbers increased from approximately 2.06×10^4 and 0.34 to 2.16×10^4 and 0.64, respectively.

6.6.3 PVT-Loop Tests

After much investigation it was found that the PVT-Loop discussed in Section 4.11 did not allow for longer time steps when analyzying the transformer model. Instead, the solutions continued to diverge at the higher time step and thus required many more solver iterations. Even the one second time step the PVT-Loop did not improve upon the solution time of the transformer. This may be attributed to the movement of the fluid cells above the core and windings. Instead, the standard segregated solution method was used to solve the transformer test cases in the next chapter.

Chapter 7

Transformer Simulations

7.1 Introduction

A method has been developed to model transient, conjugate heat transfer. The previous chapter showed the test cases used to validate the equation sets and the solution algorithms. The next step is to apply the computational model to a distribution transformer. The first transformer model was used to ensure that the theoretical model can capture the basic phenomena in a naturally oil-cooled distribution transformer. The work of Alegi and Black [1] was used to test the present model since their paper contained sufficient details for comparison with the present computer model. Once the simulated transformer model results were compared with the results of Alegi and Black, a parametric study was conducted on the same transformer configuration to show the effect of varying the ambient conditions, the load, and the description of the core and windings. Finally, a comparison was made with the ANSI loading guide [3]. These tests compared the computer-predicted hotspot temperature rise for step overloaded transformers with the ANSI tabulated values.

7.2 Comparison of Results with Alegi and Black

The results of Alegi and Black [1] were used to test the application of the present work. Using a lumped model approximation, Alegi and Black compared their theoretical model against data obtained from experimentally testing a 75 kVA distribution transformer.

7.2.1 Model Development

This section details the development of the Alegi and Black comparison model. The transformer parameters presented by Alegi and Black are reviewed, and the assumptions made by the authors are discussed in detail. This subsection then discusses the assumptions used in the comparison model.

Alegi and Black Model Summary

The Alegi and Black article [1] contains most of the information about their transformer run required to build a numerical comparison model. Some transformer specifics such as dimensional details about the windings, and the ratio of core to windings mass, had to be approximated. The basic model parameters are listed in Table 7.1.

The lumped model by Alegi and Black consists of three transient energy balances, one for each of the three transformer components shown schematically in Figure 7.1. The components are the core and winding assembly, the transformer oil, and the external transformer tank and fittings. Their model assumes that the core and windings can be approximated as a vertical cylinder with the top and bottom perfectly insulated. The core and the tank are linked by oil convection, and the tank is linked with the ambient air by convection. Correlations were used to model the convection

Parameter	Value
Full Load (Nameplate) Rating	75 kVa
Iron (No Load) Losses	0.07 kW
Full Load Copper (Full Load) Losses	0.528 kW
Top Oil Temperature Rise at Full Load	65°C
Mass of Core and Coil Assemby	532 lbm (241 kg)
Mass of Oil	278 lbm (126 kg)
Mass of Tank and Auxillary Fins	140 lbm (64 kg)
Equivalent Diameter and Height of Core and Coil	1.64×1.41 ft (0.5×0.43 m)
Diameter and Height of Tank	1.9×3.33 ft (0.58×1.01 m)

Table 7.1: Alegi and Black [1] transformer data.

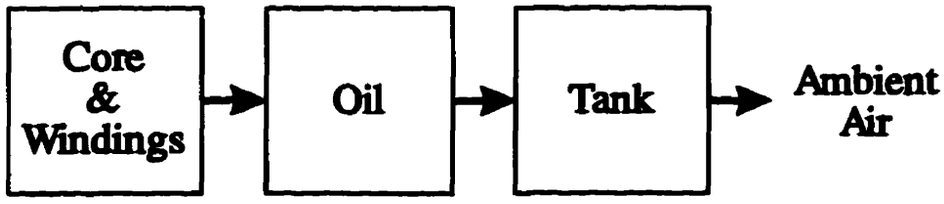

Figure 7.1: Alegi and Black lumped model energy flow diagram.

heat transfer. Alegi and Black made no attempt to model the increased convection caused by the auxillary fins. In the discussion to the paper, L. W. Pierce states that significant error is introduced by neglecting the heat transfer from the winding ducts to the oil. The present model also makes this approximation for consistency.

The Alegi and Black model used several correlations to model the convection between components. For the convective heat transfer from the sides of the core

and coil assembly to the surrounding oil, the authors stated that the curvature of a cylinder has no appreciable effects as long as the Grashof number is great than 10^6. This criterion is satisfied for a typical transformer design. Therefore the Nusselt number for the flow of oil over the core and coil assembly sides is calculated by

$$Nu_{c+w} = A\left(Gr_c Pr_{o,f}\right)^{0.25} \tag{7.1}$$

where the following expression is used for the value of A:

$$A = \left[\frac{Pr_{o,f}}{2.435 + 4.884 Pr_{o,f}^{0.5} + 4.953 Pr_{o,f}}\right]^{0.25} \tag{7.2}$$

The Grashof number of the oil is evaluated from the expression

$$Gr_{c+w} = \frac{\beta_{o,f}\, g\, (T_{c+w} - T_o)\, H_{c+w}^3}{(\nu_{o,f})^2} \tag{7.3}$$

where H_{c+w} is the height of the core and coil assembly, and $T_{c+w} - T_o$ is the difference between the core and windings, and oil temperatures. Once the Nusselt number is evaluated for the flow of oil over the core and coil, the convection heat transfer coefficient is determined by the expression

$$h_{c+w} = \frac{k_{o,f} Nu_{c+w}}{H_{c+w}} \tag{7.4}$$

Expressions for the thermophysical properties of the oil (Pr, β, ν,k) are given in Table 7.2. All oil properties are evaluated at the oil film temperature, the average of T_o and T_{c+w}.

The convection heat transfer coefficient between the oil and the inside walls of the tank is evaluated using a similiar procedure. Equations (7.1) and (7.2) still apply without modification, but the Grashof number is determined from the expression

$$Gr_t = \frac{\beta_{o,f}\, g\, (T_o - T_t)\, H_t^3}{(\nu_{o,f})^2} \tag{7.5}$$

Property ; Units	Symbol	Expression
Thermal Conductivity of Air; Btu/hr · ft·°R	k_{air}	$0.000263 + 22.50 \times 10^{-6}T$
Kinematic Viscosity of Air; ft^2/sec	ν_{air}	$-1.3663 \times 10^{-4} + 5.785 \times 10^{-7}T$
Coefficient of Thermal Expansion of Air; 1/°R	β_{air}	1/T
Prandtl Number of Air	Pr_{air}	0.70
Thermal Conductivity of Oil; Btu/hr · ft·°R	k_o	$0.07755 - 25.672 \times 10^{-6}T$
Kinematic Viscosity of Oil †; ft^2/sec	ν_o	$10^{-6} \times exp\,(32.18 - 0.0772T + 50.81 \times 10^{-6}T^2)$
Coefficient of Thermal Expansion of Oil; 1/°R	β_o	0.0004
Prandtl Number of Oil	Pr_o	$exp\,(30.36 - 0.0712T + 46.81 \times 10^{-6}T^2)$
Specific Heat of Oil; Btu/lbm·°R	$c_{p,o}$	$0.1009 + 5.849 \times 10^{-4}T$
Specific Heat of Copper; Btu/lbm·°R	$c_{p,cu}$	$0.0856 + 12.778 \times 10^{-6}T$
Specific Heat of Steel; Btu/lbm·°R	$c_{p,steel}$	$0.0726 + 60.556 \times 10^{-6}T$
Above expressions are limited to 480°R < T < 680°R, and T must be in °R.		

Table 7.2: Alegi and Black [1] thermophysical property expressions and definition of symbols.

†The expression for this property was modified from the original expression in the paper because the calculated values were unrealistic. The original expression, $exp\left[(32.18 - 0.0772T + 50.81 \times 10^{-6}) \times 10^{-6}\right]$, was missing the T^2 factor in the last term, and misplaced the $\times 10^{-6}$ term in the exponent.

where H_t is the height of the transformer tank, and $T_o - T_t$ is the difference between oil and tank temperatures. The convection heat transfer coefficient is given by

$$h_t = \frac{k_{o,f} Nu_t}{H_t} \tag{7.6}$$

where all oil properties are evaluated at the film temperature, the average of T_o and T_t.

To evaluate the convective heat transfer coefficient on the outer surface of the tank walls, the transformer tank is modelled as a vertical cylinder. For this test case, Alegi and Black modelled the tank convection heat transfer as being only natural convection. As long as the thermal boundary layer thickness over the outer surface of the tank is small compared to the effective diameter of the tank, Alegi and Black suggested using the following equations to determine the Nusselt number.

$$Nu_{t,free} = 0.555 \left(Gr_t Pr_{air}\right)^{0.25} \; ; \; Gr_t Pr_{air} < 10^9 \tag{7.7}$$

$$Nu_{t,free} = 0.021 \left(Gr_t Pr_{air}\right)^{0.40} \; ; \; Gr_t Pr_{air} > 10^9 \tag{7.8}$$

where

$$Gr_t = \frac{\beta_{air,f}\, g \left(T_t - T_\infty\right) H_t^3}{\left(\nu_{air,f}\right)^2} \tag{7.9}$$

The temperature difference, $T_t - T_\infty$, is between the tank and ambient temperatures. Expressions for the thermophysical properties used for air in the Alegi and Black model are given in Table 7.2 and they are evalulated at the film temperature, the average of T_∞ and T_t.

The convection heat transfer coefficient for free convection between the outside of the transformer tank and the air is calculated by

$$h_{t,free} = \frac{k_{air,f} Nu_{t,free}}{H_t} \tag{7.10}$$

The energy generated in the core and coil assembly is produced by two sources of electrical losses. The first loss, which is constant and independant of load, is the iron loss. This loss is the sum of hysteresis and eddy-current losses. The second loss is the copper (load) loss and it results from the electrical resistance of the windings. The magnitudes of these losses are determined from heat run test data. With this information the total heat generated, as a function of transformer load, is

$$Q_{gen} = \left\{ \left[\frac{[\text{kVA}]_{\text{load}}}{[\text{kVA}]_{\text{full load}}} \right]^2 \times Q_{w,loss} \right\} + Q_{c,loss} \tag{7.11}$$

The net radiation exchange leaving the transformer tank to the environment is modelled by the expression

$$q_{rad} = A_t \epsilon_I \sigma T_t^4 - A_t \alpha_I \sigma T_\infty^4 \tag{7.12}$$

Alegi and Black state that the emitted radiant energy from the surface of a transformer tank which has a temperature in the range of 20 to 120°C, and the absorbed energy from the surroundings at roughly the same temperature, falls predominantly in the infrared wavelength range. Assuming only infrared energy and applying Kirchhoff's law, the emissivity and the absorbtivity are assumed to be equal; $\epsilon_I = \alpha_I$. A value of 0.95 was recommended as an average for typical transformer paints.

To verify their model, Alegi and Black conducted experiments using a transformer equipped with thirty calibrated thermocouples: ten throughout the core and coil assembly, ten at various positions in the oil, and the remaining ten on the exterior surface of the tank. The thermocouple readings were averaged to provide a measure of the average component temperature. As a result, the average of the measured temperatures will be lower than the maximum temperatures that can exist in the core and coil assembly and in the oil.

Some of the thermocouples used to measure the core and coil temperature were placed in oil ducts, and some were fastened to the coil. The thermocouples used to

measure the average oil temperature were attached to ceramic rods and located at various distances from the bottom of the tank to the top of the tank over the core and oil assembly. All the tests were conducted indoors so there was no solar energy incident on the tank.

For the first test, the distribution transformer was started from a cold-start (uniformly equal to the 20°C ambient temperature) with a step load increase from 0 to 49 kVA. Once the transformer achieved steady state the transformer load was again increased stepwise from 49 to 71 kVA.

The Choice of the Two-Dimensional Transformer Model

The ideal transformer model should be able to simulate the thermal effect of every dimension of the transformer. As previously mentioned, such a model would be very complicated, and would take a prohibitive amount of computer time to solve. In an attempt to simplify the problem and to reduce the solution time, it was decided to model the transformer on a two-dimensional basis. Appendix A discusses the reasoning behind the selection of the model cross-section, and why other potentially more accurate three-dimensional models were not chosen.

Appendix B shows the grids developed for all transformer runs. This appendix will serve as a reference for all grid information presented in this chapter.

Assumptions and Approximations of the Present Model

Several assumptions had to be made for the two-dimensional transformer model because all the necessary parameters are not available in [1]. For instance, although the approximate diameter of the core and windings were given, no information was given as to how they determined the approximate diameter of the core and windings. Also,

no information was given about the position of the transformer within the tank. The present model was developed in Cartesian coordinates, and adjustments were then needed to approximate the cylindrical shape given by Alegi and Black.

In order to obtain the best approximation possible to the Alegi and Black domain, several equations were derived to maintain the basic physical properties of the Alegi and Black 75 kVA transformer. The air gap above the oil was ignored to simplifiy the model. Equation (7.13a) maintains the mass of the oil at 126 kg since the oil plays an important part in the thermal capacitance of the transformer. The nomenclature

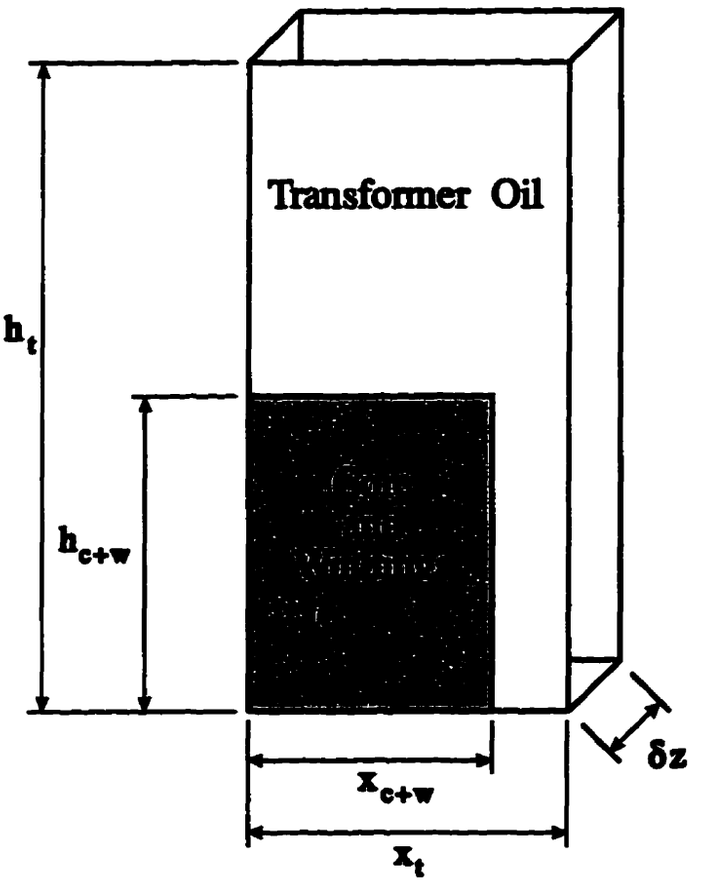

Figure 7.2: Dimension nomenclature for the Alegi and Black comparison model.

for this equation is illustrated in Figure 7.2. The total power generated within the transformer is maintained by Equation (7.13b). The surface area of the core and windings is maintained by Equation (7.13c) so that the model kept the same amount of heat flow from the core and windings to the oil. Equation (7.13d) maintains the mass of the core and windings at 241 kg. Although the surface area of the tank should also remain constant, another equation could not be added because it made it difficult to solve the equation set and maintain a domain geometry that reasonably approximates that of a distribution transformer. Instead, the convection coefficient for the tank is modified, as shown later in the chapter, to compensate for the discrepancy.

$$m_o = \rho_o (h_t x_t - h_c x_{c+w})(\delta z) \tag{7.13a}$$

$$\dot{Q}_{total} = \dot{Q}''' (h_{c+w} x_{c+w})(\delta z) \tag{7.13b}$$

$$(A_s)_{c+w} = (h_{c+w} + x_{c+w})(\delta z) \tag{7.13c}$$

$$m_{c+w} = \overline{\rho_{c+w}} (x_{c+w} h_{c+w})(\delta z) \tag{7.13d}$$

The half-width of the core and windings, x_{c+w}, is set equal to the equivalent core and winding radius as determined by Alegi and Black, and the width of the tank, x_t, is set equal to the tank radius. The equations are solved to obtain the results shown in Table 7.3.

All properties were evaluated based on the steady state temperatures determined from the Alegi and Black lumped model simulation. The properties of the oil were evaluated at 39.5°C for the 49 kVA run and 55.0°C for the 71 kVA run. The core properties were evaluated at 44°C for the 49 kVA load run, and 64°C for the 71 kVA load run. The specific heat of the core and windings was approximated by taking the volume-weighted average specific heat of pure copper and the steel of the core (using the correlations supplied by Alegi and Black). The thermal conductivity of the windings was assumed to be uniform, isotropic, and equal to 5 W/m^2K. The thermal conductivity of the core was assumed to be 42.5 W/m^2K. The present model used

Parameter	Variable	Value
Half width of core and windings	x_{c+w}	0.25 m
Half width of tank	x_t	0.29 m
Height of core and windings	h_{c+w}	0.25 m
Height of tank	h_t	0.58 m
Depth of tank	δz	0.68 m

Table 7.3: The Alegi and Black approximate model dimensions used in the present study.

a homogenous thermal conductivity for the entire core and windings block based on the harmonic mean of both the winding and steel core thermal conductivities (8.94 W/m^2K). The density of the core and windings could not be based on the properties of the core or windings because no information was given about how much of the core and windings was iron core and how much was copper windings. Therefore, the equivalent diameter and height were used to get an equivalent volume. The density was then calculated by dividing the given mass of the core and windings by this equivalent volume to produce an effective density of 2,854 kg/m^3. The power generated by the core and windings was summed according to Equation (7.11) and divided by the total volume to produce volumetric energy generation rates of 3.4750 and 6.3904 kW/m^3 for the 49 kVA and 71 kVA runs, respectively.

The Alegi and Black model simulated the convection by only considering the sides of the tank. Since a similiar assumption of insulated top and bottom tank surfaces would be expected to unrealistically change the characteristics of the oil flow within the tank, convection boundary conditions were used for the top and bottom, as well as for the side. The ambient properties of air were evaluated at 20°C. The convection

Tank Side	Natural Convection (h)	Radiation (h_r)	Overall (h_{eff})
sides	2.291 W/m^{2}K	5.762 W/m^{2}K	9.395 W/m^{2}K
top	4.192 W/m^{2}K	5.762 W/m^{2}K	11.612 W/m^{2}K
bottom	2.351 W/m^{2}K	5.762 W/m^{2}K	9.465 W/m^{2}K

Table 7.4: Tank convection coefficients for the two-dimensional transformer flow model loaded at 49 kVA for comparison with Alegi and Black.

coefficients for the external boundaries of the tank were calculated differently for each of the surfaces. They are summarized in Table 7.4. The sides of the tank were evaluated based on the steady state tank temperature, 32°C, calculated by Alegi and Black for the 49 kVA run. The correlation supplied by Alegi and Black for the ambient air convection was used to calculate the wall convection using the actual tank height of 1.01 m.

The convection coefficients for both the top and bottom of the tank were calculated based on correlations for natural convection from a horizontal flat plate given by Incropera and DeWitt [30]. The convection coefficient for the top of the tank was calculated based on a wall temperature of 32°C. The Rayleigh number was calculated by the equation

$$Ra = \frac{g\beta(T_s - T_\infty)L^3}{\nu\alpha} \tag{7.14}$$

The length is determined based on the characteristic length. This length was calculated by dividing the surface area of the plate by the perimeter, to produce a value of 0.145 m. The Rayleigh number was equal to 3.357×10^6, which corresponds to laminar flow. Since the flow is laminar, the convection coefficient for the top plate

was calculated using

$$\overline{h} = \frac{k_{air,f}}{L}\overline{Nu} \tag{7.15}$$

$$\overline{Nu} = 0.54(3.357 \times 10^6)^{1/4} \tag{7.16}$$

The convection coefficient for the bottom plate was calculated based on a tank temperature of 39°C after some preliminary runs suggested using this higher temperature. The Rayleigh number for the natural convection of the bottom surface (using Equation (7.14)) indicated that the air flow would still be laminar. Therefore the convection coefficient was calculated using

$$\overline{h} = \frac{k_{air,f}}{L}\overline{Nu} \tag{7.17}$$

$$\overline{Nu} = 0.27(3.357 \times 10^6)^{1/4} \tag{7.18}$$

The radiation exchange between the tank walls and the environment was also estimated. An effective convection coefficient was determined for the radiation using

$$h_r = \frac{\sigma\epsilon(T_t^4 - T_\infty^4)}{T_t - T_\infty} \tag{7.19}$$

For the radiation calculation, the tank temperature was assumed to be uniformly at 32°C, and the emissivity, ϵ, of the tank paint was given by Alegi and Black to be 0.95. The temperature of the surroundings was assumed to be equal to the ambient air temperature.

An overall convection coefficient correction based on the surface area ratio between the models resulted in the equation,

$$h_{eff} = 1.1666(h_r + h) \tag{7.20}$$

Table 7.5 shows the effective convection coefficients for the 71 kVA run. The tank temperature was assumed to equal 49°C.

Tank Side	Natural Convection (h)	Radiation (h_r)	Overall (h_{eff})
sides	3.200 W/m^{2}K	6.279 W/m^{2}K	11.058 W/m^{2}K
top	5.259 W/m^{2}K	6.279 W/m^{2}K	13.460 W/m^{2}K
bottom	2.629 W/m^{2}K	6.279 W/m^{2}K	10.392 W/m^{2}K

Table 7.5: Tank convection coefficients for the two-dimensional transformer flow model loaded at 71 kVA for comparison with Alegi and Black.

Grid and Time Step Independence Checks

Grid and time independence runs were performed on the two-dimensional transformer flow model that would later be used for comparison with the Alegi and Black results. For each grid, several time steps were used to determine at which point the solution is insensitive to a change in the size of the time step. The grids evaluated were 54×51, 73×73, 100×102, and 100×152. The results are presented in Appendix C. These results are based on the transformer loading of 49 kVA described in the next section. The properties were all evaluated at 300 K for the purpose of the time and grid independence runs. For those runs the model is divided into three regions: the solid, the top oil cavity, and the narrow right channel along side the core and windings. The the results of the independence checks also show the simulated results obtained by Alegi and Black for the 49 kVA loading. The top curve of each plot shows the average core temperature, the middle curve shows the average oil temperature, and the bottom curve shows the average tank temperature.

The transformer runs did not reach a steady state condition, as defined by Equation (4.85). The flow oscillated as cells of oil move around above the core and wind-

ings. This is illustrated in Section 7.2.2. Instead, two new criteria were required to determine when to stop the computations. Those two conditions, based on a relative change of energy storage and average temperature were

$$\frac{|Q_{gen} - Q_{out}|}{Q_{gen}} \leq 1.0 \times 10^{-3} \tag{7.21}$$

and

$$\frac{|T_{avg} - T^{o}_{avg}|}{T_{avg}} \leq 1.0 \times 10^{-5} \tag{7.22}$$

where Q_{gen} is the energy generated within the solid, Q_{out} is the energy leaving the tank, T_{avg} is the average overall temperature, and T^{o}_{avg} is the average overall temperature from the previous time step.

As the difference in Equation (7.21) gets smaller, the stored energy decreases. When the ratio is reduced to 1.0×10^{-3} then the energy storage is very small relative to the energy generated. Equation (7.22) is satisfied when there is little overall temperature fluctuation within the domain between time steps, even though local temperatures may vary spatially as the oil flow cells move slightly.

Appendix C shows the results of the time and grid independence tests. The results show that a time step of one second for a 73×73 grid gives optimal results based on the CPU solution time and accuracy of the average temperatures.

7.2.2 Two-Dimensional Flow Model: 49 kVA Load

This section presents and discusses the results obtained by using the two-dimensional flow model when the transformer is loaded at 49 kVA. These results are compared with the results of Alegi and Black for the same loading. A 73×73 grid was employed and the time step was chosen to be one second.

Average Temperatures

Figure 7.3 shows the nomenclature for the temperature rise, θ, at various locations in the solution domain. The subscript, R, represents the region to the right, and T represents the region above the core and windings. The plot in Figure 7.4 shows the average temperatures for the core and windings, the right oil region, and the top oil region. Note that for these and all subsequent plots, only the values for every tenth time step are plotted.

The average temperature is volume weighted for each region (since the regions have uniform specific heat). The transformer took 38:23:44.00 hours (138,224 one-second time steps) of simulated time to reach steady state. The core and windings

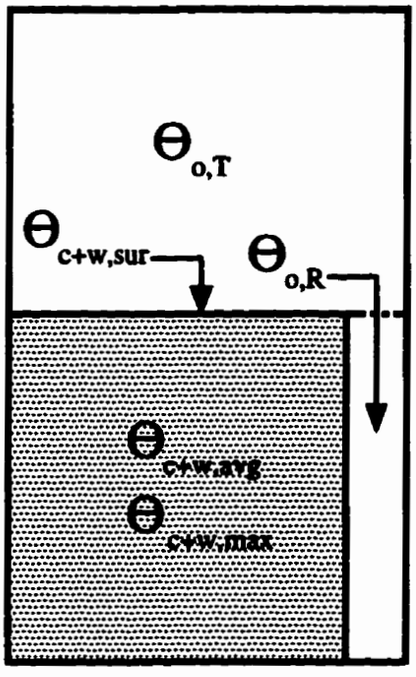

Figure 7.3: Model layout showing the nomenclature of θ, the temperature rise above ambient.

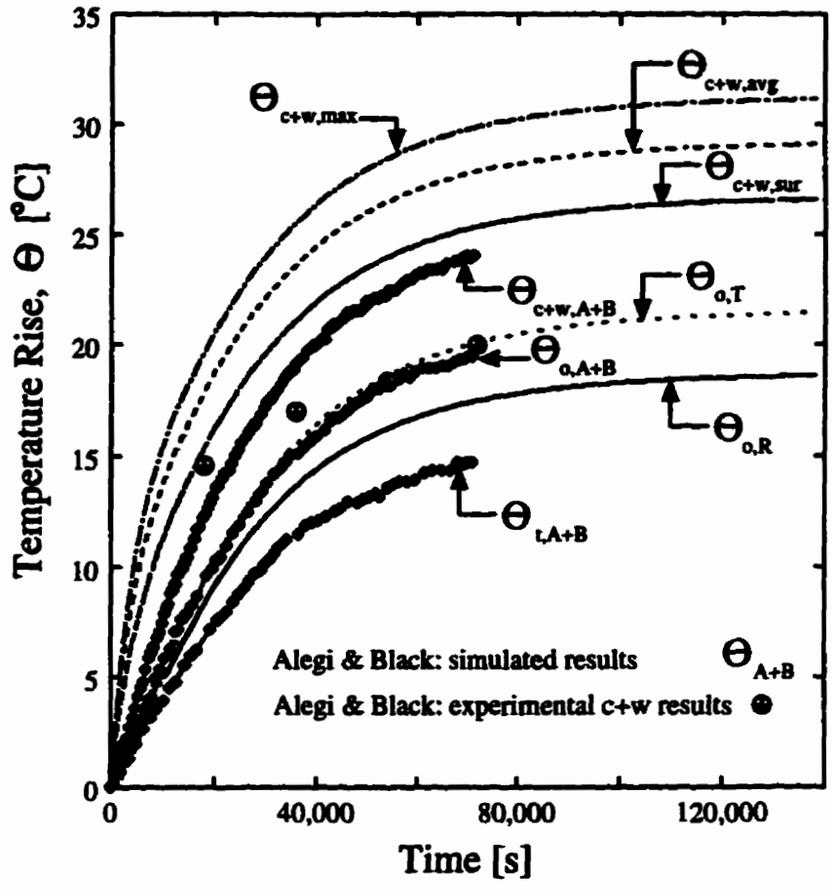

Figure 7.4: Comparison of the 49 kVA load results showing the temperature rise above the ambient temperature of 20°C.

surface temperature results only considers the surfaces in contact with the fluid oil. The surface temperature of each control volume face is determined by linear interpolation, and the average surface temperature is calculated by weighting the surface temperatures by the control volume surface and then dividing the sum by the total surface area. The average surface temperature results calculated by the computer code compare well with the Alegi and Black predicted core and windings results. Both the Alegi and Black and the present results for the surface temperature over

predict the steady state experimental results by approximately five degrees. This may be because the temperature probes were not placed within the windings and the thermocouple signal was averaged, or because no ducts were considered in either model. Note that the quantity labelled as the maximum temperature rise value in the core and windings ($\theta_{c+w,max}$) accured at different spatial locations during the simulation, but was always at the same location as steady-state conditions were approached.

The present work results capture the general trends in temperature variation in the transformer. The top oil and right side cavity average temperatures are on either side of the Alegi and Black calculated average oil temperature. This shows that the thermal characteristics of the oil are modelled similarly in both models. Although it is not shown in this plot, the Alegi and Black measured oil temperature of the transformer are close to the average tank temperature curve calculated by Alegi and Black. At steady state, the top oil temperature predicted in this work is approximately 5°C higher than the measured value.

The results from the two-dimensional flow model showed that the location of the maximum hotspot temperature moved from the center of the left boundary control volume at the coordinates (0 m, 0.10625 m) to the boundary control volume at (0 m, 0.06875 m), relative to the lower left corner of the domain. Then by 1.5 hours later it had moved slowly back up to (0 m, 0.11875 m).

Temperature and Streamline Plots

Figure 7.5 shows the temperature field snapshots every 10 seconds at "steady state". In this case, "steady state" means a sufficiently long time so that Equations (7.21) and (7.22) are met, but Equation (4.85) may not be. These and all other temperature field plots are used for a qualitative analysis of the results; the contours do not represent the same temperature value between plots. There is very little change in

the temperature fields between intervals. The only noticable changes are the small temperature fluctuations directly above the core and windings.

The streamline plots, Figures 7.6 to 7.9, show the changes in the fluid flow above the core and windings every five seconds. These plots show that the centers of the main vortices in the oil are not stationary. The oscillating flow may be due to instabilities that indicate the beginning of a transition to turbulent flow. In all plots, Figures 7.6 to 7.9, the rotation of the oil vortices is clockwise. It was observed that the changes in the oil flow patterns did not repeat themselves in a regular, periodic way.

Heat Flow

Figure 7.10 shows the heat flow out each face of the tank normalized by the generated energy. As expected, most of the energy is transfered from the side of the tank (q_R^*). More energy leaves by the bottom of the tank than the top. This may be attributed to the core and windings being modelled as sitting on the bottom of the tank. The total ratio of energy leaving the tank to the energy being generated within the core and windings was 0.9987 when the run was terminated.

Steady State Check

The results of the steady state heat flow check is shown in Figure 7.11. As the transformer approaches a steady state heat flow condition, the heat flow oscillations become more noticable. This is because the fluid cells above the core and windings are constantly moving around. Although it does not appear that the simulation satisfies Equation (7.21), the criterion was met four time steps after the last result was recorded (which is recorded every ten seconds). The steady state check based on the average temperature change was satisified (at 10^{-5}) long before the steady

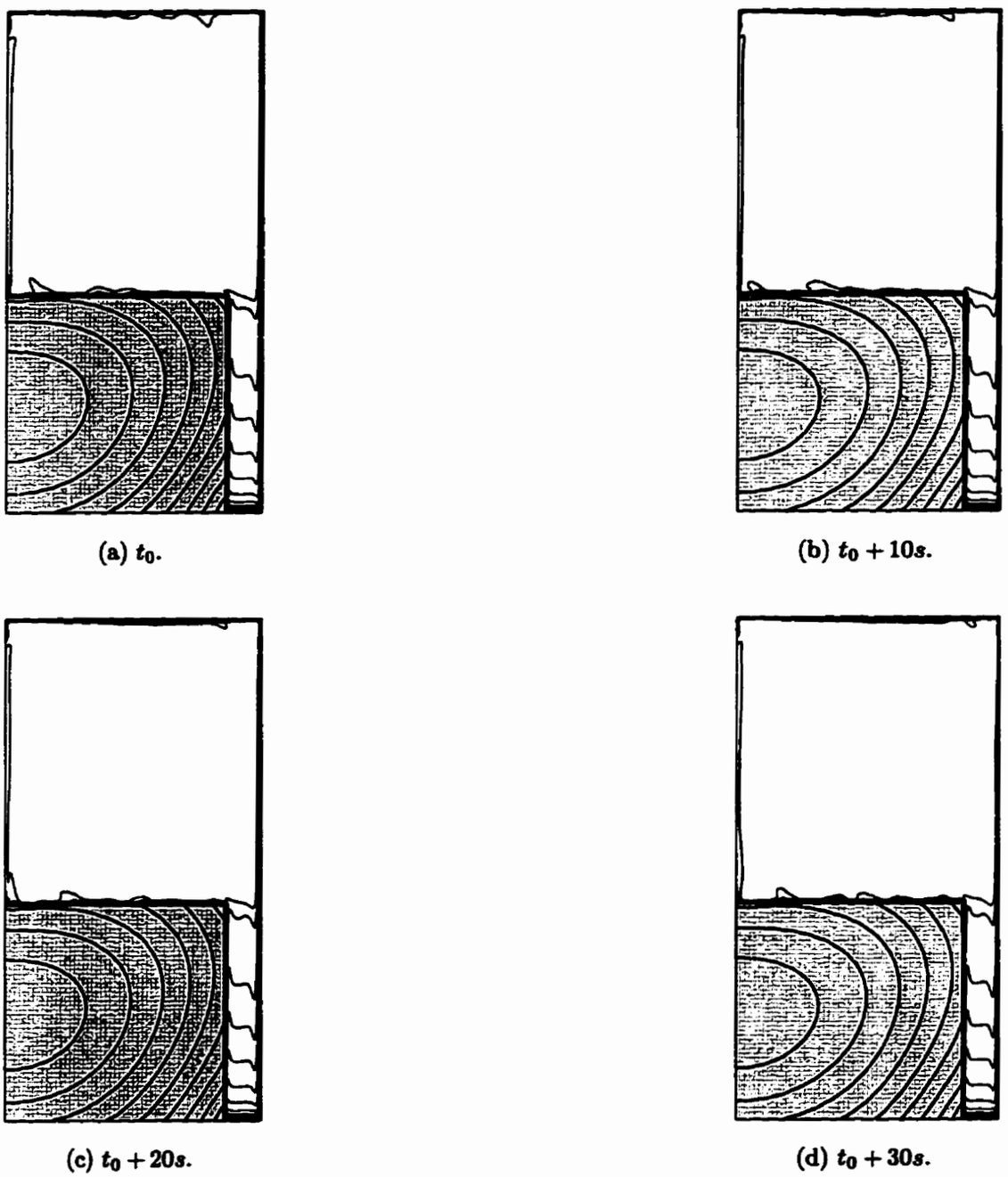

(a) t_0.

(b) $t_0 + 10s$.

(c) $t_0 + 20s$.

(d) $t_0 + 30s$.

Figure 7.5: Elapsed time temperature results at steady state; starting from a datum of $t_0 = 138,225$ seconds for the 49 kVA Alegi and Black simulation case.

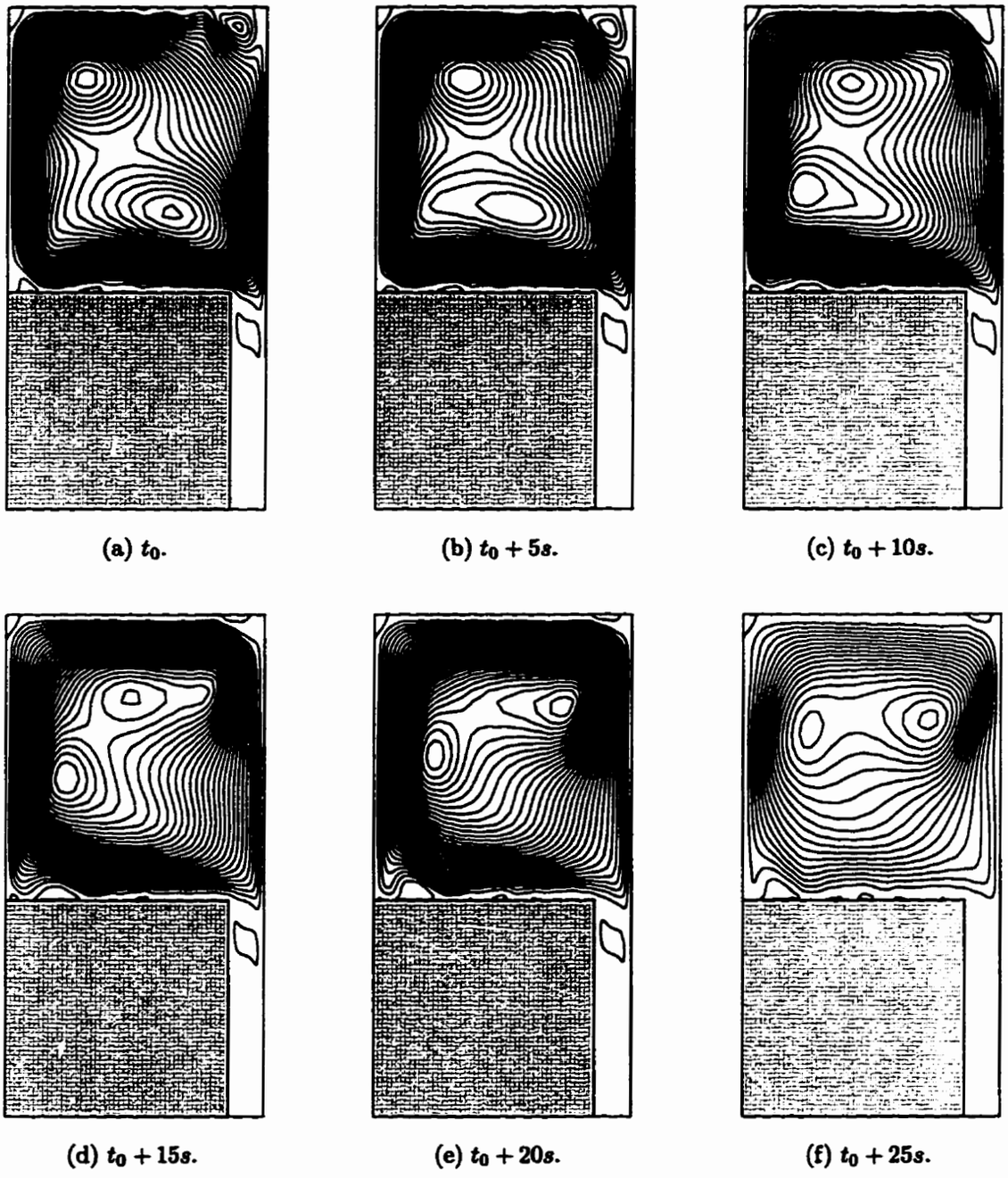

(a) t_0. (b) $t_0 + 5s$. (c) $t_0 + 10s$.

(d) $t_0 + 15s$. (e) $t_0 + 20s$. (f) $t_0 + 25s$.

Figure 7.6: Elapsed time streamline results at steady state; starting from a datum of $t_0 = 138,225$ seconds for the 49 kVA Alegi and Black simulation case.

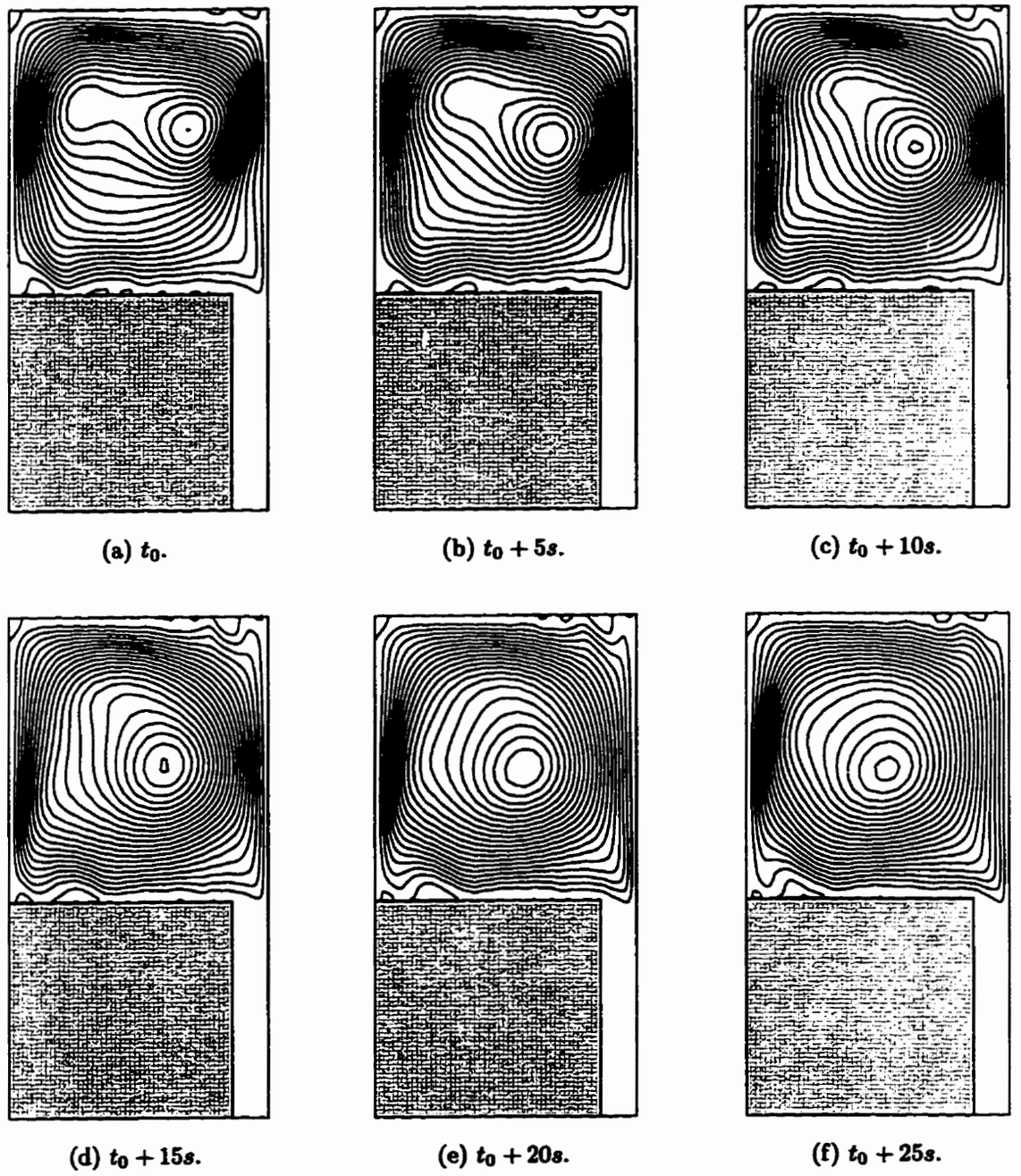

(a) t_0. (b) $t_0 + 5s$. (c) $t_0 + 10s$.

(d) $t_0 + 15s$. (e) $t_0 + 20s$. (f) $t_0 + 25s$.

Figure 7.7: Elapsed time streamline results at steady state; starting from a datum of $t_0 = 138,255$ seconds for the 49 kVA Alegi and Black simulation case.

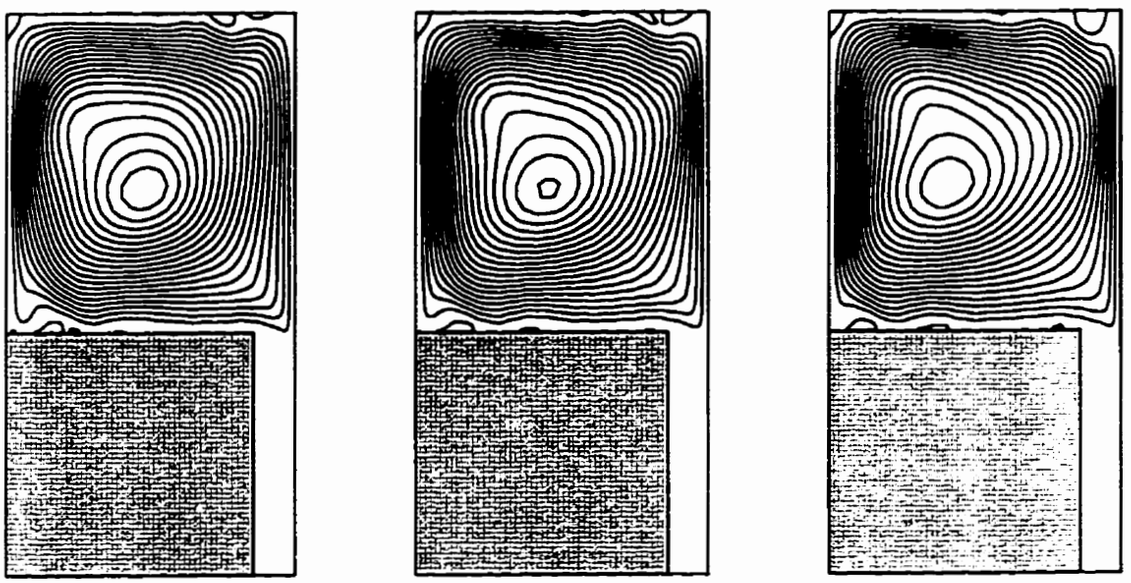

(a) t_0.

(b) $t_0 + 5s$.

(c) $t_0 + 10s$.

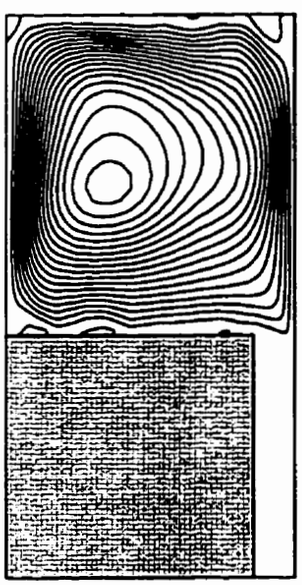

(d) $t_0 + 15s$.

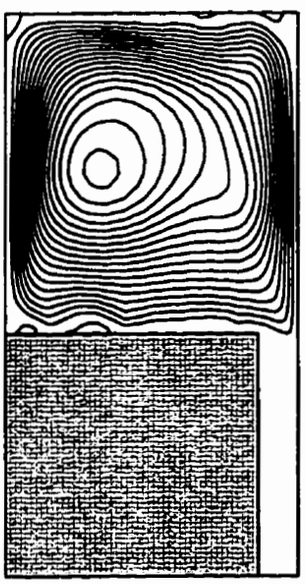

(e) $t_0 + 20s$.

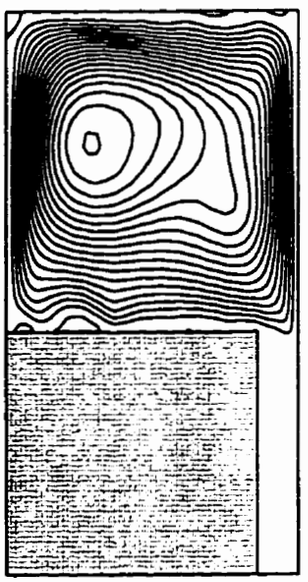

(f) $t_0 + 25s$.

Figure 7.8: Elapsed time streamline results at steady state; starting from a datum of $t_0 = 138,285$ seconds for the 49 kVA Alegi and Black simulation case.

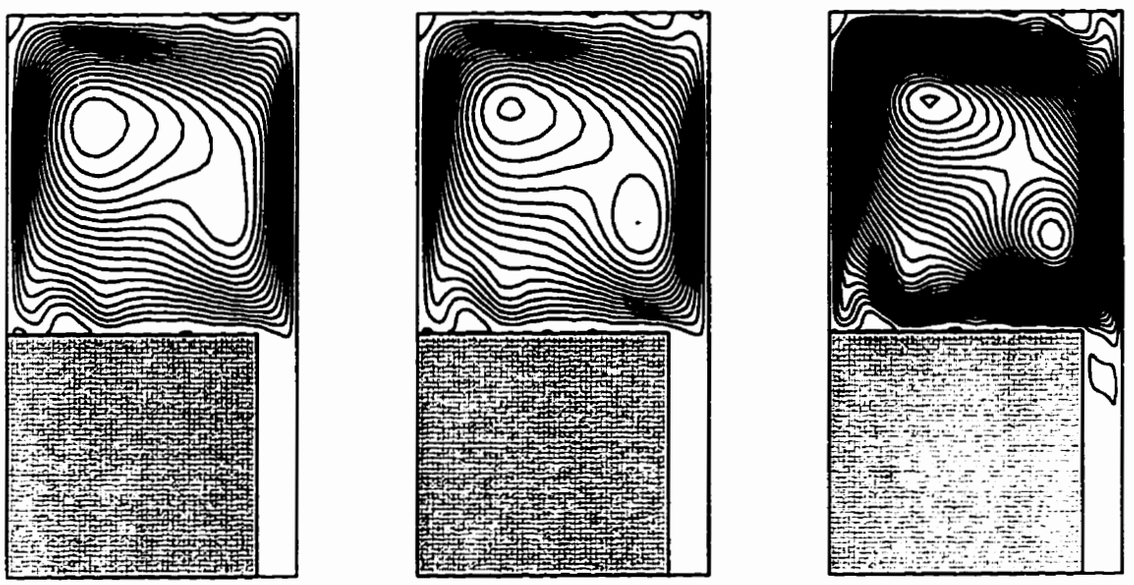

(a) t_0.

(b) $t_0 + 5s$.

(c) $t_0 + 10s$.

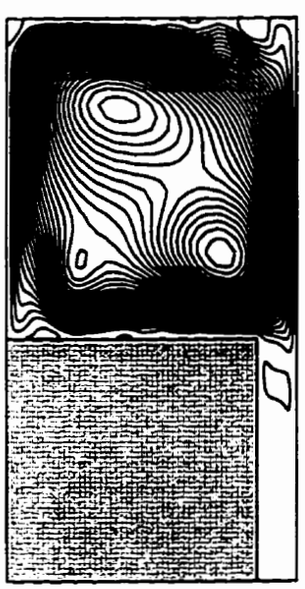

(d) $t_0 + 15s$.

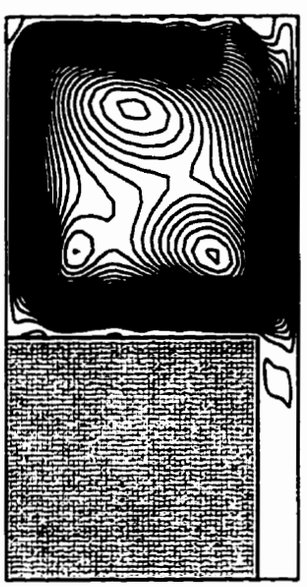

(e) $t_0 + 20s$.

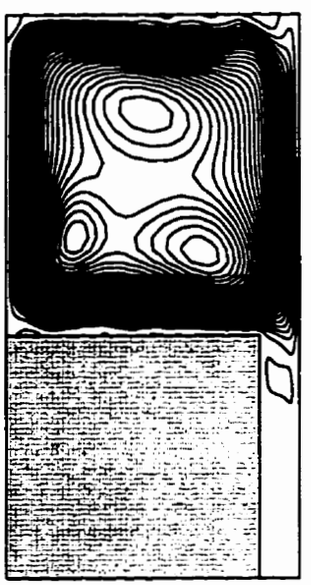

(f) $t_0 + 25s$.

Figure 7.9: Elapsed time streamline results at steady state; starting from a datum of $t_0 = 138,315$ seconds for the 49 kVA Alegi and Black simulation case.

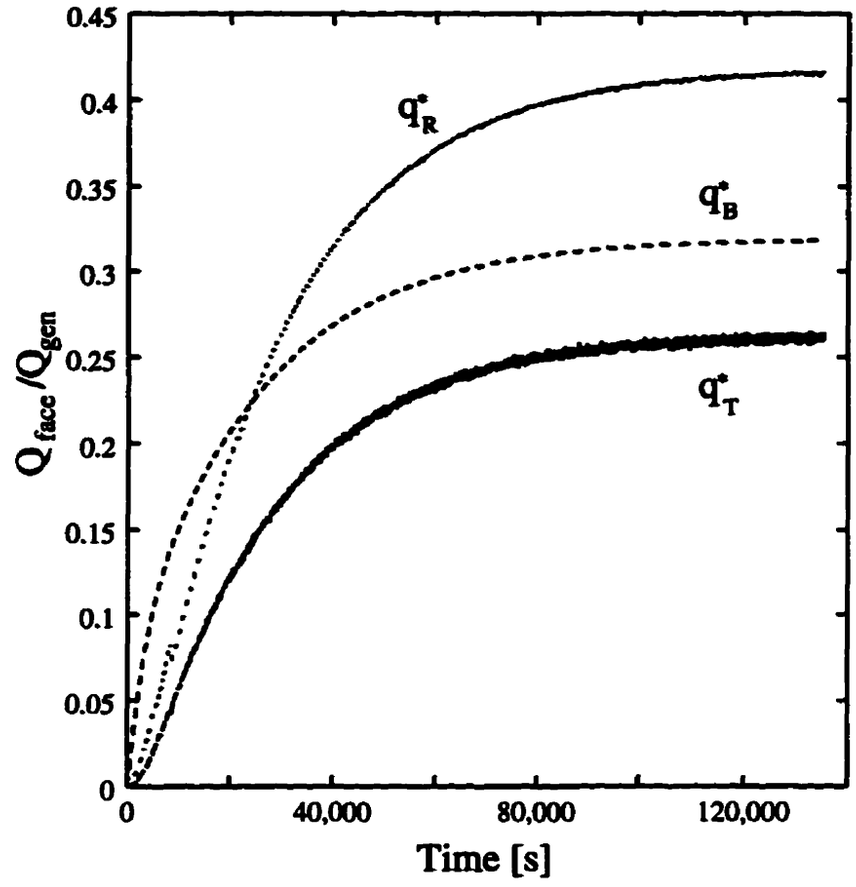

Figure 7.10: Normalized tank surface heat flow for the two-dimensional transformer flow model: 49 kVA load.

state heat flow check stopped the run. This is because the oil temperature is almost uniform.

Two tests were conducted after the 49 kVA load test case reached "steady state". The purpose of the tests was to see which equation set may have been making the solution unstable. When the temperature field was held constant, the flow field was allowed to be solved until it reached steady state in 7.5 minutes. Since the temperature was not allowed to change with the flow field, the flow field quickly settled out to a

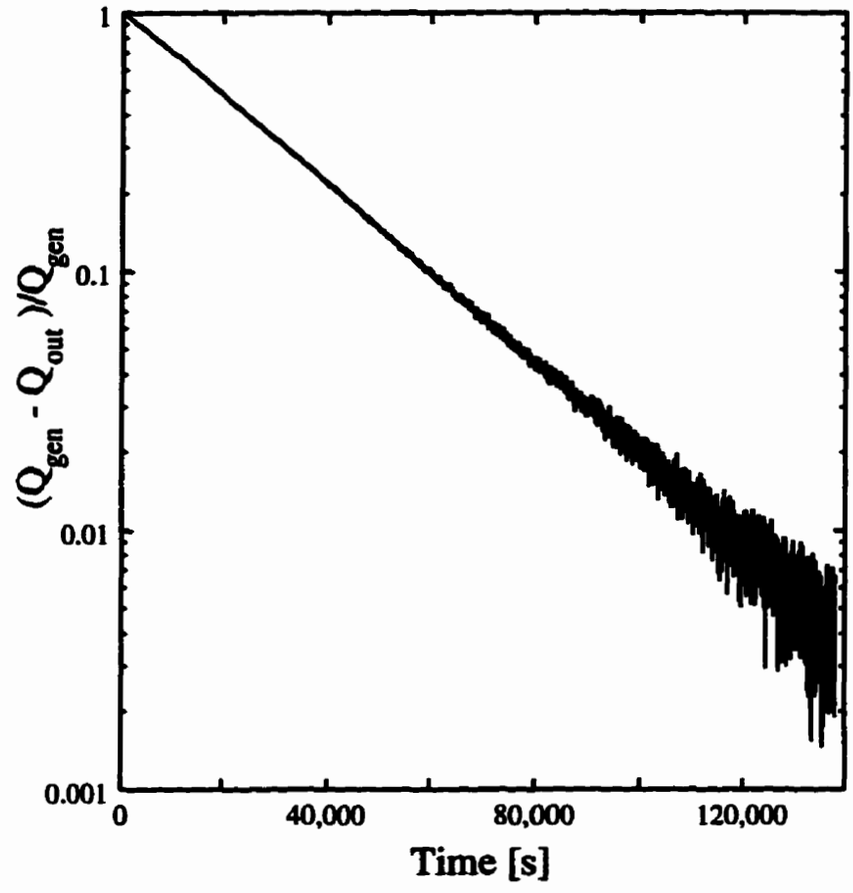

Figure 7.11: Steady state heat flow check for the two-dimensional transformer flow model: 49 kVA load.

steady state condition. The next test took the original "steady state" solution again, held the flow field constant this time, and then solved for the temperature field. The temperature field took a little over 14 minutes to reach steady state. The ratio of energy flowing out of the transformer to the energy generated also quickly converged to a value (0.0085). This means that when the flow field is held constant, the the energy equation is stable. Therefore, the coupling of the temperature and the flow field in the transformer test case is the cause for the solution instabilities.

Rayleigh Numbers

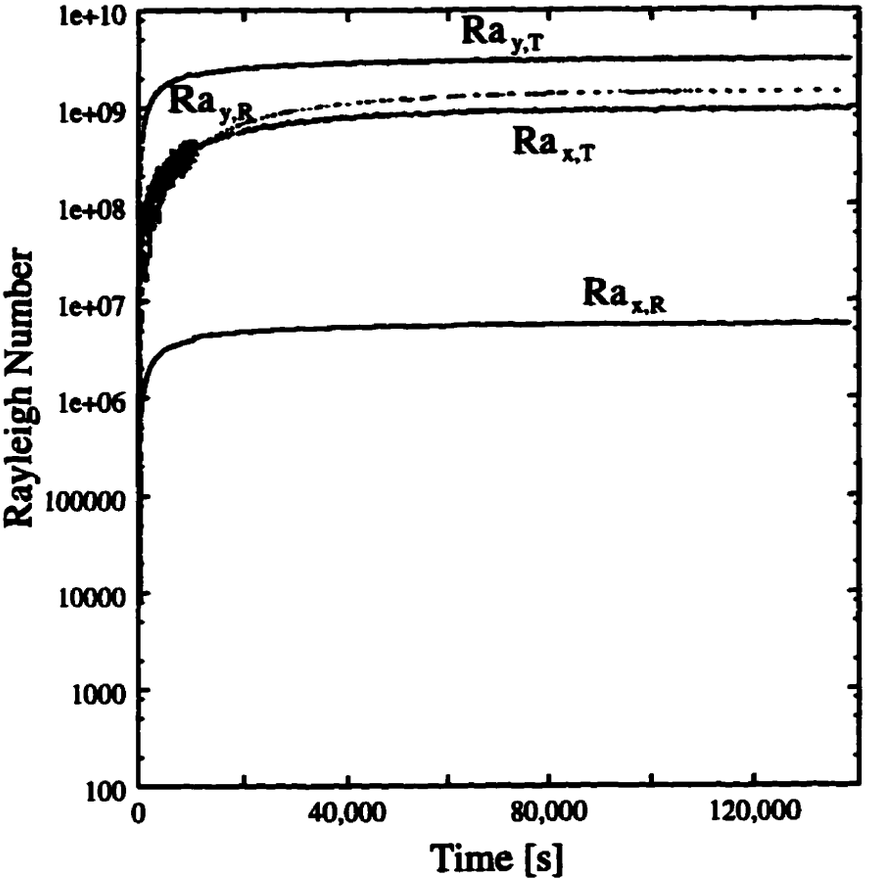

Figure 7.12: Rayleigh numbers evaluated from the two-dimensional transformer flow model: 49 kVA load.

The Rayleigh number is calculated for each oil region using Equation (6.7) by first finding an average temperature for each side. Since two fluid cells seemed to form, one in each region, approximating each as a separate rectangular cavity was considered to be appropriate. The highest Rayleigh number of 3.055×10^9 was found for the top

oil cavity based on calculating the Rayleigh number between horizontal surfaces. The Rayleigh number was also evaluated using the method suggested by Heindel et al. [24] for an array of protruding heat sources;

$$Ra^* = \frac{g\beta}{k_{oil}\alpha_{oil}\nu} q'' h_c^4 \tag{7.23}$$

where h_c is the length of the heat source face, and q'' is the heat flux at the wall on the protruding heat source. Equation (7.23) is arranged in terms of Q''' by letting $q'' = Q''' x_c$.

$$Ra^* = \frac{g\beta}{k_{oil}\alpha_{oil}\nu} Q''' x_c h_c^4 \tag{7.24}$$

This equation gives a Rayleigh number of 2.72×10^{11}. Heindel et al. only considered a Ra^* up to 10^9 for a fluid with a Prandtl number of 25, but in this case transformer oil has a Prandtl number of 167. Heindel et al. [23] stated that a Prandtl number of approximately 167 demonstrates laminar flow up to a $Ra^* = 10^{11}$, but this value may have been influenced by the geometry of Heindel et al.'s model.

Wroblewski and Joshi [64] determined that the turbulence transition Rayleigh number could be determined by $Ra = 10^9 Pr$, using the following definition:

$$Ra = \frac{g\beta Q h_c^2}{\nu \alpha k_{oil}} \tag{7.25}$$

When applied to the Alegi and Black 49 kVA test case, Equation (7.25) gave a Rayleigh number of 7.41×10^{11}, but the turbulence transition Rayleigh number was calculated to be 1.67×10^{11} (from $Ra = 10^9 Pr$).

The turbulence transition Rayleigh number presented by Lage and Bejan [35] shows that the oil flow in the transformer tank may not be turbulent. They use the definition

$$Ra = \frac{g\beta H^3 (T_h - T_c)}{\alpha\nu} \tag{7.26}$$

where H is the height of the cavity. For Prandtl numbers greater than one, they gave the criterion:

$$Ra_{crit} \sim 10^8 Pr^2 \tag{7.27}$$

to determine if the flow was begining to transition to turbulence. This produced a critical Rayleigh number of 2.78×10^{12} for the 49kVA run. The Rayleigh numbers calculated for each the top and side cavities, shown in Table 7.6, show that the oil within the transformer fall well below this criterion. This does not definitely show that there is no turbulence since the models examined by Lage and Bejan are insulated at the top and the bottom, and no upper Pr limit is given for the Rayleigh number criterion.

The Rayleigh numbers calculated for the transformer model cannot be used to accurately determine whether or not the fluid flow is turbulent because of the relatively high oil viscosity and the lack of research results for cavities with non-insulated top and bottom walls. Instead they can be used to show the relative change in Rayleigh number between the runs.

Cavity	T_h rise	T_c rise	Ra
Side	25.5°C	15.2°C	1.41×10^9
Top	22.0°C	17.6°C	1.39×10^9

Table 7.6: Rayleigh number calculated based on Equation (7.26) for the 49 kVA load Alegi and Black simulation case.

Location	Alegi and Black	Calculated from Average Temperature
Core+Windings to Oil	40.3 W/m^{2}K	38.4 W/m^{2}K
Oil to Tank	35.1 W/m^{2}K	35.0 W/m^{2}K
Tank to Ambient	8.05 W/m^{2}K	10.1 W/m^{2}K

Table 7.7: Calculated effective convection coefficients at steady state for the two-dimensional transformer flow model: 49 kVA load.

Convection Coefficients

The average convection heat transfer coefficient for the oil convection around the core and windings is calculated using the average solid temperature and the average oil temperature. The average oil and solid temperatures are calculated by volume weighting each control volume. The results are shown in Table 7.7. The ambient air properties given by Alegi and Black [1], as shown in Table 7.2, do not match the properties given by Incropera and DeWitt [30]. Therefore the latter properties were used in the convection coefficient calculations. The Alegi and Black convection coefficients were calculated based on equations given in Section 7.2.1. The tank-to-ambient effective convection coefficients include the effect of radiation between the tank and the surroundings. The core-and-windings-to-oil and oil-to-tank coefficients predicted by the current work are close to the Black and Alegi values. For this calculation, only the temperature of the oil touching the boundary of the domain was used. This temperature represents a tank temperature because the tank was considered to have negligible thermal resistance. The tank to ambient convection coefficient predicted by the code is the average convection coefficient of the model.

The coefficient for the Alegi and Black model is equal to the convection coefficient boundary condition specified on the right hand side of the comparison model, before it is multiplied by 1.1666 to account for the difference in tank surface areas.

From the calculations, the average tank wall temperature rise above ambient was found to be 16.442°C.

Time Constants

Time constants are calculated for each component of the transformer model using the normalized temperature given in Equation (7.28). The normalized temperature is the regional temperature rise divided by the steady state temperature rise of the region. It can be calculated from the equation,

$$\theta^* = \frac{(T - T_\infty)}{(T_{ss} - T_\infty)} = 1 - e^{-t/\tau} \tag{7.28}$$

The first time constant, $\tau|_{0.632}$, has elapsed when θ^* equals 0.632. It can be determined by solving Equation (7.28) for τ. Two more time constants may be determined by recording the time when θ^* equals 0.865 and 0.950, solving Equation (7.28) for $\tau|_{\theta^*=0.865}$ and $\tau|_{\theta^*=0.950}$, and then dividing these numbers by two and three, respectively. The average time constant is

$$\tau_{avg} = \frac{1}{3}(\tau_{0.632} + \tau_{0.865} + \tau_{0.950}) \tag{7.29}$$

Table 7.8 shows the time constants for each component.

The average of the time constants was then used to compare theoretical first order behavior with the computer code predicted behavior for a number of key temperatures in the transformer. Figure 7.13 shows both the temperature normalized plots of the 49 kVA load run, and a plot of the θ^* function from Equation (7.28) for the average core and winding temperature for $\tau_{avg} = 5.891$ hours. At first, the theoretical

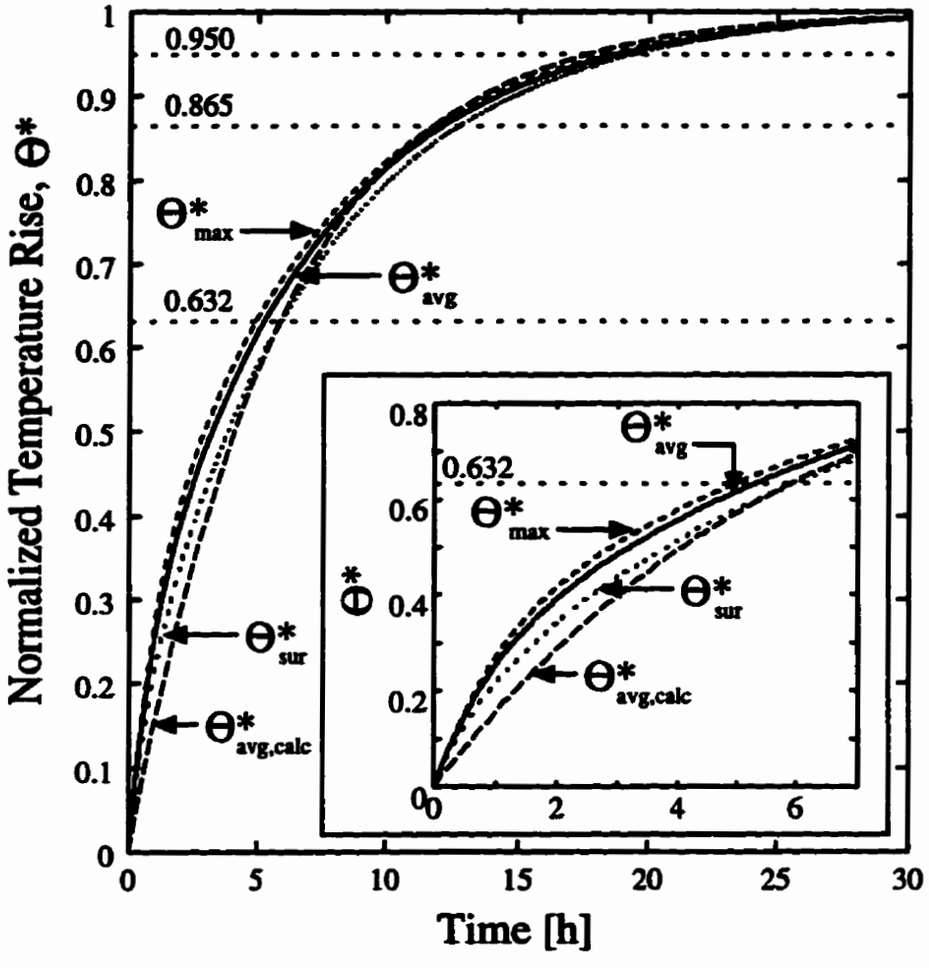

Figure 7.13: Normalized transient temperature to determine the time constants of the core and windings for the two-dimensional transformer flow model: 49 kVA load for the Alegi and Black simulated case. The calculated values were determined from Equation (7.28).

(τ_{avg}) curve increases more slowly than the calculated values. This difference can be explained by the oil not cooling the solid as much for the first few hours. Then the oil heats up and begins to move as the bouyancy forces exceed the gravitational forces. Later, the normalized temperatures slowly converge together at $\theta^* = 1.0$.

Figure 7.14 shows the normalized temperature plots for the oil regions. The theoretical curves predicted for the right and top oil regions give almost the same results, but both are much higher than the computer code values for the first ten hours. The oil is heated by the core and windings. Since the oil does not move very much at first, there is little mixing taking place and the average oil temperature is lower than theoretical curve.

At approximately three hours, there is a point where the computer program predicts a temperature oscillation for the average temperature of the right cavity. This oscillation also exists in the finer grids, as shown in the grid and time independence plots in Appendix C, but the time at which it occurs varies between grids. For the 100×148 grid, the oscillation occurs at approximately 1.4 hours after the load was

Region	$\tau_{0.632}$	$\tau_{0.865}$	$\tau_{0.950}$	τ_{avg}
C+W Average Temperature	5:325 hrs	6.068 hrs	6.280 hrs	5.891 hrs
C+W Maximum Temperature	4.957 hrs	5.920 hrs	6.177 hrs	5.685 hrs
C+W Surface Temperature	5.928 hrs	6.390 hrs	6.477 hrs	6.265 hrs
Top Oil Region Temperature	7.994 hrs	7.425 hrs	7.156 hrs	7.525 hrs
Side Oil Region Temperature	7.789 hrs	7.308 hrs	7.075 hrs	7.391 hrs

Table 7.8: Time constants evaluated from the two-dimensional transformer flow model: 49 kVA load Alegi and Black simulation case.

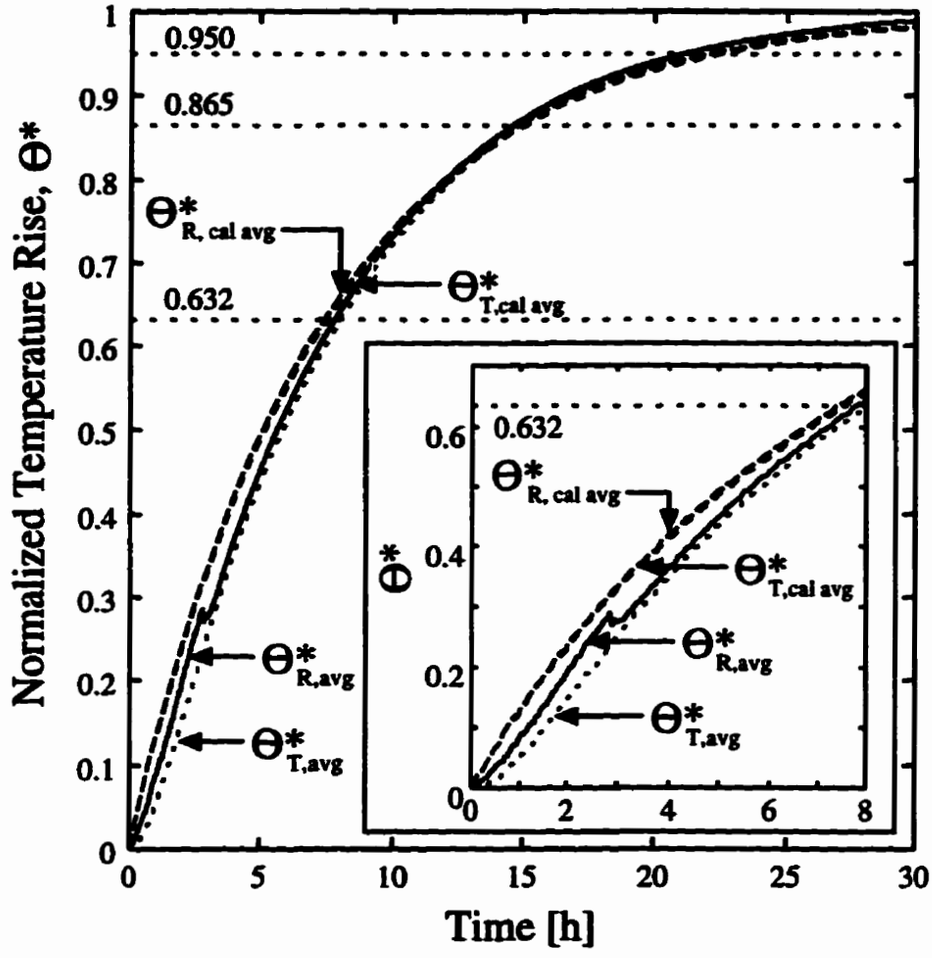

Figure 7.14: Normalized transient temperature to determine the time constants of the side and top oil regions for the two-dimensional transformer flow model: 49 kVA load for the Alegi and Black simulated case. The calculated values were determined from Equation (7.28).

applied. For the 100×102 grid, the oscillation occurs at 2.2 hours. The oscillation is grid dependent, but it is consistently part of the predicted behaviour. Its presence, however, has a negligible effect on the overall temperatures of the transformer model.

Figures 7.13 and 7.14 illustrate that the time constant of the core, windings, and the oil changes throughout the heating process of the transformer. Therefore a typical transformer may not be accurately modelled as a simple first order system.

The deviation of the detailed computer prediction from a simple first order system can be explained if the time constant is written as given by Incropera and DeWitt [30]:

$$\tau_t = \left(\frac{1}{hA_s}\right)(\rho \forall c) = R_t C_t \tag{7.30}$$

The thermal time constant of the solid, τ_t, is given as a function of the resistance to convection heat transfer, $R_t = 1/hA_s$, and the lumped thermal capacitance of the solid, $C_t = \rho \forall c$. Since the properties and the geometry were not allowed to vary in the 49 kVa run, only h changed. When starting with an uniform temperature throughout the domain, there is no convection. As the temperature of the oil near the core increases, so too does the temperature differential between the oil near the core and the oil near the tank. This difference in temperature induces a natural convection flow and thus h increases. The increase in h reduces the value of τ_t, which is consistent with the oil time constant results shown in Table 7.8.

7.2.3 Two-Dimensional Flow Model: 71 kVA Load

After reaching steady state with the 49 kVA run, the load on the transformer was increased to 71 kVA. The steady state results of the 49 kVA load run were used as the initial conditions for the 71 kVA load run. The same grid and time step was used for this test case as in the 49 kVA load run.

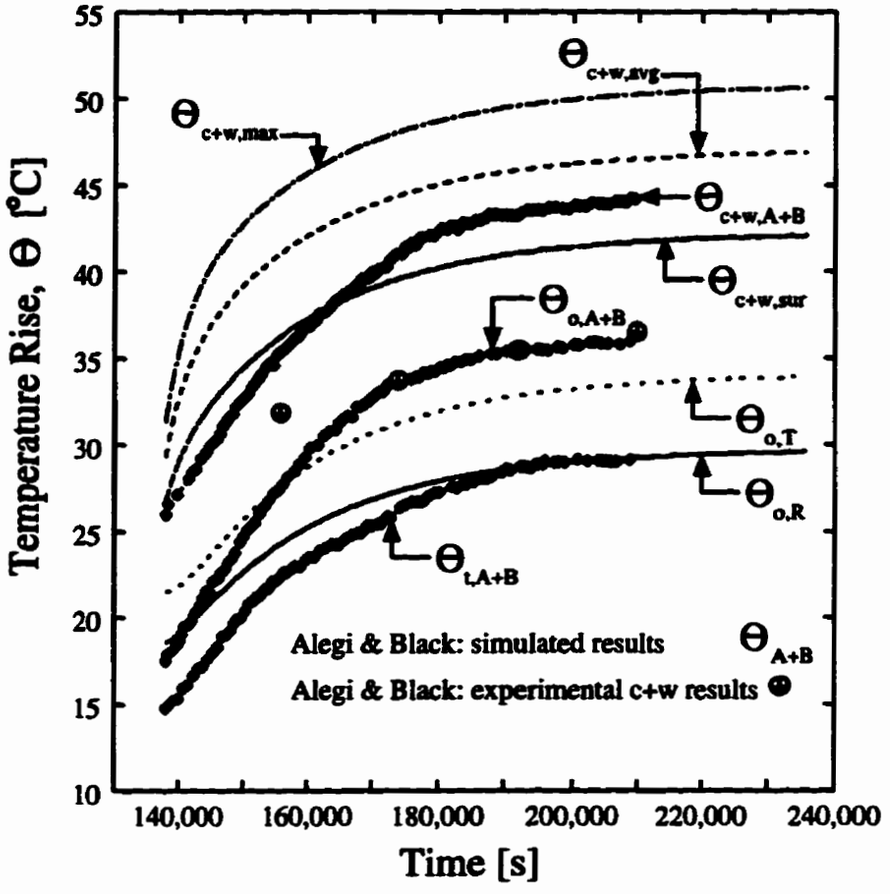

Figure 7.15: Comparison of the 71 kVA load results showing the temperature rise above the ambient temperature of 20°C.

Average Temperature

The transient temperature results are shown in Figure 7.15. The time required for steady-state of the 49 kVA case was not given by Alegi and Black [1], but steady-state conditions were assumed as the starting conditions of the 71 kVA run. For Figure 7.15, the Alegi and Black comparison results were shifted on the x-axis to match up with the steady state time from the present work for the 49 kVA simulation. The results

show that the Alegi and Black average core and winding temperature plot is bounded between the computer code calculated average core and winding temperature and the average surface temperature. This means that the temperatures calculated by the code come reasonably close to the results of Alegi and Black. Although it is not shown in the Figure 7.15, the calculated average oil temperatures for the right and top regions come closer to the Alegi and Black experimental temperature results than the values prediced by Alegi and Black for the oil. The oil experimental results are close to the calculated average tank temperature shown in the plot. The maximum temperature was found to be within the core and windings. The location of the maximum temperature moved from control volume (0 m, 0.13125 m) to (0 m, 0.10625 m), and then back to (0 m, 0.11875) relative to the lower left corner of the domain.

Temperature and Streamline Plots

Figure 7.16 shows the temperature field plots every ten seconds at "steady state". There is very little change in the temperature fields between intervals. The only noticeable changes are the small temperature fluctuations directly above the core and windings.

The streamline plots, Figures 7.17 to 7.18 show the changes in the fluid flow above the core and windings every five seconds. The flow pattern is changing slightly with time. It was also observed in this case that the changes in the flux patterns did not repeat itself in a regular, periodic way.

Heat Flow

Figure 7.19 shows the heat flow, normalized by the generated heat, out each face of the tank. The heat flow profiles are similiar to the results shown in Figure 7.10 for the 49 kVA run except that heat flow through the bottom of the tank does not exceed

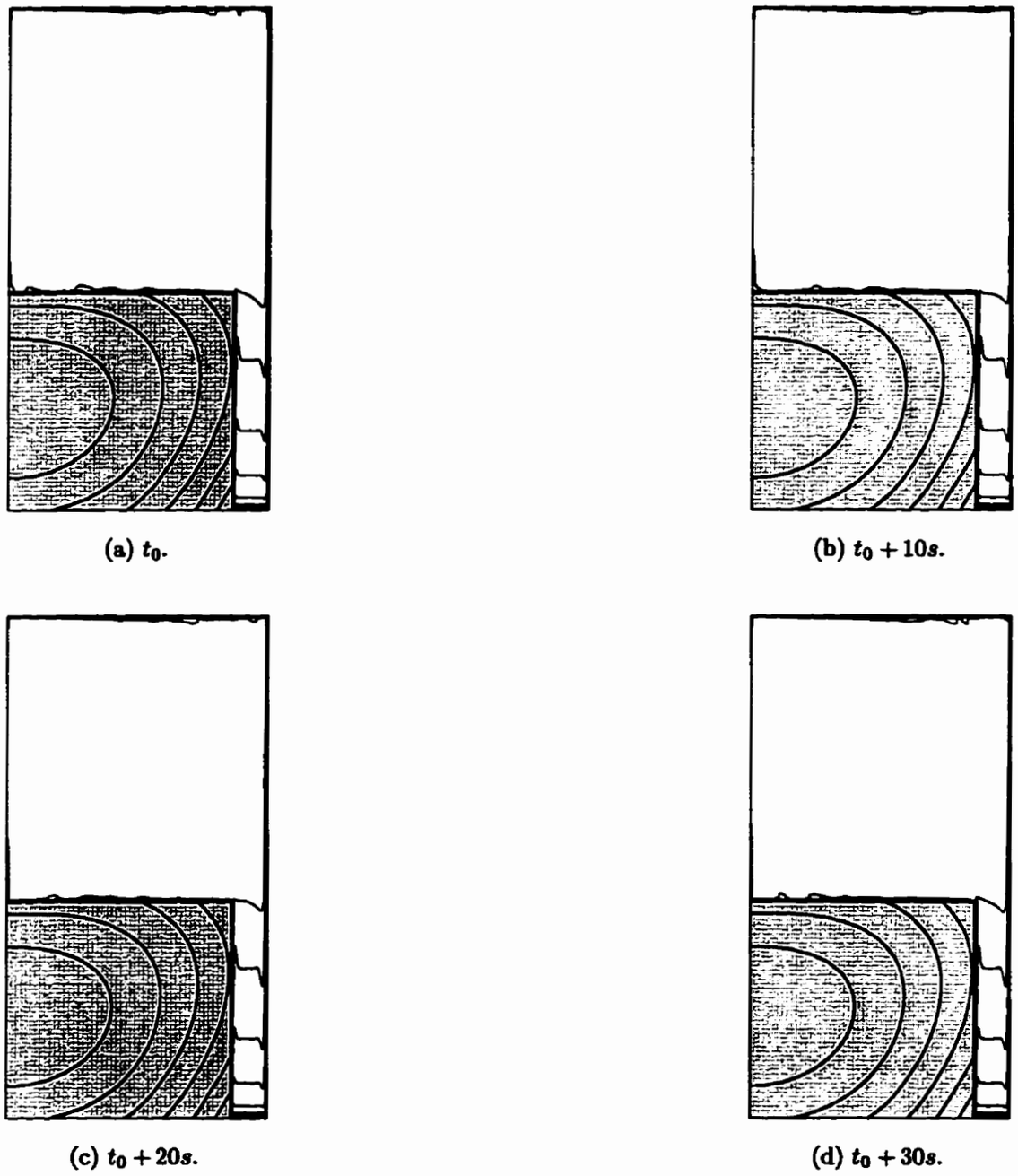

(a) t_0.

(b) $t_0 + 10s$.

(c) $t_0 + 20s$.

(d) $t_0 + 30s$.

Figure 7.16: Elapsed time temperature results at steady state; starting from a datum of $t_0 = 235,675$ seconds for the 71 kVA Alegi and Black simulation case.

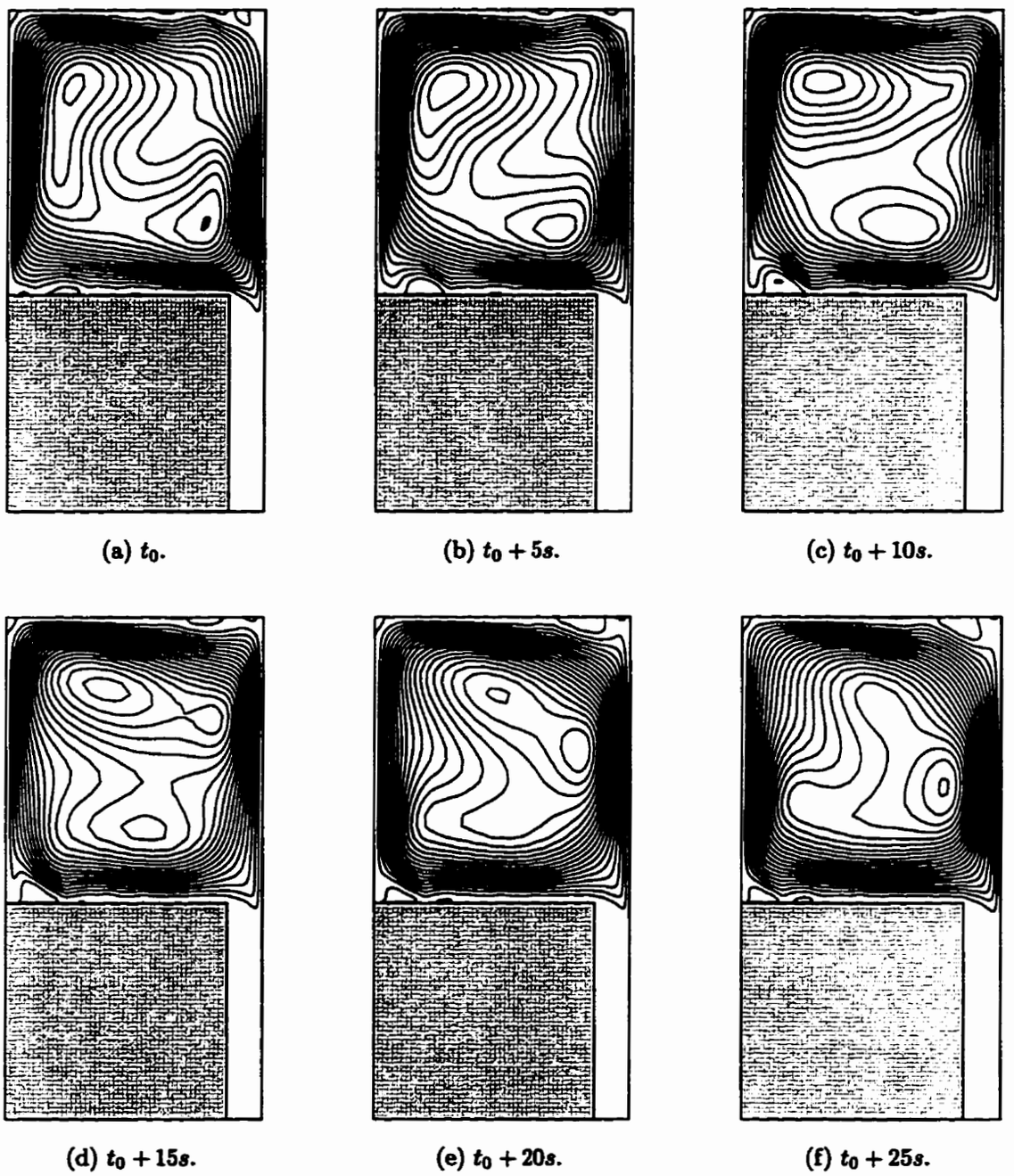

(a) t_0. (b) $t_0 + 5s$. (c) $t_0 + 10s$.

(d) $t_0 + 15s$. (e) $t_0 + 20s$. (f) $t_0 + 25s$.

Figure 7.17: Elapsed time streamline results at steady state; starting from a datum of $t_0 = 235,675$ seconds for the 71 kVA Alegi and Black simulation case.

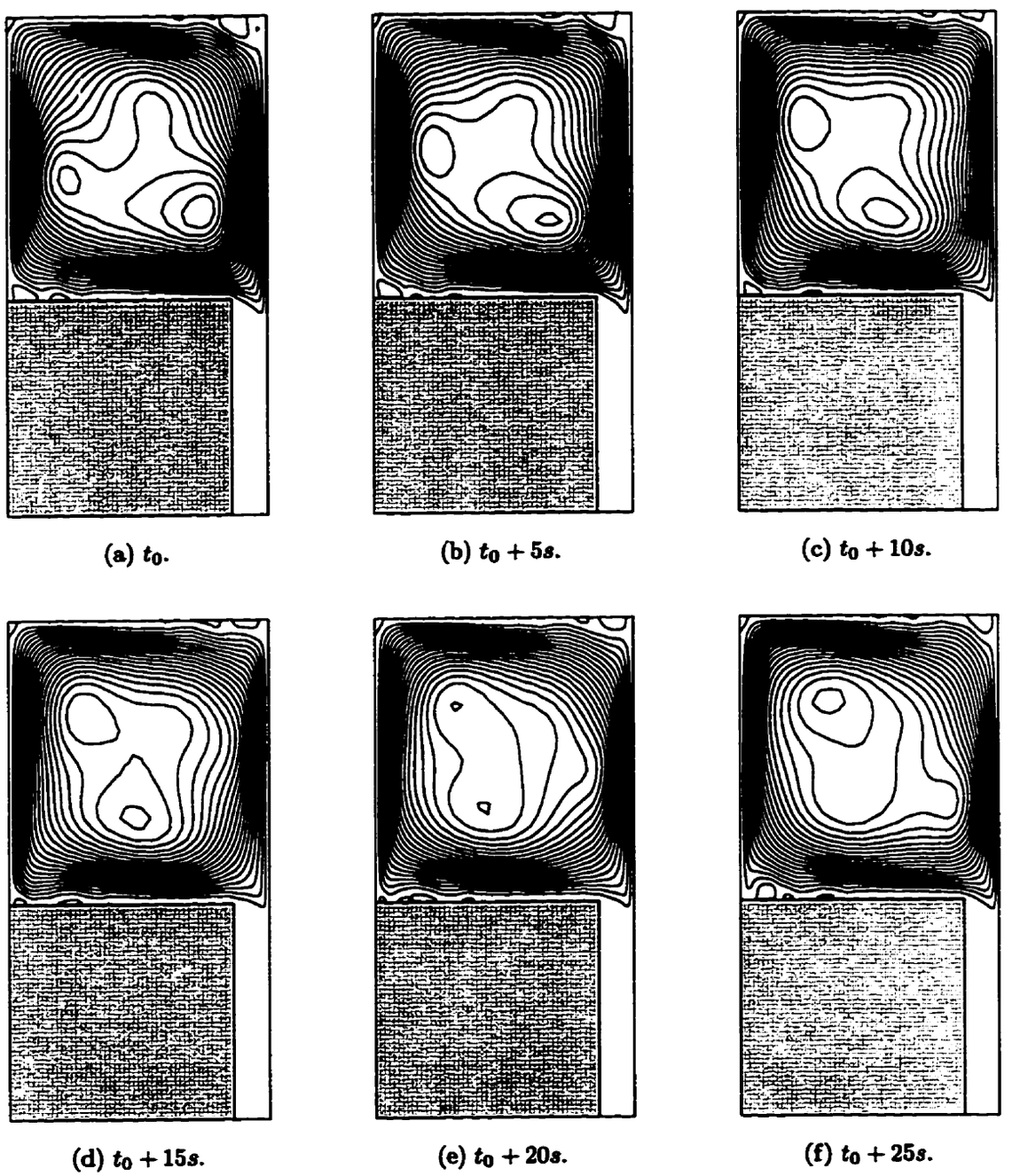

(a) t_0. (b) $t_0 + 5s$. (c) $t_0 + 10s$.

(d) $t_0 + 15s$. (e) $t_0 + 20s$. (f) $t_0 + 25s$.

Figure 7.18: Elapsed time streamline results at steady state; starting from a datum of $t_0 = 235,705$ seconds for the 71 kVA Alegi and Black simulation case.

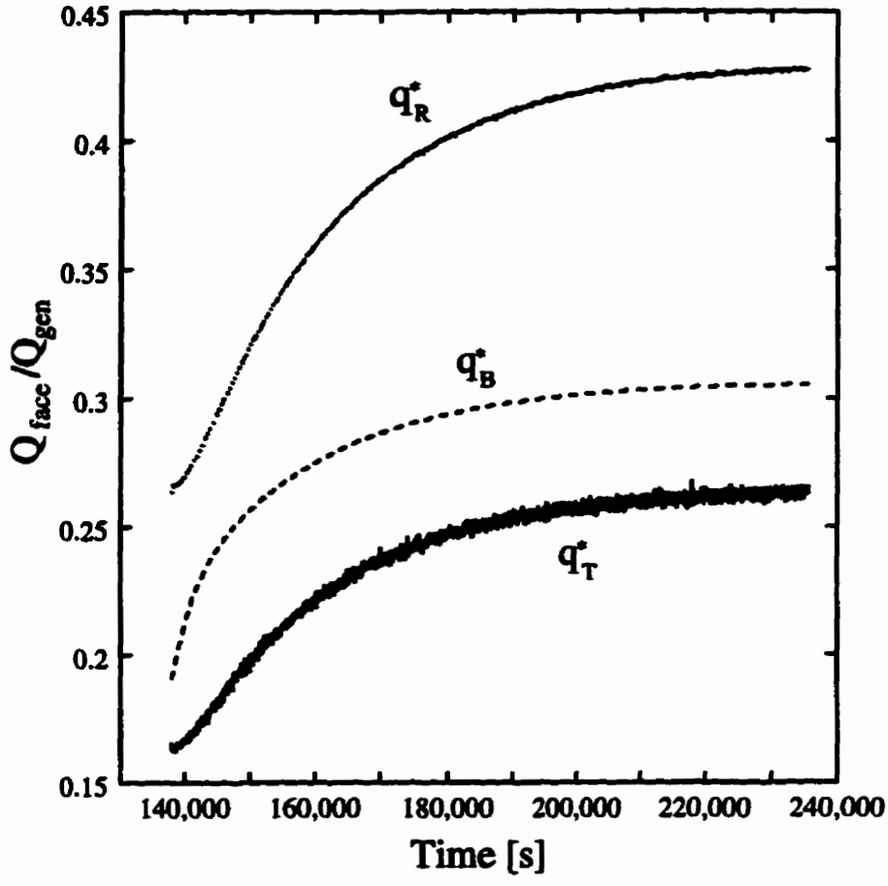

Figure 7.19: Normalized tank surface heat flow for the two-dimensional transformer flow model: 71 kVA load.

the flow out the side during any time of the run. The total ratio of heat leaving the tank to the heat being generated within the core and windings was 0.9978 when the run was terminated.

Steady State Check

The results of the steady state heat flow check is shown in Figure 7.20. As the transformer solution field approaches steady state convergence, the heat flow oscillations

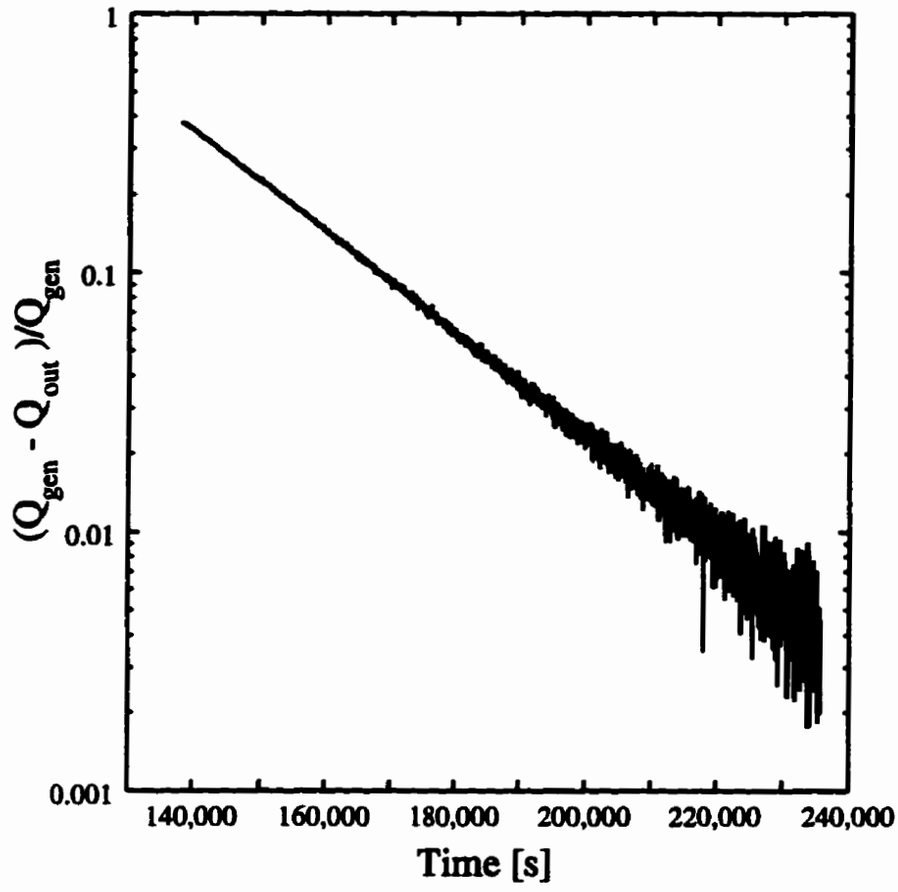

Figure 7.20: Steady state heat flow check for the two-dimensional transformer flow model: 71 kVA load.

increased. The results satisfied Equation (7.21) even though it does not appear as such from Figure 7.20. The steady state convergence criterion was met eight time steps after the last result was recorded. The steady state check, based on the average temperature change, showed oscillations similiar to those found in the 49 kVA load run. The convergence tests were both satisified to a level of 10^{-5} at approximately 150,000 seconds, or 41.7 hours, after the 71 kVA load was applied.

Rayleigh Numbers

Figure 7.21 shows that the highest Rayleigh number of 8.305×10^9 is found for the top oil cavity using the calculation for a Rayleigh number between horizontal surfaces. Table 7.9 shows the results of calculating the Rayleigh number using the different

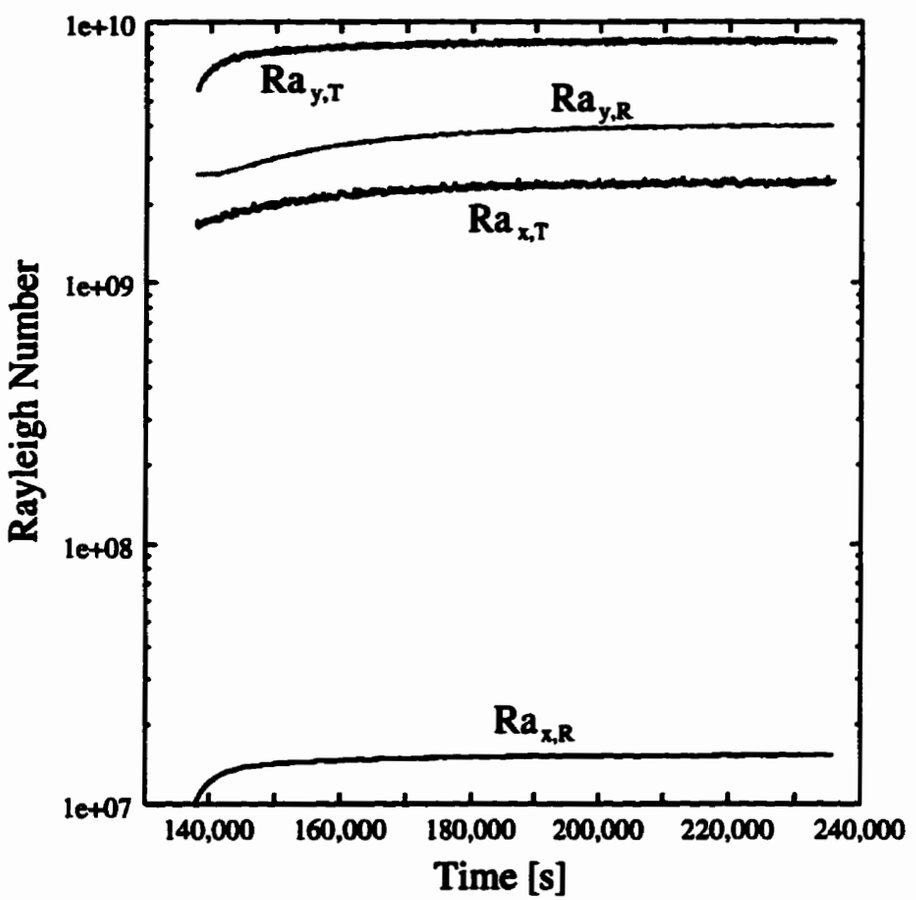

Figure 7.21: Rayleigh numbers evaluated from the two-dimensional transformer flow model: 49 kVA.

methods discussed earlier. According to the different criteria for transition some Rayleigh numbers show that the oil flow may be turbulent, and others show that the flow is still laminar. Again, the results are not conclusive because none of hte results from the literature matches the boundary conditions and Prandtl number of the situation in this work.

	Heindel et al. [24]	Wroblewski and Joshi [64]		Lage and Bejan [35]	
Cavity	Ra	Ra	Ra_{crit}	Ra	Ra_{crit}
Side	N/A	N/A	N/A	3.74×10^9	1.06×10^{12}
Top	N/A	N/A	N/A	3.64×10^9	1.06×10^{12}
Entire Domain	8.85×10^9	2.41×10^{12}	1.03×10^{11}	N/A	N/A

Table 7.9: Rayleigh numbers calculated based on several different methods from literature for the 71 kVA load run.

Convection Coefficients

The average convection coefficient results are shown in Table 7.10. The Alegi and Black values are calculated based on equations given in Section 7.2.1. Unlike in the 49 kVA load case, the core and windings to oil coefficient predicted by the code is 23% lower than the Black and Alegi approximation. The present model also predicted a higher convection coefficient from the oil to the tank than Alegi and Black. The value predicted by the code is higher than the Alegi and Black calculations by a factor of 1.247 (compared to the 1.1666 surface are ratio correction factor that was multiplied to the boundary conditions). This difference in convection coefficients shows that the Alegi and Black correlations do not compare well with the detailed computer model

Location	Black and Alegi	Calculated from Average Temperature
Core+Windings to Oil	54.9 W/m^{2}K	42.3 W/m^{2}K
Oil to Tank	37.9 W/m^{2}K	43.7 W/m^{2}K
Tank to Ambient	9.46 W/m^{2}K	11.8 W/m^{2}K

Table 7.10: Calculated effective convection coefficients at steady state for the two-dimensional transformer flow model: 71 kVA load Alegi and Black simulation case.

under these conditions.

The average tank wall temperature rise above ambient was equal to 26.380°C.

7.3 Parametric Study

After comparing the computer model with the results of Alegi and Black [1], the next step was to examine the sensitivity of the model to changes in a few selected parameters. The purpose of this parametric study was to determine the effects of ambient conditions, variable oil viscosity, and the manner in which the core and windings are modelled (i.e. homogeneous or nonhomogeneous), on the results of the transformer simulation. Because a single simulation requires approximately two to three weeks of CPU time on a Sun Microsystems Sparc station 20, the parametric study was limited to twelve cases. The transformer two-dimensional flow model used for these runs is the same as the one described in the previous section, except that the load was changed to 50 kVA and 75 kVA, both starting from ambient conditions.

Table 7.11 shows the various cases considered in the parametric study. The runs

Run	Load		$k_x = k_y$		$\mu(T)$		T_∞		Final Results
	(50 kVA)	(75 kVA)	yes	no	no	yes	30°C	−5°C	Figure Number
A1	X		X		X		X		Figure 7.22
A2	X		X			X	X		Figure 7.23
A3	X			X	X		X		Figure 7.24
A4	X			X		X	X		Figure 7.25
B1		X	X		X		X		Figure 7.26
B2		X	X			X	X		Figure 7.27
B3		X		X	X		X		Figure 7.28
B4		X		X		X	X		Figure 7.29
C2	X		X			X		X	Figure 7.30
C4	X			X		X		X	Figure 7.31
D2		X	X			X		X	Figure 7.32
D4		X		X		X		X	Figure 7.33

Table 7.11: Parametric study run matrix.

were categorized into four groups, and labelled *A*, *B*, *C*, or *D*. Runs *A* and *B* are setup with an ambient temperature of 30°C, and runs *C* and *D* are at a temperature of −5°C. Simulations *A* and *C* are loaded at 50 kVA, and *B* and *D* are loaded at 75 kVA. Runs C1, C3, D1, and D3, were not included because, by the matrix in Table 7.11, the results would be equal to A1, A3, B1, B3, respectively, since they are all insensitive to absolute temeperatures (i.e. viscosity is not a function of temperature).

The transformer was assumed to be a 55°C rise transformer based on the 71 kVA test run in the previous section because the average winding temperature rise

was not more than 50°C and the hottest-spot winding rise was not more than 65°C. Table 7.12 shows the assumed transformer characteristics at rated load as determined by ANSI [3]. Note that the tiem constant given for the hottest spot temperature is much lower than the 5.7 hours calculated during the run loaded at 49 kVA.

Average Winding Rise	55°C
Hottest Spot Conductor Temperature Rise	65°C
Top-Oil Temperature Rise	45°C
Top-Oil Time Constant	3.0 hr
Hottest Spot Conductor Time Constant	0.0834 hr

Table 7.12: Assumed transformer characteristics at rated load from Table 3 in ANSI [3].

The same boundary conditions as the 71 kVA Alegi and Black comparison model were used for the entire parametric study. The uniform initial temperature of the entire transformer was set equal to the ambient temperature of the run.

7.3.1 Properties

To simplify the parametric study, the properties and the ambient conditions were evaluated at one representative temperature for all runs (referred to here as the baseline temperature). Using the ANSI predicted rises above ambient, the expected average top-oil temperature at steady state is 57.5°C, and average winding temperature is 67.5°C. The average top-oil baseline temperature was determined by adding the

Region	k_x $[W/m^2K]$	k_y $[W/m^2K]$	ρ $[kg/m^3]$	c_p $[J/kgK]$	μ $[Ns/m^2]$	β
Core	42.179	42.179	2982.2	459.42	N/A	N/A
L.V. Winding	0.91564	3.39345	2966.0	603.22589	N/A	N/A
H.V. Winding	0.38667	2.12779	2482.5	844.91925	N/A	N/A
Oil	0.10777	0.10777	861.86	1879.9	5.5086×10^{-3}	0.00072

Table 7.13: Properties for the nonhomogeneous model.

top-oil rise (45°C) to the ambient temperatures, and then calculating the average oil temperature for all runs. The average winding baseline temperature was determined by adding the average winding rise to the ambient temperature, then the average between the two ambient conditions was taken. The temperature correction in the ANSI loading guides for ambient temperatures below 30°C was not used. The oil properties are determined based on the property correlations provided by Alegi and Black at 57.5°C. For some of the runs (cases A2, A4, B2, B4, C2, C4, D2, and D4), the viscosity was allowed to change as a function of temperature.

Table 7.13 shows the properties used for all the nonhomogeneous, anisotropic core and windings cases (i.e. cases A3, A4, B3, B4, C4, and D4). The thermal properties of the windings were calculated using the equivalent circuits method discussed in Appendix D. The winding conductor is assumed to have a rectangular cross-section. The constant heat flow thermal circuit (Equations (D.8) and (D.12)) was selected because the parallel isotherm circuit created a higher thermal resistance than would be expected. Since the parallel isotherm circuit is a series of parallel subcircuits, if one parallel subcircuit had a high thermal resistance (i.e. the paper insulation) it would dramatically increase the overall resistance of the circuit. Instead, with a constant heat flow circuit, most of the energy would be able to "flow around" the areas of higher thermal resistance. All the winding properties are evaluated at 67.5°C. The

Dimension	L.V. Winding	H. V. Winding
conductor - width (A_y)	0.490 m	0.0885 m
conductor - thickness (A_x)	0.265 m	0.0636 m
paper thickness - around conductor ($t_x = t_y$)	0.007 m	0.0017 m
paper thickness - between layers (P_x)	0.020 m	0.020 m

Table 7.14: Dimensions assumed for the square conductor windings.

assumptions for the winding dimensions are shown in Table 7.14. These dimensions are based on the conductor dimensions of an existing 50 kVA transformer with square conductor windings [14]. The winding conductor is copper, and since the oil-saturated paper has properties close to oil, the paper properties are assumed to equal that of oil. For the nonhomogeneous test case, the region representing the core and windings is divided equally into two: the core on the left and the windings on the right. The windings are further divided into two halves: low voltage windings on the left and high voltage windings on the right. Since the same grid was to be used for all runs, the region divisions were made as close as possible to the grid boundaries. In the final configuration, the width of the core was 0.1275 m, the low voltage winding wide was 0.06417 m, and the high voltage winding width was 0.05833 m.

The properties of the solid for the homogeneous cases are summarized in Table 7.15. The windings are first lumped together using equivalent circuits. For the x direction, the harmonic mean of the two thermal conductivities was taken. For the y direction, the average thermal conductivity of the two windings is used. In this calculation, the winding thermal conductivity was taken as the average of the x and y direction thermal conductivities. The harmonic mean is calculated between the core and the final winding thermal conductivity to get the thermal conductivity of a

Region	k [W/m K]	ρ [kg/m^3]	c_p [J/kg K]
Core + Windings	3.1798	2854	591.75

Table 7.15: Properties for the homogeneous solid regions.

homogeneous core and windings model. The specific heat is volume-averaged for the solid. Although the density for the core and windings remained at 2854 kg/m^3 for the homogenous cases, densities for each component are required for the nonhomogeneous cases. For the nonhomogeneous cases, the overall mass of the core and windings was maintained by adjusting the densities of each solid so that the total mass of the core and windings would equal the measured value of Alegi and Black.

Power generation is treated differently between the homogeneous and nonhomogeneous test cases. For the homogeneous cases, the power generation was calculated using Equation (7.11) and yielded 3,588 W/m^3 for the 50 kVA load run and 7,035 W/m^3 for the 75 kVA load run. For the nonhomogeneous cases, the core generated 1,615 W/m^3. The windings were each assumed to generated the same amount of energy; 5,642 W/m^3 for the 50 kVA load run and 12,677 W/m^3 for the 75 kVA load run.

7.3.2 Results of Parametric Study

This subsection details the results of the parametric study. Figures 7.22 through to 7.33 each show the transient temperature history of the transformer runs and a plot of the steady-state temperature contours. The temperature contour plots are for qualitative discussion of the temperature gradients within the transformer and to indicate the location of the hotspot. In the case where the core and windings solid

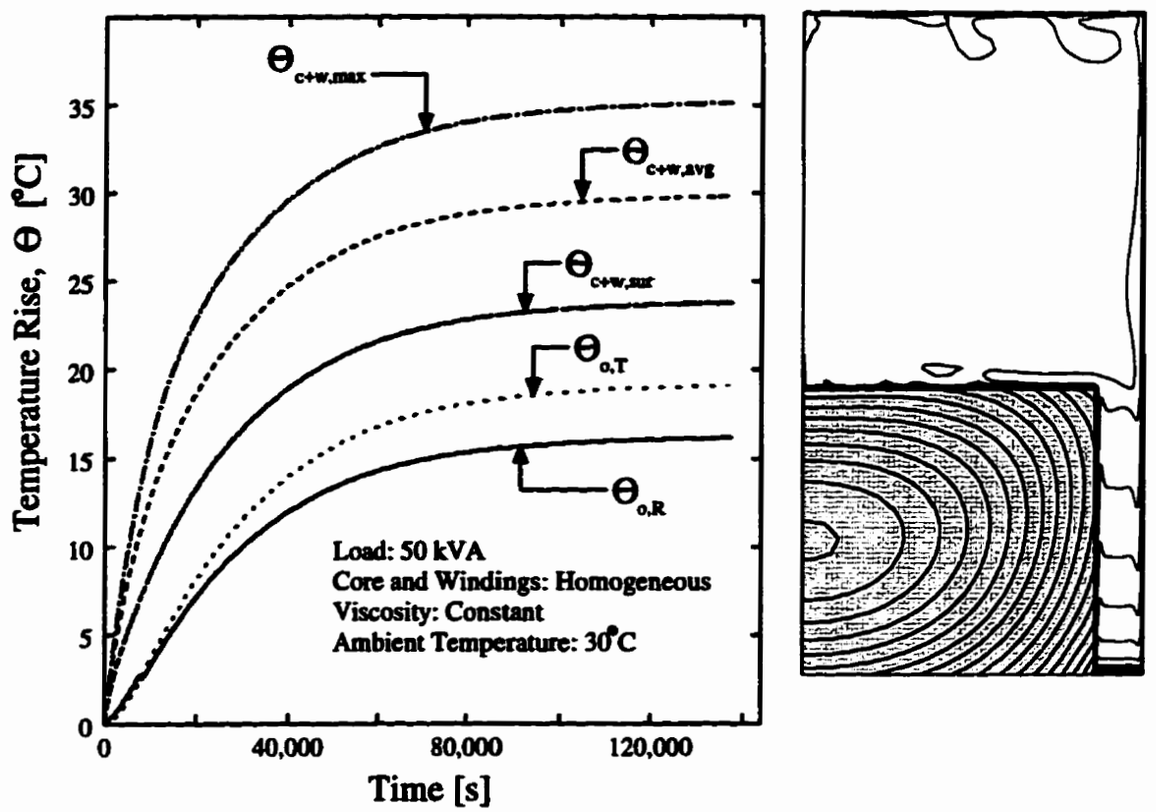

(a) Temperature rise with time. (b) Temperature contours.

Figure 7.22: Parametric study case A1: transient temperature rise results and temperature contours at t = 137,435 seconds.

is not homogeneous, the hot-spot temperature moved from the model symmetry line to a location within the windings. The hot spot location is approximately half way from the top of the windings in all cases. In literature, experimental results indicate that the hotspot is usually located down one third from the top of the windings.

The transient temperature history shows that the general trends are similiar for all cases. For the non-homogeneous solid cases the average temperature of the windings

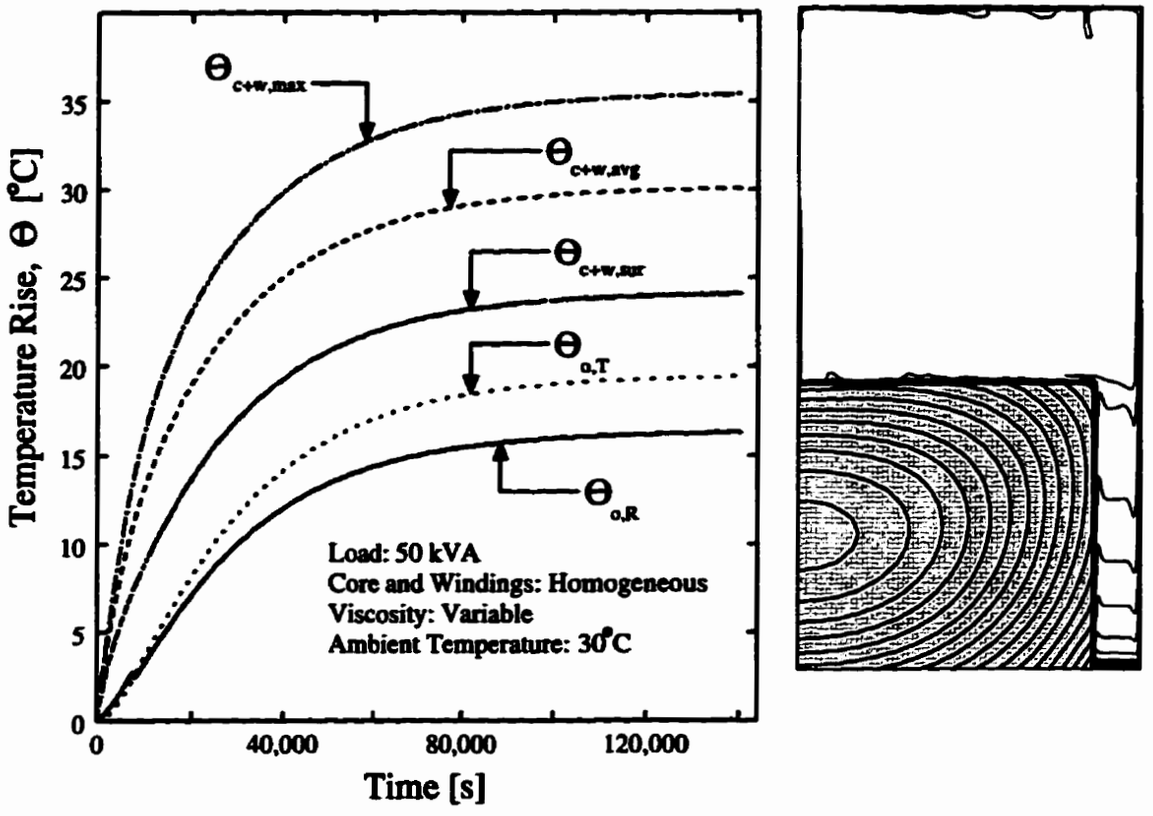

(a) Temperature rise with time. (b) Temperature contours.

Figure 7.23: Parametric study case A2: transient temperature rise results and temperature contours at time = 140,415 seconds.

is plotted along with the average temperature of both the core and windings together to show the relative difference between the two. Table 7.16 shows the steady state temperature rises above ambient. Those results indicate that the effect of variable viscosity, instead of a constant viscosity, on the steady state temperature rise is at most a 3°C difference. The final location of the hotspot for the runs is approximately in the same location for all the homogeneous core and windings cases. The location, although different, was also the same for all the nonhomogeneous core and windings runs. The effect of the nonhomogeneous core and windings was only to shift the

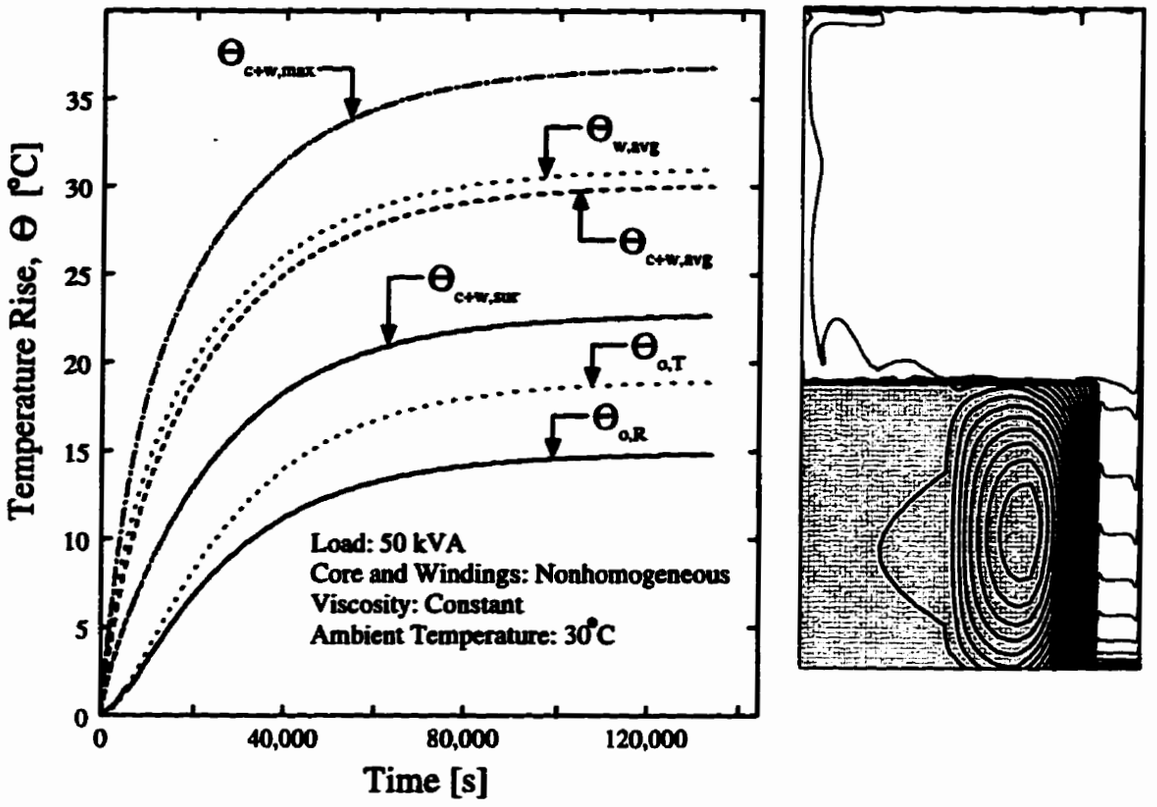

(a) Temperature rise with time. (b) Temperature contours.

Figure 7.24: Parametric study case A3: transient temperature results and temperature contours at time = 133,989 seconds.

hotspot location horizontally (from the homogeneous test case position) so that the hotspot was located within the windings. The hotspot temperature was also predicted to be higher for the nonhomogeneous runs.

Table 7.17 shows the simulated time required for the transformers to reach steady state, and the normalized heat flow outside the tank walls. The table shows that the runs with an ambient temperature of −5°C took significantly longer to reach steady state than the 30°C runs. Another observation is that the variable viscosity test cases required a less time to reach steady state than their constant viscosity counterparts.

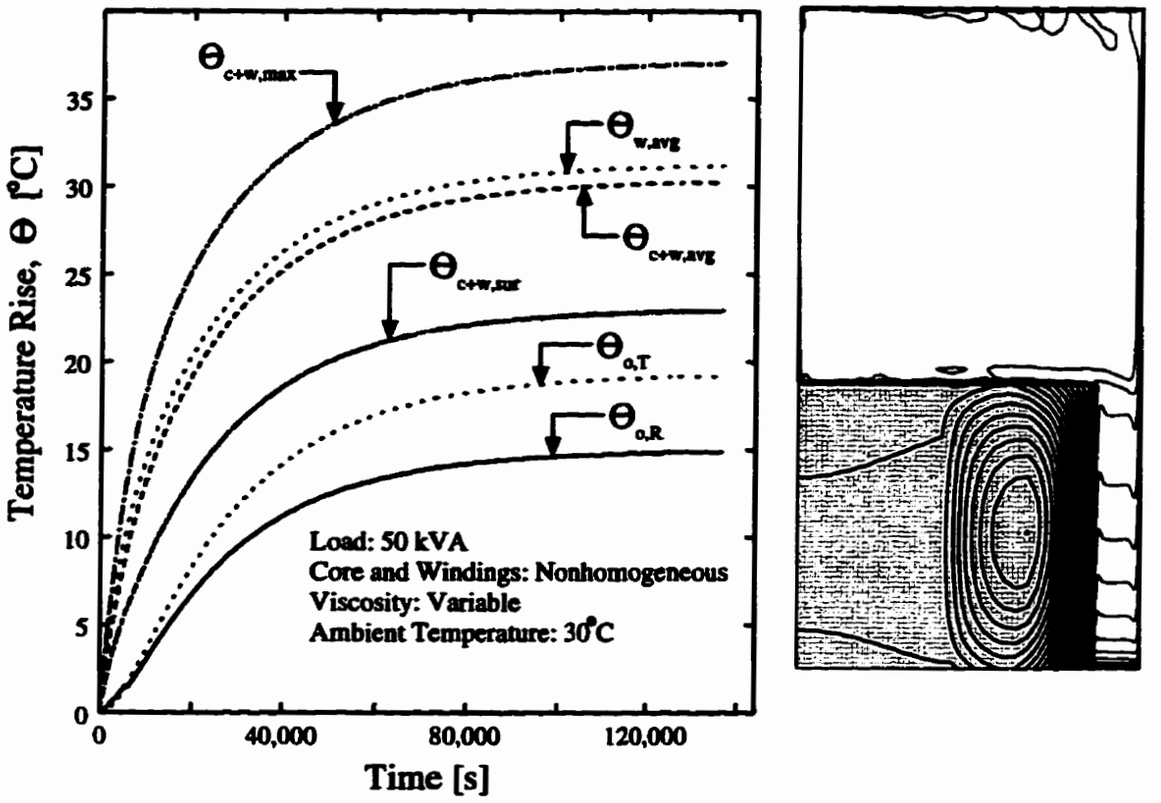

(a) Temperature rise with time. (b) Temperature contours.

Figure 7.25: Parametric study case A4: transient temperature results and temperature contours at time = 136,755 seconds.

The basic trends for all the normalized heat flow (q_{face}/q_{gen}) are basically the same between all the runs. The steady state values for the flows out each face are very similiar.

Table 7.18 shows Rayleigh numbers calculated from Equation (6.7) by using the average temperature of each side of the fluid region. The Rayleigh number of the variable viscosity runs are calculated based on the average viscosity. The results show that the Rayleigh number of the 50 kVA load run was equal to approximately half of the Rayleigh number of the 75 kVA load run.

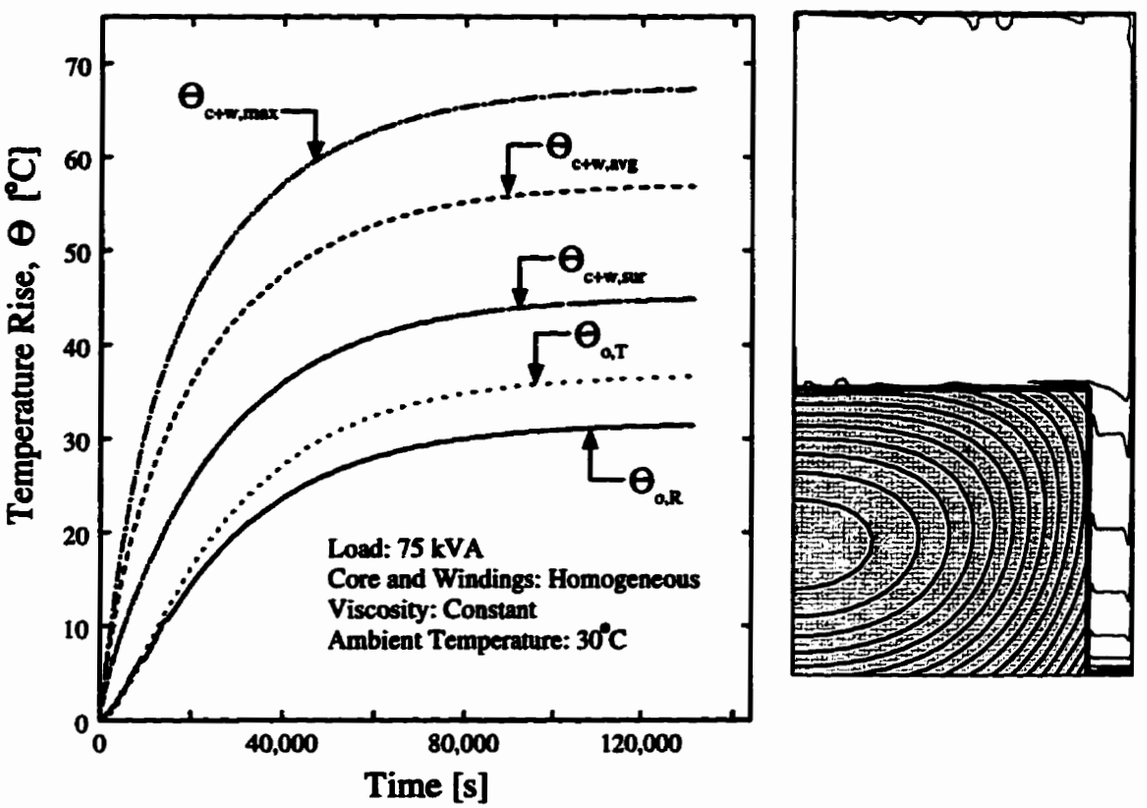

(a) Temperature rise with time. (b) Temperature contours.

Figure 7.26: Parametric study case B1: transient temperature results and temperature contours at time = 131,512 seconds.

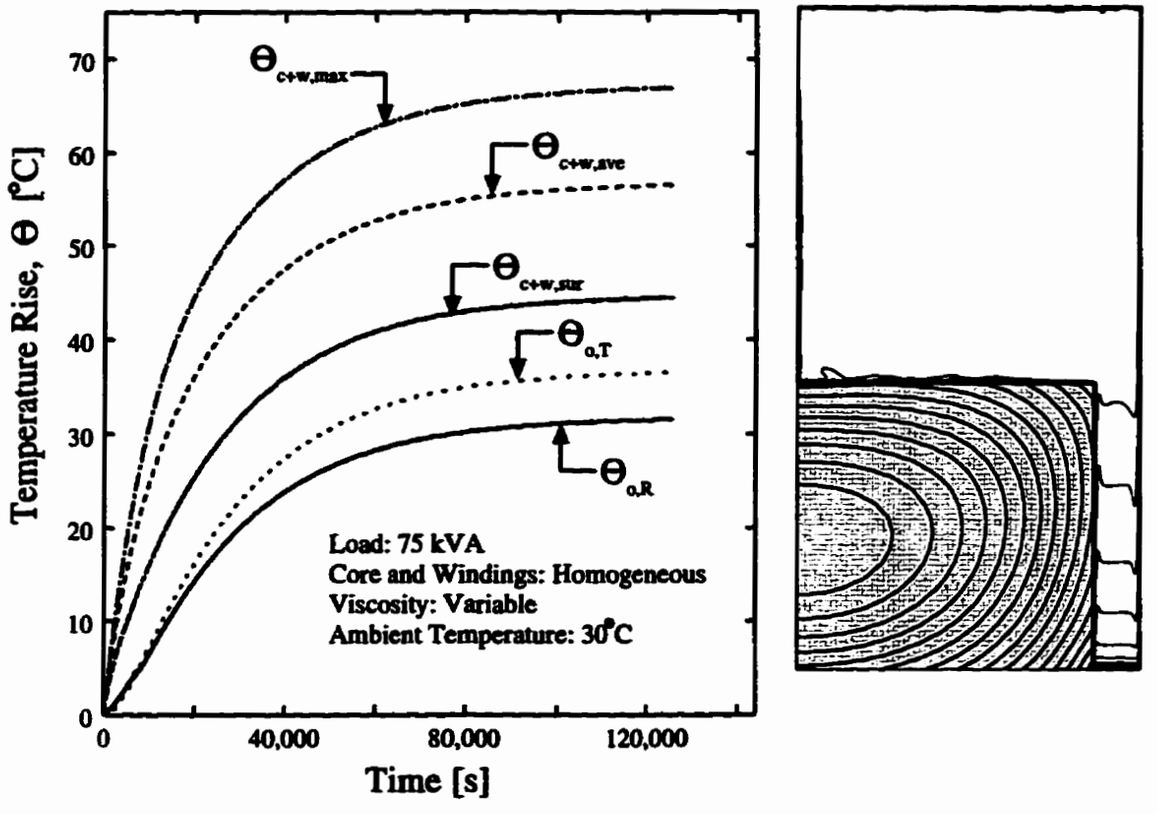

(a) Temperature rise with time. (b) Temperature contours.

Figure 7.27: Parametric study case B2: transient temperature results and temperature contours at time = 125,649 seconds.

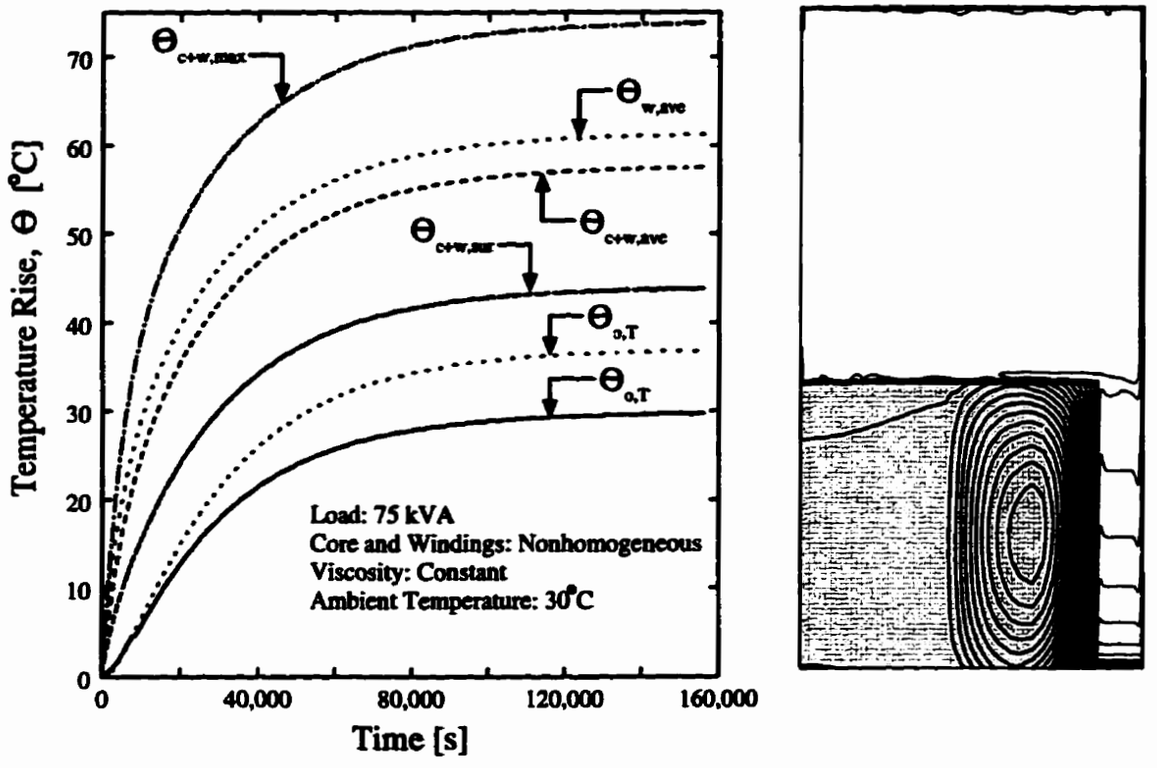

(a) Temperature rise with time. (b) Temperature contours.

Figure 7.28: Parametric study case B3: transient temperature results and temperature contours at time = 156,142 seconds.

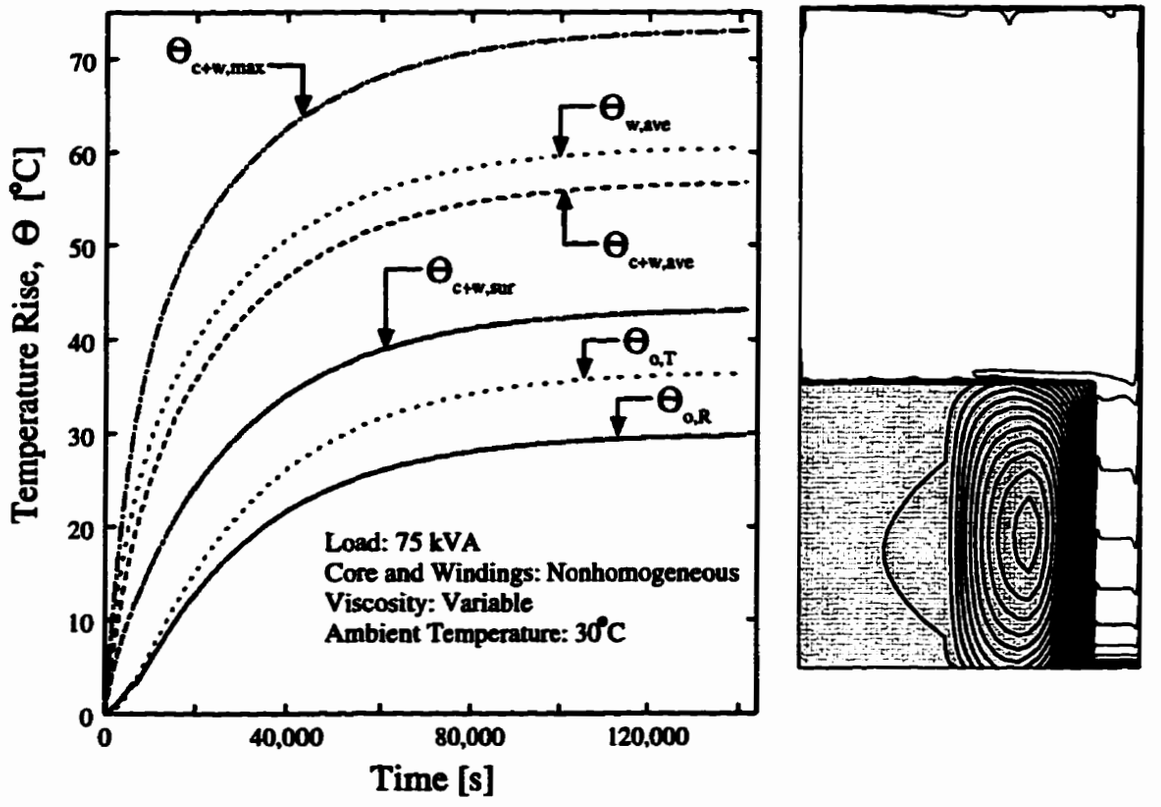

(a) Temperature rise with time. (b) Temperature contours.

Figure 7.29: Parametric study case B4: transient temperature results and temperature contours at time = 141,447 seconds.

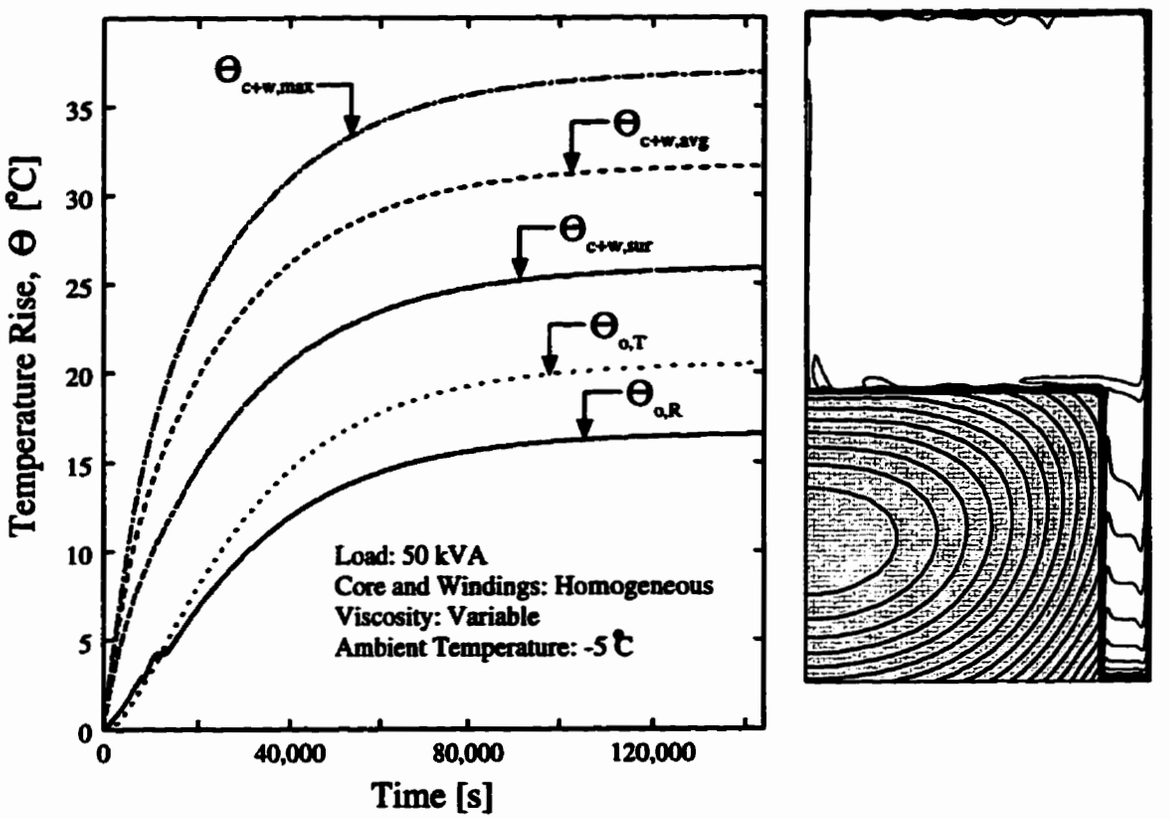

(a) Temperature rise with time. (b) Temperature contours.

Figure 7.30: Parametric study case C2: transient temperature results and temperature contours at time = 145,226 seconds.

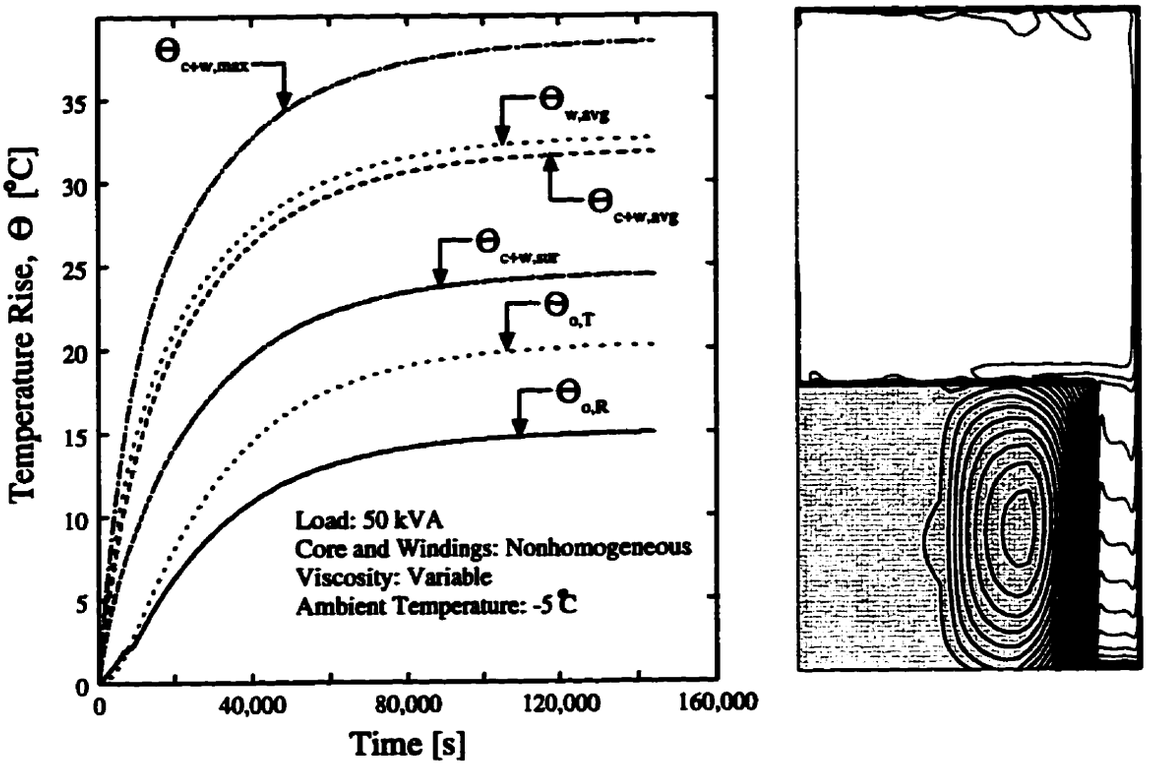

(a) Temperature rise with time.

(b) Temperature contours.

Figure 7.31: Parametric study case C4: transient temperature results and temperature contours at time = 144,197 seconds.

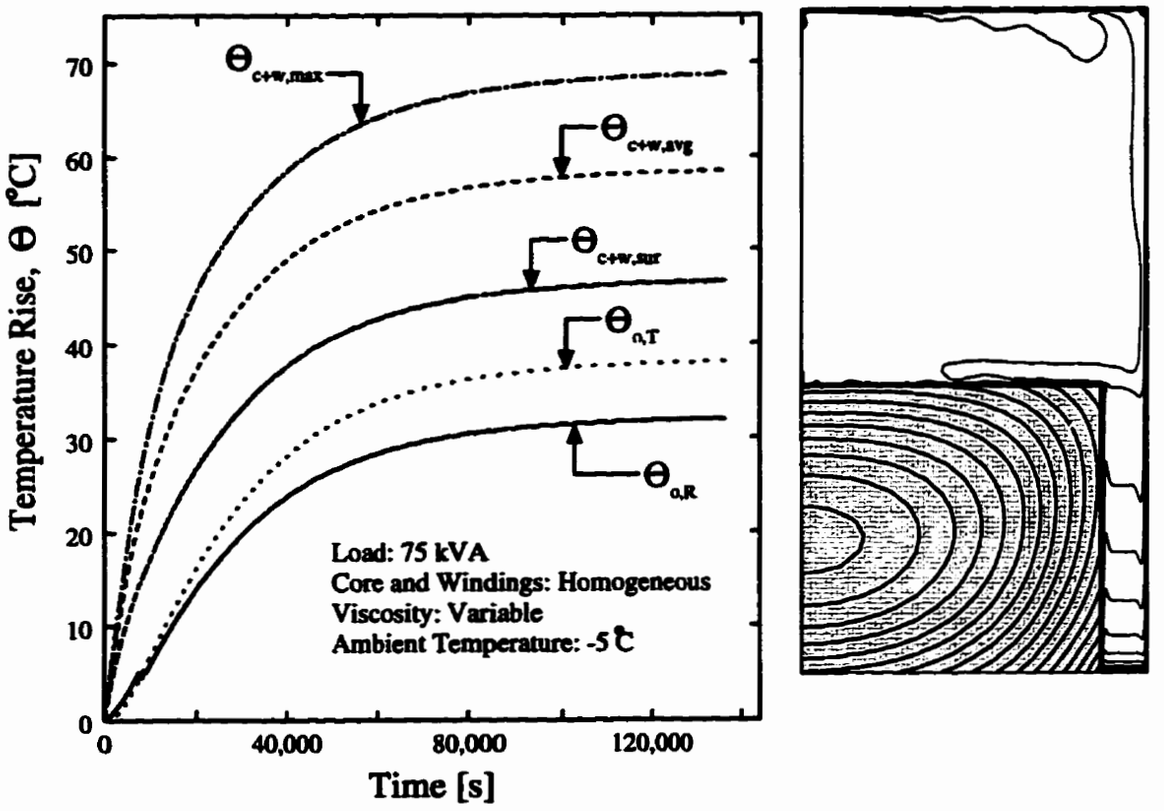

(a) Temperature rise with time. (b) Temperature contours.

Figure 7.32: Parametric study case D2: transient temperature results and temperature contours at time = 136,109 seconds.

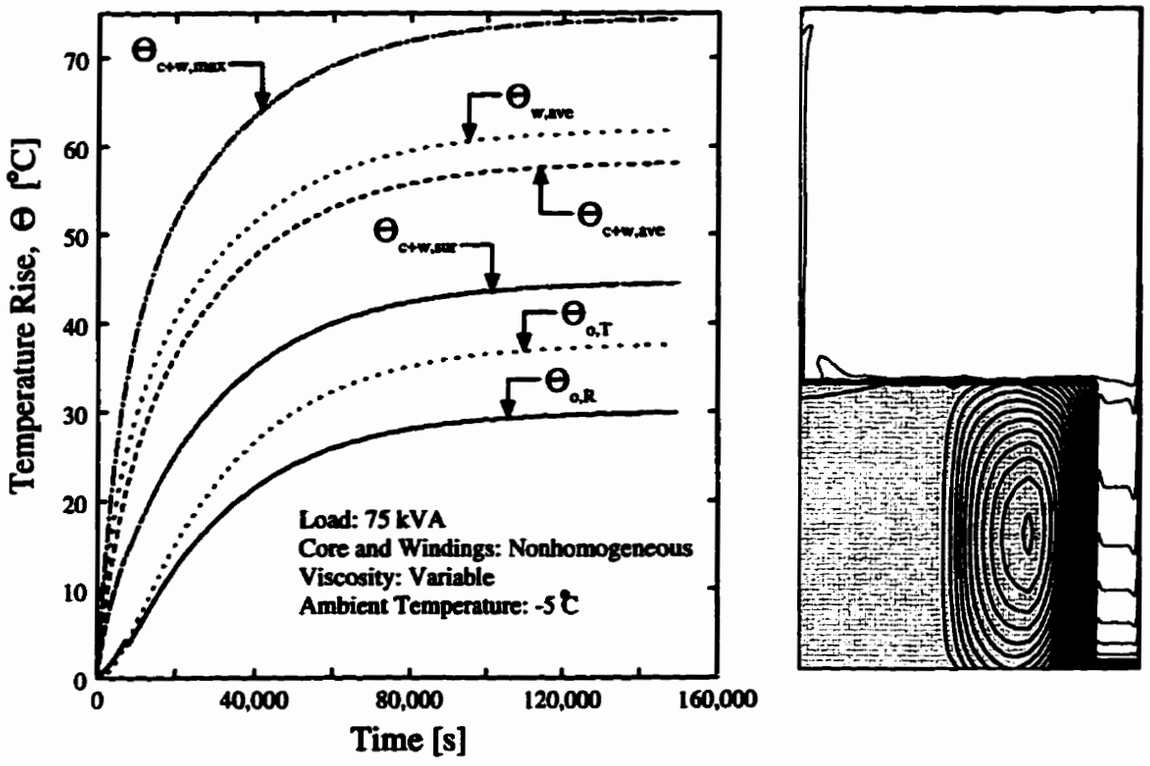

(a) Temperature rise with time. (b) Temperature contours.

Figure 7.33: Parametric study case D4: transient temperature results and temperature contours at time = 149,545 seconds.

Run	Side Oil	Top Oil	Core & Windings		Windings Only
	θ_{avg}	θ_{avg}	θ_{avg}	θ_{max}	θ_{avg}
A1	16.15°C	19.11°C	29.82°C	35.13°C (0.000 m, 0.119 m)	N/A
A2	16.28°C	19.42°C	30.10°C	35.40°C (0.000 m, 0.119 m)	N/A
A3	14.81°C	18.94°C	30.03°C	36.77°C (0.196 m, 0.119 m)	30.95°C
A4	14.88°C	19.24°C	30.28°C	37.01°C (0.196 m, 0.119 m)	31.19°C
B1	31.43°C	36.63°C	56.89°C	67.26°C (0.000 m, 0.119 m)	N/A
B2	31.54°C	36.50°C	56.53°C	66.92°C (0.000 m, 0.119 m)	N/A
B3	29.68°C	36.83°C	57.49°C	73.77°C (0.196 m, 0.119 m)	61.17°C
B4	29.74°C	36.41°C	56.68°C	73.02°C (0.196 m, 0.119 m)	60.42°C
C2	16.57°C	20.50°C	31.64°C	36.91°C (0.000 m, 0.119 m)	N/A
C4	14.95°C	20.23°C	31.79°C	38.45°C (0.187 m, 0.119 m)	32.63°C
D2	32.01°C	38.11°C	58.41°C	68.72°C (0.000 m, 0.119 m)	N/A
D4	29.88°C	37.58°C	58.04°C	74.32°C (0.196 m, 0.119 m)	61.74°C

Table 7.16: Parametric study temperature rise results.

Run	Steady State Time (hours)	Normalized Heat Out-Flow			
		Left Face	Right Face	Bottom Face	Top Face
A1	38:10:35	0.000	0.418	0.317	0.264
A2	39:00:15	0.000	0.417	0.320	0.262
A3	37:13:09	0.000	0.404	0.335	0.259
A4	37:59:15	0.000	0.402	0.337	0.260
B1	36:31:52	0.000	0.422	0.312	0.265
B2	34:54:09	0.000	0.423	0.310	0.265
B3	43:22:22	0.000	0.411	0.326	0.262
B4	39:17:27	0.000	0.412	0.322	0.264
C2	40:20:26	0.000	0.406	0.332	0.262
C4	40:03:17	0.000	0.388	0.352	0.259
D2	37:48:29	0.000	0.417	0.318	0.265
D4	41:32:25	0.000	0.407	0.329	0.263

Table 7.17: Parametric study steady state heat flow distribution.

Run	Side Oil Cavity		Top Oil Cavity	
	Ra_x	Ra_y	Ra_x	Ra_y
A1	9.361×10^6	2.719×10^9	1.617×10^9	5.722×10^9
A2	6.826×10^6	1.933×10^9	1.375×10^9	4.568×10^9
A3	6.762×10^6	2.985×10^9	1.662×10^9	6.253×10^9
A4	4.773×10^6	2.025×10^9	1.379×10^9	4.884×10^9
B1	1.636×10^7	5.000×10^9	2.778×10^9	9.893×10^9
B2	1.761×10^7	5.591×10^9	3.377×10^9	1.249×10^{10}
B3	9.377×10^6	3.893×10^9	2.017×10^9	7.644×10^9
B4	1.155×10^7	5.149×10^9	3.092×10^9	1.172×10^{10}
C2	2.157×10^6	5.261×10^8	4.767×10^8	1.460×10^9
C4	1.521×10^6	5.160×10^8	4.888×10^8	1.519×10^9
D2	6.373×10^6	1.795×10^9	1.495×10^9	4.713×10^9
D4	5.368×10^6	2.113×10^9	1.652×10^9	5.620×10^9

Table 7.18: Parametric study Rayleigh number results.

7.4 Comparison with ANSI

The last comparison made in this work was between the results obtained from the two-dimensional transformer flow model and from the ANSI loading guides. The only parameters required to determine the ANSI loading guide for the present runs are the magnitude of the overload and the duration of the overload. The loading guides will then give the maximum temperature rise of the transformer and the maximum top oil rise.

These simulations are meant as an initial investigation of how the two-dimensional transformer flow model predictions compare to the ANSI loading guides. This is the beginning of work to address the question of how to use the new detailed thermal model prediction relative to the established ANSI guide.

7.4.1 Model Setup

As shown in Table 7.19, there were four test cases analyzed for comparison with the loading guides. The runs were divided up into two categories: uniform viscosity and variable viscosity. The core and windings were modelled as non-homogeneous, as described for the parametric study model.

First, the two transformer models were run to steady state at 50% load (corresponding to an energy generation rate of $3.169 \times 10^3\,\mathrm{W/m^3}$) for each of the two viscosity conditions. Each of the steady state results was then used as the initial condition for both transformer step loading cases. For each category, the transformer was subjected to a sudden increase in power, to 260% of the nameplate rating ($85.70 \times 10^3\,\mathrm{W/m^3}$). This is illustrated in Figure 7.34. One run subjected the transformer model to the step increase for a duration of one hour. The other step overload lasted for two hours.

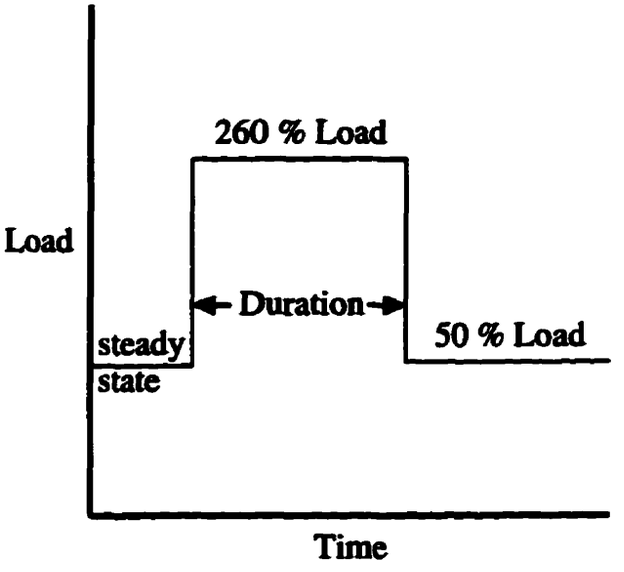

Figure 7.34: Step loading the transformer.

Run	Viscosity	Duration of Overload
ANSI1	constant	1 hour
ANSI2	constant	2 hour
ANSI3	variable	1 hour
ANSI4	variable	2 hour

Table 7.19: Breakdown of runs used for the ANSI load guides comparison.

The approximate transformer model is identical to the two-dimensional transformer flow model used for comparison with the results of Alegi and Black, as described in Section 7.2. The ambient temperature was set to 0°C. The temperature at which the properties were evaluated was determined by assuming that the transformer

is a 55°C rise transformer and then finding the maximum hottest spot temperature and highest average oil temperature predicted for these conditions. Using the maximum temperature rise predicted by ANSI for the one hour power step up as the basis for the material properties, the oil properties were calculated for 65°C. Assuming that the average core and windings temperature is ten degrees below the hottest-spot temperature (as given for 100% name plate load conditions; shown in Table 7.12) the properties of the core and windings were evaluated at 147°C. The Alegi and Black property correlations, shown in Table 7.2, were used to get most property values (except density which was determined from Incropera and DeWitt [30]). The ambient boundary conditions are the same as those used for the 71 kVA load Alegi and Black comparison test case. Table 7.20 shows a summary of the properties.

Region	k_x $[W/m^2K]$	k_y $[W/m^2K]$	ρ $[kg/m^3]$	c_p $[J/kgK]$	μ $[Ns/m^2]$	β
Core	41.71	41.71	2959.9	500.3	N/A	N/A
L.V. Winding	0.90869	3.36741	2998.5	658.43	N/A	N/A
H.V. Winding	0.38374	2.11152	2450.4	954.15	N/A	N/A
Oil	0.10062	0.10062	731.88	2274.4	1.1831×10^{-3}	0.00072

Table 7.20: Properties for the ANSI loading guide comparison model.

7.4.2 Results

The results of the four ANSI comparison runs are summarized in Table 7.21. Figures 7.35 to 7.38 show the transient temperature response of each run. A vertical line is drawn on each plot to show where the overload is removed and the transformer is once again loaded at 50% of the nameplate rating.

Run	Max. T Rise at 50% Power	Avg. Top Oil Rise at 50% Power	Max. T Rise		Max. Top Oil Rise		
			ANSI	Present Work	ANSI	Present Work	
						After Overload	Max.
ANSI1	23.6°C	12.6°C	157°C	144.0°C	65°C	21.9°C	31.8°C
ANSI2	23.57°C	12.6°C	187°C	214.5°C	95°C	39.2°C	50.49°C
ANSI3	25.12°C	13.6°C	157°C	145.5°C	65°C	22.8°C	33.0°C
ANSI4	25.12°C	13.6°C	187°C	216.1°C	95°C	40.6°C	51.8°C

Table 7.21: Average temperature rise over ambient temperature; results for the ANSI comparison runs.

The first two columns of Table 7.21 show the steady state temperatures of the 50% nameplate loading computer simulation. The maximum temperature rise is the highest temperature rise of the entire domain, and it is located within the windings. The table entry labelled, *Avg. Top Oil Rise*, corresponds to the average temperature of the top fluid region. The results show that the addition of variable viscosity (ANSI3 and ANSI4) only increases the temperatures by less than 2°C.

The next two columns, labelled *Max. T Rise*, show the maximum temperature of the windings at the time when the overload is removed. The computer code results are compared with the ANSI loading guide predictions. The computer model predicted a 13°C lower maximum temperature than ANSI for the one hour overload. Variable viscosity only increases the maximum temperature rise by 1.5°C. For the two hour overload, the computer model predicts a 28°C higher temperature than ANSI. Having viscosity change as a function of temperature again only causes a small increase in temperature. With only four test cases to work with, it is difficult to determine what is the cause of the discrepancies in maximum temperature rise. It may be because the Alegi and Black 75 kVA transformer does not follow the predictions of a 55°C rise transformer very well. It is apparent that more work is required.

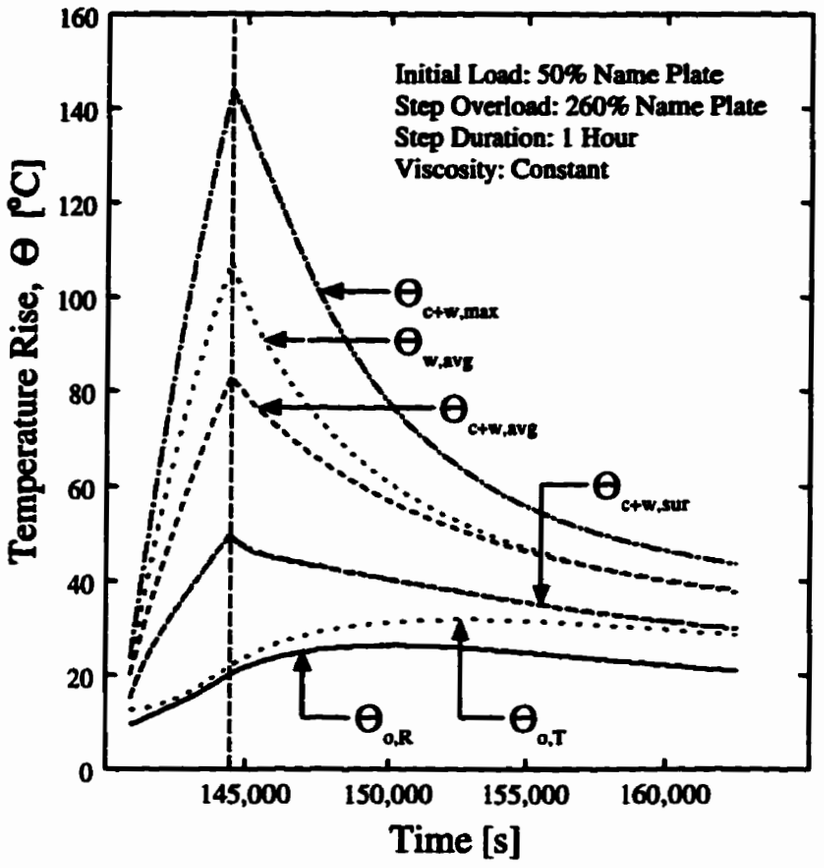

Figure 7.35: Transient temperature monitoring for run ANSI1.

The last three columns of Table 7.21 show the effect of the overload on the top oil. The computer code predicted maximum top oil rise temperatures much lower than ANSI. The code calculates the top oil temperature by calculating the average oil temperature for the top region (Figure 7.3 shows the location for the calculated parameters).

Figures 7.35 to 7.38 show that the oil continues to increase in temperature up to two and a half hours after the overload is removed. The ANSI loading guides predict a much higher top oil temperature than the present model. The results from

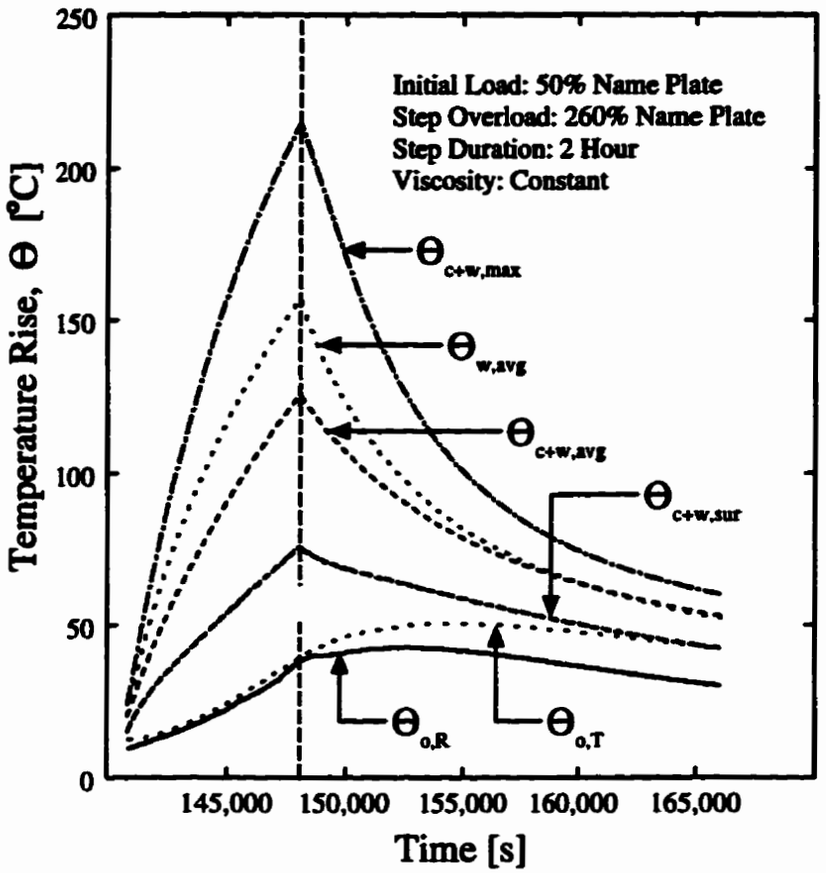

Figure 7.36: Transient temperature monitoring for run ANSI2.

the variable viscosity cases are closer to the ANSI guide values than the results for the constant viscosity cases. The dependence of the viscosity on temperature causes the oil average temperature to rise faster since higher viscosity fluid is more resistant to bouyant forces. This in turn reduces the ability of the oil to remove heat to the ambient conditions outside the tank. It is difficult to determine the accuracy of the top oil temperature since this parameter is not well defined in literature.

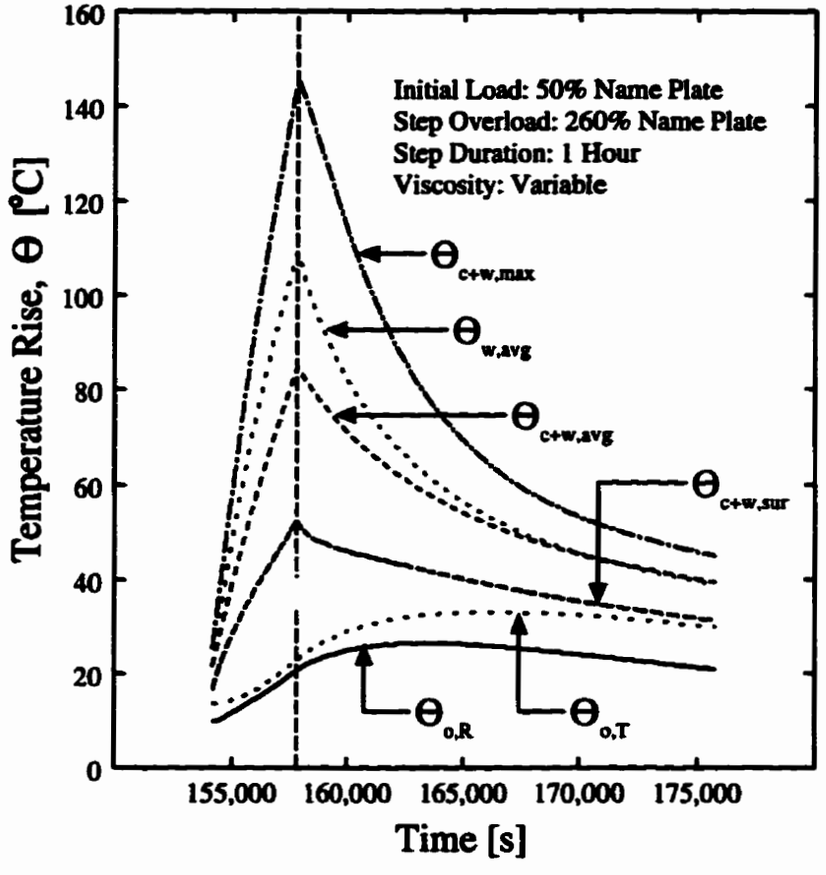

Figure 7.37: Transient temperature monitoring for run ANSI3.

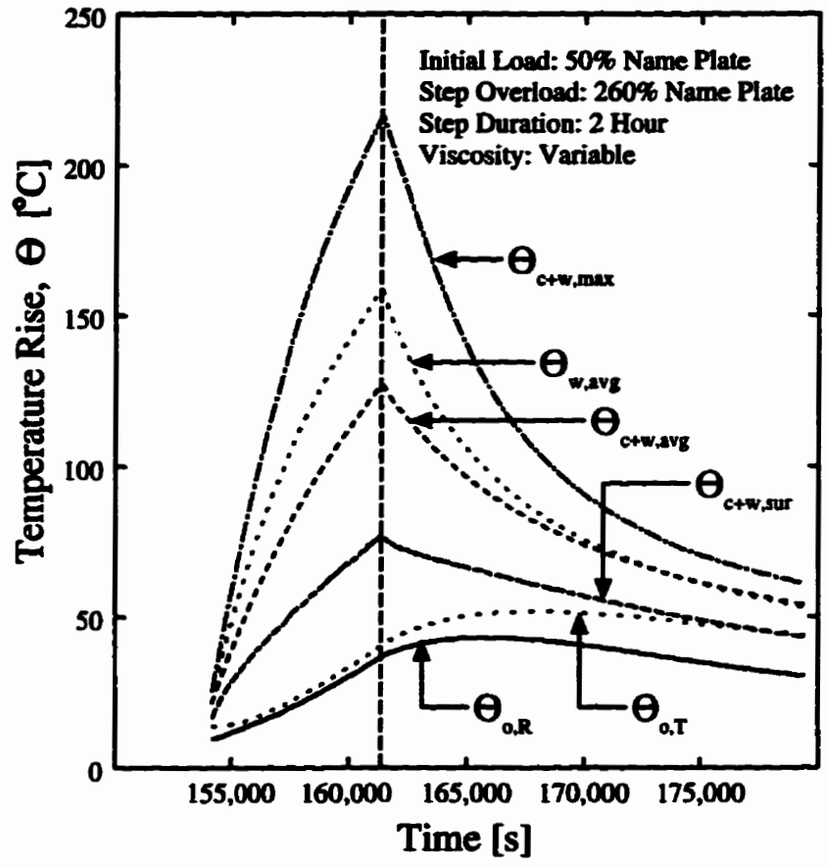

Figure 7.38: Transient temperature monitoring for run ANSI4.

Chapter 8

Closure

8.1 Summary

This thesis described a numerical model for conjugate heat transfer in an oil-immersed distribution transformer that is cooled by natural convection. The mathematical model consisted of a set of differential equations expressing conservation of mass, momentum, and energy, in a Cartesian coordinate system. The energy equation was modified to allow for an anisotropic thermal conductivity in part of the solid region.

The governing transport equations were discretized using a finite volume approach, employing an exponential upwind approximation of the advection terms. The equation sets were solved on a non-uniformly spaced grid. The pressure-velocity coupling was handled by the SIMPLEC method.

The algebraic equations were solved using a LGS2d solver that was accelerated using an improved additive correction multigrid method. The multigrid algorithm was modified to ensure that coarser grids did not straddle a solid-fluid interface. A relatively small time step was required to avoid the convergence difficulty caused by inter-equation coupling. In some cases the oil viscosity was a function of temperature.

After the code was validated against benchmark problems from the literature, the Alegi and Black [1] 75 kVA transformer was used as a test problem. A computer model was set up based on the parameters supplied by Alegi and Black, and the transformer was run at 49 kVA until it reached a steady state condition. Then the transformer load was stepped up to 71 kVA and again run to steady state. The average and maximum temperatures calculated by the computer code was compared against the average temperature results of Alegi and Black.

The Alegi and Black comparison was followed by a parametric study that focussed on the effect of two ambient temperatures (-5°C and 30°C), two load conditions (50kVA and 75kVA), modelling the core and windings as a homogeneous solid, and modelling viscosity as a function of temperature. The final computer code application was a test in which the computer model results were compared with the ANSI loading guides [3]. Starting from steady state at 50% load, a step load up to 260% of the nameplate rating was applied for one and two hours. The time variation of key system temperatures was compared.

8.2 Conclusions

The benchmark test problem comparisons verified the computer code implementation. Although an adequate conjugate heat transfer test benchmark problem could not be found in the literature, the computer code was tested by modelling a fluid cavity with conduction in thick walls. Grid and time step independance tests conducted for the transformer simulation indicated that consistent results were produced by the computer code.

The additive correction multigrid solver performance was demonstrated to work best on the solution of the pressure correction equation set. The conjugate additive

corrective multigrid solver helped increase the convergence of the pressure correction equation set since it prevented coarser grid blocks from overlapping regions of different fluids.

The ratio of thermal conductivities between the core and windings and the oil had a significant impact on the number of iterations required for the equation set to converge for a given time step. A narrow channel beside a solid was also shown to increase the number of iterations required for convergence.

It was found that a one second time step with a 73×73 non-uniform grid produced satisfactory results for the two-dimensional transformer flow model. During these runs it was observed that the transformer oil flow did not reach a true steady state condition. The transformer flow model results showed that the oil flow around the core and windings is unstable and sensitive to small fluctuations in the temperature field. This may be a highly unstable transient flow, or the beginning of transition to turbulent flow. The locations and size of the vorticies in the region above the core and windings changed with time, even after the average temperature of the transformer components had stabilized. Therefore it was determined that two other criteria were required to determine adequate *steady state* convergence: the reduction of the energy storage term relative to the generated power, and the realative change of the overall average temperature between time steps. When the Rayleigh number was calculated based on average wall temperatures, the values approach 1×10^{10}. A review of the literature offered no conclusive turbulence transition criterion because of the unique arrangement of the domain and boundary conditions in the present work.

The comparison with the Alegi and Black 49kVA and 71kVA load results showed that the present work predicted similiar trends in temperatures to those calculated by Alegi and Black. The greatest deviation between the present work and the work of Alegi and Black for the average temperature of the core and windings and the oil

was 10°C. In some instances, the present model shows better agreement with the experimental results than the Alegi and Black model.

It was found that the time constants of the transformer components changed throughout the history of a transformer run. The results indicated that the time constants change with time as the effective heat transfer coefficient for natural convection of the oil changes with the oil flow development. As the oil temperature increases, the natural convection circulation begins and the time constant of the core and windings decreases in magnitude.

The parametric study of twelve different runs generated similiar temperature trends between all the runs. The proportion of heat flow out of each tank wall was similiar between all runs. Lowering the ambient temperature increased the time required for the transformer oil flow to reach steady state. The effect of having a homogeneous block represent both the core and windings was a reduction in the hot-spot temperature. The nonhomogeneous test cases predicted a hotspot in the windings that was located half way up the windings, and beside the core.

For the ANSI loading guide comparison, the code predicted slightly higher winding maximum temperatures than the loading guides for the two hour 260% overload (over nameplate rating). For the one hour overload the present model predicts a lower maximum temperature. While the ANSI loading guides gave conservative results for the one hour step overload when compared to the code results, the loading guides suggested hotspot temperatures much lower than the code for the two hour step overload. The results showed only a one to two degree difference between maximum temperatures for the the constant and variable viscosity cases. The largest difference came from the top oil temperature where the variable viscosity test cases produced temperatures approximately 20°C higher than the constant viscosity cases.

8.3 Recommendations

The present study indicated that more research is required in the development of a transformer model that includes conjugate heat transfer. Further research must also establish if the tranformer oil flow is turbulent. In that case, a turbulence model must be added to the equation set.

The present study was restricted by the computer CPU time required to perform a simulation. A means of coupling the energy and momentum equations must be explored as a means of reducing the solution time. An attempt was made to add another iterative loop within each time step but initial tests indicated that it did not reduce the solution time. With a reduced solution time, a greater scope of tests could be performed and the model could be refined. Instead of simplifying the core and windings as a block, a better approximation of the transformer geometries could be used and the oil ducts could then be included. A three-dimensional model could also be attempted, but a lot more detailed knowledge would be required.

The effect of temperature on the thermal and electrical properties of the transformer could also be a subject of further investigation. The electrical resistance of the windings could be modelled as a function of temperature. This would cause the power generated from the windings to change with time. With an increased solution stability, the effect of varying other properties and geometries, as well as transient ambient conditions and transformer loading, could be explored. And if access could be gained to get more detailed information about a set of experimental runs, the accuracy of the transformer comparison model could be improved since all of the transformer dimensions would be known.

Bibliography

[1] ALEGI, G. L. ., AND BLACK, W. Z. Real-time thermal model for an oil-immersed forced-air cooled transformer. *IEEE Transactions on Power Delivery 5*, 2 (1990), 991–999.

[2] ALLEN, P. H. G., AND CHILDS, E. P. Conjugated heat transfer in disc-type power transformer windings. *Proceedings of the Eighth International Heat Transfer Conference 6* (1986), 2977–2982.

[3] AMERICAN NATIONAL STANDARDS INSTITUTE, INC. (ANSI). *American National Standard - Guide for Loading Mineral-Oil-Immersed Overhead and Pad-Mounted Distribution Transformers*, c57.91 ed. New York, NY, 1981.

[4] AUBIN, J., DUVAL, M., AND LANGHAME, Y. Hot spot measurement in power transformers. Tech. Rep. 78-62 A, Hydro-Quebec, Varennes, Quebec, 1981.

[5] BARRIOS, L., AND COUNCIL, M. E. Technique for establishing winter loading guidelines for 15, 25, and 50 kVA pole and pad mounted distribution transformers based on the direct measurement of winding and oil temperatures. 21–28.

[6] BEAVERS, M. F. The flow rate in a self-cooled transformer. *AIEE Transactions PAS-100* (1981), 956–963.

[7] BERNSTEIN, B. S., AND BRANCATO, E. L. Aging of equipment in the electrical utilities. *IEEE Transactions on Electrical Insulation 28*, 28 (1993), 866–875.

[8] BUCHAN, P. G. A hot spot measuring device for power transformers. Tech. Rep. 157 T 351, Ontario Hydro, Toronto, Ontario, 1984.

[9] BUCHAN, P. G., AND GREEN, M. A. Thermal behaviour of hot spots in distribution transformers. Tech. Rep. 103 D 202, Ontario Hydro Research Division, Toronto, Ontario, 1984.

[10] CARRUTHERS, M. G., AND NORRIS, E. T. Thermal rating of transformers, introduction of multiflow principle. *Proceedings IEE 116*, 9 (1969), 1564–1570.

[11] CARSTEA, I. T. Program for heat transfer analysis in large power transformer windings. *Modelling, Measurement & Control 57*, 3 (1994), 31–39.

[12] CHENG, S. C., AND VACHON, R. I. The prediction of the thermal conductivity of two and three phase solid heterogeneous mixtures. *Internation Journal of Heat and Mass Transfer 12* (1969), 249–264.

[13] CRANE, R. A., AND VACHON, R. I. A prediction of the bounds on the effective thermal conductivity of granular materials. *International Journal of Heat and Mass Transfer 20* (1977), 711–723.

[14] CROSS, J. Personal communications. *Carte International* (1995).

[15] DAVIS, G. D. V. Natural convection of air in a square cavity: A bench mark numerical solution. *Internation Journal for Numerical Methods in Fluids 3* (1983), 249–264.

[16] DOOHER, B. P., AND ELLIOTT, E. Dynamic thermal testing and winding temperature response of a 30-MVA transformer. *Proceedings of the American Power Conference, 5th Annual Meeting 55-II* (1993), 1652–1657.

[17] DOORMAAL, J. P. V., AND RAITHBY, G. D. Enhancement of the SIMPLE method. *Numerical Heat Transfer 7* (1984), 147–163.

[18] EASTGATE, C. Sub-zero operation of oil-immersed transformers. *Electrical Review 3* (1967), 648–651.

[19] GALPIN, P. F., DOORMAAL, J. P. V., AND RAITHBY, G. D. Solution of the incompressible mass and momentum equations by application of a coupled equation line solver. *International Journal for Numerical Methods in Fluids 5* (1985), 615–625.

[20] GHIA, U., GHIA, K. N., AND SHIN, C. T. High-re solutions for incompressible flow using the navier-stokes equations and a multigrid method. *Journal of Computational Physics 48* (1982), 387–411.

[21] GOEL, N. S., GERBOC, J. S., AND LEHMANN, G. A simple model for heat conduction in heterogeneous materials and irregular boundaries. *Int. Comm. Heat Mass Transfer 19* (1992), 519–530.

[22] GUPTA, B., MCDERMID, W., POLOVICK, G., SHENOY, V., AND TRINIH, G. Transformer insulation aging - a review of the state of the art. *The Electricity '95 Conference* (1995).

[23] HEINDEL, T. J., INCROPERA, F. P., AND RAMADHYANI, S. Enhancement of natural convection heat transfer from an array of discrete heat sources. *International Journal of Heat and Mass Transfer 39* (1996), 479–490.

[24] HEINDEL, T. J., RAMADHYANI, S., AND INCROPERA, F. P. Conjugate natural convection from an array of protruding heat sources. *Numerical Heat Transfer, Part A 29* (1996), 1–18.

[25] HORTMANN, M., PERIC, M., AND SCHEUERER, G. Finite volume multigrid prediction of laminar natural convection: Bench-mark solutions. *International Journal for Numerical Methods in Fluids 11* (1990), 189–207.

[26] HUTCHINSON, B. R., GALPIN, P. F., AND RAITHBY, G. D. Application of additive correction multigrid to the coupled fluid flow equations. *Numerical Heat Transfer 11* (1988), 133–147.

[27] HUTCHINSON, B. R., AND RAITHBY, G. D. A multigrid method based on the additive correction strategy. *Numerical Heat Transfer 9* (1986), 511–537.

[28] HWANG, M. D., GRADY, W. M., AND H. WALTER SANDERS, J. Calculation of winding temperatures in distribution transformers subjected to harmonic currents. *IEEE Transaction on Power Delivery 3*, 3 (1988), 1074–1079.

[29] IMRE, L., SZABO, I., AND BITAI, A. Determination of the steady state temperature field in naturally oil-cooled disc-type transformers. *Proceedings of the Sixth International Heat Transfer Conference 2* (1978), 123–128.

[30] INCROPERA, F. P., AND DEWITT, D. P. *Fundamentals of Heat and Mass Transfer*, third edition ed. John Wiley & Sons, Toronto, 1990.

[31] JESSEE, J. P., AND FIVELAND, W. A. A cell-vertex algorithm for the incompressible navier-stokes equations on non-orthogonal grids. *Numerical Developments in CFD, ASME 215* (1995), 35–45.

[32] KIM, D. M., AND VISKANTA, R. Effect of wall conduction and radiation on natural convection in a rectangular cavity. *Numerical Heat Transfer 7* (1984), 449–470.

[33] KIM, D. M., AND VISKANTA, R. Effect of wall heat conduction on natural convection heat transfer in a square enclosure. *Journal of Heat Transfer 107* (1985), 139–146.

[34] KUNES, J. J. Characteristics of thermosiphon flow in a model transformer oil circuit. *AIEE Power Apparatus and Systems*, 34 (1958), 973–977.

[35] LAGE, J. L., AND BEJAN, A. The ra-pr domain of laminar natural convection in an enclosure from the side deheat. *Numerical Heat Transfer, Part A 19* (1991), 21–41.

[36] LAHOTI, B. D., AND FLOWERS, D. E. Evaluation of transformer loading above nameplate rating. *Electrical Power Systems Research* (1980).

[37] LAMPE, W. Power transformers and shunt reactors for arctic regions. *IEEE Transactions on Power Delivery PWRD-1*, 1 (1986), 217–224.

[38] LANGHAME, Y., CASTONGUAY, J., BEDARD, N., AND ST-ONGE, H. Low temperature performance of naphthenic and paraffinic oils in transformers and automatic circuit reclosers. *IEEE Transactions on Power Apparatus and Systems PAS-104*, 4 (1985), 910–917.

[39] LINDSAY, J. F. Temperature rise of an oil-filled transformer with varying load. *IEEE Transactions on Power Apparatus and Systems PAS-103*, 9 (1984), 2530–2535.

[40] MCNUTT, W. J., MCIVER, J. C., LEIBINGER, G. E., FALLON, D. J., AND WICKERSHEIM, K. A. Direct measurement of transformer winding hot spot temperature. *IEEE Transactions on Power Apparatus and Systems PAS-103*, 6 (1984), 1155–1162.

[41] MILLER, W. H., SERHAL, A. S., AND MORRIS, E. Cold load prediction in electrically heated homes. *Proceedings of the American Power Conference 48* (1986), 495–500.

[42] MONTSINGER, V. M., AND WETHERILL, L. Effect of color of tank on temperature of self-cooled transformers under service conditions. *Transactions A. I. E. E.* (1930), 41–51.

[43] MOORE, A. D. Dissipation of heat by radiation. *Transactions A. I. E. E.* (1930), 359–365.

[44] NAUERT, P. How to specify a transformer heat run. *Electrical World* (August 1994), 43–46.

[45] NELSON, D. J., AND JESSEE, J. P. A coupled thermal-magnetic model for high frequency transformers: Part I - Model formulation and material properties. In *InterSociety Conference on Thermal Phenomena* (1992), pp. 23–31.

[46] PATANKAR, S. V. *Numerical Heat Transfer and Fluid Flow.* Hemisphere Publishing Corporation, 1980.

[47] PIERCE, L. W. An investigation of the temperature distribution in cast resin transformer windings. *IEEE Transactions on Power Delivery 7*, 2 (1992), 920–926.

[48] PIERCE, L. W. An investigation of the thermal performance of an oil filled transformer winding. *IEEE Transactions on Power Delivery 7*, 3 (1992), 1347–1356.

[49] PIERCE, L. W. Current developments for predicting transformer loading capacity. *1993 Minnesota Power Systems Conference* (1993).

[50] PIERCE, L. W. Hottest spot temperatures in ventilated dry type transformers. *IEEE Transactions on Power Delivery 9*, 1 (1993), 257–264.

[51] PIERCE, L. W. Predicting hottest spot temperatures in ventilated dry type transformer windings. *IEEE Transactions on Power Delivery 9*, 2 (1994), 1160–1172.

[52] PIERCE, L. W. Predicting liquid filled transformer loading capability. *IEEE Transactions on Industry Applications 30*, 1 (1994), 170–178.

[53] PIERCE, L. W. Improved equations for a more accurate hot-spot temperature prediction in transformers. *Electricity '95 Conference* (1995).

[54] RAITHBY, G. D. Excerpts of me780 course notes. *Department of Mechanical Engineering* (1995).

[55] RAITHBY, G. D., AND SCHNEIDER, G. E. Elliptic systems: Finite difference methods II. In *Handbook of Numerical Heat Transfer*, W. J. Minhowycz, E. M. Sparrow, G. E. Schneider, and R. H. Pletcher, Eds. John Wiley & Sons, New York, 1988, ch. 7, p. 253.

[56] RELE, A. *Thermal Design of Transformers (presentation).* Westinghouse Canada Limited, 1972.

[57] RELE, A., AND PALMER, S. Determination of temperatures in transformer windings. *IEEE Transactions on Power Apparatus and Systems PAS-94*, 5 (1975), 1763–1769.

[58] SOLIMAN, H. M., SIMS, G. E., AND TRIM, D. W. On the one-dimensional approximation of heat conduction in composite walls. *Int. Comm. Heat Mass Transfer 17* (1990), 305–316.

[59] STENKVIST, E. Temperature and conditions of oilflow in large oil-immersed transformers. *Technical Achievements of ASEA Research* (1946), 248–257.

[60] SUN, Y. S., AND EMERY, A. F. Multigrid computation of natural convection in enclosures with a conductive baffle. *Numerical Heat Transfer, Part A 25* (1994), 575–592.

[61] SZPIRO, O., ALLEN, P. H. G., AND RICHARDS, C. W. Coolant distribution in disc type transformer winding horizontal ducts and its influence on coil temperatures. *Proceedings of the Seventh International Heat Transfer Conference 6* (1982), 251–256.

[62] TAYLOR, E. D., BERGER, B., AND WESTERN, B. E. An experimental approach to the cooling of transformer coils by natural convection. *The Institution of Electrical Engineers* (1958), 141–152.

[63] WILDE, R. L. Effects of cold load pickup at the distribution substation transformer. Tech. Rep. 131 D 247, RLW Engineering Ltd., Regina, Saskatchewan, 1983.

[64] WROBLEWSKI, D. E., AND JOSHI, Y. Computations of liquid immersion cooling for a protruding heat source in a cubical enclosure. *International Journal of Heat and Mass Transfer 36* (1993), 1201–1218.

[65] YAMAGUCHI, M., KUMASAKA, T., INUI, Y., AND ONO, S. Determination of effective oil temperature in a transformer. *IEEE Transactions on Power Apparatus and Systems 69* (1950), 703–710.

[66] YEUNG, G. A., AND WALKER, D. Transformer testing under cold load pickup conditions. Tech. Rep. 77-46 Phase II, Saskatchewan Power Corporation, Regina, Saskatchewan, 1983.

Appendix A

Transformer Model Selection

There are many ways that the transformer could be approximated. The most important criterion of the model is that it should be able to simulate oil flow induced by natural convection around a heated solid region. This appendix justifies the two-dimensional Cartesian model selected over some of the other model types.

A.1 Three-Dimensional Models

If a three-dimensional model were to be used it would be necessary to identify and fit a grid for all the geometric details of the transformer shown in Figure A.1. In that case an attempt would be made to model each of the transformer components as closely as possible. Such a model would required many hundreds of thousands of control volumes to resolve the detailed three-dimensional model. The model would require a large amount of computational time, and it would take a long time to perform a thorough parametric study because there would be many more parameters to be considered. The requirements of the complicated model would introduce a large amount of geometric uncertaintly since the exact design information for a transformer

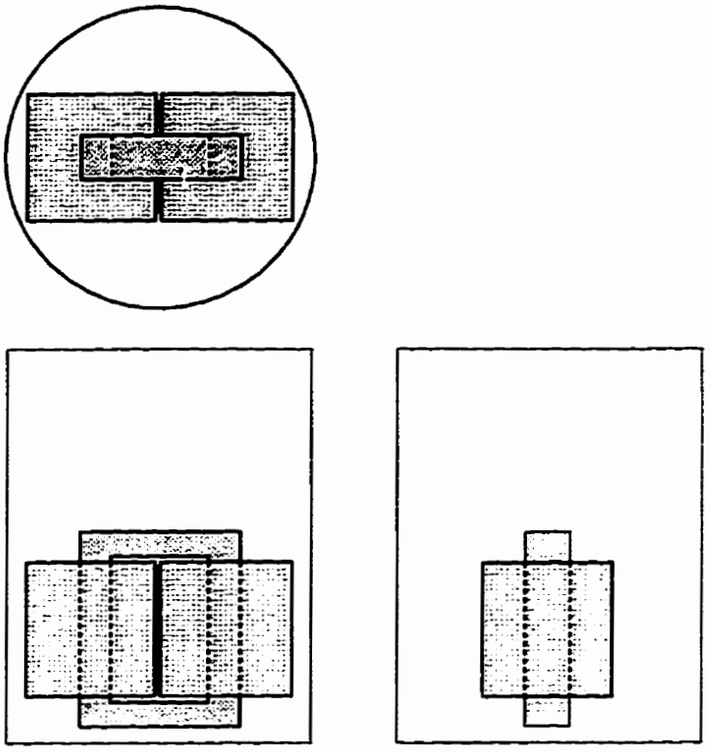

Figure A.1: Various views of a two winding transformer.

would be difficult to get.

Based on these points, it was decided that a two-dimensional approximate model would be a better first estimate for simulating a transformer run.

A.2 Two-Dimensional Models

This section will describe the benefits and disadvantages of three types of two-dimensional models: the cylindrical model, front profile, and side profile. All three models significantly reduce the number of control volumes required to do a simulation when compared to a three-dimensional model.

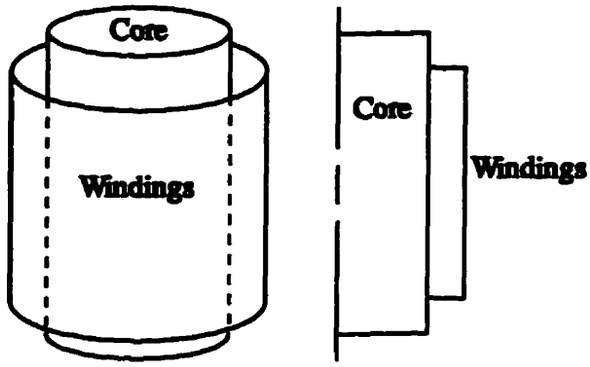

Figure A.2: Cylindrical model of a single winding and the core.

A.2.1 Cylindrical Model: Single Winding and Core

The transformer could be divided in half so that only part of the core, and one winding, would be modelled together as a cylinder. This model is shown in Figure A.2. A lot less work is required relative to the three-dimensional models to derive the equations and code them. The volume of the windings and the core could be adjusted to account for the less than perfect fit to a cylinder.

On the other hand, this model neglects the effect of the rest of the core. It is difficult to model the tank as a perfect cylinder with any degree of accuracy since the transformer was cut in half. The core is approximated as a cylinder when actually it is rectangular. The windings are not cylindrical either; they are rectangular with rounded edges. The ducts through the windings can only be modelled as a continuous duct around the windings, or neglected completely. In actual fact, the duct should only go through part of the windings.

To summarize, it is difficult to model the tank and the rest of the core with the two-dimensional cylindrical model. Cylindrical windings may not be a valid approximation of the windings.

A.2.2 Front Profile Model

Using Cartesian coordinates, the transformer could be modelled by taking a slice down the center through the core and both windings. Using symmetry, the model could then be simplified so that only one winding would be considered. The model makes it fairly easy to determine the properties of the core and winding section, as shown in Figure A.3, since the ratio of core and windings is constant through the section. This model requires less time to derive, and then program, the discretization equations than a three-dimensional model.

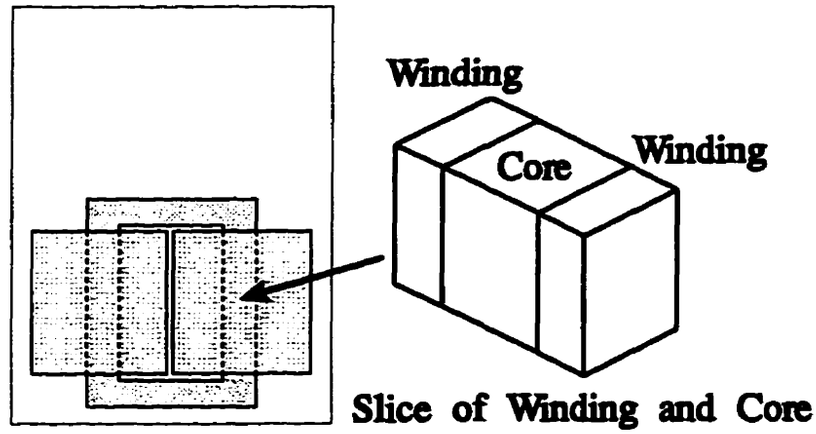

Figure A.3: Front profile model of a tranformer.

On the other hand, the model does not capture the three-dimensional aspects of the windings. The heat should be close to being symmetric around the core since heat will be more likely to travel along the windings than through the insulation around them. The ducts cannot be modelled using this cross-section since they typically run parallel to the core (relative to the long side of the core). Also, this model cannot

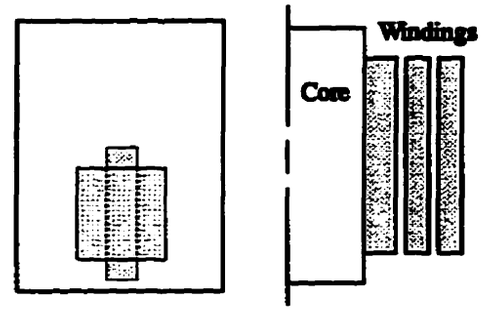

Figure A.4: 2-D side profile model of a transformer.

simulate the effects of varying the distance from the core and windings to the tank.

Although this model looks fairly good for the current work, there must be some trial-and-error to get the specified heat generation to correctly represent the heat generated in an actual core and windings. Trial-and-error must also be used to find the dimension for the distance between the core and the tank. No attempt could be made to model the ducts.

A.2.3 Side Profile Model

The 2-D side profile model, as shown in Figure A.4, makes use of symmetry to model the slice of one of the windings and part of the core. This model requires very few control volumes compared to the three-dimensional models. The ducts can be modelled through the windings, and the tank can be modelled adequately. This model has the ducts going through the entire winding cross-section. Therefore the duct width may have to be modified to improve the approximation of the heat transfer from the windings to the oil in the ducts.

This model is satisfactory for this work. Trial-and-error must be used to find the effective duct size, as well as to determine the windings to tank distance.

Appendix B

Details of the Computation Grids

This appendix shows how each grid is broken down into non-uniform control volumes. These transformer grids are used throughout Chapter 7, but are presented here for comparison purposes. Chapter 3 gives a detailed explanation on how the grids were generated for the domain.

B.1 54×51 Grid

The domain is broken up into five x grid regions and six y grid regions, as shown in Figure B.1. The specified details on each grid region are shown in Table B.1. Figure B.2 shows the complete grid.

Region	Specified Grid Parameters		
	Length	Number of Nodes	Other Parameter
X Grid Regions			
X1	0.10 m	15	$\Delta x_n = 0.00916$ m
X2	0.11 m	12	uniform
X3	0.04 m	9	$\eta_p = 0.9$
X4	0.02 m	9	$\eta_p = 1.0$
X5	0.02 m	9	$\eta_p = 1.0$
Y Grid Regions			
Y1	0.05 m	5	$\Delta y_n = 0.01250$ m
Y2	0.15 m	12	uniform
Y3	0.05 m	6	$\eta_p = 1.0$
Y4	0.05 m	6	$\eta_p = 1.0$
Y5	0.23 m	16	uniform
Y6	0.05 m	6	$\eta_p = 1.0$

Table B.1: Grid region specified parameters for the 54 × 51 grid.

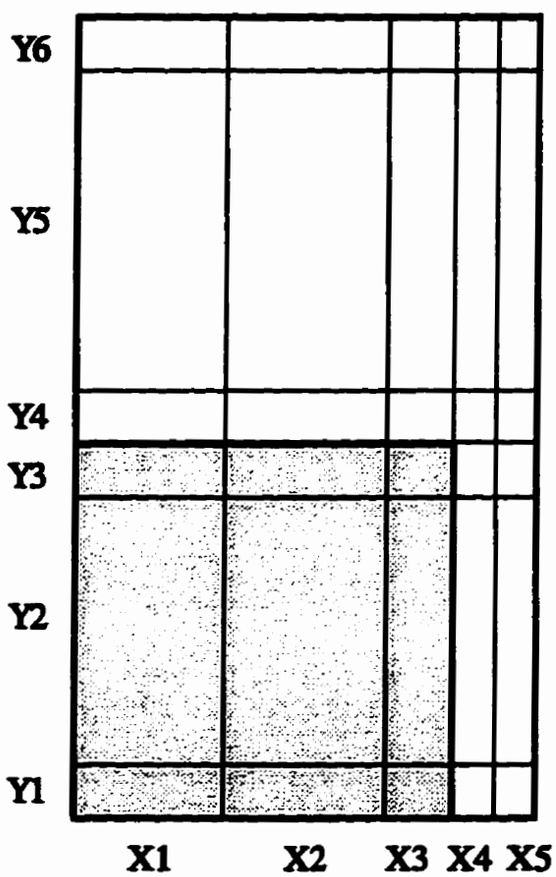

Figure B.1: Grid regions for the grid independence transformer grid.

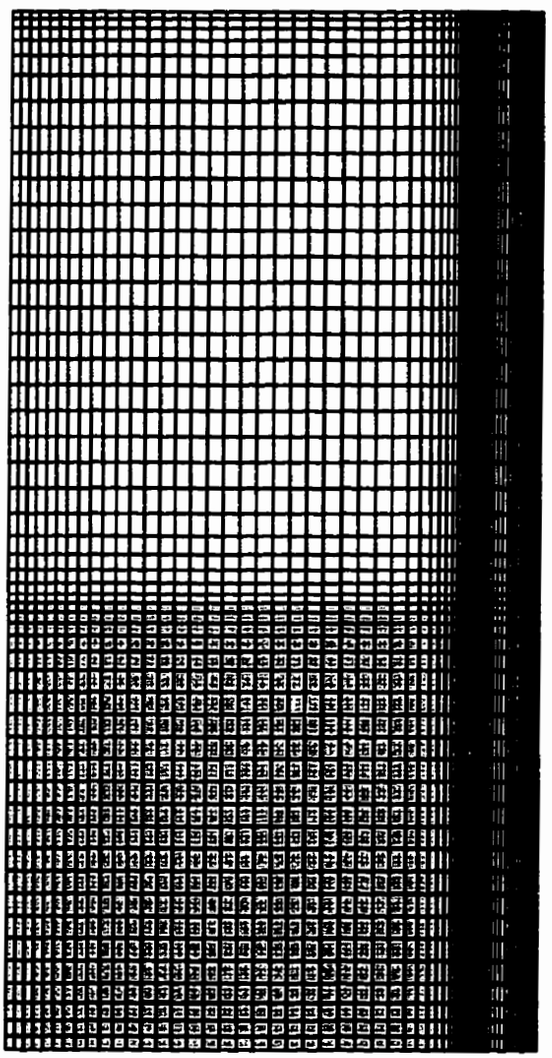

Figure B.2: 54 × 51 Grid for the grid independence check.

B.2 73 × 73 Grid

The domain is broken up into five x grid regions and six y grid regions, as shown in Figure B.1. The details on each grid region is shown in Table B.2, and Figure B.3 shows the complete grid.

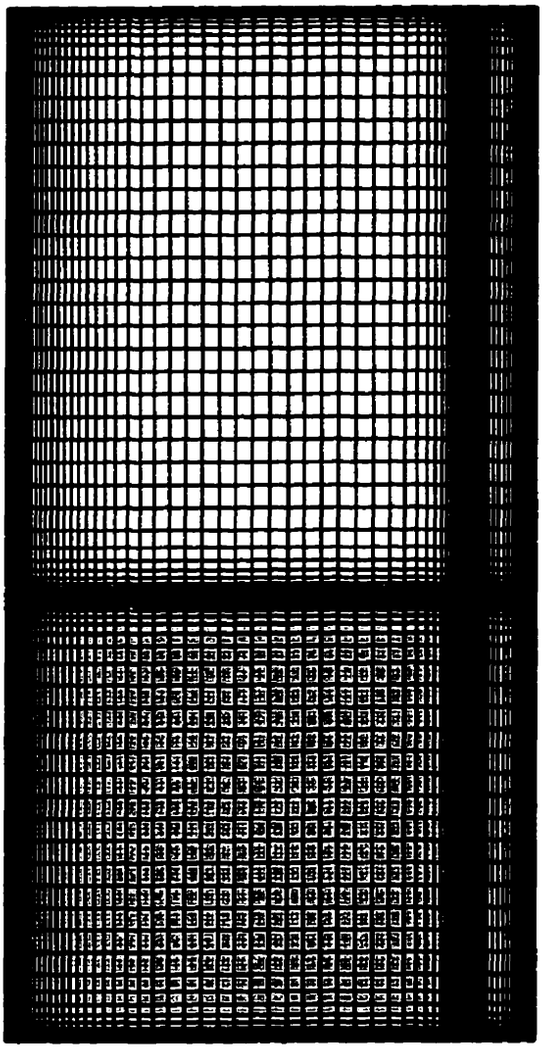

Figure B.3: 73 × 73 Grid for the grid independence check.

Region	Specified Grid Parameters		
	Length	Number of Nodes	Other Parameter
X Grid Regions			
X1	0.10 m	25	$\Delta x_n = 0.00916$ m
X2	0.11 m	12	uniform
X3	0.04 m	12	$\eta_p = 0.9$
X4	0.02 m	12	$\eta_p = 1.0$
X5	0.02 m	12	$\eta_p = 1.0$
Y Grid Regions			
Y1	0.05 m	10	$\Delta y_n = 0.01250$ m
Y2	0.15 m	12	uniform
Y3	0.05 m	11	$\eta_p = 1.0$
Y4	0.05 m	11	$\eta_p = 1.0$
Y5	0.23 m	18	uniform
Y6	0.05 m	11	$\eta_p = 1.0$

Table B.2: Grid region parameters for the 73×73 grid.

B.3 100 × 102 Grid

The domain is broken up into five x grid regions and six y grid regions, as shown in Figure B.1. The details on each grid region is shown in Table B.3, and Figure B.4 shows the complete grid.

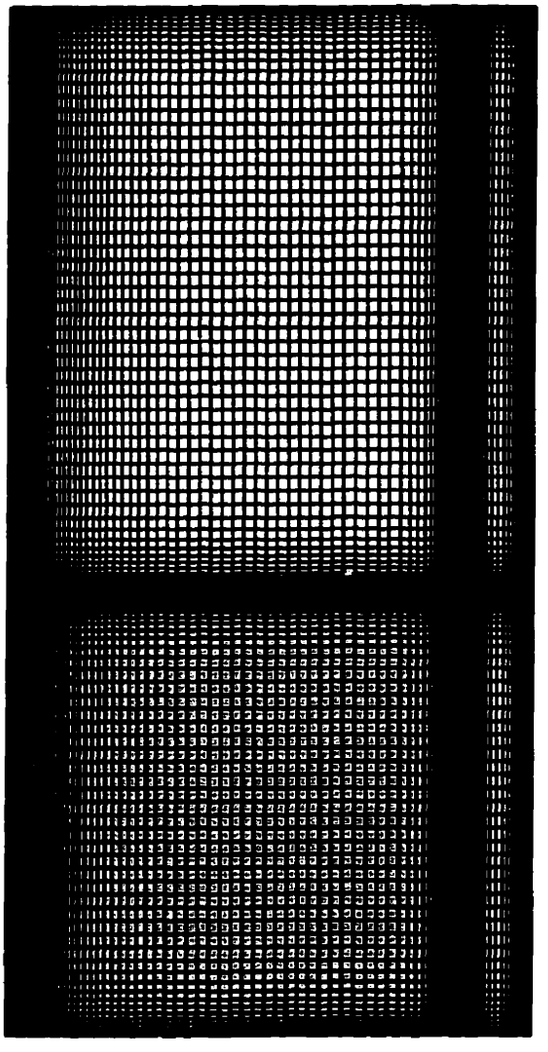

Figure B.4: 100 × 102 Grid for the grid independence check.

Region	Specified Grid Parameters		
	Length	Number of Nodes	Other Parameter
X Grid Regions			
X1	0.10 m	32	$\Delta x_n = 0.006111$ m
X2	0.11 m	18	uniform
X3	0.04 m	20	$\eta_p = 1.0$
X4	0.02 m	15	$\eta_p = 1.0$
X5	0.02 m	15	$\eta_p = 1.0$
Y Grid Regions			
Y1	0.05 m	12	$\Delta y_n = 0.007500$ m
Y2	0.15 m	20	uniform
Y3	0.05 m	14	$\eta_p = 1.0$
Y4	0.05 m	14	$\eta_p = 1.0$
Y5	0.23 m	30	uniform
Y6	0.05 m	12	$\eta_p = 1.0$

Table B.3: Grid region parameters for the 100×102 grid.

B.4 100 × 152 Grid

The domain is broken up into five x grid regions and six y grid regions, as shown in Figure B.1. The details on each grid region is shown in Table B.4, and Figure B.5 shows the complete grid.

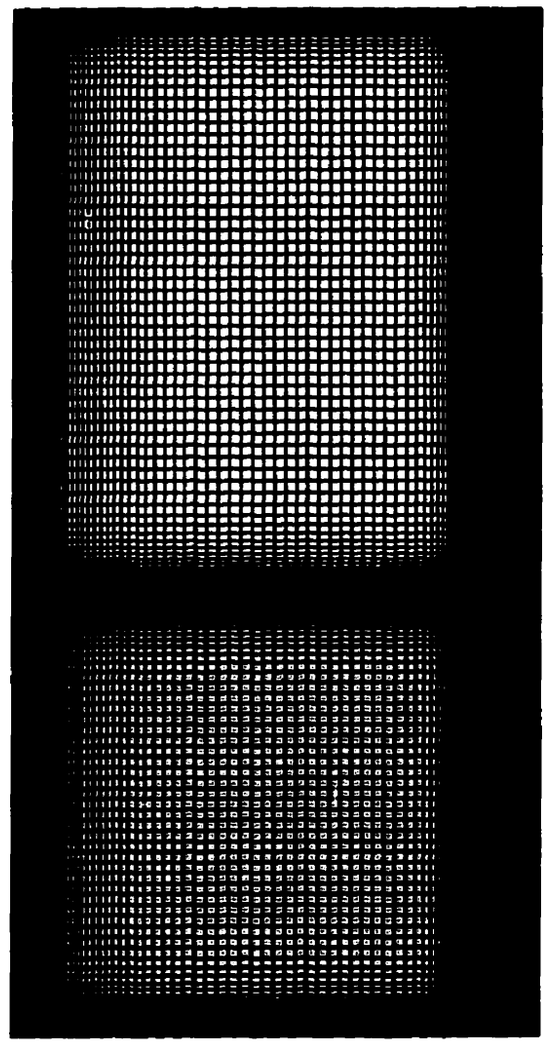

Figure B.5: 100 × 152 Grid for the grid independence check.

Region	Specified Grid Parameters		
	Length	Number of Nodes	Other Parameter
X Grid Regions			
X1	0.10 m	37	$\Delta x_n = 0.006111$ m
X2	0.11 m	18	uniform
X3	0.04 m	15	$\eta_p = 1.0$
X4	0.02 m	15	$\eta_p = 1.0$
X5	0.02 m	15	$\eta_p = 1.0$
Y Grid Regions			
Y1	0.05 m	30	$\Delta y_n = 0.006000$ m
Y2	0.15 m	25	uniform
Y3	0.05 m	21	$\eta_p = 1.0$
Y4	0.05 m	21	$\eta_p = 1.0$
Y5	0.23 m	34	uniform
Y6	0.05 m	21	$\eta_p = 1.0$

Table B.4: Grid region parameters for the 100×152 grid.

Appendix C

Time and Grid Independence Test Results

This appendix contains all the time and grid independence results in the form of plots. These are all based on the 49 kVA Alegi and Black comparison runs in Chapter 7.

Time Step	54 × 51	73 × 73	100 × 102	100 × 152
0.25 s	14 hrs	12 hrs	7 hrs	-
0.50 s	-	24 hrs	24 hrs	12 hrs
1.00 s	S.S.	S.S.	S.S.	-
2.00 s	-	-	diverged	-
3.00 s	-	S.S.	-	-
5.00 s	S.S.	S.S.	diverged	-
10.0 s	S.S.	-	-	-

Table C.1: Time and grid independence run matrix.

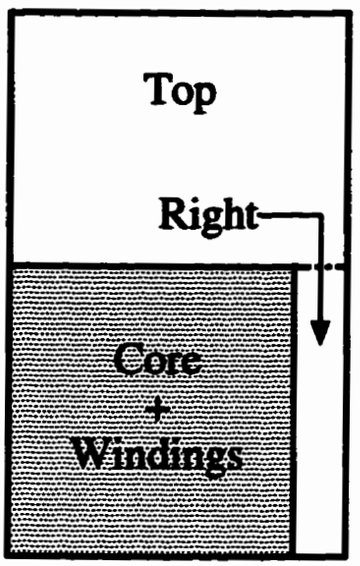

Figure C.1: Region layout for transformer model.

These runs were used to determine the best grid and largest time step that could be used without sacrificing accuracy. Table C.1 shows the runs performed at each time step and grid size. Figure C.1 shows how the transformer model is divided into regions.

C.1 Time Independence

This section shows the results of the time independence runs. There are three plots shown for each run; one for each component: core and windings, right oil cavity, and the top oil cavity.

The time independence of the transformer flow model was examined first. The top oil region showed little dependence on the time step. On the other hand, the core showed little dependence on time step for the 54×51 grid but the 73×73 grid showed

a large dependence on the time step. From Figure C.8, it was determined that a one second time step is the best choice. Although the 0.5 second and 0.25 second time steps showed a very close agreement when compared with each other, they required a long run time. The relatively small error introduced by the 1.0 second time step was considered acceptable. The 100×102 grid showed very little time dependence for the core when comparing a 0.5 and 1.0 second time step results.

The right oil cavity showed a dependence on time step. Although the steady state results for the 54×51 grid are the same for all time steps, there is a large temperature difference after the first eight hours of the transformer run. The 73×73 and the 100×102 grid runs did not show this dependence on the time step. Therefore, the one second time step is used for the rest of the transformer runs.

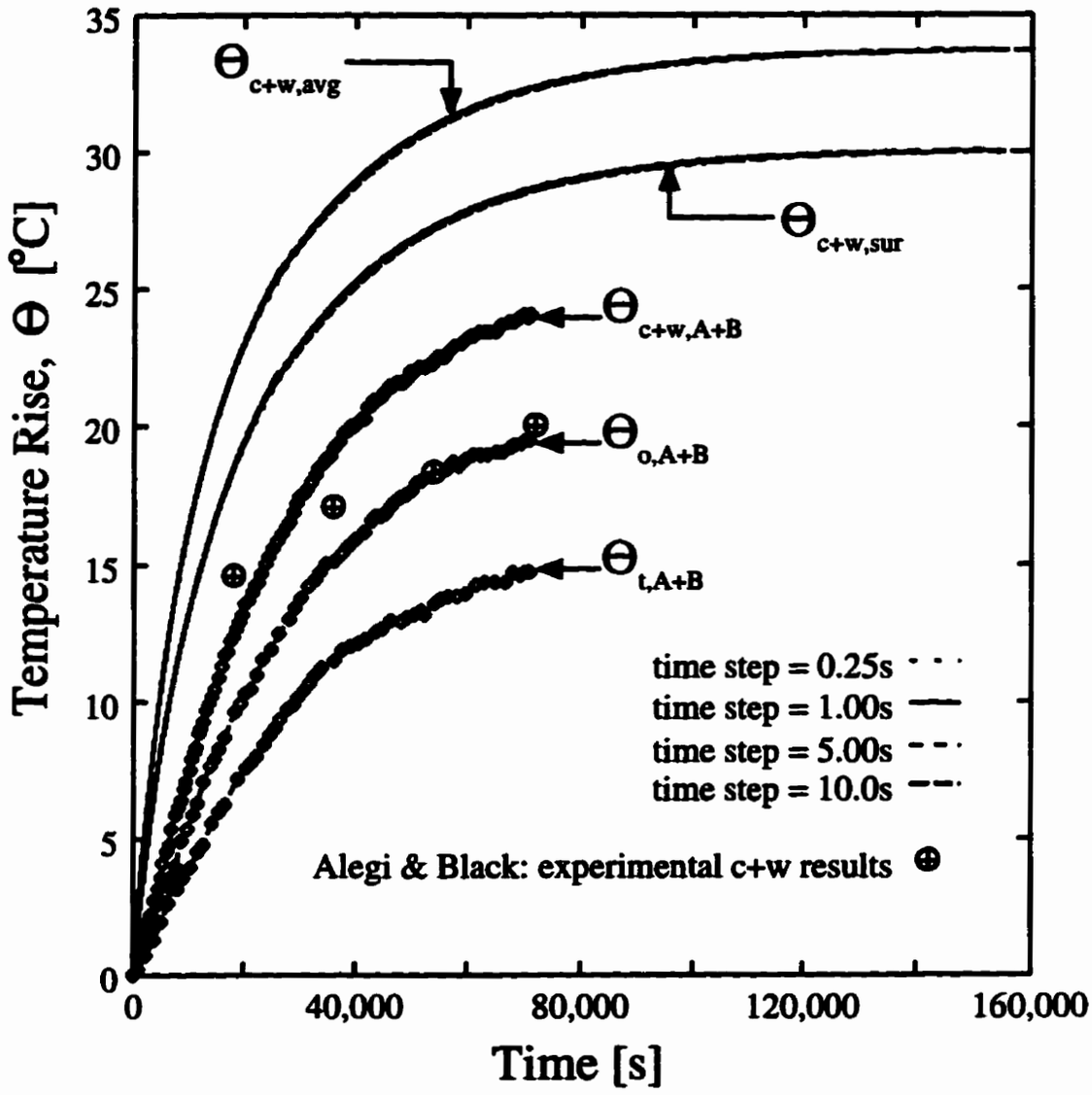

Figure C.2: Alegi and Black time independence run for 54x41 grid: core and windings.

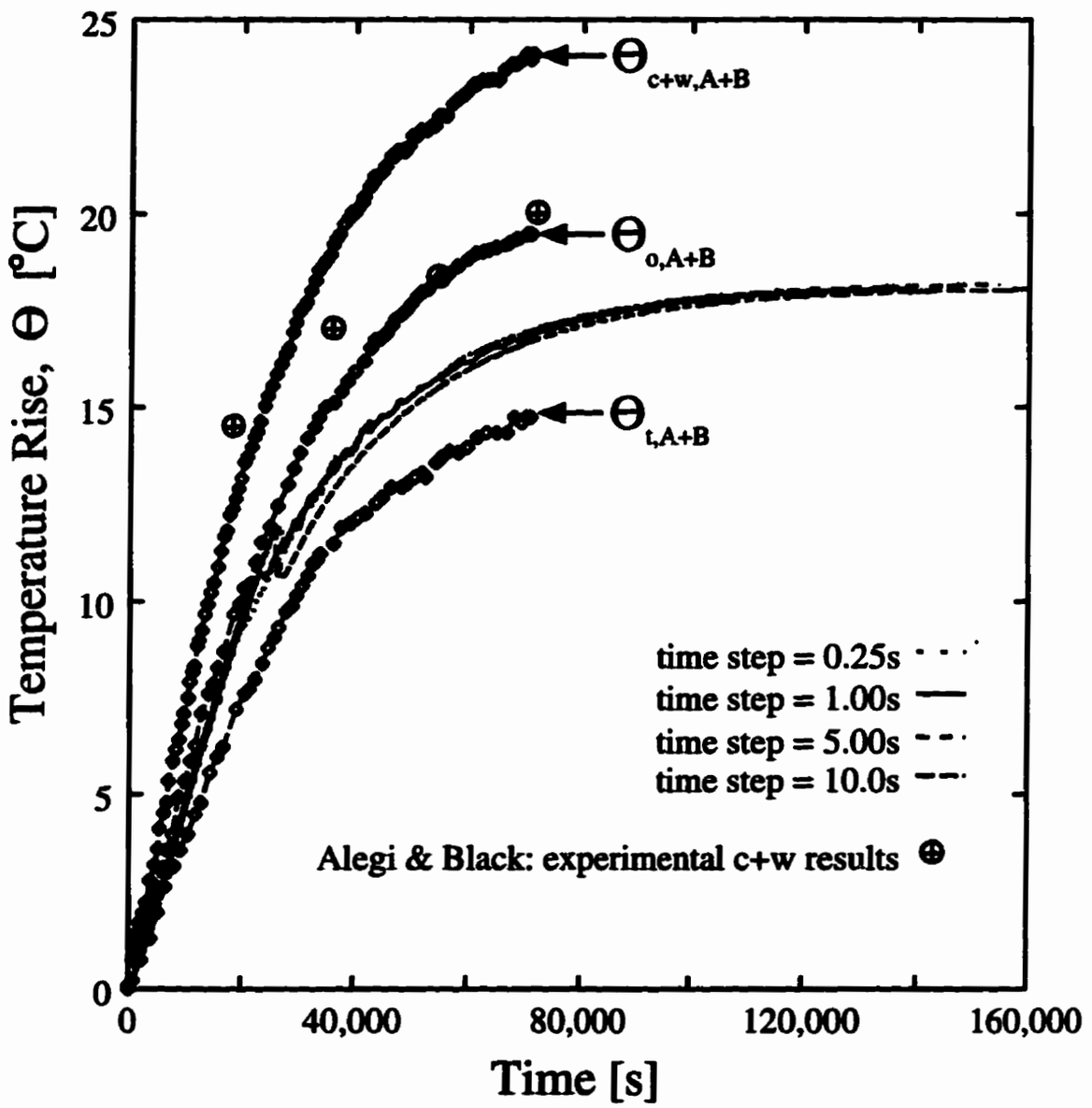

Figure C.3: Alegi and Black time independence run for 54x41 grid: right oil cavity.

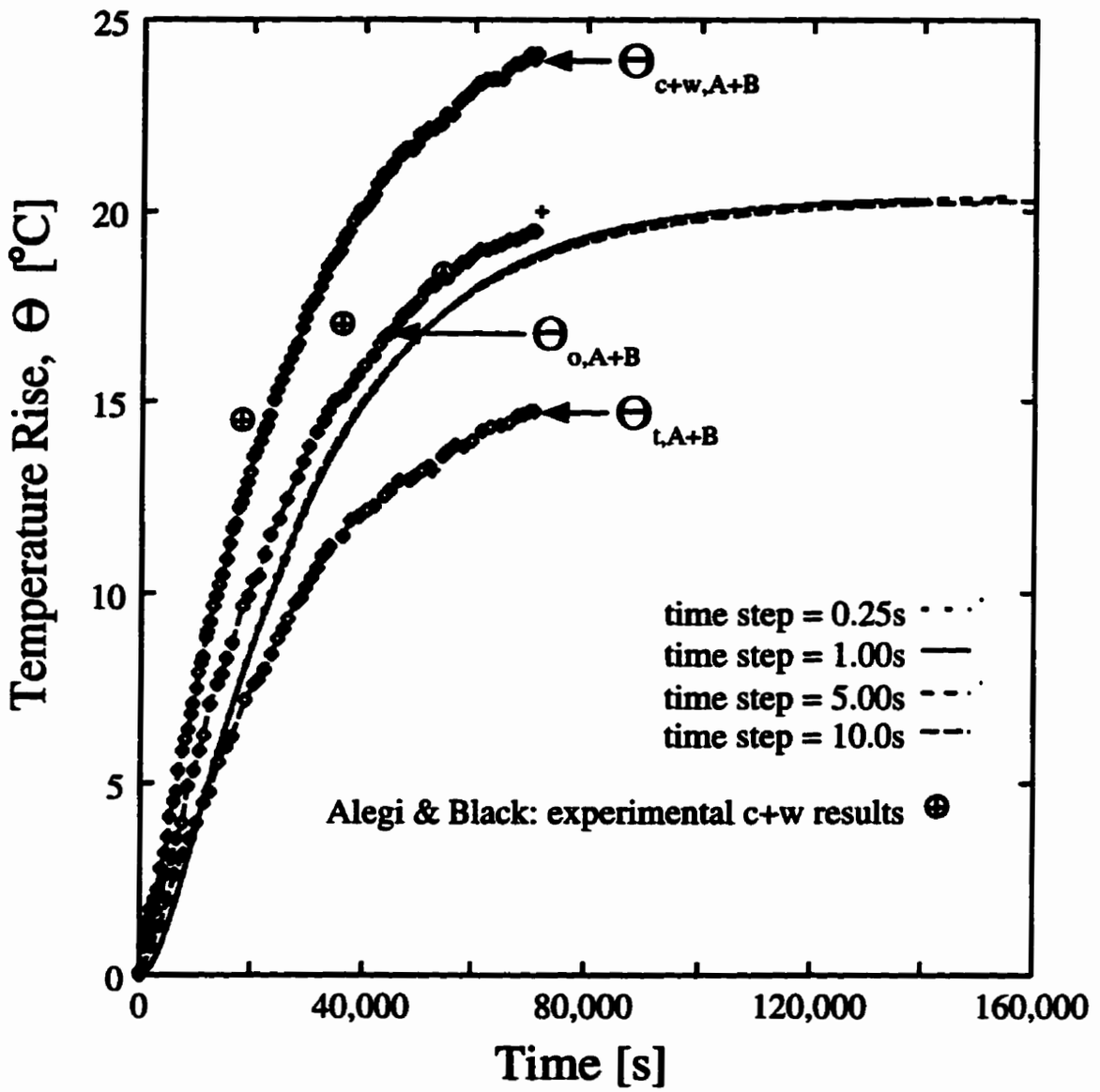

Figure C.4: Alegi and Black time independence run for 54x41 grid: top oil cavity.

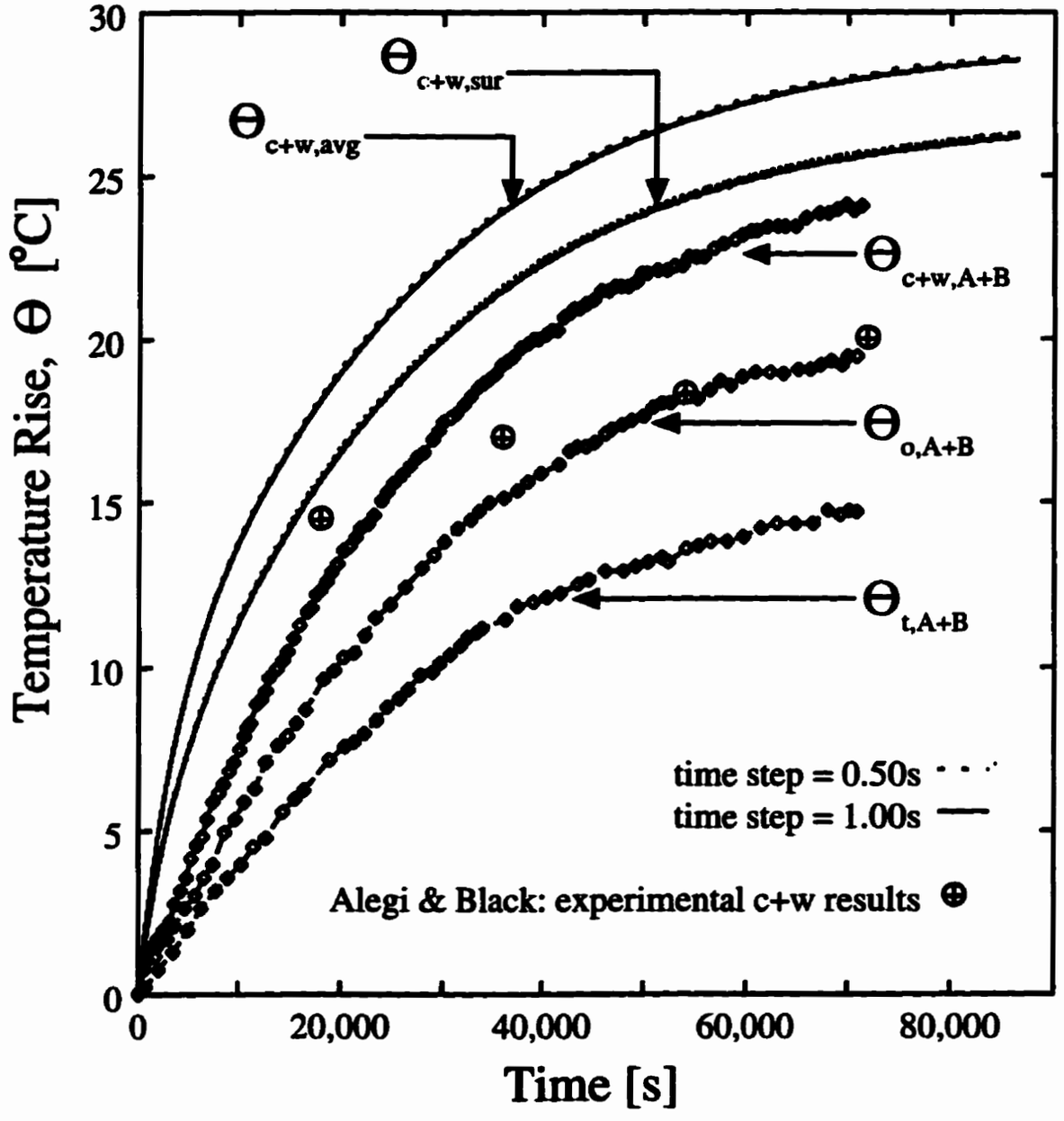

Figure C.5: Alegi and Black time independence run for 100x102 grid: core and windings.

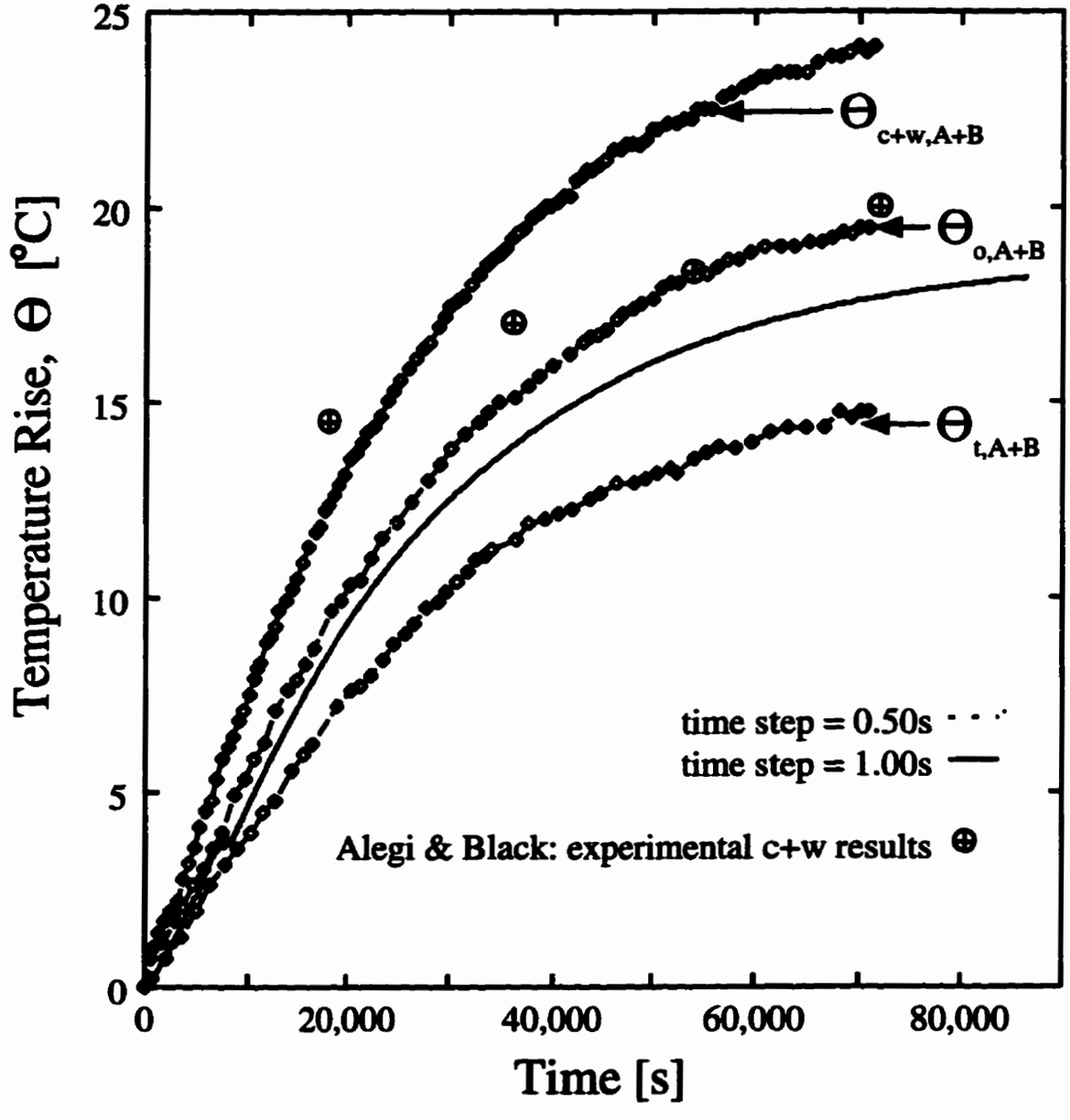

Figure C.6: Alegi and Black time independence run for 100x102 grid: right oil cavity.

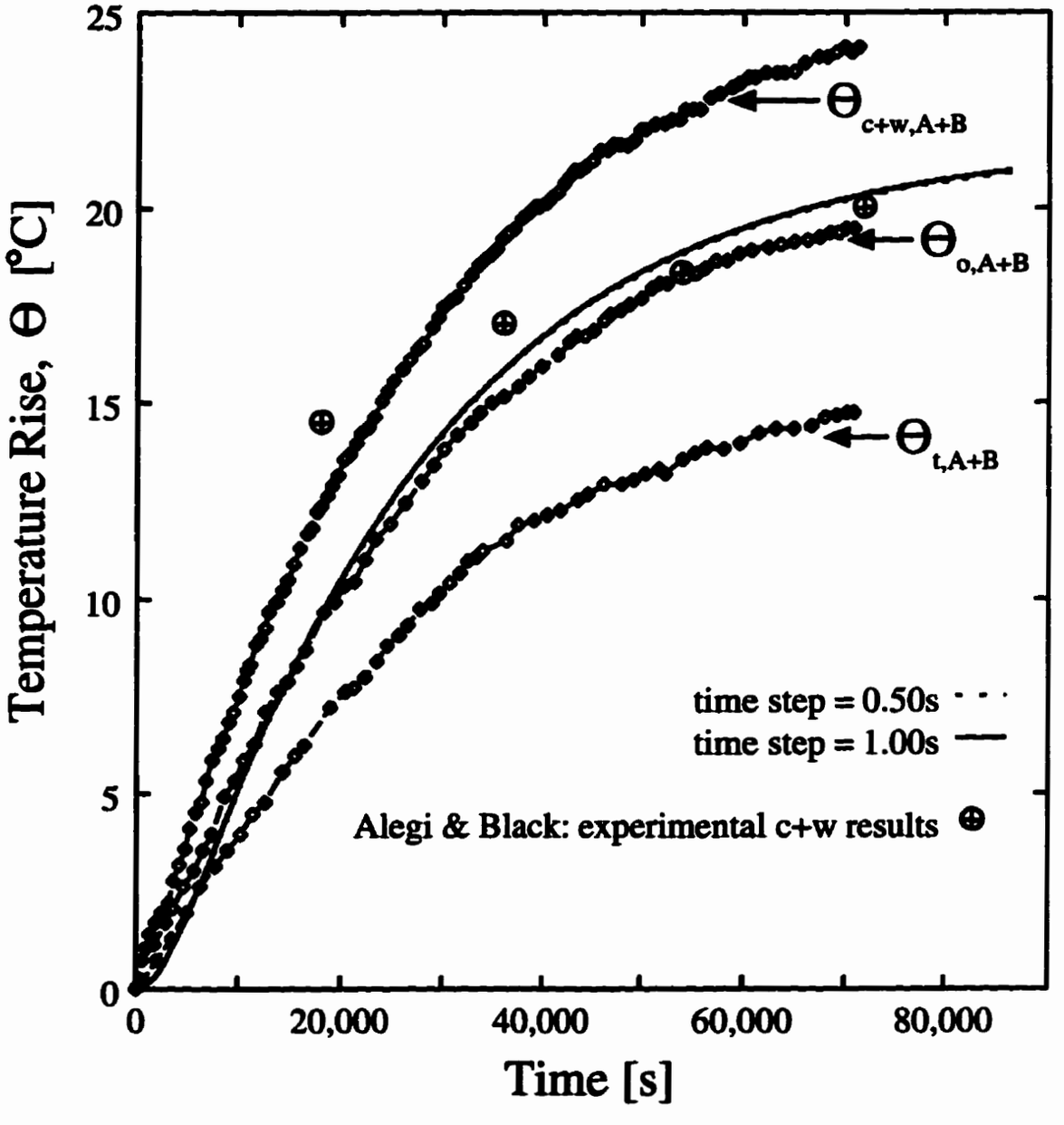

Figure C.7: Alegi and Black time independence run for 100x102 grid: top oil cavity.

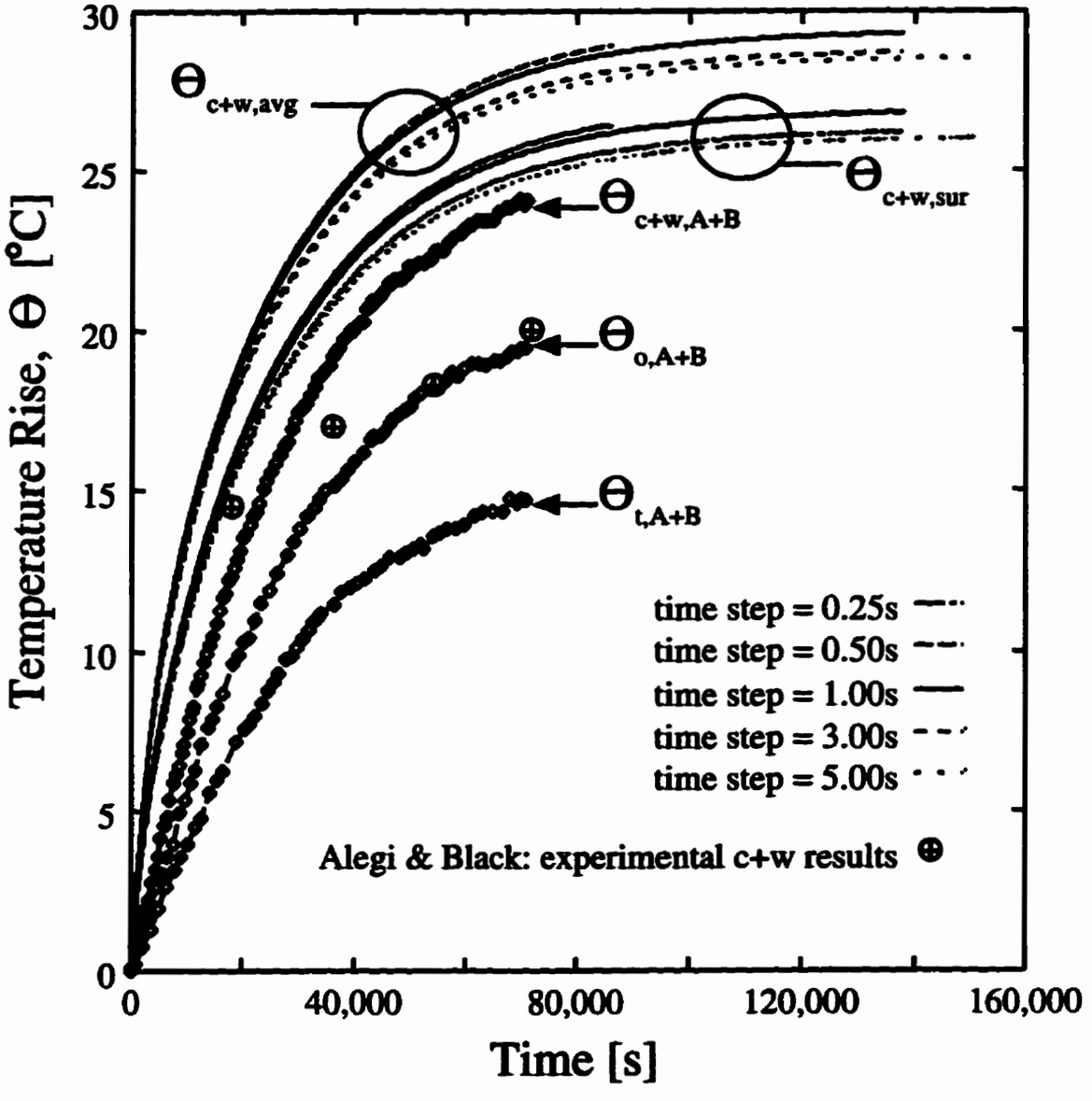

Figure C.8: Alegi and Black time independence run for 73x73 grid: core and windings.

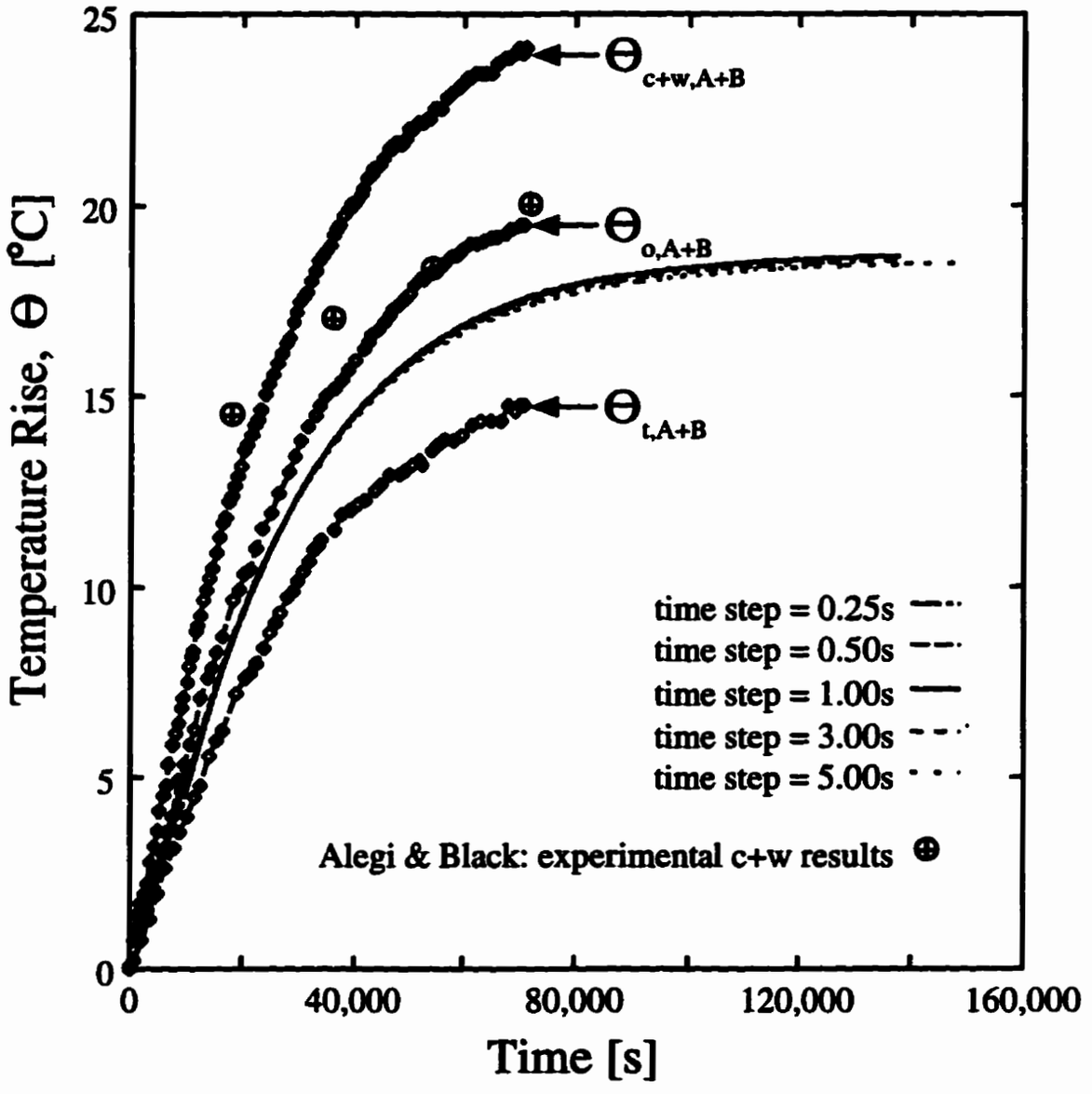

Figure C.9: Alegi and Black time independence run for 73x73 grid: right oil cavity.

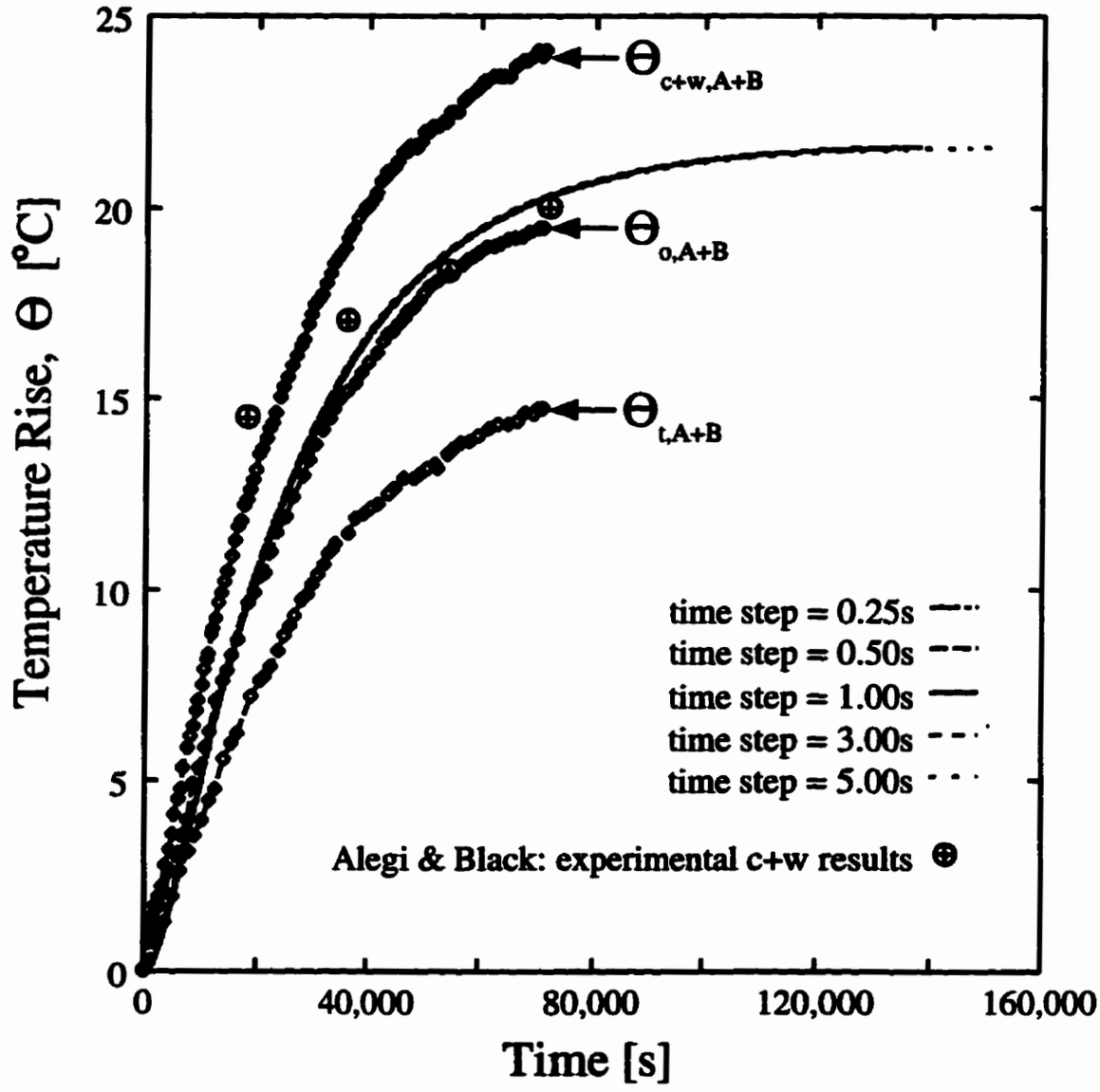

Figure C.10: Alegi and Black time independence run for 73x73 grid: top oil cavity.

C.2 Grid Independence

This section shows the results of the grid independence runs. There are three plots, Figures C.11 through C.13; one for each component: core and windings, right oil cavity, and the top oil cavity. All the runs are shown for a one second time step, except the 100×152 grid since only one run was conducted for this case. Only the 54×51 grid showed a discrepancy in the results. The 54×51 grid produced average core temperatures almost five degrees higher than the other grids. Therefore, the 73×73 grid was used for the analysis of all the other transformer test models since it produced results close to those of the finer meshes, and required less time to solve.

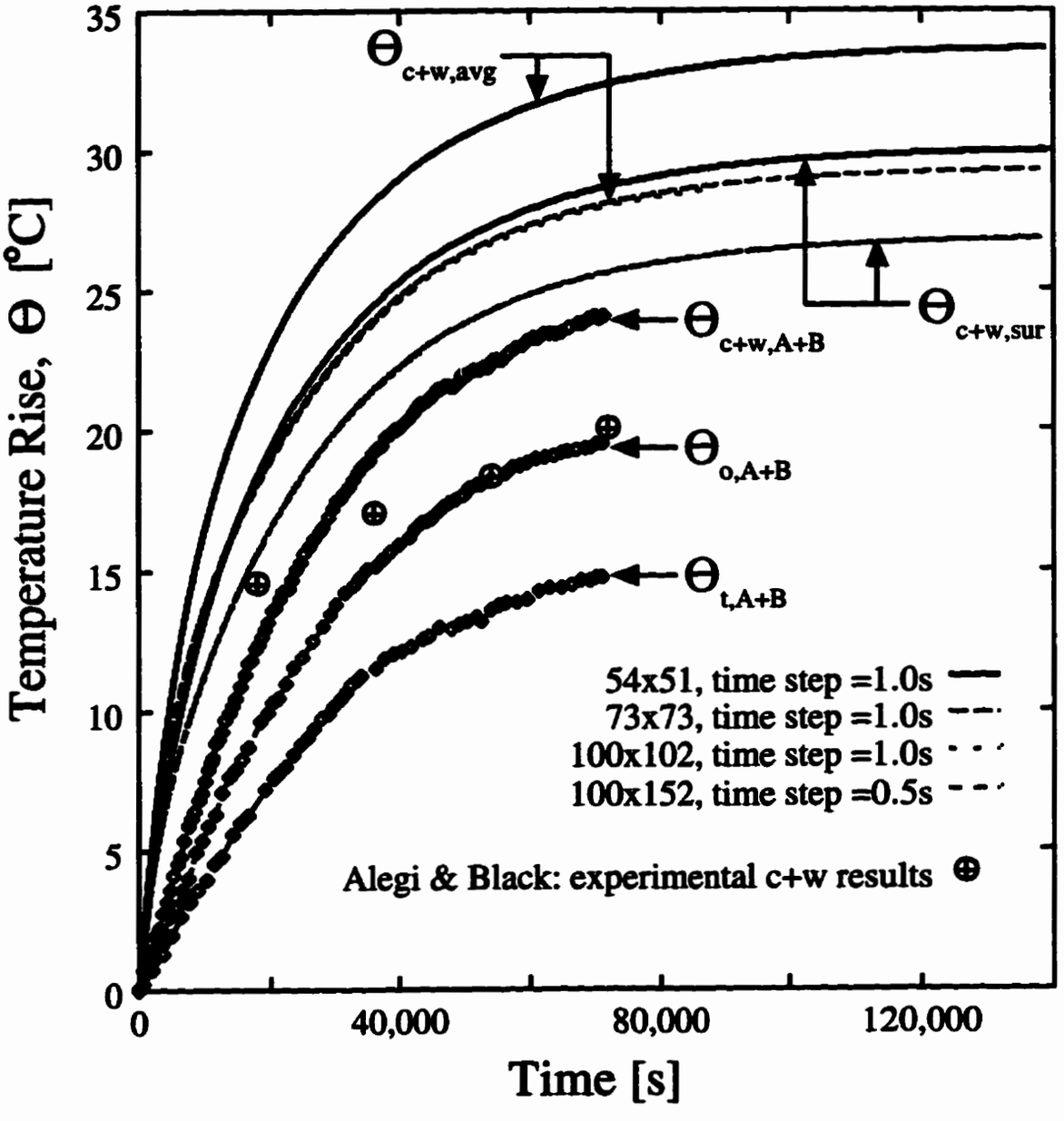

Figure C.11: Alegi and Black grid independence run: core and windings.

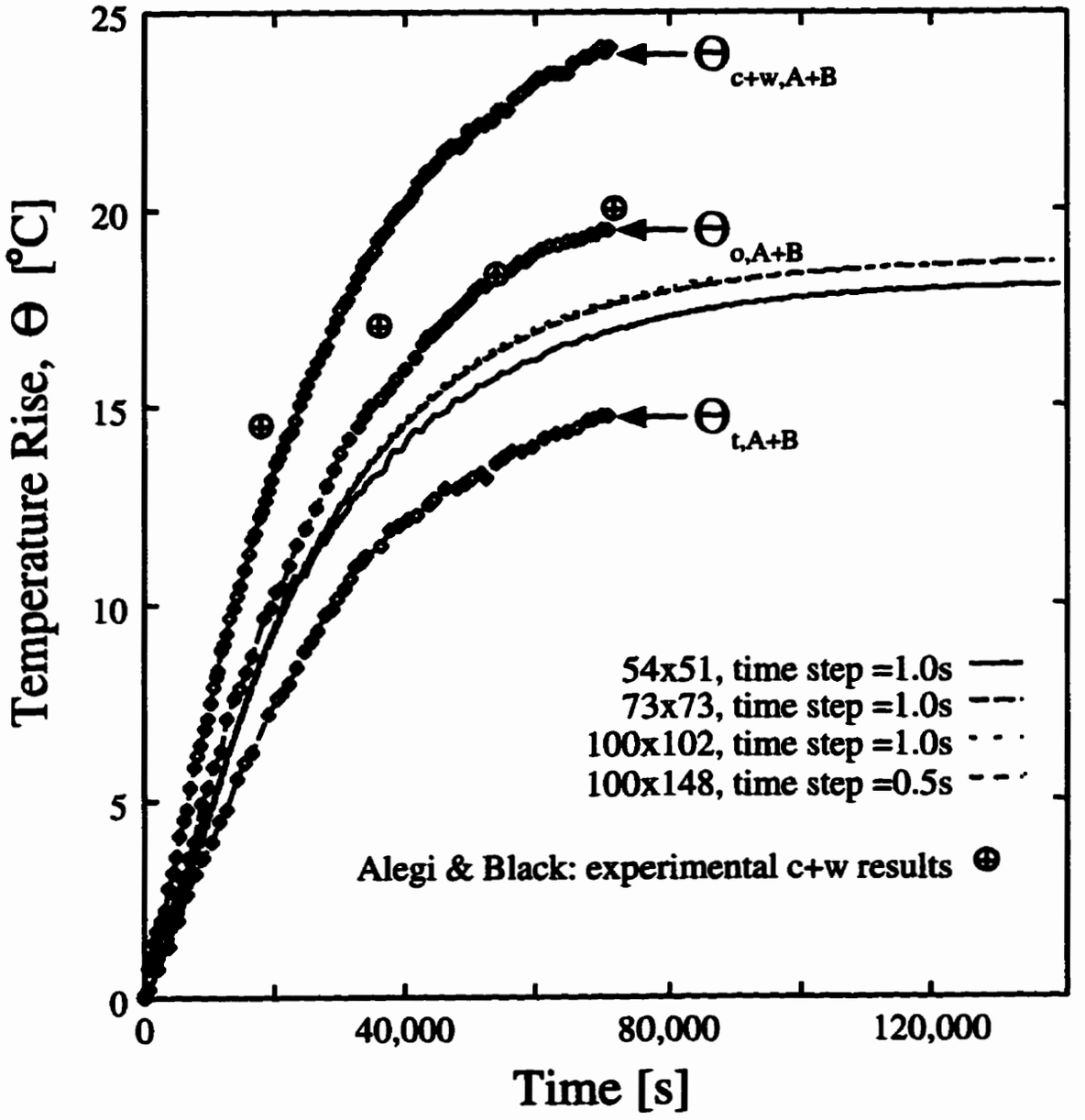

Figure C.12: Alegi and Black grid independence run: right oil cavity.

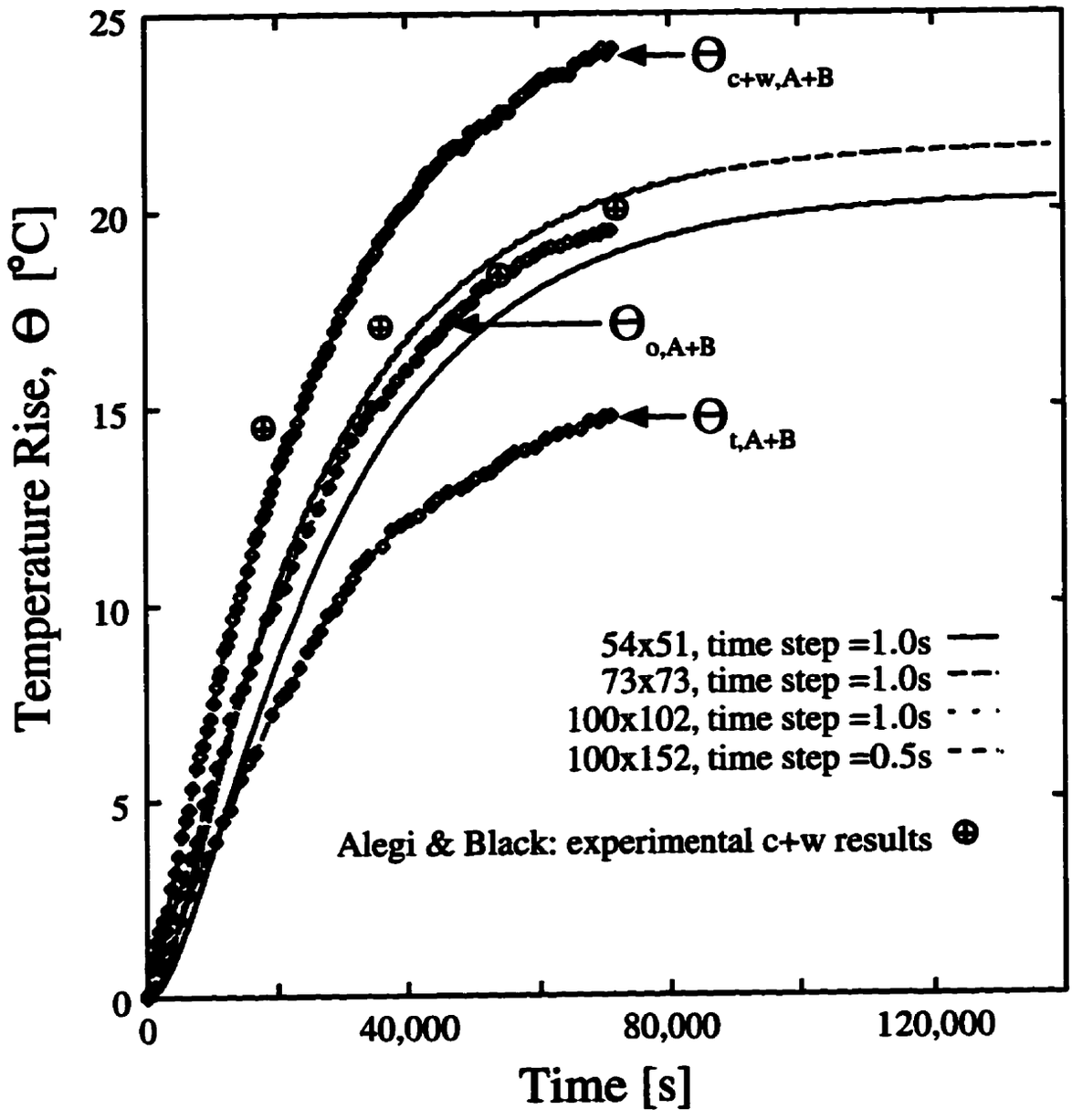

Figure C.13: Alegi and Black grid independence run: top oil cavity.

Appendix D

Effective Winding Thermal Conductivity

In order to reduce the number of control volumes, the components of the windings are lumped together to constuct a homogeneous model of equivalent thermal properties. This appendix describes the method used to calculate the equivalent thermal conductivity for this homogeneous material.

D.1 Background

A two-dimensional nonhomogeneous region must be simplified so that it can be represented by an equivalent x direction thermal conductivity, y direction thermal conductivity, overall specific heat, and average density. The specific heat and the density are volume averaged.

A two-dimensional problem is shown to be *equivalent* to a combination of two thermal circuits as discribed by Soliman et al. [58]. These approximations are validated against a direct analytical solution of the domain. Their research shows that

the choice of approximations depends on parameters such as geometry and thermal conductivity.

Using the same theory as [58], Crane and Vachon [13] show that a square, three-dimensional domain can be given an equivalent thermal conductivity. The concept of a uniform heat flux and parallel isotherm model is used to give two thermal conductivities for granular materials. The experimental results showed that the two equations bounded the experimental data. Cheng and Vachon [12] also compared experimental results with their equivalent thermal circuit model. A equivalent thermal resistance is calculated by integrating over the domain.

Goel et al. [21] calculate the effective thermal conductivity by using parallel, uniform heat flux strips integrated across the face of the medium. A separate thermal conductivity is calculated for the x and the y directions for use in a finite difference model. The results are compared against a finite element-based numerical modelling software package known as ANSYS. A comparison of the finite element and the finite difference runs showed that the approximate thermal conductivity produced excellent results.

D.2 Theory for Equivalent Thermal Conductivity

Many distribution transformer windings are made up of conductor, paper insulation, and oil, components. Figure D.1 shows a typical section of the windings. To simplify the model, the thermal conductivity of this region must be replaced with effective thermal conductivities for both the x and y directions.

There are two ways of finding the equivalent thermal conductivity: constant heat flow and parallel isotherms. Figures D.2 and D.3 shows the two different thermal circuits.

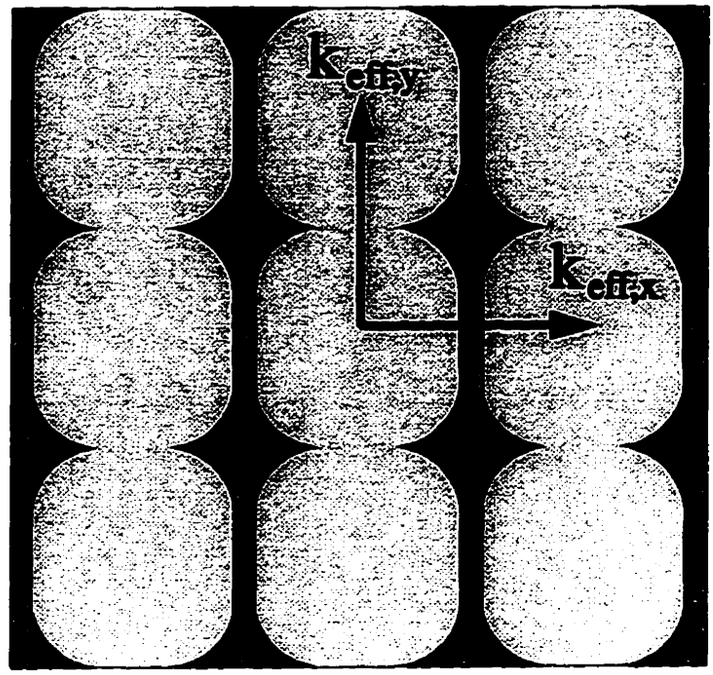

Figure D.1: A typical windings section that must have effective thermal conductivities calculated for both the x and y directions.

Constant Heat Flow Circuit

The constant heat flow approximation assumes that heat will flow in a straight line from one side of the region to the opposite side. The thermal circuit consists of parallel circuits, and the equation for the equivalent circuit takes the form

$$\frac{1}{R_{eq}} = \sum_{j=1}^{n} \frac{1}{R_j} \tag{D.1}$$

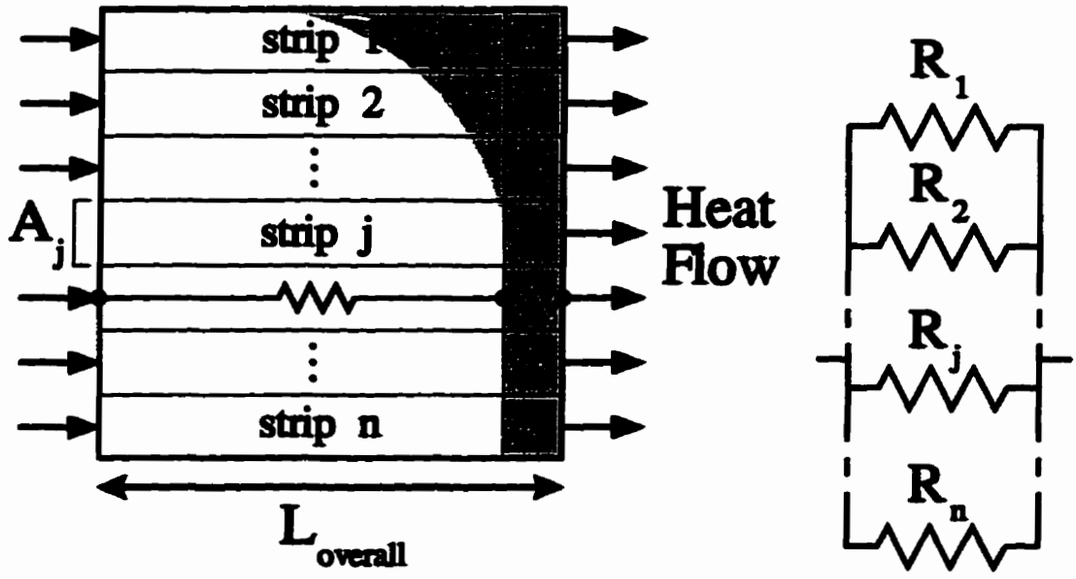

(a) Winding cross-section. (b) Equivalent thermal circuit.

Figure D.2: Equivalent circuit illustration for constant heat flow. The grayed areas represent different materials.

where R is the one-dimensional plane wall thermal resistance (L/kA). When Equation (D.1) is expanded with the definition of R it becomes

$$\frac{k_{eq}A_{overall}}{L_{overall}} = \sum_{j=1}^{n} \frac{k_j A_j}{L_{overall}} \tag{D.2}$$

where k_{eq} is the equivalent thermal conductivity and k_j is the thermal conductivity of each parallel strip. For more complicated structures, this equation can be replaced with an integration (as was done by Goel et al [21]). Within each strip there may be several materials. In this case, the equivalent thermal conductivity is calculated for each strip before the overall equivalent thermal conductivity is determined. This

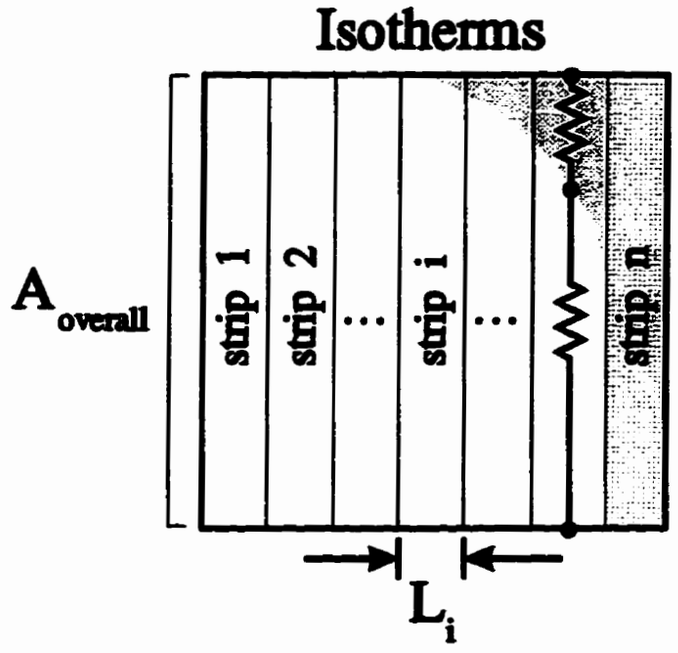

a) Winding cross-section

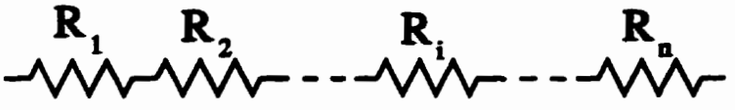

b) Equivalent thermal circuit.

Figure D.3: Equivalent circuit illustration for parallel isotherms. The grayed areas represent different materials.

may be accomplished by considering the strip as a thermal circuit in series.

$$\frac{L_{overall}}{k_{j,eq}A_j} = \sum_{i=1}^{n} \frac{L_i}{k_i A_j} \tag{D.3}$$

Parallel Isotherm Circuit

The parallel isotherm approximation assumes that the isotherms run parallel to each other and perpendicular to the direction being measured. The equation for the eqi-

valent circuit takes the form

$$R_{eq} = \sum_{i=1}^{n} R_i \tag{D.4}$$

which may be expanded to get

$$\frac{L_{overall}}{k_{eq}A_{overall}} = \sum_{i=1}^{n} \frac{L_i}{k_i A_{overall}} \tag{D.5}$$

The equivalent thermal conductivity of each strip is determined by treating each strip as thermal resistance circuit in parallel.

$$\frac{k_i A_{overall}}{L_i} = \sum_{j=1}^{n} \frac{k_j A_j}{L_i} \tag{D.6}$$

Choosing which thermal conductivity to use for each direction is problem dependent since it depends mainly on the geometry and the thermal conductivities involved.

D.3 Square Windings

Some winding conductors may be approximated by a rectangular cross-section. Figure D.4 shows an example of a winding conductor with a square cross-section. The winding cross-section may be simplified using symmetry. Paper insulates each layer of winding, as well as each individual turn of winding. The effective thermal conductivity is calculated by constant heat flow and parallel isotherm circuits for both the x and y directions.

Equivalent Thermal Conductivity in the X Direction

Figure D.5 shows the equivalent thermal circuit for constant heat flow in the x direction. Using the theory developed in Section D.2, the equivalent thermal conductivity

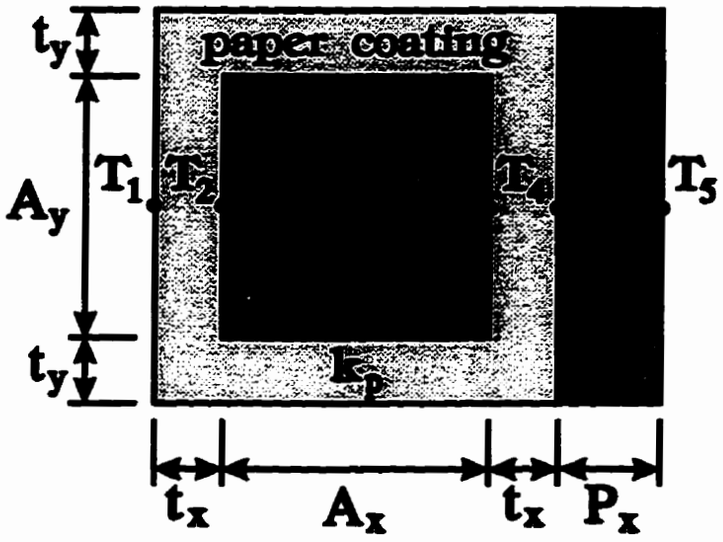

Figure D.4: Cross-section of the square winding (making use of symmetry).

is calculated from

$$\frac{1}{R_{x,eq1}} = \frac{2}{R_1} + \frac{1}{R_2 + R_3 + R_4} \tag{D.7}$$

Note that since T_4 has the same material on either side it is neglected in the thermal

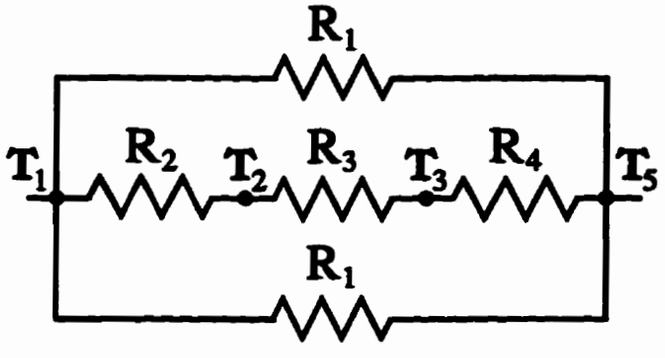

Figure D.5: Equivalent circuit illustration for constant heat flow in the x direction of the square winding.

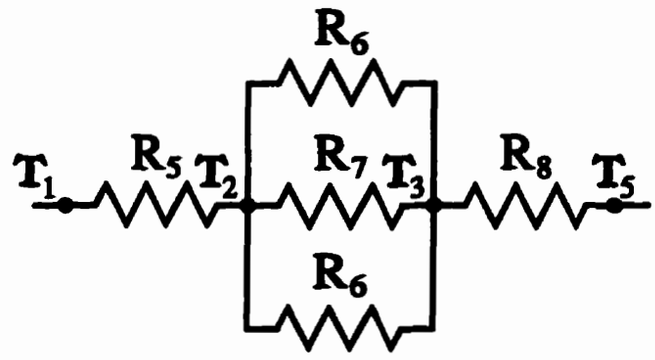

Figure D.6: Equivalent circuit illustration for parallel isotherms in the x direction of the square winding.

circuit. Equation (D.7) is expanded, then rearranged, to get

$$\frac{k_{x,eq1}\,(2t_y + A_y)}{2t_x + A_x + P_x} = \frac{2k_p t_y}{2t_x + A_x + P_x} + \frac{A_y}{\frac{2t_x P_x}{k_p} + \frac{A_x}{k_c}} \tag{D.8}$$

Figure D.6 shows the equivalent thermal circuit for parallel isotherms for the x direction, and the thermal resistance equation is then derived to be

$$R_{x,eq2} = R_5 + \frac{1}{\frac{2}{R_6} + \frac{1}{R_7}} + R_8 \tag{D.9}$$

This is expanded, then rearranged, to get

$$\frac{2t_x + A_x + P_x}{k_{x,eq2}\,(2t_y + A_y)} = \frac{2t_x + Px}{k_p\,(2t_y + A_y)} + \frac{A_x}{2k_p t_y + k_c A_y} \tag{D.10}$$

Equivalent Thermal Conductivity in the Y Direction

Another two equivalent thermal conductivities are derived for the y direction. These are based on thermal circuits similiar to the thermal circuits for the x direction equivalent thermal conductivity. The equivalent thermal conductivity for constant heat flow can be written as:

$$\frac{1}{R_{y,eq1}} = \frac{1}{R_1} + \frac{1}{R_2 + R_3 + R_4} + \frac{1}{R_5} \tag{D.11}$$

$$\frac{k_{y,eq}\,(2t_x + A_x + P_x)}{2t_y + A_y} = \frac{k_p\,(2t_x + P_x)}{2t_y + A_y} + \frac{A_x}{\frac{2t_y}{k_p} + \frac{A_y}{k_c}} \tag{D.12}$$

The equivalent thermal conductivity for parallel isotherms in the y direction can be written as:

$$R_{y,eq2} = 2R_5 + \frac{1}{\frac{1}{R_6} + \frac{1}{R_7} + \frac{1}{R_8}} \tag{D.13}$$

$$\frac{2t_y + A_y}{k_{y,eq2}\,(2t_x + A_x + P_x)} = \frac{2t_y}{k_p\,(2t_x + A_x + P_x)} + \frac{A_y}{k_p\,(2t_x + P_x) + k_c A_x} \tag{D.14}$$